Self-Assembly of Globular Protein-Polymer Diblock Copolymers

by

Carla S. Thomas

B.S. Chemical & Biological Engineering
University of Wisconsin – Madison, 2009

Submitted to the Department of Chemical Engineering
in partial fulfillment of the requirements for the degree of

Doctor of Philosophy in Chemical Engineering

at the

MASSACHUSETTS INSTITUTE OF TECHNOLOGY

February 2014

Signature of Author. _____
Department of Chemical Engineering
September, 2013

Certified by: _____
Bradley D. Olsen
Assistant Professor of Chemical Engineering
Thesis Supervisor

Accepted by: _____
Patrick S. Doyle
Professor of Chemical Engineering
Chairman, Departmental Committee on Graduate Students

Self-Assembly of Globular Protein-Polymer Diblock Copolymers

by

Carla S. Thomas

Submitted to the Department of Chemical Engineering on September 25, 2013
in partial fulfillment of the requirements for the degree of
Doctor of Philosophy in Chemical Engineering

Abstract

Self-assembly of protein-polymer block copolymers provides a simple bottom-up approach towards protein nanopatterning for the fabrication of more effective and efficient bioelectronic and biocatalytic devices. Changes in shape and surface chemistry between protein-polymer conjugates and classical coil-coil block copolymers result in significant differences between the self-assembly of these two classes of molecules. A model material is used to explore the self-assembly behavior of globular protein-polymer block copolymers as well as investigate protein functionality, stability, and secondary structure in the resulting nanostructured materials.

Across a wide range of polymer coil fractions from 0.21 to 0.82, a variety of morphologies including hexagonally packed cylinders, lamellae, perforated lamellae, weakly ordered nanostructures and a disordered phase are observed. Surprisingly, a lyotropic re-entrant order-disorder transition is observed in all materials between 30 and 70 wt% indicating the solvent-mediated effective interaction potential is non-monotonic with concentration. Solid state materials are prepared through evaporation of aqueous solvent, which leads to the formation of kinetically determined nanostructured morphologies. The type of nanostructure is strongly determined by the solvent quality for the polymer block. Good solvents produce well-ordered nanostructures similar to those observed in coil-coil block copolymers, while poor solvents produced an aggregated micellar structure. Importantly, protein secondary structure remains largely unaltered, even in a completely dehydrated environment. As much as 80% of the protein solution functionality is retained in these solid state materials. This quantity depends primarily on the processing conditions, but also the polymer fraction, with ambient temperatures and materials composed of 45-60% polymer retaining the highest levels of protein functionality. Interestingly, there exists some fraction of protein functionality which is reversibly lost in the solid state and regained upon rehydration. The addition of small molecule osmolytes is demonstrated to eliminate this reversible loss and improve protein functionality retention up to 100% in the solid state. Osmolytes with a high glass transition temperature are capable of increasing the thermal stability of dehydrated films by 15 °C, while those with a low glass transition temperature decrease it.

Thesis Supervisor: Bradley D. Olsen
Title: Paul M. Cook Career Development Assistant Professor of Chemical Engineering

In memory of Gwendolyn Thomas.

Table of Contents

List of Figures

List of Tables

List of Schemes

Chapter 1 Introduction

1.1 The Utility of Proteins and Enzymes

Enzymes are nature's catalysts. In most cases, they have evolved over many, many years to excel in the performance of a single task or a set of related reactions. They have adapted to perform one reaction extremely quickly and efficiently under mild conditions. Typical turnover frequencies (k_{cat}) for enzymes range from 10^{-1} up to 10^{7} s^{-1}, and substrate binding affinities ($\sim 1/K_m$) are often large as well.[1-2] More importantly, substrate specificities (k_{cat}/K_m) can be extremely high signifying that side reactions and undesired products are rare.[1-2] In contrast, current traditional synthetic catalysts tend to have turnover frequencies in the range of $10^{-2} - 10^{2}$, and they can be more susceptible to side reactions due to non-selective substrate binding which could dramatically limit their utility in certain situations when the feedstock contains impurities.[3-4] Additionally, enzymes are biodegradable and renewable unlike many synthetic catalysts which often rely on expensive precious metals. As a result of these factors, there is a growing interest in the incorporation of enzymes into a variety of biocatalytic devices with applications as varied as the enzymes themselves.[5-7] Bioelectronic devices are created through the incorporation of reaction centers,[8] photosynthetic complexes,[9] or even fluorescent proteins[10] into highly efficient materials for light harvesting. Biosensors capable of detecting extremely low levels of analyte are becoming increasingly prevalent in the medical diagnostics field pioneered by the huge success of glucose oxidase for the detection of glucose in diabetes patients as well as the detection of hormones in home pregnancy test devices.[11-13] And in the pharmaceutical industry, enzymes have been widely used for synthesizing drug compounds.[14] Biofuel cells utilizing enzyme catalysis have been successful at producing a number of

commodity chemicals or valuable precursors.[15-17] Additionally, a number of biocatalytic devices have utilized the highly efficient nature of enzymes to fabricate devices for carbon sequestration,[18] carbon dioxide reduction,[19-21] and hydrogen production.[22-24]

1.2 Challenges for Enzyme Use

Although there are clearly benefits for the incorporation of enzymes into functional devices, limitations to their widespread use exist. One of the biggest concerns is the stability of the enzyme. While the native protein structure is robust enough to self-assemble in its natural environment, it may be prone to denaturation or unfolding when placed in a foreign environment.[25] Protein performance also often depends on the surrounding environment, and many proteins will typically only function in aqueous solutions within some narrow pH and temperature range.[26-27] In addition to ensuring that the protein remains properly folded, access to the active site must remain unobstructed to allow for substrate binding and product release. Maintaining fast and efficient transport of substrates, products, and cofactors throughout is also necessary for efficient, long-lasting devices.[28-29] Good transport of electrons is particularly important for the successful implementation of enzymatic biofuel cells.[15-16] Additionally, achieving high enzyme loading densities will be crucial for the fabrication of new high impact devices which are not reaction limited or for devices in which size is a limiting constraint.[30] These challenges must be addressed in order to compete both catalytically and economically with traditional synthetic catalysts.

1.3 Techniques for Nanopatterning Proteins

Nanopatterning of enzymes is a promising option for mitigating the challenges previously outlined. Through the use of nanopatterning techniques, the positioning of enzymes can be controlled in three dimensions. In addition, protein orientation can be selected to allow for

optimal arrangement of active sites for substrate and product transport.[31] Using the precise placement afforded by nanopatterning, high loading densities of functional enzyme can be achieved.[32] Enzyme stability concerns can also be addressed through the use of nanopatterning. A number of studies have investigated the use of various forms of nanopatterning or protein immobilization to improve enzyme performance,[32-34] and many approaches fit into one of the following categories: covalent immobilization, physical adsorption, affinity immobilization, or encapsulation in a matrix.[35-41]

Covalent immobilization. Covalent immobilization of proteins on surfaces has been achieved using a variety of synthetic schemes. In many cases, the surface is pre-treated to display a desired functionality, compatible with the chosen immobilization chemistry. The covalent bond between the protein and surface ensures that the protein is not washed or eroded away during subsequent processing steps or during use. Chemistries utilizing a variety of functional groups including amines, carboxyls, thiols, epoxies, and photoactive materials have been developed for protein immobilization.[5, 37, 41-42] Glutaraldehyde has been shown to be a viable option for enzyme immobilization on a variety of surfaces due to the ability of glutaraldehyde to react with a range of nucleophiles.[43] Amine and carboxyl chemistries are especially popular because many proteins contain solvent accessible lysine, aspartate and glutamate residues. However, there are many potential attachment sites on the protein surface, and when utilizing these types of non-site specific chemistries enzymes often end up in a variety of orientations, some of which do not remain catalytically active.[44-45] Other chemistries using less prevalent functionalities such as thiols make it possible to constrain protein orientation to some extent.[46-48] By carefully choosing the immobilization chemistry as well as using site directed mutagenesis where possible to present desired protein surface chemistries, the orientation of the immobilized enzyme can be

guided.[44] Glucose oxidase is one of the most studied enzymes; as a result, a wide range of more specialized immobilization strategies have been extensively examined with this system including covalent attachment to self-assembled monolayers[49] and gold nanoparticles[50] to fabricate stable and effective biosensors. In a creative approach to covalent immobilization, a serine esterase was covalently attached to a surface which had been functionalized with an inhibitor which selectively binds to the enzyme active site.[51] This approach was then generalized and became known as a SNAP-tag by creating fusion proteins with the serine esterase so that other enzymes could be immobilized effectively.[51-52]

In order to maintain the highest levels of enzymatic activity after surface immobilization, a short linker is often used to connect the protein with the surface.[5] Enzymes which are immobilized with many attachment points have been shown to be more stable to heat, detergent, and organic solvent stressors than enzymes with only a single attachment point.[53-55] Multipoint attachment techniques such as those making use of epoxies have been shown to effectively immobilize a variety of enzymes while often retaining high levels of native enzyme activity.[56]

Physical adsorption. Physical adsorption is another common technique used to immobilize proteins on a surface.[57-59] This method typically relies on electrostatic, ionic, hydrophobic, or hydrogen bonding interactions between the protein and the substrate, and results in surface coverage that is more prone to erosion than covalent immobilization.[57, 60] However, the lack of covalent modifications to the protein makes this technique appealing for more sensitive proteins which may be more likely to denature upon covalent attachment.[61] This technique also allows for some control over enzyme orientation because certain configurations may be preferred as a result of different substrate surface chemistries and various ionic and electrostatic

interactions.[57,62-63] A variety of enzymes have been immobilized on self-assembled monolayers, demonstrating the efficacy of physical adsorption for protein nanopatterning.[64]

A related technique that relies on protein adsorption is layer-by-layer assembly in which many layers of protein may be built up by alternating between positively and negatively charged species, and in this way, three dimensional nanopatterns can be assembled.[65-66] In many cases, enzymes are layered with polyelectrolytes to create a series of nanodomains which are just a few nanometers thick.[67-68] This technique has been used to fabricate biosensor and biocatalytic devices, and in some cases has shown no enzymatic activity loss as a result of the nanopatterning process.[67] The accompanying polymer can also be designed such that it conducts electrons or other species necessary for enzyme activity and the fabrication of functional biocatalytic devices.[69-70]

Affinity interactions. The third technique for protein nanopatterning, affinity-based immobilization, shares similarities with both covalent immobilization and physical adsorption. Although affinity tag approaches are non-covalent, the interaction between the protein and substrate can still be very strong and nearly permanent. For example, the interaction between biotin and avidin has an association constant of 10^{15} $L \cdot mol^{-1}$.[71] By taking advantage of this strong interaction, enzymes can be immobilized on a variety of surfaces including carbon fiber, platinum electrodes, or polymer coated surfaces to fabricate sensors for glucose or peroxide detection.[72-74] Through the use of alternating layers of avidin and biotinylated enzymes, highly functional biosensor devices can be fabricated which are composed of multiple types of enzymes.[75] Nanopatterning of antibodies which specifically recognize certain proteins has also been employed for the construction of immobilized arrays of oriented enzymes.[31, 76-77] By covalently attaching a multivalent nitrilotriacetic acid functional group to the substrate surface,

His-tagged proteins can be tightly bound to the surface in a desired orientation.[78-80] When this was performed with horseradish peroxidase, more than 85% of the native enzyme activity was retained.[81]

Embedding in a matrix. A fourth technique which is relatively common for protein immobilization is embedment in a protective matrix. The matrix provides a structural framework with mechanical integrity and generally allows for increased flexibility in terms of the types of processing procedures for device fabrication that can be tolerated by the enzymes. For example, the rigidity provided by a matrix of organic molecules helps to improve protein stability, and the small pore sizes help prevent enzyme loss due to leaching.[82-83] The pore sizes within the materials are such that the enzyme is not lost due to leaching, while small substrates and cofactors are permitted to diffuse through the material. Additionally, the potential for UV transparency of these types of materials makes them attractive scaffolds for the fabrication of biosensor devices.[84-85] Several enzymes have been shown to remain active upon encapsulation in sol-gel matrices including, myoglobin, glucose oxidase, and cytochrome *c*.[82-84, 86-87] Typically, encapsulation in a sol-gel matrix results in enzymes which remain functional much longer while still following traditional Michaelis-Menten kinetics. The enzymes also have slightly lower substrate binding constants and turnover frequencies.[83, 88] While sol-gels are among the most popular materials in which to embed proteins, other polymeric materials such as epoxies, polyvinyl plastics, polyurethane foams, silicone elastomers, and silk have also been utilized.[89-95] For example, glucose oxidase was immobilized in polytyramine which formed a protective matrix and was shown capable of maintaining high levels of enzymatic activity.[96] Also, phosphotriesterase (organophosphate hydrolase; OPH) entrapped in a polyurethane foam was demonstrated to retain more than 50% of its activity after three months of storage.[97]

Templated surfaces. With the previously described covalent and non-covalent surface immobilization techniques, three dimensional protein patterns can be generated by choosing a suitable substrate. Nanoparticles, electrospun fibers, and mesoporous silica have all been utilized to create different geometries, each of which are capable of maintaining high levels of enzymatic activity.[35, 98-99] The fibers and mesoporous materials are especially intriguing because they have a very high surface area to volume ratio for maximal enzyme loading.[98] For example, one study demonstrated that carbonic anhydrase immobilized on a mesoporous substrate maintained activity levels similar to that of free enzyme in solution and was able to remain active for at least 20 days.[100] By covalently immobilizing α-chymotrypsin on electrospun polystyrene nanofibers, the catalytic activity in nonaqueous solvents increased several thousand-fold over the native enzyme in the same organic solvent.[101] This corresponds to an activity retention of approximately 65% of native aqueous enzymatic activity. Additionally, all of these surface immobilization techniques can take advantage of developed technologies such as photolithography, dip-pen lithography, and microcontact printing to produce desired template geometries for nanopatterning.[52,62,75,102-105] For example, covalent immobilization in microfluidic devices has been successfully used to create enzymatic microreactors.[106]

Polymeric materials can also be used to create templates for protein patterning by taking advantage of their intrinsic self-assembly properties.[107-111] For example, a polystyrene-block-poly(ethylene oxide) block copolymer was self-assembled with protein which had several short poly(ethylene oxide) chains covalently attached, and it was demonstrated that the protein was selectively segregated to the poly(ethylene oxide) domains of the block copolymer.[112] In another study, the aqueous self-assembly of Pluronics block copolymers was used to template Light Harvesting Complex II protein to fabricate a device for photo-dependent hydrogen production.[113]

And in other research, photosynthetic reaction center enzymes were templated by the self-assembly of lipid-based materials to create a light harvesting device.[114]

1.4 Block Copolymer Self-Assembly

Block copolymer self-assembly offers a simple and elegant approach for nanopatterning materials.[115] Diblock copolymers are composed of two chemically dissimilar polymers which are covalently linked at a single point. The self-assembly behavior of these materials is governed by a balance between enthalpic interactions which are dominated by unfavorable mixing between the two blocks and an entropic penalty for chain stretching at the interface between the two polymers.[116] The utility of block copolymers lies in their ability to self-assemble into uniform, periodic structures on the length scale of 5-100 nm. The size and geometry of the nanostructures formed from self-assembly of coil-coil diblock copolymers in the bulk depends on the relative volume fraction of one block, f_A, and the interaction between the two blocks characterized by the Flory-Huggins parameter, χN.[117-118] A variety of thermodynamically stable morphologies have been achieved including spheres, cylinders, gyroids, and lamellae.[119-122]

The small interconnected nanodomains formed by block copolymers makes them ideal for efficient transport of substrates, products, and charge carriers necessary for a functioning device.[123-124] In that respect, block copolymers can also serve as excellent membranes which can be tailored to selectively allow the passage of certain molecules while restricting the flow of other species.[125-128] Block copolymers have also been used for templating materials in a variety of complex geometries for applications such as integrated circuit fabrication.[129-132] By incorporating an enzyme as one of the blocks of the block copolymer, a huge variety of added functionality becomes accessible. Now, in addition to having multiphase transport available,

devices could be made in which enzymes act as the catalyst for unique and challenging chemical transformations.

1.5 Challenges for Protein-Polymer Block Copolymer Self-Assembly

While there are many potential benefits for the incorporation of enzymes into block copolymers, there are also several challenges associated with the self-assembly behavior of these types of materials. First, enzymes do not adopt a random coil conformation as seen with synthetic coil polymers. Instead, they have a specific geometry as a result of α-helical and β-sheet motifs that define their folded structure. Second, protein surfaces are decorated with a variety of amino acids which present a heterogeneous surface unlike that found in synthetic polymers. The surface coverage of amino acids creates a patchy surface of hydrophobic, ionic, and hydrogen bond interactions. This will lead to complex interactions between the protein block and the polymer block. Finally, functional enzymes are typically sensitive to their surrounding environment, so the usual processing techniques for block copolymers such as thermal annealing are not feasible. Block copolymers are typically annealed above their glass transition temperature in order to remove defects and speed up the kinetics of self-assembly.[133] This approach will not be possible when using enzymes, as the protein structure would unfold before the glass transition temperature is reached. This means that solvent casting and annealing is required, and indicates that an understanding of the kinetics of self-assembly will be very important.[134-139] At this point, it is unclear how these additional complexities in geometry, chemistry, and stability will ultimately affect the self-assembly behavior of these types of protein-polymer block copolymer materials. In this thesis, some of these additional complications for self-assembly associated with protein-polymer block copolymers will be studied.

1.6 Variations on Block Copolymer Architecture

Several areas of research have focused on understanding the self-assembly of synthetic block copolymers with non-traditional geometries. For example, rod-coil block copolymers are becoming increasingly popular, in part due to the ability of some rod homopolymers to conduct charges.[140-142] Several studies have investigated their self-assembly behavior and have observed a variety of morphologies including zigzag and arrowhead structures unique to these systems.[143-147] Because of the asymmetry inherent in rod-coil block copolymers, the phase diagram is not symmetrical as in coil-coil block copolymers.[148-149] Due to the highly extended nature of rod polymers, lamellar and hexagonal morphologies are found in different regions of phase space than for coil-coil block copolymers, while other types of morphologies have never been observed in rod-coil block copolymers.[150-151] Additionally, the liquid crystalline behavior typical in rod-coil block copolymers leads to unique interfacial and packing constraints.[152] Importantly, two more parameters in addition to f_A and χN are required to fully describe the phase behavior of these materials: the Maier-Saupe interaction parameter and the coil to rod length ratio.[148] Combinations of these parameters lead to a variety of amorphous and liquid crystalline phases with several observed order-order transitions.[153]

As with rod-coil diblock copolymers, the phase diagram for disk-coil block copolymers is also no longer symmetric. In this system, three parameters are required to fully describe the self-assembly behavior: the coil fraction, the reduced temperature, and the central monomer interaction parameter.[154-155] These types of disk-shaped molecules also self-assemble into a variety of amorphous and nematic phases.[156] Columnar nanostructures are often observed as a result of π-π stacking, hydrogen bonding, and hydrophobic interactions among the disks.[157-158]

A third variation on block copolymer morphology is dendrimer-coil block copolymers. Here, the symmetry of the system is altered primarily due to the change in interfacial curvature introduced by the bulky dendrimer block.[159-160] As with the other block copolymer variations, the nanostructures formed by these materials can be highly dependent on processing conditions.[161] Amphiphilic Janus dendrimers have been shown to self-assemble into a variety of morphologies in solution including polygonal dendrimersomes, ribbon micelles, and disklike micelles.[162] The formation of these unique structures which are typically not observed in coil-coil block copolymers can be partially attributed to the molecular rigidity of the dendrimer architecture.

1.7 Protein-Polymer Bioconjugates

Bioconjugate synthesis. A vast array of synthetic techniques and approaches have been used for creating a wide variety of protein-polymer bioconjugates.[163] These design schemes can be broadly classified into the following categories: grafting-from, grafting-to, cofactor reconstitution, and affinity binding.[164-166] All four of these techniques can site-specifically link a single polymer with a protein; however, both the grafting-from and grafting-to approaches have also been used extensively for attaching many polymers to a single protein molecule.[167-168] For all these approaches, an abundance of controlled polymerization techniques, most notably atom transfer radical polymerization (ATRP) and reversible addition-fragmentation chain transfer (RAFT) polymerization, have been used in order to obtain bioconjugates with consistent and uniform sizes.[168-169] Typically, lower molecular weight polymers are used because they tend to produce higher coupling efficiencies and are easier to synthesize with low polydispersities.[169]

In the grafting-to approach, a polymer is covalently attached to a protein using a wide range of chemistries, many of which are similar to those used for covalent

immobilization.[164-165,170-171] Popular approaches include amine and carboxylic acid chemistries which are most commonly observed in cases where multiple polymer attachments are desired.[172-173] Other site-specific reactions such as thiol-maleimide coupling,[174-175] native chemical ligation,[176-177] Staudinger ligation,[178-179] and azide-alkyne click chemistry[180-182] are becoming increasingly popular as researchers strive to gain more control over the molecular topology of bioconjugate materials. The grafting-to approach is often utilized partly because of the broad range of polymerization conditions available which do not necessarily have to be compatible with proteins.

In the grafting-from approach, a polymer is grown off of the protein itself, removing the need for a potentially tricky bioconjugation reaction with a large polymer molecule.[183-184] With this technique the likelihood of unconjugated protein is strongly diminished; however, the polymerization reaction must be compatible with the protein and reaction conditions must not cause denaturation.

Cofactor reconstitution has been used particularly with proteins which have a metal coordination or heme center such as myoglobin or horseradish peroxidase.[185-188] In this case, the cofactor is covalently bound to a polymer, and upon mixing with the apoprotein, a bioconjugate is formed.

Affinity binding for bioconjugation is very similar to that for immobilization. In one approach, the protein is synthesized with a His-tag and the corresponding polymer is end-functionalized with nickel nitrilotriacetic acid.[189-191] In another method, biotin functionalized polymers are conjugated with streptavidin protein to create bioconjugate molecules.[192-193] While both cofactor reconstitution and affinity binding are not permanent bonds, they are often quite strong.

Self-assembly behavior. In addition to exploring new methods for synthesizing protein-polymer block copolymers, several research groups have also studied the self-assembly behavior of these materials. Much of the effort thus far has focused on observing and quantifying the behavior of these molecules in dilute or semi-dilute solution. Commonly studied PEGylated proteins have been widely used to enhance the lifetime of proteins in the biopharmaceutical industry.[194-195] While some bioconjugates are amphiphilic at ambient conditions, many take advantage of a responsive polymer which becomes insoluble upon exposure to stimuli such as light, temperature or pH to drive self-assembly.[196-199] A variety of kinetically trapped morphologies have been observed including micelles, vesicles, and toroids.[200-201] These morphologies are typically strongly dependent on the relative polymer coil fraction as well as the processing conditions used to prepare the sample.[200] By conjugating a thermoresponsive polymer with ferritin, bionanoparticles suitable for controlled release applications were formed reversibly upon raising the solution temperature above the thermal transition of the polymer block.[202] Several proteins have been conjugated to poly(N-isopropyl acrylamide) and reversible aggregate structures have been demonstrated by dynamic light scattering and electron microscopy.[174, 202-209] The types of nanostructures formed have been most dependent on the polymer molecular weight as well as the rate of heating.[210] Similar results have been obtained using other thermoresponsive polymers, with the thermal transition temperature being tuned by using different polymer chemistry.[211-212] Recently, fusion proteins constructed completely biosynthetically from an enzymatically functional protein and a thermoresponsive elastin-like protein, have been shown to self-assemble into aggregate nanoparticles similar to those formed by protein-polymer conjugates.[213-214] Other bioconjugates, such as those containing poly(ethylene glycol) or polystyrene are amphiphilic and form nanostructures without the need

for an external stimulus.[188, 215-219] Bioconjugates with polystyrene-b-poly(ethylene glycol) block copolymers attached to myoglobin and horseradish peroxidase were shown to form a variety of micellar aggregates in water depending on the length of the insoluble polystyrene block.[187] Also, protein-lipid conjugates have been demonstrated to orient proteins within a bilayer structure.[220]

Fewer studies have examined the self-assembly of protein-polymer conjugates in a concentrated gel or solid material. A few research groups have demonstrated the ability to self-assemble protein-polymer conjugates with compatible coil-coil diblock copolymers as a method for protein nanopatterning in a dehydrated environment.[112, 221] Bulk ionic complexes between proteins and polymers have shown the ability to retain significant levels of protein activity in a solvent-free environment.[222-223] Other studies of ionic complexation of a protein with micelle-forming block copolymers demonstrated the formation of nanotemplated films upon the removal of water.[224] Finally, studies of protein-polymer diblock copolymers demonstrate that these materials self-assemble in 30-50 wt% gels with good long-range ordering.[225]

1.8 Thesis Overview

This thesis describes the synthesis and self-assembly behavior of a model globular protein-polymer diblock copolymer, mCherry-b-poly(N-isopropyl acrylamide). Chapter 2 contains a detailed description of the synthesis methods and characterization techniques employed throughout this work. Chapter 3 presents the first demonstration of the bulk self-assembly of the protein-polymer block copolymer in the solid state. Here, it is shown that the protein retains some functionality in the solid state, and initial evidence suggests that nanostructure formation is highly dependent on material processing history. In Chapter 4 the processing dependent self-assembly behavior is explored in more detail as the effect of solvent selectivity for the protein and polymer blocks during both sample casting and solvent annealing

is studied. The ability to improve protein functionality retention in solid state nanostructures using small molecule osmolytes is studied in Chapter 5. Finally, in Chapter 6 a phase diagram for the self-assembly of this model globular protein-polymer diblock copolymer is presented as a function of polymer coil fraction and conjugate concentration.

1.9 References

1. T. D. H. Bugg, *Introduction to Enzyme and Coenzyme Chemistry*, John Wiley & Sons, Ltd, 2012, pp. 26-49.
2. S. G. Burton, D. A. Cowan and J. M. Woodley, *Nat. Biotechnol.*, 2002, **20**, 37-45.
3. D. K. Chakrabarty and B. Viswanathan, *Heterogeneous Catalysis*, Tunbridge Wells, New Age Science, 2009.
4. A. F. Carley and M. W. Roberts, *Surface Chemistry and Catalysis*, Kluwer Academic/Plenum Publishers, 2002.
5. I. Willner and E. Katz, *Angew. Chem., Int. Ed.*, 2000, **39**, 1180-1218.
6. D. A. LaVan and J. N. Cha, *Proc. Natl. Acad. Sci. U.S.A.*, 2006, **103**, 5251-5255.
7. S. J. Benkovic and S. Hammes-Schiffer, *Science*, 2003, **301**, 1196-1202.
8. R. J. Cogdell, A. Gall and J. Köhler, *Q. Rev. Biophys.*, 2006, **39**, 227-324.
9. R. Das, P. J. Kiley, M. Segal, J. Norville, A. A. Yu, L. Y. Wang, S. A. Trammell, L. E. Reddick, R. Kumar, F. Stellacci, N. Lebedev, J. Schnur, B. D. Bruce, S. G. Zhang and M. Baldo, *Nano Lett.*, 2004, **4**, 1079-1083.
10. J. W. Choi and M. Fujihira, *Appl. Phys. Lett.*, 2004, **84**, 2187-2189.
11. M. M. Rahman, A. J. S. Ahammad, J. H. Jin, S. J. Ahn and J. J. Lee, *Sensors*, 2010, **10**, 4855-4886.
12. B. E. Rapp, F. J. Gruhl and K. Länge, *Anal. Bioanal. Chem.*, 2010, **398**, 2403-2412.
13. S. A. Butler, S. A. Khanlian and L. A. Cole, *Clin. Chem.*, 2001, **47**, 2131-2136.
14. R. N. Patel, *Coord. Chem. Rev.*, 2008, **252**, 659-701.
15. J. A. Cracknell, K. A. Vincent and F. A. Armstrong, *Chem. Rev.*, 2008, **108**, 2439-2461.
16. E. H. Yu and K. Scott, *Energies*, 2010, **3**, 23-42.
17. S. D. Minteer, B. Y. Liaw and M. J. Cooney, *Curr. Opin. Biotechnol.*, 2007, **18**, 228-234.
18. N. Favre, M. L. Christ and A. C. Pierre, *J. Mol. Catal. B: Enzym.*, 2009, **60**, 163-170.
19. T. Reda, C. M. Plugge, N. J. Abram and J. Hirst, *Proc. Natl. Acad. Sci. U. S. A.*, 2008, **105**, 10654-10658.
20. B. A. Parkinson and P. F. Weaver, *Nature*, 1984, **309**, 148-149.
21. S. Kuwabata, R. Tsuda and H. Yoneyama, *J. Am. Chem. Soc.*, 1994, **116**, 5437-5443.
22. A. A. Karyakin, S. V. Morozov, E. E. Karyakina, S. D. Varfolomeyev, N. A. Zorin and S. Cosnier, *Electrochem. Commun.*, 2002, **4**, 417-420.
23. M. Hambourger, M. Gervaldo, D. Svedruzic, P. W. King, D. Gust, M. Ghirardi, A. L. Moore and T. A. Moore, *J. Am. Chem. Soc.*, 2008, **130**, 2015-2022.
24. H. Krassen, A. Schwarze, B. Friedrich, K. Ataka, O. Lenz and J. Heberle, *ACS Nano*, 2009, **3**, 4055-4061.
25. C. M. Dobson, *Nature*, 2003, **426**, 884-890.
26. A. S. Yang and B. Honig, *J. Mol. Biol.*, 1994, **237**, 602-614.

27. N. Poklar, G. Vesnaver and S. Lapanje, *Biophys. Chem.*, 1993, **47**, 143-151.
28. D. Rotticci, T. Norin and K. Hult, *Org. Lett.*, 2000, **2**, 1373-1376.
29. V. Calabrò, S. Curcio and G. Iorio, *J. Membr. Sci.*, 2002, **206**, 217-241.
30. J. Ge, D. N. Lu, Z. X. Liu and Z. Liu, *Biochem. Eng. J.*, 2009, **44**, 53-59.
31. J. Turková, *J. Chromatogr. B*, 1999, **722**, 11-31.
32. L. Q. Cao, *Curr. Opin. Chem. Biol.*, 2005, **9**, 217-226.
33. C. Mateo, J. M. Palomo, G. Fernandez-Lorente, J. M. Guisan and R. Fernandez-Lafuente, *Enzyme Microb. Technol.*, 2007, **40**, 1451-1463.
34. C. Garcia-Galan, A. Berenguer-Murcia, R. Fernandez-Lafuente and R. C. Rodrigues, *Adv. Synth. Catal.*, 2011, **353**, 2885-2904.
35. J. Kim, J. W. Grate and P. Wang, *Chem. Eng. Sci.*, 2006, **61**, 1017-1026.
36. S. D. Minteer, *Enzyme Stabilization and Immobilization*, Springer, New York, 2010.
37. F. Rusmini, Z. Y. Zhong and J. Feijen, *Biomacromolecules*, 2007, **8**, 1775-1789.
38. D. Brady and J. Jordaan, *Biotechnol. Lett.*, 2009, **31**, 1639-1650.
39. A. Sassolas, L. J. Blum and B. D. Leca-Bouvier, *Biotechnol. Adv.*, 2012, **30**, 489-511.
40. U. Hanefeld, L. Gardossi and E. Magner, *Chem. Soc. Rev.*, 2009, **38**, 453-468.
41. W. Tischer and F. Wedekind, *Immobilized Enzymes: Methods and Applications*, 1999.
42. L. S. Wong, F. Khan and J. Micklefield, *Chem. Rev.*, 2009, **109**, 4025-4053.
43. L. Betancor, F. López-Gallego, A. Hidalgo, N. Alonso-Morales, G. Mateo, R. Fernández-Lafuente and J. M. Guisán, *Enzyme Microb. Technol.*, 2006, **39**, 877-882.
44. K. Hernandez and R. Fernandez-Lafuente, *Enzyme Microb. Technol.*, 2011, **48**, 107-122.
45. M. Minier, M. Salmain, N. Yacoubi, L. Barbes, C. Méthivier, S. Zanna and C. M. Pradier, *Langmuir*, 2005, **21**, 5957-5965.
46. M. T. Neves-Petersen, T. Snabe, S. Klitgaard, M. Duroux and S. B. Petersen, *Protein Sci.*, 2006, **15**, 343-351.
47. M. S. Belluzo, M. E. Ribone, C. Camussone, I. S. Marcipar and C. M. Lagier, *Anal. Biochem.*, 2011, **408**, 86-94.
48. C. A. Godoy, O. Romero, B. de la Rivas, C. Mateo, G. Fernandez-Lorente, J. M. Guisan and J. M. Palomo, *J. Mol. Catal. B: Enzym.*, 2013, **87**, 121-127.
49. I. Willner, A. Riklin, B. Shoham, D. Rivenzon and E. Katz, *Adv. Mater.*, 1993, **5**, 912-915.
50. W. W. Yang, J. X. Wang, S. Zhao, Y. Y. Sun and C. Q. Sun, *Electrochem. Commun.*, 2006, **8**, 665-672.
51. C. D. Hodneland, Y. S. Lee, D. H. Min and M. Mrksich, *Proc. Natl. Acad. Sci. U. S. A.*, 2002, **99**, 5048-5052.
52. S. Engin, V. Trouillet, C. M. Franz, A. Welle, M. Bruns and D. Wedlich, *Langmuir*, 2010, **26**, 6097-6101.
53. J. M. Bolivar, J. Rocha-Martin, C. Mateo, F. Cava, J. Berenguer, D. Vega, R. Fernandez-Lafuente and J. M. Guisan, *J. Mol. Catal. B: Enzym.*, 2009, **58**, 158-163.
54. V. Grazú, F. López-Gallego, T. Montes, O. Abian, R. González, J. A. Hermoso, J. L. García, C. Mateo and J. M. Guisán, *Process Biochem.*, 2010, **45**, 390-398.
55. C. Mateo, O. Abian, G. Fernández-Lorente, J. Pedroche, R. Fernández-Lafuente and J. M. Guisan, *Biotechnol. Prog.*, 2002, **18**, 629-634.
56. C. Mateo, R. Torres, G. Fernández-Lorente, C. Ortiz, M. Fuentes, A. Hidalgo, F. López-Gallego, O. Abian, J. M. Palomo, L. Betancor, B. C. C. Pessela, J. M. Guisan and R. Fernández-Lafuente, *Biomacromolecules*, 2003, **4**, 772-777.

57. K. Nakanishi, T. Sakiyama and K. Imamura, *J. Biosci. Bioeng.*, 2001, **91**, 233-244.
58. A. Sadana, *Chem. Rev.*, 1992, **92**, 1799-1818.
59. R. Fernandez-Lafuente, P. Armisén, P. Sabuquillo, G. Fernández-Lorente and J. M. Guisán, *Chem. Phys. Lipids*, 1998, **93**, 185-197.
60. S. Hudson, E. Magner, J. Cooney and B. K. Hodnett, *J. Phys. Chem. B*, 2005, **109**, 19496-19506.
61. A. Salis, D. Meloni, S. Ligas, M. F. Casula, M. Monduzzi, V. Solinas and E. Dumitriu, *Langmuir*, 2005, **21**, 5511-5516.
62. X. Z. Wang, D. J. Zhou, K. Sinniah, C. Clarke, L. Birch, H. T. Li, T. Rayment and C. Abell, *Langmuir*, 2006, **22**, 887-892.
63. J. Wiesbauer, J. M. Bolivar, M. Mueller, M. Schiller and B. Nidetzky, *ChemCatChem*, 2011, **3**, 1299-1303.
64. K. Wadu-Mesthrige, N. A. Amro and G. Y. Liu, *Scanning*, 2000, **22**, 380-388.
65. Y. Wang, A. S. Angelatos and F. Caruso, *Chem. Mater.*, 2008, **20**, 848-858.
66. O. S. Sakr and G. Borchard, *Biomacromolecules*, 2013, **14**, 2117-2135.
67. F. Caruso and C. Schüler, *Langmuir*, 2000, **16**, 9595-9603.
68. C. A. Constantine, S. V. Mello, A. Dupont, X. H. Cao, D. Santos, O. N. Oliveira, F. T. Strixino, E. C. Pereira, T. C. Cheng, J. J. Defrank and R. M. Leblanc, *J. Am. Chem. Soc.*, 2003, **125**, 1805-1809.
69. S. A. Emr and A. M. Yacynych, *Electroanaylysis*, 1995, **7**, 913-923.
70. J. C. Vidal, E. Garcia-Ruiz and J. R. Castillo, *Microchim. Acta*, 2003, **143**, 93-111.
71. M. González, L. A. Bagatolli, I. Echabe, J. L. R. Arrondo, C. E. Argaraña, C. R. Cantor and G. D. Fidelio, *J. Biol. Chem.*, 1997, **272**, 11288-11294.
72. T. Hoshi, J. Anzai and T. Osa, *Anal. Chem.*, 1995, **67**, 770-774.
73. P. Pantano and W. G. Kuhr, *Anal. Chem.*, 1993, **65**, 623-630.
74. S. V. Rao, K. W. Anderson and L. G. Bachas, *Biotechnol. Bioeng.*, 1999, **65**, 389-396.
75. D. C. Kim, J. I. Sohn, D. J. Zhou, T. A. J. Duke and D. J. Kang, *ACS Nano*, 2010, **4**, 1580-1586.
76. P. Peluso, D. S. Wilson, D. Do, H. Tran, M. Venkatasubbaiah, D. Quincy, B. Heidecker, K. Poindexter, N. Tolani, M. Phelan, K. Witte, L. S. Jung, P. Wagner and S. Nock, *Anal. Biochem.*, 2003, **312**, 113-124.
77. M. Saleemuddin, *Bioaffinity Based Immobilization of Enzymes*, 1999.
78. S. Lata and J. Piehler, *Anal. Chem.*, 2005, **77**, 1096-1105.
79. N. Haddour, S. Cosnier and C. Gondran, *J. Am. Chem. Soc.*, 2005, **127**, 5752-5753.
80. T. Yu, Q. Wang, D. S. Johnson, M. D. Wang and C. K. Ober, *Adv. Funct. Mater.*, 2005, **15**, 1303-1309.
81. R. Blankespoor, B. Limoges, B. Schöllhorn, J. L. Syssa-Magalé and D. Yazidi, *Langmuir*, 2005, **21**, 3362-3375.
82. D. Avnir, S. Braun, O. Lev and M. Ottolenghi, *Chem. Mat.*, 1994, **6**, 1605-1614.
83. W. Jin and J. D. Brennan, *Anal. Chim. Acta*, 2002, **461**, 1-36.
84. R. Gupta and N. K. Chaudhury, *Biosens. Bioelectron.*, 2007, **22**, 2387-2399.
85. E. H. Lan, B. C. Dave, J. M. Fukuto, B. Dunn, J. I. Zink and J. S. Valentine, *J. Mater. Chem.*, 1999, **9**, 45-53.
86. I. Gill, *Chem. Mat.*, 2001, **13**, 3404-3421.
87. M. T. Reetz, A. Zonta and J. Simpelkamp, *Biotechnol. Bioeng.*, 1996, **49**, 527-534.

88. R. B. Bhatia, C. J. Brinker, A. K. Gupta and A. K. Singh, *Chem. Mat.*, 2000, **12**, 2434-2441.
89. I. Gill and A. Ballesteros, *Trends Biotechnol.*, 2000, **18**, 469-479.
90. Z. Yang, A. J. Mesiano, S. Venkatasubramanian, S. H. Gross, J. M. Harris and A. J. Russell, *J. Am. Chem. Soc.*, 1995, **117**, 4843-4850.
91. P. B. Dennis, A. Y. Walker, M. B. Dickerson, D. L. Kaplan and R. R. Naik, *Biomacromolecules*, 2012, **13**, 2037-2045.
92. I. Gill, E. Pastor and A. Ballesteros, *J. Am. Chem. Soc.*, 1999, **121**, 9487-9496.
93. H. G. Zhu, R. Srivastava, J. Q. Brown and M. J. McShane, *Bioconjugate Chem.*, 2005, **16**, 1451-1458.
94. S. Z. Lu, X. Q. Wang, Q. Lu, X. Hu, N. Uppal, F. G. Omenetto and D. L. Kaplan, *Biomacromolecules*, 2009, **10**, 1032-1042.
95. E. A. Simone, T. D. Dziubla, F. Colon-Gonzalez, D. E. Discher and V. R. Muzykantov, *Biomacromolecules*, 2007, **8**, 3914-3921.
96. M. Situmorang, J. J. Gooding, D. B. Hibbert and D. Barnett, *Biosens. Bioelectron.*, 1998, **13**, 953-962.
97. K. E. LeJeune and A. J. Russell, *Biotechnol. Bioeng.*, 1996, **51**, 450-457.
98. Z. G. Wang, L. S. Wan, Z. M. Liu, X. J. Huang and Z. K. Xu, *J. Mol. Catal. B: Enzym.*, 2009, **56**, 189-195.
99. S. Phadtare, A. Kumar, V. P. Vinod, C. Dash, D. V. Palaskar, M. Rao, P. G. Shukla, S. Sivaram and M. Sastry, *Chem. Mat.*, 2003, **15**, 1944-1949.
100. M. Vinoba, K. S. Lim, S. H. Lee, S. K. Jeong and M. Alagar, *Langmuir*, 2011, **27**, 6227-6234.
101. H. F. Jia, G. Y. Zhu, B. Vugrinovich, W. Kataphinan, D. H. Reneker and P. Wang, *Biotechnol. Prog.*, 2002, **18**, 1027-1032.
102. K. L. Christman, V. D. Enriquez-Rios and H. D. Maynard, *Soft Matter*, 2006, **2**, 928-939.
103. S. K. Kwak, G. S. Lee, D. J. Ahn and J. W. Choi, *Mater. Sci. Eng. C Biomimetic Supramol. Syst.*, 2004, **24**, 151-155.
104. S. A. Alang Ahmad, L. S. Wong, E. ul-Haq, J. K. Hobbs, G. J. Leggett and J. Micklefield, *J. Am. Chem. Soc.*, 2011, **133**, 2749-2759.
105. D. Falconnet, D. Pasqui, S. Park, R. Eckert, H. Schift, J. Gobrecht, R. Barbucci and M. Textor, *Nano Lett.*, 2004, **4**, 1909-1914.
106. D. S. Peterson, T. Rohr, F. Svec and J. M. J. Fréchet, *Anal. Chem.*, 2002, **74**, 4081-4088.
107. M. Matsusaki, M. Omichi, K. Kadowaki, B. H. Kim, S. O. Kim, I. Maruyama and M. Akashi, *Chem. Commun.*, 2010, **46**, 1911-1913.
108. K. H. A. Lau, J. Bang, D. H. Kim and W. Knoll, *Adv. Funct. Mater.*, 2008, **18**, 3148-3157.
109. N. Kumar, O. Parajuli and J. Hahm, *J. Phys. Chem. B*, 2007, **111**, 4581-4587.
110. J. C. Eloi, S. E. W. Jones, V. Poor, M. Okuda, J. Gwyther and W. Schwarzacher, *Adv. Funct. Mater.*, 2012, **22**, 3273-3278.
111. D. Liu, T. Wang and J. L. Keddie, *Langmuir*, 2009, **25**, 4526-4534.
112. A. D. Presley, J. J. Chang and T. Xu, *Soft Matter*, 2011, 7, 172-179.
113. M. B. Cardoso, D. Smolensky, W. T. Heller, K. Hong and H. O'Neill, *Energy Environ. Sci.*, 2011, **4**, 181-188.
114. P. D. Laible, R. F. Kelley, M. R. Wasielewski and M. A. Firestone, *J. Phys. Chem. B*, 2005, **109**, 23679-23686.

115. C. Park, J. Yoon and E. L. Thomas, *Polymer*, 2003, **44**, 6725-6760.
116. M. W. Matsen and F. S. Bates, *Macromolecules*, 1996, **29**, 1091-1098.
117. F. S. Bates and G. H. Fredrickson, *Phys. Today*, 1999, **52**, 32-38.
118. I. W. Hamley, *The Physics of Block Copolymers*, Oxford University Press, New York, 1998.
119. V. Abetz and P. F. W. Simon, in *Block Copolymers I*, Springer-Verlag, Berlin, 2005, pp. 125-212.
120. T. P. Lodge, *Macromol. Chem. Phys.*, 2003, **204**, 265-273.
121. T. Smart, H. Lomas, M. Massignani, M. V. Flores-Merino, L. R. Perez and G. Battaglia, *Nano Today*, 2008, **3**, 38-46.
122. K. Almdal, K. A. Koppi, F. S. Bates and K. Mortensen, *Macromolecules*, 1992, **25**, 1743-1751.
123. E. D. Gomez, A. Panday, E. H. Feng, V. Chen, G. M. Stone, A. M. Minor, C. Kisielowski, K. H. Downing, O. Borodin, G. D. Smith and N. P. Balsara, *Nano Lett.*, 2009, **9**, 1212-1216.
124. X. Yang and J. Loos, *Macromolecules*, 2007, **40**, 1353-1362.
125. T. J. Peckham and S. Holdcroft, *Adv. Mater.*, 2010, **22**, 4667-4690.
126. N. W. Deluca and Y. A. Elabd, *J. Polym. Sci. Part B: Polym. Phys.*, 2006, **44**, 2201-2225.
127. J. Kim, B. Kim and B. Jung, *J. Membr. Sci.*, 2002, **207**, 129-137.
128. D. A. Olson, L. Chen and M. A. Hillmyer, *Chem. Mat.*, 2008, **20**, 869-890.
129. I. W. Hamley, *Nanotechnology*, 2003, **14**, R39-R54.
130. C. A. Ross and J. Y. Cheng, *MRS Bull.*, 2008, **33**, 838-845.
131. M. P. Stoykovich, M. Müller, S. O. Kim, H. H. Solak, E. W. Edwards, J. J. de Pablo and P. F. Nealey, *Science*, 2005, **308**, 1442-1446.
132. J. K. Kim, S. Y. Yang, Y. Lee and Y. Kim, *Prog. Polym. Sci.*, 2010, **35**, 1325-1349.
133. A. M. Welander, H. M. Kang, K. O. Stuen, H. H. Solak, M. Müller, J. J. de Pablo and P. F. Nealey, *Macromolecules*, 2008, **41**, 2759-2761.
134. S. H. Kim, M. J. Misner, T. Xu, M. Kimura and T. P. Russell, *Adv. Mater.*, 2004, **16**, 226-231.
135. K. A. Cavicchi, K. J. Berthiaume and T. P. Russell, *Polymer*, 2005, **46**, 11635-11639.
136. R. A. Segalman, *Mater. Sci. Eng., R*, 2005, **48**, 191-226.
137. J. N. L. Albert and T. H. Epps, *Mater. Today*, 2010, **13**, 24-33.
138. G. Kim and M. Libera, *Macromolecules*, 1998, **31**, 2569-2577.
139. T. P. Lodge, B. Pudil and K. J. Hanley, *Macromolecules*, 2002, **35**, 4707-4717.
140. B. D. Olsen and R. A. Segalman, *Mater. Sci. Eng. R*, 2008, **62**, 37-66.
141. M. Dante, C. Yang, B. Walker, F. Wudl and T. Q. Nguyen, *Adv. Mater.*, 2010, **22**, 1835-1839.
142. A. de Cuendias, R. C. Hiorns, E. Cloutet, L. Vignau and H. Cramail, *Polym. Int.*, 2010, **59**, 1452-1476.
143. M. Lee, B. K. Cho and W. C. Zin, *Chem. Rev.*, 2001, **101**, 3869-3892.
144. H. A. Klok and S. Lecommandoux, *Adv. Mater.*, 2001, **13**, 1217-1229.
145. S. I. Stupp, *Curr. Opin. Colloid Interface Sci.*, 1998, **3**, 20-26.
146. J. T. Chen, E. L. Thomas, C. K. Ober and S. S. Hwang, *Macromolecules*, 1995, **28**, 1688-1697.
147. K. K. Tenneti, X. F. Chen, C. Y. Li, Y. F. Tu, X. H. Wan, Q. F. Zhou, I. Sics and B. S. Hsiao, *J. Am. Chem. Soc.*, 2005, **127**, 15481-15490.

148. B. D. Olsen, M. Shah, V. Ganesan and R. A. Segalman, *Macromolecules*, 2008, **41**, 6809-6817.
149. M. W. Matsen and C. Barrett, *J. Chem. Phys.*, 1998, **109**, 4108-4118.
150. J. T. Chen, E. L. Thomas, C. K. Ober and G. P. Mao, *Science*, 1996, **273**, 343-346.
151. L. H. Radzilowski, B. O. Carragher and S. I. Stupp, *Macromolecules*, 1997, **30**, 2110-2119.
152. G. Mao and C. K. Ober, *Acta Polym.*, 1997, **48**, 405-422.
153. L. Y. Shi, Y. Zhou, X. H. Fan and Z. Shen, *Macromolecules*, 2013, **46**, 5308-5316.
154. Y. Kim, E. Ha and A. Alexander-Katz, *Macromolecules*, 2011, **44**, 7016-7025.
155. Y. Kim and A. Alexander-Katz, *J. Chem. Phys.*, 2011, **135**.
156. L. Cui, J. J. Miao, L. Zhu, I. Sics and B. S. Hsiao, *Macromolecules*, 2005, **38**, 3386-3394.
157. J. A. A. W. Elemans, A. E. Rowan and R. J. M. Nolte, *J. Mater. Chem.*, 2003, **13**, 2661-2670.
158. L. Brunsveld, H. Zhang, M. Glasbeek, J. A. J. M. Vekemans and E. W. Meijer, *J. Am. Chem. Soc.*, 2000, **122**, 6175-6182.
159. D. J. Pochan, L. Pakstis, E. Huang, C. Hawker, R. Vestberg and J. Pople, *Macromolecules*, 2002, **35**, 9239-9242.
160. M. A. Johnson, J. Iyer and P. T. Hammond, *Macromolecules*, 2004, **37**, 2490-2501.
161. I. Gitsov and J. M. J. Fréchet, *Macromolecules*, 1993, **26**, 6536-6546.
162. V. Percec, D. A. Wilson, P. Leowanawat, C. J. Wilson, A. D. Hughes, M. S. Kaucher, D. A. Hammer, D. H. Levine, A. J. Kim, F. S. Bates, K. P. Davis, T. P. Lodge, M. L. Klein, R. H. DeVane, E. Aqad, B. M. Rosen, A. O. Argintaru, M. J. Sienkowska, K. Rissanen, S. Nummelin and J. Ropponen, *Science*, 2010, **328**, 1009-1014.
163. M. A. Gauthier and H. A. Klok, *Polym. Chem.*, 2010, **1**, 1352-1373.
164. J. Kalia and R. T. Raines, *Curr. Org. Chem.*, 2010, **14**, 138-147.
165. J. C. M. van Hest, *Polym. Rev.*, 2007, **47**, 63-92.
166. C. Boyer, X. Huang, M. R. Whittaker, V. Bulmus and T. P. Davis, *Soft Matter*, 2011, **7**, 1599-1614.
167. K. L. Heredia and H. D. Maynard, *Org. Biomol. Chem.*, 2007, **5**, 45-53.
168. B. Le Droumaguet and J. Nicolas, *Polym. Chem.*, 2010, **1**, 563-598.
169. J. Nicolas, G. Mantovani and D. M. Haddleton, *Macromol. Rapid Commun.*, 2007, **28**, 1083-1111.
170. M. A. Gauthier and H. A. Klok, *Chem. Commun.*, 2008, 2591-2611.
171. H. A. Klok, *J. Polym. Sci., Part A: Polym. Chem.*, 2005, **43**, 1-17.
172. F. Lecolley, L. Tao, G. Mantovani, I. Durkin, S. Lautru and D. M. Haddleton, *Chem. Commun.*, 2004, 2026-2027.
173. O. Yemul and T. Imae, *Biomacromolecules*, 2005, **6**, 2809-2814.
174. M. Li, P. De, H. Li and B. S. Sumerlin, *Polym. Chem.*, 2010, **1**, 854-859.
175. G. Mantovani, F. Lecolley, L. Tao, D. M. Haddleton, J. Clerx, J. J. L. M. Cornelissen and K. Velonia, *J. Am. Chem. Soc.*, 2005, **127**, 2966-2973.
176. I. van Baal, H. Malda, S. A. Synowsky, J. L. J. van Dongen, T. M. Hackeng, M. Merkx and E. W. Meijer, *Angew. Chem., Int. Ed.*, 2005, **44**, 5052-5057.
177. Y. Xia, S. C. Tang and B. D. Olsen, *Chem. Commun.*, 2013, **49**, 2566-2568.
178. C. I. Schilling, N. Jung, M. Biskup, U. Schepers and S. Bräse, *Chem. Soc. Rev.*, 2011, **40**, 4840-4871.

179. C. S. Cazalis, C. A. Haller, L. Sease-Cargo and E. L. Chaikof, *Bioconjugate Chem.*, 2004, **15**, 1005-1009.
180. B. Le Droumaguet and K. Velonia, *Macromol. Rapid Commun.*, 2008, **29**, 1073-1089.
181. A. J. Dirks, S. S. van Berkel, N. S. Hatzakis, J. A. Opsteen, F. L. van Delft, J. J. L. M. Cornelissen, A. E. Rowan, J. C. M. van Hest, F. P. J. T. Rutjes and R. J. M. Nolte, *Chem. Commun.*, 2005, 4172-4174.
182. M. Li, P. De, S. R. Gondi and B. S. Sumerlin, *Macromol. Rapid Commun.*, 2008, **29**, 1172-1176.
183. K. L. Heredia, D. Bontempo, T. Ly, J. T. Byers, S. Halstenberg and H. D. Maynard, *J. Am. Chem. Soc.*, 2005, **127**, 16955-16960.
184. H. Li, M. Li, X. Yu, A. P. Bapat and B. S. Sumerlin, *Polym. Chem.*, 2011, **2**, 1531-1535.
185. X. J. Wan and S. Y. Liu, *Macromol. Rapid Commun.*, 2010, **31**, 2070-2076.
186. I. Hamachi, K. Nakamura, A. Fujita and T. Kunitake, *J. Am. Chem. Soc.*, 1993, **115**, 4966-4970.
187. I. C. Reynhout, J. L. M. Cornelissen and R. J. M. Nolte, *J. Am. Chem. Soc.*, 2007, **129**, 2327-2332.
188. M. J. Boerakker, J. M. Hannink, P. H. H. Bomans, P. M. Frederik, R. J. M. Nolte, E. M. Meijer and N. A. J. M. Sommerdijk, *Angew. Chem., Int. Ed.*, 2002, **41**, 4239-4241.
189. H. Y. Cho, M. A. Kadir, B. S. Kim, H. S. Han, S. Nagasundarapandian, Y. R. Kim, S. B. Ko, S. G. Lee and H. J. Paik, *Macromolecules*, 2011, **44**, 4672-4680.
190. B. R. Griffith, B. L. Allen, A. C. Rapraeger and L. L. Kiessling, *J. Am. Chem. Soc.*, 2004, **126**, 1608-1609.
191. C. Wang, R. J. Stewart and J. Kopeček, *Nature*, 1999, **397**, 417-420.
192. D. Bontempo, R. C. Li, T. Ly, C. E. Brubaker and H. D. Maynard, *Chem. Commun.*, 2005, 4702-4704.
193. J. M. Hannink, J. Cornelissen, J. A. Farrera, P. Foubert, F. C. De Schryver, N. Sommerdijk and R. J. M. Nolte, *Angew. Chem., Int. Ed.*, 2001, **40**, 4732-4734.
194. M. Y. Kim, J. S. Kwon, H. J. Kim and E. K. Lee, *J. Biotechnol.*, 2007, **131**, 177-179.
195. O. Kinstler, G. Molineux, M. Treuheit, D. Ladd and C. Gegg, *Adv. Drug Deliv. Rev.*, 2002, **54**, 477-485.
196. E. S. Gil and S. M. Hudson, *Prog. Polym. Sci.*, 2004, **29**, 1173-1222.
197. O. D. Krishna and K. L. Kiick, *Pept. Sci.*, 2010, **94**, 32-48.
198. A. K. Shakya, H. Sami, A. Srivastava and A. Kumar, *Prog. Polym. Sci.*, 2010, **35**, 459-486.
199. A. S. Hoffman, P. S. Stayton, V. Bulmus, G. H. Chen, J. P. Chen, C. Cheung, A. Chilkoti, Z. L. Ding, L. C. Dong, R. Fong, C. A. Lackey, C. J. Long, M. Miura, J. E. Morris, N. Murthy, Y. Nabeshima, T. G. Park, O. W. Press, T. Shimoboji, S. Shoemaker, H. J. Yang, N. Monji, R. C. Nowinski, C. A. Cole, J. H. Priest, J. M. Harris, K. Nakamae, T. Nishino and T. Miyata, *J. Biomed. Mater. Res.*, 2000, **52**, 577-586.
200. I. C. Reynhout, J. L. M. Cornelissen and R. J. M. Nolte, *Acc. Chem. Res.*, 2009, **42**, 681-692.
201. P. van Rijn and A. Böker, *J. Mater. Chem.*, 2011, **21**, 16735-16747.
202. N. C. Mougin, P. van Rijn, H. Park, A. H. E. Müller and A. Böker, *Adv. Funct. Mater.*, 2011, **21**, 2470-2476.
203. A. Chilkoti, G. H. Chen, P. S. Stayton and A. S. Hoffman, *Bioconjugate Chem.*, 1994, **5**, 504-507.

204. Z. Ding, G. Chen and A. S. Hoffman, *J. Biomed. Mater. Res.*, 1998, **39**, 498-505.
205. P. S. Stayton, T. Shimoboji, C. Long, A. Chilkoti, G. Ghen, J. M. Harris and A. S. Hoffman, *Nature*, 1995, **378**, 472-474.
206. C. Boyer, V. Bulmus, J. Liu, T. P. Davis, M. H. Stenzel and C. Barner-Kowollik, *J. Am. Chem. Soc.*, 2007, **129**, 7145-7154.
207. Z. F. Cao, Y. Jin, B. A. Zhang, Q. Miao and C. Y. Ma, *Iran. Polym. J.*, 2010, **19**, 689-698.
208. T. Shiroya, M. Yasui, K. Fujimoto and H. Kawaguchi, *Colloids Surf., B*, 1995, **4**, 275-285.
209. P. De, M. Li, S. R. Gondi and B. S. Sumerlin, *J. Am. Chem. Soc.*, 2008, **130**, 11288-11289.
210. S. Kulkarni, C. Schilli, A. H. E. Müller, A. S. Hoffman and P. S. Stayton, *Bioconjugate Chem.*, 2004, **15**, 747-753.
211. C. Lavigueur, J. G. García, L. Hendriks, R. Hoogenboom, J. J. L. M. Cornelissen and R. J. M. Nolte, *Polym. Chem.*, 2011, **2**, 333-340.
212. T. Shimoboji, E. Larenas, T. Fowler, A. S. Hoffman and P. S. Stayton, *Bioconjugate Chem.*, 2003, **14**, 517-525.
213. S. M. Janib, M. F. Pastuszka, S. Aluri, Z. Folchman-Wagner, P. Y. Hsueh, P. Shi, Y. A. Lin, H. Cui and J. A. MacKay, *Polym. Chem.*, 2014, ***Advance Article***.
214. D. E. Meyer and A. Chilkoti, *Nat. Biotechnol.*, 1999, **17**, 1112-1115.
215. S. S. Pai, B. Hammouda, K. Hong, D. C. Pozzo, T. M. Przybycien and R. D. Tilton, *Bioconjugate Chem.*, 2011, **22**, 2317-2323.
216. K. Velonia, A. E. Rowan and R. J. M. Nolte, *J. Am. Chem. Soc.*, 2002, **124**, 4224-4225.
217. M. J. Boerakker, N. E. Botterhuis, P. H. H. Bomans, P. M. Frederik, E. M. Meijer, R. J. M. Nolte and N. Sommerdijk, *Chem. Eur. J.*, 2006, **12**, 6071-6080.
218. A. J. Dirks, R. J. M. Nolte and J. J. L. M. Cornelissen, *Adv. Mater.*, 2008, **20**, 3953-3957.
219. Y. Kumashiro, Y. Ikezoe, K. Tamada and M. Hara, *J. Phys. Chem. B*, 2008, **112**, 8291-8297.
220. A. E. F. Nassar, Z. Zhang, V. Chynwat, H. A. Frank, J. F. Rusling and K. Suga, *J. Phys. Chem.*, 1995, **99**, 11013-11017.
221. Y. X. Hu, D. Samanta, S. S. Parelkar, S. W. Hong, Q. A. Wang, T. P. Russell and T. Emrick, *Adv. Funct. Mater.*, 2010, **20**, 3603-3612.
222. A. W. Perriman, A. P. S. Brogan, H. Cölfen, N. Tsoureas, G. R. Owen and S. Mann, *Nat. Chem.*, 2010, **2**, 622-626.
223. F. X. Gallat, A. P. S. Brogan, Y. Fichou, N. McGrath, M. Moulin, M. Härtlein, J. Combet, J. Wuttke, S. Mann, G. Zaccai, C. J. Jackson, A. W. Perriman and M. Weik, *J. Am. Chem. Soc.*, 2012, **134**, 13168-13171.
224. B. Kim, C. N. Lam and B. D. Olsen, *Macromolecules*, 2012, **45**, 4572-4580.
225. C. N. Lam and B. D. Olsen, *Soft Matter*, 2013, **9**, 2393-2402.

Chapter 2 Detailed Synthetic and Experimental Methods

2.1 Protein Biosynthesis

Protein cloning. Throughout this work, the red fluorescent protein mCherry was used as a model globular protein. It was selected for its fluorescence properties, established high-yield expression protocols, and lack of cysteine residues in the amino acid sequence.[1-2] The absence of cysteines in the native sequence allows the use of thiol-maleimide bioconjugation to synthesize the protein-polymer block copolymer material. A single cysteine residue was introduced at position 131 in the protein sequence to replace the naturally occurring serine residue. This residue is located on a loop region on the opposite end of the β-barrel as both the N and C-termini.[2] This location is an excellent candidate for bioconjugation to a polymer due to its exposed position on the end of a loop. Additionally, protein folding was not expected to be altered because cysteine and serine have very similar chemical structures.

A gene encoding the mutant protein mCherryS131C (Figure 2-1) with codons optimized for expression in *E. coli* was purchased. By flanking the protein gene sequence with BamHI and HindIII restriction sites, a double digest followed by ligation was performed to place the gene into the pQE9 plasmid (Figures 2-2, 2-3). This plasmid encodes for ampicillin resistance, as well as an N-terminal 6xHis-tag which is used for protein purification. The completed plasmid was subsequently transformed into SG13009 *E. coli* cells for high-level protein expression. These cells contain pREP4, a plasmid with kanamycin resistance that encodes for *lac* repressor. The repressor protein limits production of the desired protein until expression is induced by isopropyl β-$_D$-1-thiogalactopyranoside (IPTG).

MRGSHHHHHHGSMVSKGEEDNMAIIKEFMRFKVHMEGSVNGHEFEIEGEGEGRPYEG

TQTAKLKVTKGGPLPFAWDILSPQFMYGSKAYVKHPADIPDYLKLSFPEGFKWERVM

NFEDGGVVTVTQDSSLQDGEFIYKVKLRGTNFPCDGPVMQKKTMGWEASSERMYPE

DGALKGEIKQRLKLKDGGHYDAEVKTTYKAKKPVQLPGAYNVNIKLDITSHNEDYTI

VEQYERAEGRHSTGGMDELYK

Figure 2-1. Amino acid sequence for expressed mCherryS131C protein including the 6xHis-tag.

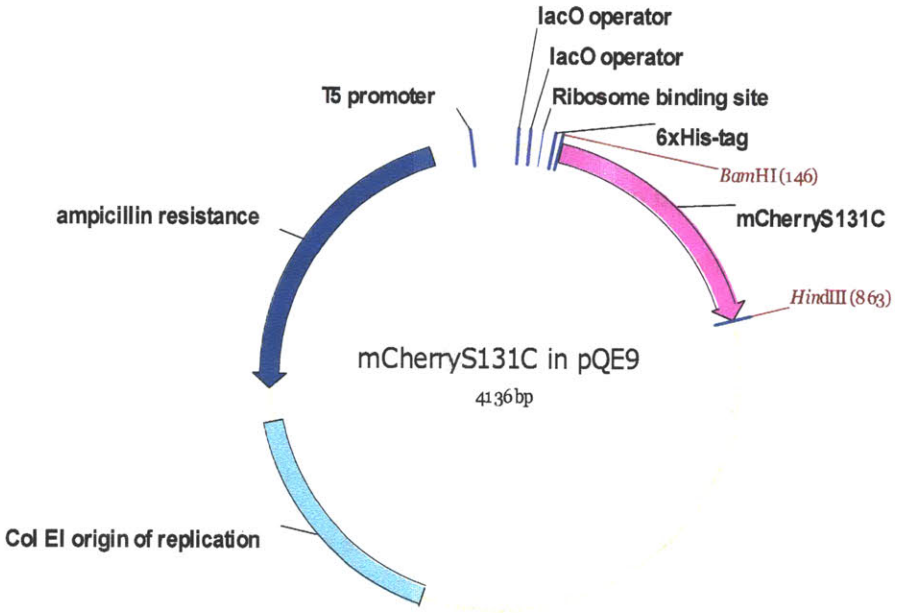

Figure 2-2. Map of plasmid used in this work. The gene of interest, mCherryS131C, is placed between BamHI and HindIII in the plasmid vector, pQE9. Prior to the mCherry gene, a region encoding for a 6xHis-tag is present.

lacO operator lacO operator
CTCGAGAAATCATAAAAAATTTATTTGCTTTGTGAGCGGATAACAATTATAATAGATTCAATTGTGAGCGGATAA
ribosome binding site 6xHis-tag
CAATTTCACACAGAATTCATTAAAGAGGAGAAATTAACTATGAGAGGATCGCATCACCATCACCATCACGGATC
mCherryS131C
CATGGTGTCTAAAGGTGAAGAAGATAACATGGCCATCATCAAAGAATTTATGCGTTTCAAAGTGCATATGGAAGGTAGCGTTAA
TGGCCACGAATTTGAAATTGAAGGCGAAGGTGAAGGTCGTCCGTATGAAGGTACCCAGACGGCAAAACTGAAAGTGACCAAA
GGCGGTCCGCTGCCGTTTGCCTGGGATATTCTGTCTCCGCAGTTCATGTATGGTAGTAAAGCGTACGTTAAACATCCGGCCG
ATATCCCGGATTATCTGAAACTGTCTTTTCCGGAAGGCTTCAAATGGGAACGTGTGATGAACTTCGAAGATGGCGGTGTGGTT
ACCGTTACGCAGGATAGCTCTCTGCAGGATGGTGAATTTATCTACAAAGTGAAACTGCGCGGTACCAATTTCCCGTGCGATGG
CCCGGTTATGCAGAAGAAAACCATGGGCTGGGAAGCCAGTAGCGAACGTATGTACCCGGAAGATGGTGCACTGAAAGGCGA
AATCAAACAGCGCCTGAAACTGAAAGATGGCGGTCACTATGATGCAGAAGTGAAAACCACGTACAAAGCGAAAAAACCGGTG
CAGCTGCCGGGTGCATACAACGTTAACATCAAACTGGATATCACCAGCCATAACGAAGATTATACGATCGTTGAACAGTACGA
ACGTGCAGAAGGTCGTCACTCTACCGGTGGTATGGATGAACTGTACAAATAAAAGCTTAATTAGCTGAGCTTGGACTCCTGTT
GATAGATCCAGTAATGACCTCAGAACTCCATCTGGATTTGTTCAGAACGCTCGGTTGCCGCCGGGCGTTTTTTATTGGTGAGA
ATCCAAGCTAGCTTGGCGAGATTTTCAGGAGCTAAGGAAGCTAAAATGGAGAAAAAAATCACTGGATATACCACCGTTGATAT
ATCCCAATGGCATCGTAAAGAACATTTTGAGGCATTTCAGTCAGTTGCTCAATGTACCTATAACCAGACCGTTCAGCTGGATAT
TACGGCCTTTTTAAAGACCGTAAAGAAAAATAAGCACAAGTTTTATCCGGCCTTTATTCACATTCTTGCCCGCCTGATGAATGC
TCATCCGGAATTTCGTATGGCAATGAAAGACGGTGAGCTGGTGATATGGGATAGTGTTCACCCTTGTTACACCGTTTTCCATG
AGCAAACTGAAACGTTTTCATCGCTCTGGAGTGAATACCACGACGATTTCCGGCAGTTTCTACACATATATTCGCAAGATGTG
GCGTGTTACGGTGAAAACCTGGCCTATTTCCCTAAAGGGTTTATTGAGAATATGTTTTTCGTCTCAGCCAATCCCTGGGTGAGT
TTCACCAGTTTTGATTTAAACGTGGCCAATATGGACAACTTCTTCGCCCCCGTTTTCACCATGGGCAAATATTATACGCAAGGC
GACAAGGTGCTGATGCCGCTGGCGATTCAGGTTCATCATGCCGTTTGTGATGGCTTCCATGTCGGCAGAATGCTTAATGAATT
ACAACAGTACTGCGATGAGTGGCAGGGCGGGGCGTAATTTTTTTAAGGCAGTTATTGGTGCCCTTAAACGCCTGGGGTAATG
ACTCTCTAGCTTGAGGCATCAAATAAAACGAAAGGCTCAGTCGAAAGACTGGGCCTTTCGTTTTATCTGTTGTTTGTCGGTGAA
CGCTCTCCTGAGTAGGACAAATCCGCCCTCTAGAGCTGCCTCGCGCGTTTCGGTGATGACGGTGAAAACCTCTGACACATGC
AGCTCCCGGAGACGGTCACAGCTTGTCTGTAAGCGGATGCCGGGAGCAGACAAGCCCGTCAGGGCGCGTCAGCGGGTGTT
GGCGGGTGTCGGGGCGCAGCCATGACCCAGTCACGTAGCGATAGCGGAGTGTATACTGGCTTAACTATGCGGCATCAGAGC
AGATTGTACTGAGAGTGCACCATATGCGGTGTGAAATACCGCACAGATGCGTAAGGAGAAAATACCGCATCAGGCGCTCTTC
CGCTTCCTCGCTCACTGACTCGCTGCGCTCGGTCGTTCGGCTGCGGCGAGCGGTATCAGCTCACTCAAAGGCGGTAATACG

GTTATCCACAGAATCAGGGGATAACGCAGGAAAGAACATGTGAGCAAAAGGCCAGCAAAAGGCCAGGAACCGTAAAAAGGCC
Col EI origin of replication
GCGTTGCTGGCGTTTTTCCATAGGCTCCGCCCCCCTGACGAGCATCACAAAAATCGACGCTCAAGTCAGAGGTGGCGAAACC
CGACAGGACTATAAAGATACCAGGCGTTTCCCCCTGGAAGCTCCCTCGTGCGCTCTCCTGTTCCGACCCTGCCGCTTACCGG
ATACCTGTCCGCCTTTCTCCCTTCGGGAAGCGTGGCGCTTTCTCATAGCTCACGCTGTAGGTATCTCAGTTCGGTGTAGGTCG
TTCGCTCCAAGCTGGGCTGTGTGCACGAACCCCCCGTTCAGCCCGACCGCTGCGCCTTATCCGGTAACTATCGTCTTGAGTC
CAACCCGGTAAGACACGACTTATCGCCACTGGCAGCAGCCACTGGTAACAGGATTAGCAGAGCGAGGTATGTAGGCGGTGC
TACAGAGTTCTTGAAGTGGTGGCCTAACTACGGCTACACTAGAAGGACAGTATTTGGTATCTGCGCTCTGCTGAAGCCAGTTA
CCTTCGGAAAAAGAGTTGGTAGCTCTTGATCCGGCAAACAAACCACCGCTGGTAGCGGTGGTTTTTTTGTTTGCAAGCAGCAG
ATTACGCGCAGAAAAAAAGGATCTCAAGAAGATCCTTTGATCTTTTCTACGGGGTCTGACGCTCAGTGGAACGAAAACTCACG
TTAAGGGATTTTGGTCATGAGATTATCAAAAAGGATCTTCACCTAGATCCTTTTAAATTAAAAATGAAGTTTTAAATCAATCTAAA
ampicillin resistance
GTATATATGAGTAAACTTGGTCTGACAGTTACCAATGCTTAATCAGTGAGGCACCTATCTCAGCGATCTGTCTATTTCGTTCAT
CCATAGTTGCCTGACTCCCCGTCGTGTAGATAACTACGATACGGGAGGGCTTACCATCTGGCCCCAGTGCTGCAATGATACC
GCGAGACCCACGCTCACCGGCTCCAGATTTATCAGCAATAAACCAGCCAGCCGGAAGGGCCGAGCGCAGAAGTGGTCCTGC
AACTTTATCCGCCTCCATCCAGTCTATTAATTGTTGCCGGGAAGCTAGAGTAAGTAGTTCGCCAGTTAATAGTTTGCGCAACGT
TGTTGCCATTGCTACAGGCATCGTGGTGTCACGCTCGTCGTTTGGTATGGCTTCATTCAGCTCCGGTTCCCAACGATCAAGGC
GAGTTACATGATCCCCCATGTTGTGCAAAAAAGCGGTTAGCTCCTTCGGTCCTCCGATCGTTGTCAGAAGTAAGTTGGCCGCA
GTGTTATCACTCATGGTTATGGCAGCACTGCATAATTCTCTTACTGTCATGCCATCCGTAAGATGCTTTTCTGTGACTGGTGAG
TACTCAACCAAGTCATTCTGAGAATAGTGTATGCGGCGACCGAGTTGCTCTTGCCCGGCGTCAATACGGGATAATACCGCGC
CACATAGCAGAACTTTAAAAGTGCTCATCATTGGAAAACGTTCTTCGGGGCGAAAACTCTCAAGGATCTTACCGCTGTTGAGA
TCCAGTTCGATGTAACCCACTCGTGCACCCAACTGATCTTCAGCATCTTTTACTTTCACCAGCGTTTCTGGGTGAGCAAAAACA
GGAAGGCAAAATGCCGCAAAAAAGGGAATAAGGGCGACACGGAAATGTTGAATACTCATACTCTTCCTTTTTCAATATTATTGA
AGCATTTATCAGGGTTATTGTCTCATGAGCGGATACATATTTGAATGTATTTAGAAAAATAAACAAATAGGGGTTCCGCGCACA
T5 promoter
TTTCCCCGAAAAGTGCCACCTGACGTCTAAGAAACCATTATTATCATGACATTAACCTATAAAAATAGGCGTATCACGAGGCCC
TTTCGTCTTCAC

Figure 2-3. Gene sequence for entire plasmid including mCherryS131C gene.

Protein expression. High yields of mCherry protein were obtained by bacterial culture in 1 L Fernbach flasks. The composition of the media in which protein expression occurred was critical for obtaining high yields of properly folded protein. The superior performance of 2XYT as compared with other common media for bacterial expression led to its use in all future experiments. Expression in 2XYT media produced cultures and cell pellets that were bright pink and resulted in high yields of mature protein. LB media produced satisfactory results in terms of protein folding and chromophore maturation, but yielded approximately 20% less purified material. In contrast, expression in more nutrient filled TB media led to incomplete chromophore maturation in a significant fraction of the mCherry protein population, resulting in a much lower absorbance of the fluorescent protein chromophore peak at 586 nm relative to the absorbance peak at 280 nm from aromatic amino acid residues in the protein. This decrease in absorbance was readily apparent in the expression media because many of the cultures did not turn visibly pink during expression.

Expression media containing 200 mg/L ampicillin and 50 mg/L kanamycin was inoculated with 5 mL overnight culture, grown at 37 °C, and induced with 1 mM IPTG at optical density OD_{600} = 1. The cells were cultured for approximately 5 hours after induction. When it was time to harvest the cells, the cultures were bright pink instead of the typical brown color of the expression media alone. The cells containing the expressed protein were then harvested by centrifugation at 6,000 rpm for 10 minutes at 4 °C. The cell pellets were stored at -80 °C until purification was performed. Fermentation was also briefly considered for high throughput protein expression. However, due to a combination of high cell densities and fast protein expression rates characteristic of fermentations, low yields of properly folded proteins were observed as for growth in TB media. It should be noted that minimal effort was made to

optimize protein expression conditions in these experiments, and that further effort would likely result in successful fluorescent protein expression by fermentation.

Protein purification. The presence of the 6xHis-tag on the mCherry protein allowed for purification by metal affinity chromatography operated in batch mode. Protein was purified under native conditions as described in the QIAexpressionist.[3] Purification was performed on a bench at ambient temperature; however all buffers for purification were stored at 4 °C when not in use. Additionally, all buffers contained low levels of β-mercaptoethanol (BME) in order to prevent the occurrence of protein dimers through the formation of disulfide bonds between cysteine residues. First, cell pellets were resuspended in 100 mL lysis buffer (50 mM monobasic sodium phosphate, 300 mM sodium chloride, 10 mM imidazole, 10 mM BME, pH = 8.0) per liter culture. This was followed by incubation with 100 mg lysozyme per liter culture for at least 30 minutes at 4 °C. To complete cell lysis, sonication was performed on ice for 15 minutes at 70% power on a 50% duty cycle using a Branson Sonifier 250 with a 0.5 inch horn. Next, the lysate was centrifuged at 10,000 x g and 4 °C for 30 minutes to remove cell debris and other insoluble proteins. The clarified lysate from one liter of culture was then mixed with 10 mL nickel-nitrilotriacetic acid (Ni-NTA) resin and allowed to bind for at least 2 hours at 4 °C. Then, the lystae/Ni-NTA mixture was added to a column and the flow-through was discarded. The column was washed with 10 column volume equivalents of wash buffer (50 mM monobasic sodium phosphate, 300 mM sodium chloride, 20 mM imidazole, 10 mM BME, pH = 8.0), followed by elution with 4 column volumes of elution buffer (50 mM monobasic sodium phosphate, 300 mM sodium chloride, 250 mM imidazole, 10 mM BME, pH = 8.0). The eluate was collected and dialyzed against 20 mM tris(hydroxymethyl)aminomethane (Tris) buffer at pH = 8.0 (molecular weight cutoff = 3,500 Da). Purified protein solutions were stored at 4 °C

and shielded from light using aluminum foil to prevent photobleaching of the chromophore. For best results, protein should be used within one to three weeks after purification.

Protein yield was determined spectrophotometrically using the absorbance peak at 586 nm (extinction coefficient of 72,000 $M^{-1}cm^{-1}$).[1] Typical protein yields were between 80 and 100 mg/L culture. After purification and dialysis, mCherryS131C was typically at a concentration of 2-3 mg/mL. The ratio of the peak absorbance at 586 nm to that at 280 nm varied somewhat from batch to batch, depending on the fraction of protein in which the chromophore was fully mature and optically active. Typical values for this ratio were around 1.5 after protein dialysis, and ranged from 1.2 to 1.6. Any batches of protein with values below 1.3 were not used for final experiments.

Protein purity was assessed using both native and denaturing protein gels as well as matrix-assisted laser desorption ionization mass spectrometry (MALDI-MS). Denaturing protein gels (SDS-PAGE) of mCherry show three bands at approximately 28, 19 and 9 kDa (Figure 2-4a). The band at 28 kDa corresponds to the full mCherry protein, while the bands at 19 and 9 kDa are present as the result of cleavage of the acylimine bond in the chromophore during the harsh gel preparation conditions.[4-5] When protein gels were run at much lower concentrations, as has typically been done in the literature,[6-7] the two lower molecular weight bands are extremely faint. Native gels of purified mCherry show two bands, one corresponding to mCherry monomer, and another corresponding to protein dimer as a result of disulfide bond formation (Figure 2-4b). The band corresponding to the dimer is significantly diminished by the addition of BME. MALDI was used to further confirm protein purity. A mass of 28,201 Da was obtained experimentally, in good agreement with the expected mass of 28,134 Da. No peak was observed corresponding to the higher molecular weight fragment (18,896 Da expected molecular

weight), however a small peak was observed for the smaller fragment (9,256 Da expected molecular weight) which is consistent with the preferential observation of low molecular weight species by MALDI.

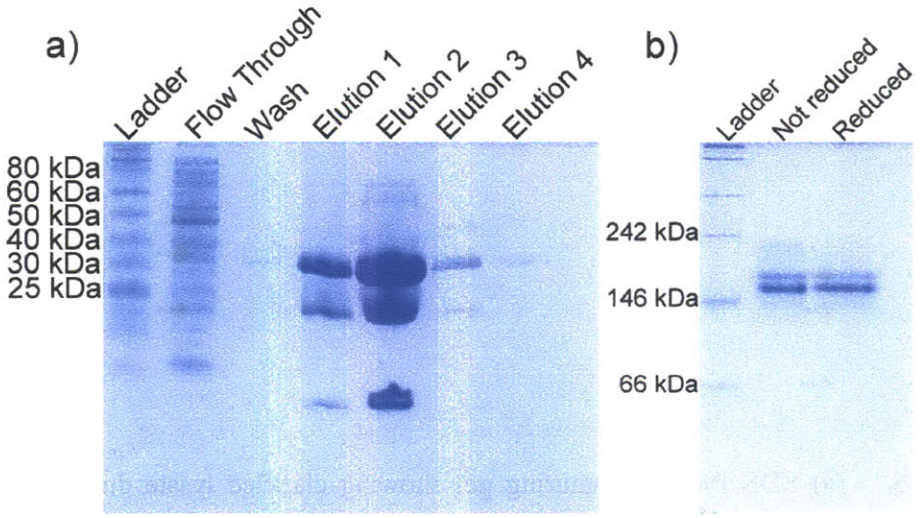

Figure 2-4. (a) SDS PAGE denaturing gel showing mCherryS131C purity. The two smaller molecular weight segments result from cleavage of the acylimine bond in the chromophore during protein boiling. When the protein is at low concentrations as in Elution 4, only the band corresponding to the fully intact protein is visible. (b) Native gel showing that mCherry remains intact throughout the purification process. A higher molecular weight band shows the presence of dimers formed through disulfide bonds. The presence of dimers can be reduced by adding an equimolar amount of β-mercaptoethanol.

During the process of identifying the cause of the three bands in denaturing gels of mCherry, a number of small changes to the protocol were examined. The addition of protease inhibitor cocktail or 1 mM ethylenediaminetetraacetic acid (EDTA) into the lysis buffer along with the lysozyme did not have any effect on protein purity (Figure 2-5a). A gene with codons optimized for eukaryotes instead of prokaryotes was purchased, but did not change the purity or

yield of mCherry. Additionally, expression was tested in other cells lines including BL21(DE3) and DH10B (Figure 2-5b). BL21 cells are known to contain fewer proteases, but neither cell line performed any better or worse.

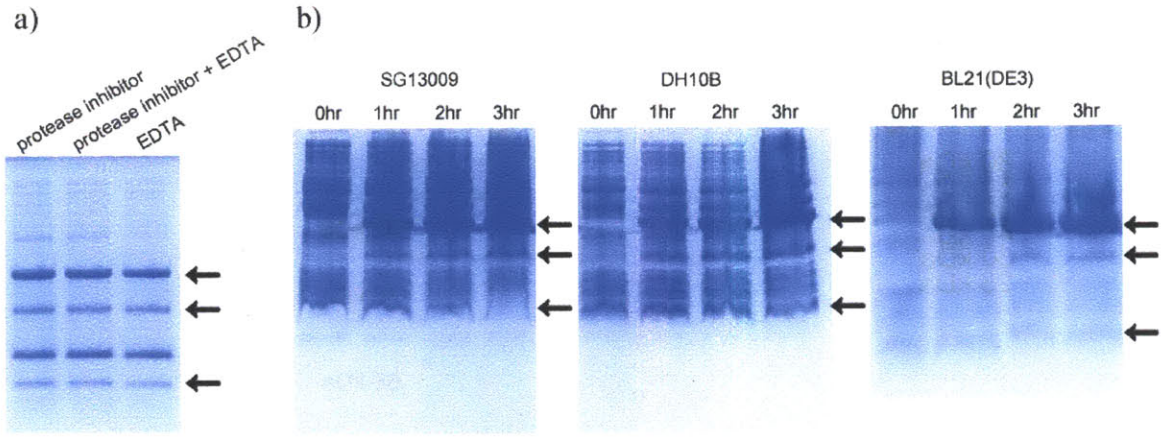

Figure 2-5. (a) SDS PAGE denaturing gel showing clarified lysate during purification of mCherryS131C with protease inhibitor and/or EDTA. Neither of these additions prevented the appearance of multiple bands from mCherry. The three black arrows point out the bands from mCherry, while the second band from the bottom is due to lysozyme. (b) SDS PAGE denaturing gel showing test expressions comparing cell lines SG13009 and DH10B at 0, 1, 2, and 3 hours after induction. No significant differences are observed in the different cell lines. The black arrows again denote the three bands due to mCherry.

Protein storage. For best results, mCherry protein should be used within one to three weeks after purification. This guideline is suggested not only to ensure that cysteine thiols do not degrade before use but also so that the chromophore of mCherry is able to retain as much functionality as possible. Several experiments were performed to explore the possibility of storing purified protein for later use. Dialyzed protein in 20 mM Tris buffer at pH = 8.0 was stored for one month at -20 °C or -80 °C. Samples were prepared containing either no additional

components or some level of glycerol (5, 10, 25, or 50 wt%) or sucrose (20, 50, 100, 500, or 1,000 mM). Glycerol and sucrose were chosen because they are known to be good cryoprotectants for proteins. Representative results for 10 wt% glycerol and 100 mM sucrose are shown in Figure 2-6. Generally, all levels of glycerol or sucrose performed similarly, with slightly better results occasionally observed at higher loading levels. Importantly, samples stored at -20 °C retained more mCherry functionality than samples stored at -80 °C or 4 °C. For this work, it was decided to always use freshly purified protein; however, these results suggest that it may be possible to preserve nearly fully functional protein for later use.

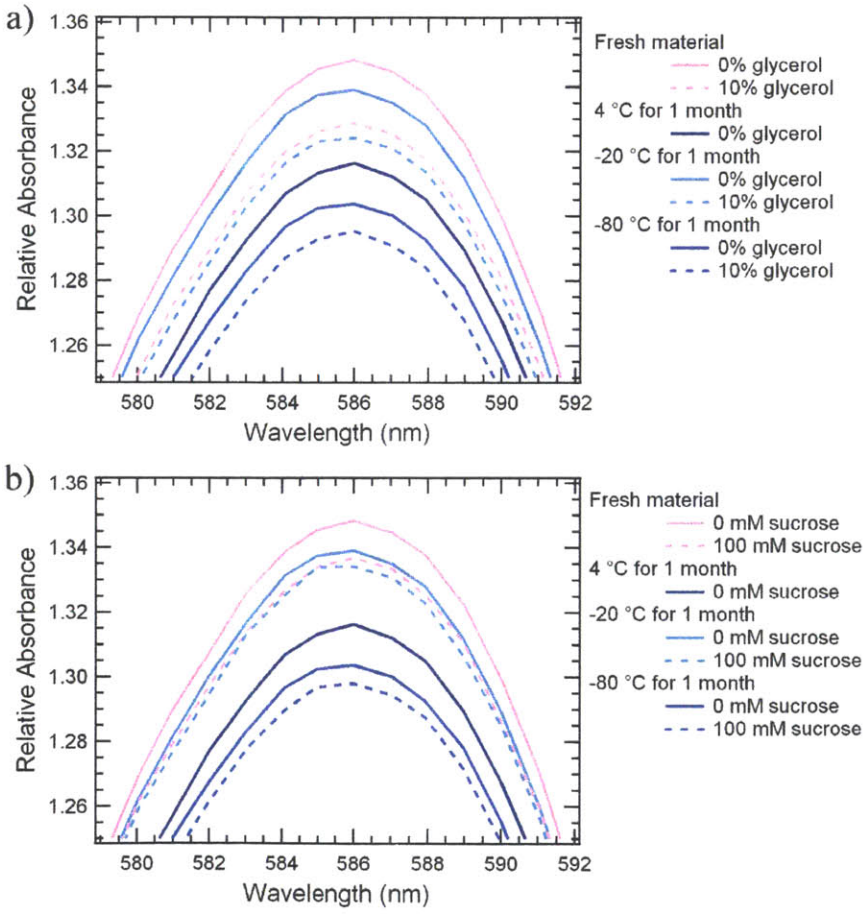

Figure 2-6. UV-vis data showing the effect of (a) glycerol and (b) sucrose on the characteristic absorption peak of mCherry after one month of storage.

2.2 Polymer Synthesis

Monodisperse poly(N-isopropylacrylamide) (PNIPAM) was synthesized using reversible addition-fragmentation chain-transfer (RAFT) polymerization. Maleimide end functionality was desired for protein bioconjugation through thiol-maleimide coupling. However, any maleimide present during the polymerization would participate in the reaction through its double bond. Therefore, the RAFT chain transfer agent (CTA) used in this work was functionalized with a furan protected maleimide which could be deprotected after polymerization.[8] Two components of the CTA were synthesized in parallel and then coupled together to yield the final product.

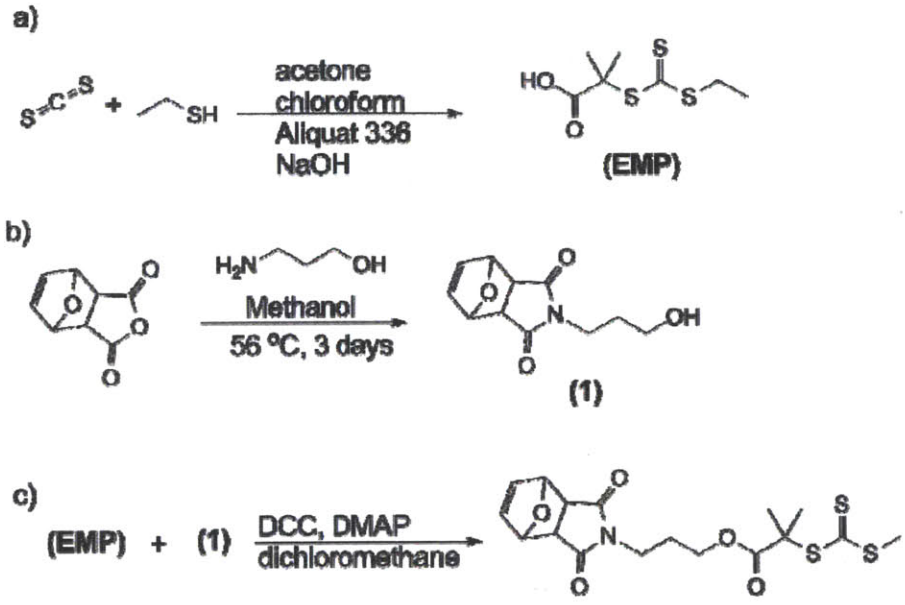

Scheme 2-1. Synthesis of (a) EMP (b) protected maleimide (compound **1**) (c) EMP-imide RAFT chain transfer agent.

Synthesis of 2-ethylsulfanylthiocarbonyl sulfanyl-2-methylpropionic acid (EMP). This procedure was adapted from the work of You and Oupický.[9] First, fresh (< ~1 year old) ethanethiol (6.2 g, 0.1 mol) was added to the reaction flask followed by Aliquat 336 (1.0 g, 0.002

mol) and acetone (73 mL), and the mixture was cooled in an ice bath under nitrogen. Next, 9 mL 50% aqueous solution of sodium hydroxide (4.5 g, 0.1 mol) was added dropwise over 10 minutes. Then, a solution of carbon disulfide (6.03 mL, 7.6 g, 0.1 mol) in acetone (12.6 mL) was added dropwise to the reaction over 30 minutes. This was followed by the addition of chloroform (12 mL, 17.8 g, 0.15 mol). Finally, 80 mL of 50% sodium hydroxide solution (40 g, 1.0 mol) was added dropwise over 20 minutes. The reaction was stirred overnight under nitrogen, and became a deep red solution with a yellow precipitate.

The next day, 100 mL of water was added to the reaction mixture and the contents were transferred to a separatory funnel. An additional 100 mL water was used to rinse the remaining contents of the reaction flask into the funnel. Then, 80 mL hydrochloric acid was added. This resulted in the formation of a yellow aqueous layer with a dark red organic layer on top. Next, the product was extracted in the organic phase with 3x100 mL diethyl ether. The first extraction fraction was dark red, and the second and third were yellow. After the final extraction, the aqueous phase was colorless. Next, ether was removed by rotary evaporation to obtain approximately 30 mL red liquid. A quick column was performed using 100 mL silica gel and 1:1 hexanes:diethyl ether as the mobile phase. The first and third fractions were yellow and discarded. The second fraction which contained the product was dark red/brown. Because an additional purification step was required after the column, as much of the reddish-brown product was collected as possible. Then, the solvent was removed from the product under vacuum. The final purification step was vacuum distillation using a microdistillation apparatus without the cooling water jacket. Distillation was started at 80 °C and the temperature was slowly raised 5-10 °C every 10-20 minutes. The yellow material which distilled first was not the product. A heat gun was used to speed the process; however caution was required, as the mixture had a

tendency to bump. Over the course of approximately 5 hours, the temperature was increased to 180 °C. At this point, the heat gun was used to keep the glassware hot enough for distillation to continue successfully. Once the deep orange/red product began to distill over, a new collection flask was used. For the next hour, the heat gun was used constantly to help transfer the product over to the collection flask. Finally, the purified product was transferred to a glass vial while still hot and significantly less viscous. After cooling to room temperature, the product was stored in the freezer. This reaction typically yielded 7-8 g EMP (30-35% yield), and NMR was used to confirm purity. ^{1}H NMR ($CDCl_3$, δ): 1.33 (t, 3H, $-CH_2CH_3$), 1.72 (s, 6H, $-C(CH_3)_2COOH$), 3.30 (q, 2H, $-CH_2CH_3$).

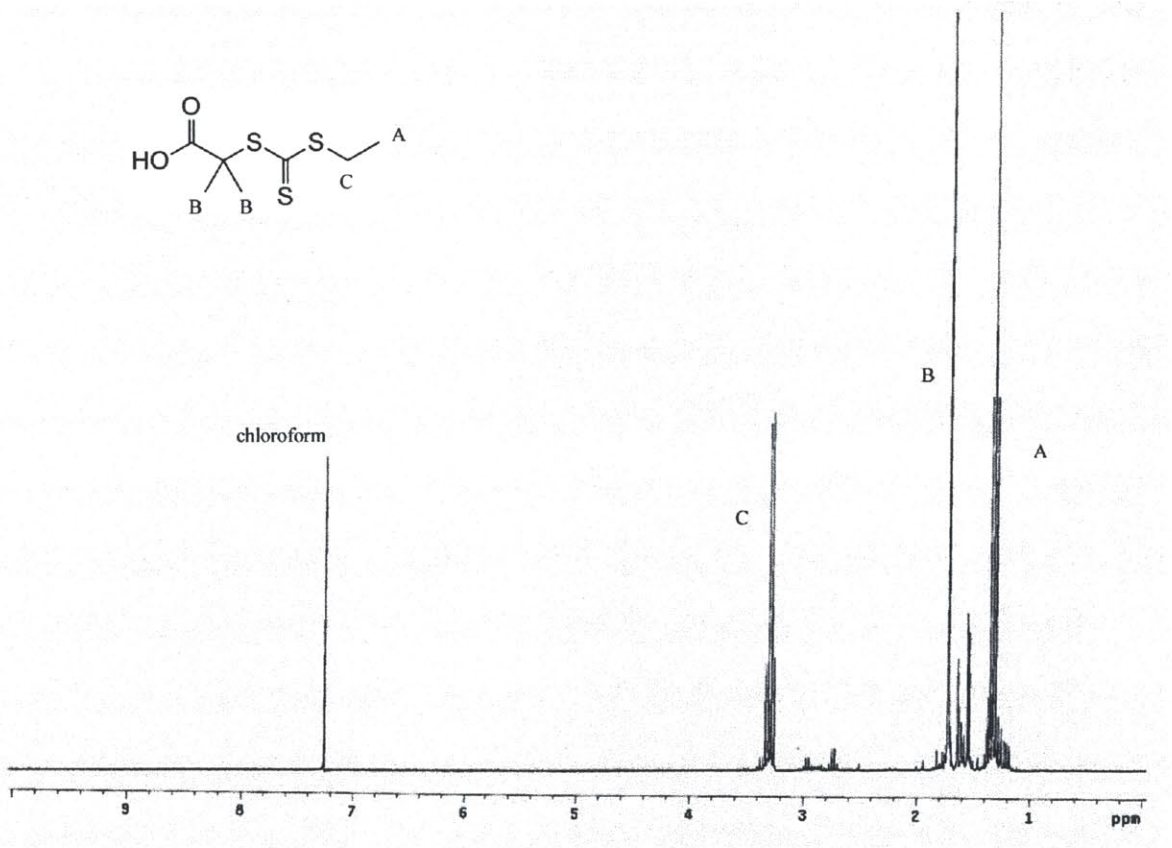

Figure 2-7. ^{1}H-NMR of 2-ethylsulfanylthiocarbonyl sulfanyl-2-methylpropionic acid (EMP) in deuterated chloroform.

Synthesis of exo-3a,4,7,7a-Tetrahydro-2-(3-hydroxypropyl)-4,7-epoxy-14-isoindole-1,3(2H)-dione (1). For this reaction, the work of Neubert and Snider was followed.[10] To the reaction flask, 500 mL methanol was added followed by exo-3,6-epoxy-1,2,3,6-tetrahydrophthalic anhydride (9.0 g, 0.054 mol). The mixture was allowed to stir at room temperature for 5-10 minutes. Then, 3-amino-1-propanol (4.08 g, 0.054 mol) was added dropwise. The reaction was stirred at 56 °C for at least 3 days under ambient atmosphere.

Once the reaction was complete, methanol was removed by rotary evaporation. The resulting yellow oil was dissolved in 100 mL dichloromethane and washed with saturated sodium chloride in water (3x75 mL). The organic phase was then dried with sodium sulfate, concentrated by rotary evaporation, and finally dried under vacuum overnight. This yielded approximately 2.5 g product (20% yield). Purity was confirmed by NMR. ^{1}H NMR ($CDCl_3$, δ): 1.75 (tt, 2H, -$CH_2(CH_2)CH_2$-), 2.88 (s, 2H, -NC(O)CH-), 3.52 (t, 2H, -CH_2O-), 3.65 (t, 2H, -NCH_2-), 5.27 (s, 2H, -CH(O)-), 6.52 (s, 2H, -CHCH-).

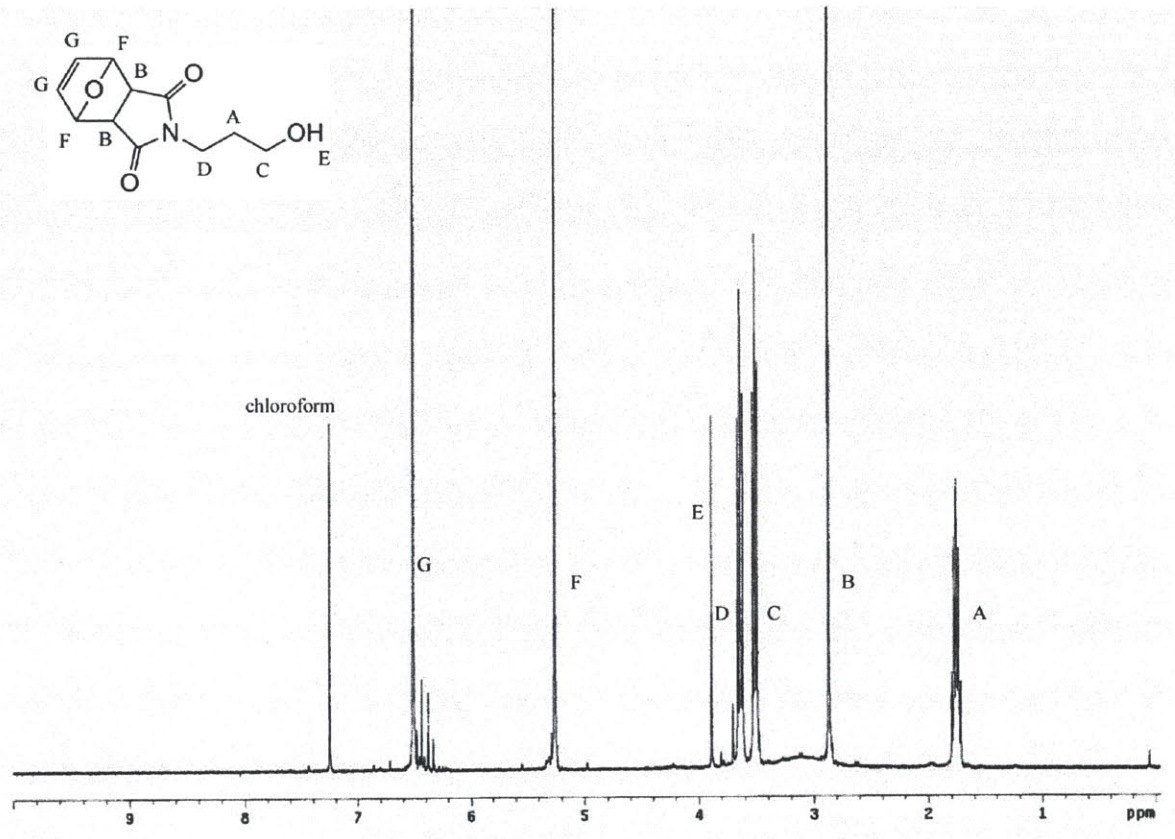

Figure 2-8. ^{1}H-NMR of exo-3a,4,7,7a-Tetrahydro-2-(3-hydroxypropyl)-4,7-epoxy-14-isoindole-1,3(2H)-dione (**1**) in deuterated chloroform.

Synthesis of EMP-imide RAFT agent. An N,N'-dicyclohexylcarbodiimide (DCC) coupling reaction was used to synthesize the final product as detailed in Bays *et al.*[8] EMP, **1**, DCC, and 4-dimethylaminopyridine (DMAP) were combined in the molar ratio of 1:1.1:1.2:0.1 with a basis of approximately 2.3 g (0.01 mol) EMP. The reaction was performed in anhydrous dichloromethane with stirring at room temperature under ambient atmosphere overnight. A column was run with 100 mL silica gel and 1:1 hexanes:ethyl acetate as the mobile phase and was monitored by thin layer chromatography (TLC). TLC confirmed that the second yellow fraction to come off the column ($R_f \approx 0.38$) was the desired product. Finally, solvent was

removed by rotary evaporation, the product was dried overnight under vacuum, and purity was confirmed by NMR. ^{1}H NMR ($CDCl_3$, δ): 1.29 (t, 3H, -S-CH_2CH_3), 1.69 (s, 6H, -$C(CH_3)_2$-), 1.85-2.00 (tt, 2H, -$CH_2(CH_2)CH_2$-), 2.83 (s, 2H, -NC(O)CH-), 3.26 (q, 2H, -CH_2CH_3), 3.55 (t, 2H, -NCH_2-), 4.05 (t, 2H, -CH_2O-), 5.24 (s, 2H, -CH(O)-), 6.49 (s, 2H, -CHCH-).

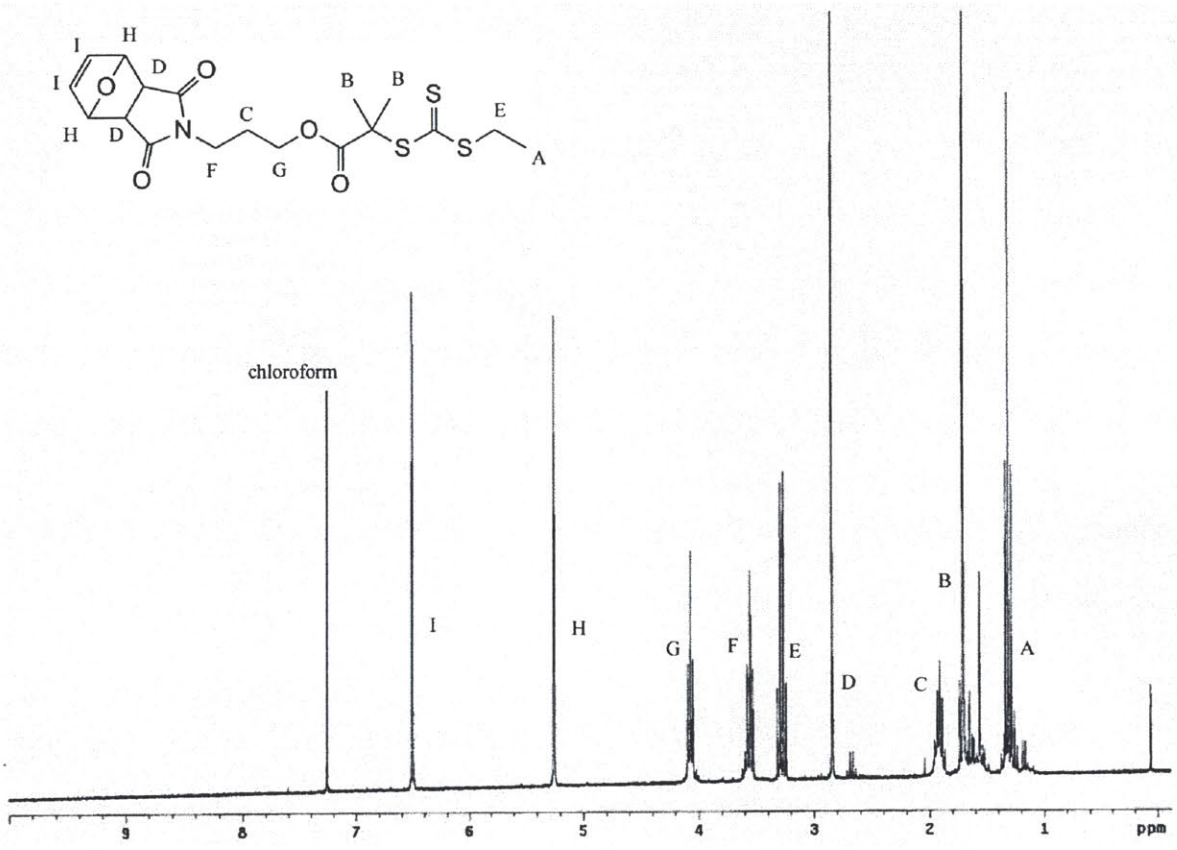

Figure 2-9. ^{1}H-NMR of EMP-imide RAFT agent in deuterated chloroform.

PNIPAM polymerization. NIPAM monomer was purified by sublimation at 65 °C under vacuum, and azobisisobutyronitrile (AIBN) was used as received. The final polymer molecular weight was tuned using a combination of the ratio of RAFT agent to monomer and polymerization time (Figure 2-10). The monomer:CTA ratio ranged from 70:1 up to 1500:1, and

polymerization times were between 55 and 190 minutes. All polymerization reactions were run at a monomer concentration of 2.0 M in acetonitrile and with a CTA:initiator ratio of 1:0.5. The reaction scale was also found to affect the time needed to reach a given conversion, so most reactions were run on a 40 g NIPAM scale.

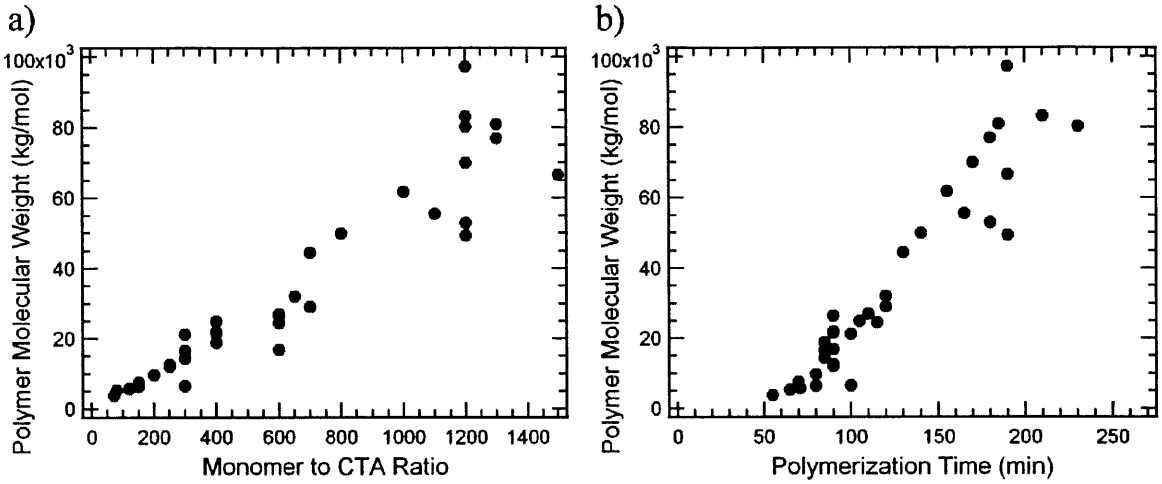

Figure 2-10. Calibration curve showing final polymer molecular weight as a function of (a) monomer:CTA ratio and (b) polymerization time.

With the EMP-imide RAFT CTA used in the polymerizations, coupling of polymer chains typically occurred to a small extent even at low conversions. This produced a population with a molecular weight approximately double that of the majority of the polymer chains. When unmodified EMP was used, no coupling was observed. Therefore, it is believed that the double bond in the protecting group is slightly reactive during the polymerization. To help reduce the extent to which coupling occurs, the reactions were run at low conversions of approximately 35-45%.

In a typical polymerization reaction, first 40 g of monomer was dissolved in approximately 150 mL acetonitrile in a beaker with stirring at room temperature. Then, the

appropriate amount of RAFT CTA and initiator was added. The solution was then transferred to an airfree synthesis flask using a calibrated glass pipet which allowed for an exact measurement of the total solution volume. Next, an appropriate volume of fresh acetonitrile was added to dilute the solution to 2.0 M. To degas the reaction, three cycles of freeze-pump-thaw were used. For the most consistent results, the vacuum level during the final pump step should be 2-3 mTorr higher than the closed system vacuum level. During the final thaw step, the reaction mixture was allowed to warm up to room temperature. Then the reaction flask was slowly backfilled with nitrogen while stirring, and the flask was sealed. It was then placed into a pre-heated oil bath at 55 °C and allowed to polymerize for the prescribed amount of time. The reaction was terminated by opening the flask to air and removing it from the oil bath. Reactions were run at 55 °C instead of 65 °C as is typical for polymerizations using AIBN as an initiator in order to reduce the frequency of coupling. Since the rate of polymerization is also somewhat slower, there is a wider timeframe to achieve the desired polymer molecular weight.

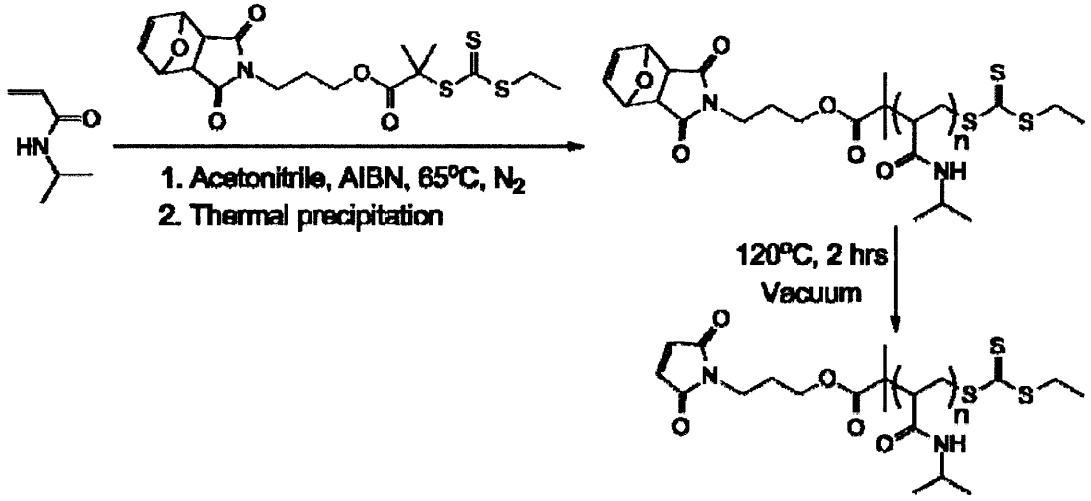

Scheme 2-2. Polymerization and purification of poly(N-isopropylacrylamide).

PNIPAM purification. PNIPAM is purified by thermal precipitation cycling which is made possible by its lower critical solution temperature (LCST) behavior in water which results in the polymer becoming insoluble in solutions above 32 °C.[11-12] Precipitation into ether was also considered for polymer purification, but was rejected due to low polymer recoveries and the large volumes of solvent required. For the thermal precipitation method, the polymerization solvent was first removed by rotary evaporation at 30-40 °C. The dried contents were then dissolved in approximately 200 mL nanopure water at 4 °C overnight. Then the solution was filtered to remove any remaining AIBN from solution. Next, the aqueous solution was centrifuged at 40 °C and 1200 rpm for 90 minutes. The supernatant containing unreacted monomer was discarded and the pellet was suspended in water at 4 °C. This solution was centrifuged at 40 °C once again, and the pellet was dried under vacuum for approximately 2 days. Finally, the protecting group on the RAFT CTA was removed using a retro Diels-Alder reaction[8] under vacuum at 120 °C for two hours. Experiments to optimize this deprotection technique were performed by another member of the lab. It should be noted that boiling in toluene, as reported in the literature for the deprotection of smaller molecules,[8] was not successful with our polymers. The deprotection step ultimately resulted in maleimide end-functionalized PNIPAM in approximately 30-35% yield relative to the initial monomer mass.

Polymer molecular weight and polydispersity were determined by gel permeation chromatography (GPC) with an Agilent 1260 Infinity HPLC using N,N-dimethylformamide (DMF) with 0.01 M lithium bromide as the mobile phase. Three identical columns in series were used to enhance separation of the polymer species and provide better molecular weight resolution. Both a refractive index detector and a Wyatt Mini-Dawn three-angle light scattering detector were employed to enable absolute molecular weight determination. Solutions were

filtered with a 0.45 μm filter prior to analysis to remove particulates which would alter the data and foul the columns. For quantifying the refractive index signal, the dn/dc for PNIPAM was measured to be 0.0761 mL/g by injecting several known concentrations of PNIPAM into the GPC detector. GPC traces typically showed two peaks: a large primary peak and a minor peak present due to coupling through the double bond on the furan protecting group. Both of these peaks were fit to a Gaussian, and the relative areas under those curves were used to determine the extent of coupling. Coupling was generally minor, and most polymers displayed only 4-7% coupling. It is important to note that the coupling peak is diminished significantly or not observed at all when using a GPC which has lower molecular weight resolution because only two columns are used.

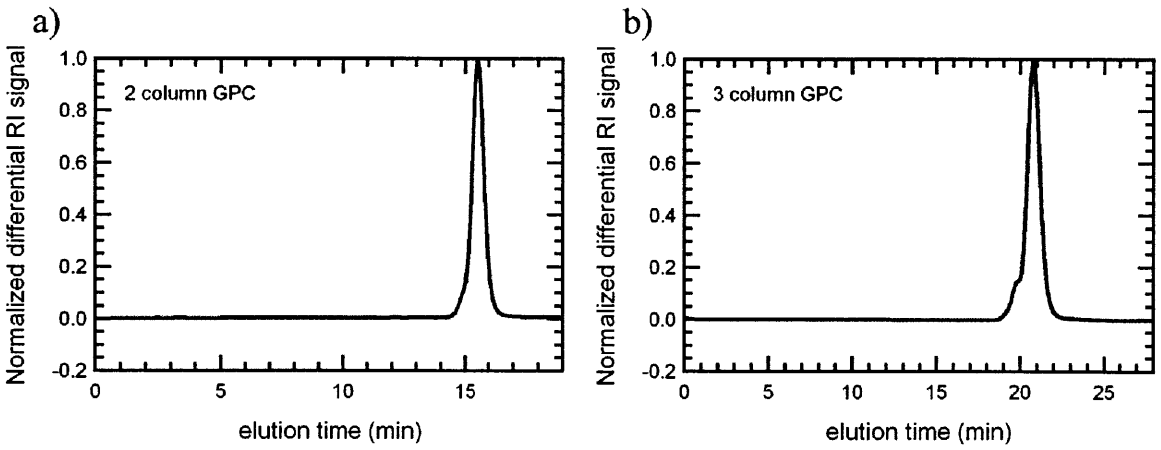

Figure 2-11. GPC traces of polymer with M_n = 15,660 g/mol and PDI = 1.09 using (a) 2 column GPC and (b) 3 column GPC.

2.3 Bioconjugate Synthesis

Bioconjugation reaction. Site specific bioconjugation of mCherry to PNIPAM was achieved through thiol-maleimide coupling. First, any disulfide bonds between cysteine thiols were

reduced with the addition of a 10-fold molar excess of tris(2-carboxyethyl)phosphine (TCEP).[13] TCEP was gently stirred with the purified protein solution for several minutes at 4 °C, and then a 3-fold molar excess of PNIPAM was added and allowed to react with stirring. Three to six hours later, an additional 3-fold molar excess of PNIPAM was added, and the reaction proceeded overnight. The reaction was performed at 4 °C to ensure macrophase separation of PNIPAM did not occur. When using polymers with molecular weights above approximately 60 kg/mol, greater conversions may be achieved by allowing the reaction to proceed for up to 48 hours. Typical reaction conversions were between 60 and 80%, with higher conversions observed when using lower molecular weight polymers. These conversions were roughly measured using denaturing protein gels by comparing the intensities of the bands due to unconjugated protein with those from bioconjugate. This technique is discussed in greater detail in the following section.

Several reaction conditions were tested to determine which combination resulted in the highest conversion (Figure 2-12). These initial test bioconjugations were performed with a 2 kg/mol maleimide end-functionalized poly(ethylene glycol) (PEG). Tris, phosphate and 2-[4-(2-hydroxyethyl)piperazin-1-yl]ethanesulfonic acid (HEPES) buffers were tested at pH 6.5 and 7.5. The TCEP excess was also tested at 5x, 10x and 25x, and PEG excesses of 5x, 10x, 20x, and 50x were examined. These experiments showed that Tris buffer was superior, a 10 fold excess of polymer was best, and a TCEP excess of 10x was sufficient. Next, a more thorough study of pH conditions was conducted with Tris buffers at pH = 7.1, 7.3, 7.5, 7.7, and 7.9, and from this study pH = 8 was chosen. Later experiments performed using PNIPAM were conducted to explore the possibility of decreasing the polymer excess required in order to conserve material.

This resulted in a decrease of the molar excess to 6x. Subsequent experiments found that adding polymer in two aliquots improved yields slightly.

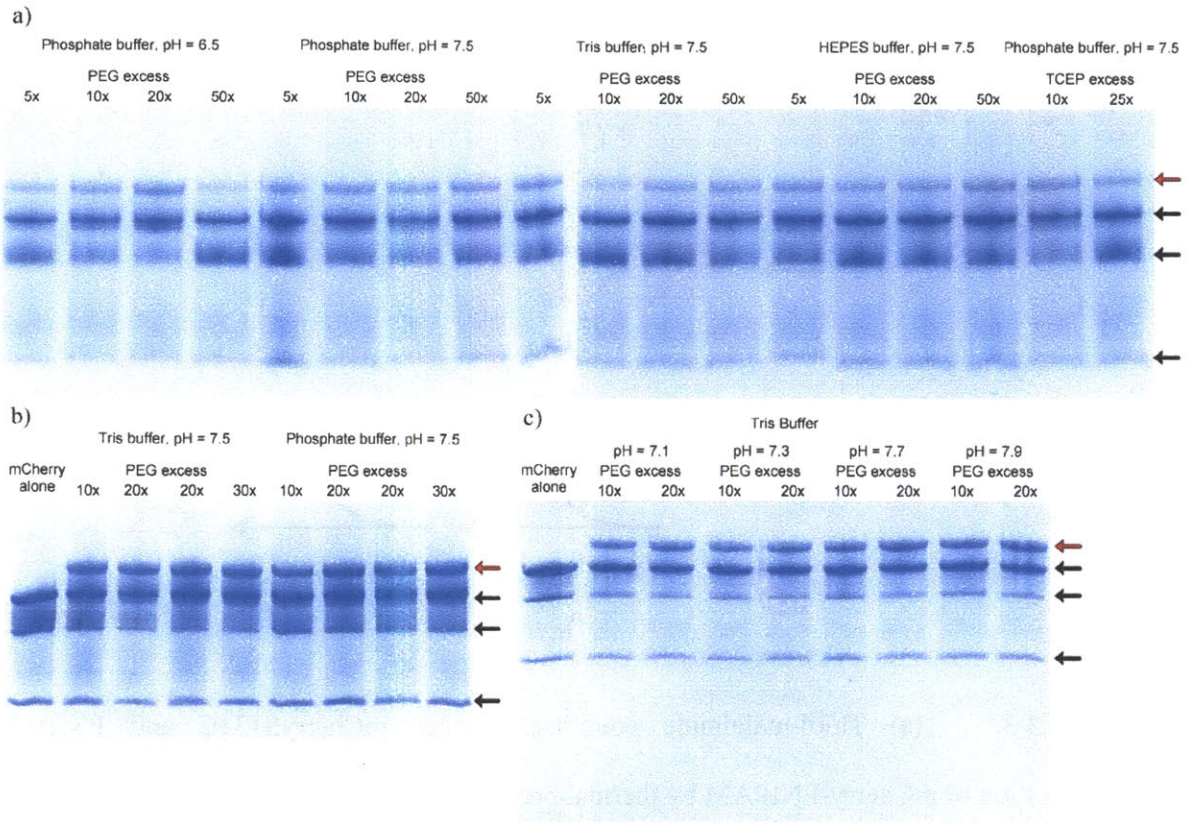

Figure 2-12. Denaturing protein gels showing the results of test bioconjugations with mCherry and PEG. The black arrows denote bands due to unconjugated mCherry and the red arrows point to bioconjugate.

Bioconjugation purification and purity determination. Bioconjugates were purified using a combination of thermal precipitation and affinity chromatography (Scheme 2-3). Because PNIPAM exhibits LCST behavior, thermal cycling can be employed to obtain purified materials quickly and inexpensively. In the case of purifying mCherry bioconjugate, ammonium sulfate salt was added to lower the transition temperature such that polymer precipitation occurred at

room temperature, and no additional heating was required. Following precipitation, an affinity chromatography column was used to remove unconjugated polymer, resulting in purified bioconjugate. The affinity chromatography column step was performed last so less Ni-NTA was required.

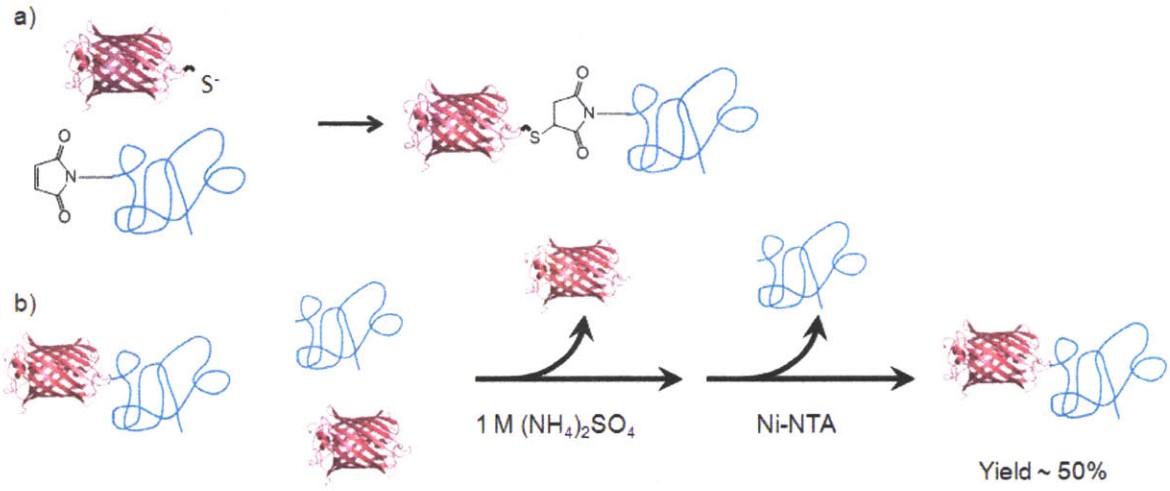

Scheme 2-3. (a) Thiol-maleimide coupling between mCherryS131C and PNIPAM. (b) Purification of mCherry-PNIPAM by thermal precipitation and affinity chromatography.

To purify mCherry-PNIPAM bioconjugates, one part reaction mixture was combined with one part 20 mM tris buffer at pH = 8 and one part 3 M ammonium sulfate solution at pH = 8. For bioconjugate reactions with very large polymers, a 1:1.5:0.5 ratio may be used to obtain better pellet formation and better separation. This mixture was centrifuged at 10,000 rpm for 90 minutes at room temperature. The supernatant containing unreacted mCherry protein was then discarded, and the pellet containing unreacted polymer as well as bioconjugate was resuspended at 4 °C in one part 20 mM tris buffer at pH = 8.

Next, the resuspended solution was divided into parts (one part for every 50 mg of mCherry used in the bioconjugation reaction) which were run on separate columns. Approximately 15 mL of Ni-NTA was added to each part and allowed to bind with the bioconjugate overnight at 4 °C. Bioconjugates with polymers larger than 40 kDa may require additional binding time up to 24 hours. This mixture was then loaded into a column at 4 °C, washed with 10 column volume equivalents of wash buffer (50 mM monobasic sodium phosphate, 300 mM sodium chloride, 20 mM imidazole), and eluted with 3 column volumes of elution buffer (50 mM monobasic sodium phosphate, 300 mM sodium chloride, 250 mM imidazole). The flow-through was usually rebound to Ni-NTA along with any wash fractions which were sufficiently pink. This mixture was allowed to bind with the Ni-NTA for at least 3-6 hours before another column was run. For bioconjugates with very large polymers, this rebinding process may need to be repeated a third time. The eluate from all columns was collected and dialyzed (molecular weight cutoff = 3,500 Da) against nanopure water. Bioconjugate yield was determined spectrophotometrically using the absorbance peak at 586 nm. Yields were typically between 35 and 60%, with lower PNIPAM coil fractions resulting in higher yields.

Bioconjugate purity was assessed using both denaturing and native protein gels (Figure 2-13). In a denaturing gel, several bands were observed. Unconjugated mCherry appeared in 3 bands at 28, 19, and 9 kDa due to cleavage at the acylimine bond in the chromophore. The conjugate appeared in 2 broad bands. The first was at the expected conjugate molecular weight in which the PNIPAM is attached to the intact protein. This band appeared very broad and smeared primarily as a result of polymer attachment, but also because of the polymer polydispersity. The second conjugate band appeared as a result of the case where PNIPAM was

attached to mCherry protein in which the chromophore bond had been cleaved. The thiol in mCherryS131C is located on the protein fragment that is approximately 19 kDa. The conjugate purity was calculated by dividing the band intensity due to bioconjugates by the sum of the band intensity due to the bioconjugate and the mCherry band at 28 kDa.

For mCherry-PNIPAM materials, bioconjugate purity was assessed more accurately using native gels. In a denaturing gel, the multiple bands resulting from chromophore cleavage can result in two different species appearing in the same region. Also, there is the possibility that the thiol-maleimide bond may be cleaved during the gel preparation process due to the presence of BME and the reactivity of the maleimide by thiol exchange,[14] resulting in a lower measured purity. In a native gel, unconjugated mCherry bands at apparent molecular weights of 170 kDa (very faint) and 200 kDa correspond to protein monomers and dimers, respectively. Each conjugate was seen in two bands: one band of conjugate with the average molecular weight PNIPAM attached and a higher molecular weight band with the coupled PNIPAM attached. At high polymer molecular weights, these bands were not clearly resolvable.

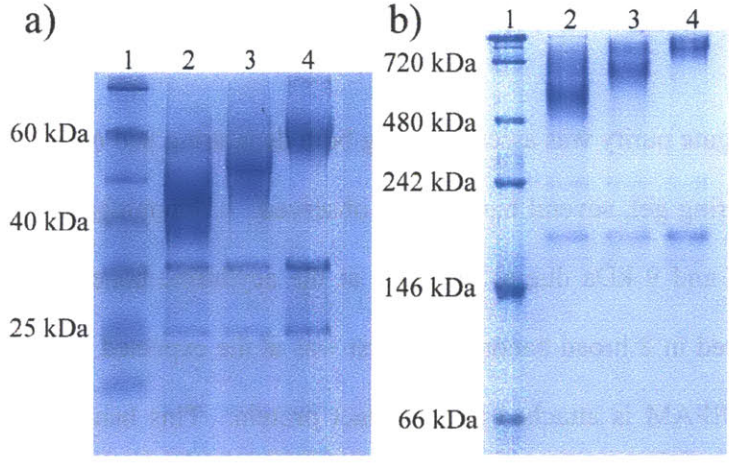

Figure 2-13. Typical denaturing gel (a) and native gel (b) for bioconjugate materials with f_{PNIPAM} = 0.42, 0.53, 0.69 in lanes 2, 3, and 4, respectively.

Lane analysis of these protein gels showed that bioconjugates were typically between 92 and 99% pure. The purity of each conjugate was estimated using lane analysis software (Image Lab by Bio-Rad Laboratories) by dividing the integrated intensity resulting from the bioconjugate band by the total integrated intensity from all bands. This molar purity is then converted to a mass-based purity using the molecular weights of mCherry and PNIPAM. It was found that bioconjugates with lower PNIPAM coil fractions typically resulted in higher purities. This is likely the result of a combination of higher reaction conversion and better binding of bioconjugate to Ni-NTA with lower molecular weight PNIPAM polymers.

2.4 Sample Preparation and Data Acquisition Techniques

After the purified protein-polymer block copolymers are dialyzed to pure water, they must be concentrated before being processed into solid state samples. Concentration was performed using Millipore Ultra-15 centrifugal filters with a molecular weight cutoff of 10 kDa. The bioconjugate was concentrated to approximately 70-100 mg/mL by repeated centrifugation at 5,000 x g at 4 °C for 20 minutes. After concentration, the pH was adjusted using formic acid and any small molecule osmolyes were added in the proper ratios as necessary.

Small-angle X-ray scattering (SAXS). Bulk samples for X-ray scattering were prepared by removing water at room temperature under vacuum or at 40 °C at ambient pressure. Initially, vacuum levels for solvent evaporation were controlled by hand, but this was found to result in variations from sample to sample. Therefore, the solvent evaporation rate at room temperature was adjusted using a vacuum controller with a ramp rate of 50 Torr/hr and a setpoint of 300 Torr to slowly remove water. Then, full vacuum was applied overnight to complete the drying process. Moulds for casting bulk SAXS samples consisted of washers with a 5 mm inner

diameter and a 1 mm height with Kapton tape on one side (Figure 2-14a). Typically 2-3 aliquots of 40 μL of concentrated bioconjugate solution were required to fill the mould. These solid state samples may be stored for extended periods of time (at least one year) in a cool, dry and dark place without noticeable changes in morphology.

After casting, a subset of samples was solvent annealed. The solvent annealing setup consisted of approximately 1 cm of solvent in the bottom of a sealed glass jar with an inverted beaker on which the sample was placed, giving a sample to liquid distance of 4 cm (Figure 2-14c). The solvent was usually water, but in one study it was a 1 vol% formic acid solution. Solvent annealing was performed for 8, 12, 24 or 72 hours, and no appreciable loss of solvent occurred during annealing. After annealing, the samples were allowed to dry under ambient conditions (below the glass transition temperature of the material), kinetically arresting the process of structure evolution.

Solution state samples were initially cast under vacuum from the concentrated solution. Small pellets approximately 1 mg in mass were prepared by drying 20 μL droplets of concentrated block copolymer solution on a Teflon sheet (Figure 2-14b). A vacuum ramp rate of 300 Torr/hr with a setpoint of 50 Torr was used, followed by exposure to full vacuum. These pellets were then weighed and transferred to eppendorf tubes for solution preparation. To each tube, nanopure water was added to create approximately 30 mg of each block copolymer solution at the desired mass fraction. The tubes were then centrifuged at approximately 20,000 x g for 2 minutes to ensure both the pellets and water were at the bottom of the tube to facilitate good mixing. The solutions were protected from light with aluminum foil and placed at 4 °C for sample hydration. The centrifugation process could be repeated over the next several days to ensure homogeneous solutions. For concentrations of 50 wt% and below, 24 hours was

sufficient hydration time, but for 60 and 70 wt% solutions, several days were required. Once sample hydration was complete, the solutions were transferred to washers prepared with Kapton tape on one side. Then another piece of Kapton tape was placed on the other side to seal the sample in place. Samples were stored at 4 °C shielded from light until use. Sample pellets could be prepared up to several months in advance; however, once samples were hydrated, they were used within one month in order to ensure that the Kapton tape seal did not allow significant water evaporation.

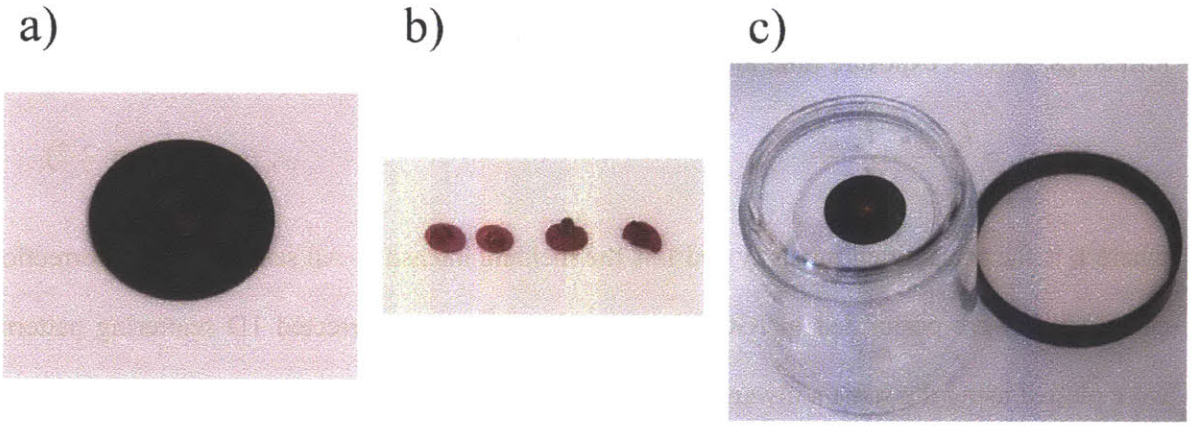

Figure 2-14. (a) Solid state mCherry-PNIPAM sample cast in a washer (b) Solid mCherry-PNIPAM pellets after vacuum drying on Teflon sheet (c) Solvent annealing apparatus consisting of a glass jar with an inverted beaker on which the solid state sample is placed.

Synchrotron SAXS data was collected at the National Synchrotron Light Source (NSLS) at Brookhaven National Lab (Beamlines X27C and X9) and at the Advanced Photon Source at Argonne National Lab (Beamline 12-ID-B) following the standard operating procedures at each beamline. Images were reduced to one dimensional scattering patterns using the software provided at each beamline. At the NSLS (where the majority of the data was collected), scattering patterns for solid state samples were acquired for 5 minutes at 25 °C, while data for

solution state samples was acquired for 30 seconds. For temperature dependent data collected on solution state samples, an equilibration time of 10 minutes at each temperature was sufficient. Scattering data was corrected for empty and dark field scattering using the following equation:

$$I_{corrected} = \frac{1}{T_{sample} \cdot BC_{sample}} \left[\left(\frac{S_{sample} - S_{background}}{t_{sample}} \right) - \left(\frac{S_{dark} - S_{background}}{t_{dark}} \right) \right] - \frac{1}{T_{empty} \cdot BC_{empty}} \left[\left(\frac{S_{empty} - S_{background}}{t_{empty}} \right) - \left(\frac{S_{dark} - S_{background}}{t_{dark}} \right) \right] \quad \text{(Eqn. 2-1)}$$

where S is the 1D reduced scattering intensity, T is transmittance, BC is beam current in milliamps, and t is exposure time in seconds. Transmittance was calculated using:

$$T_{sample} = \frac{I_{t,sample}}{I_{i,sample}} \cdot \frac{I_{i,open}}{I_{t,open}} \quad \text{(Eqn. 2-2)}$$

where I_t is the transmitted intensity and I_i is the incident intensity. All scattering data correction calculations were performed in IGOR Pro (version 6.1.2.1). Corrected 1D scattering patterns were plotted using the same software.

In the scattering correction formula above, the background was an acquisition with the shutter closed for a very short time (~ 1 second). This allows for corrections of any abnormal and systematic errors in pixel readings from the detection camera. The dark was an acquisition with the shutter closed for a longer time (ideally the same time as the sample acquisition). This provides information necessary to correct for detection events which occur even in the absence of the X-ray source. The empty was an acquisition (ideally the same length of time as the sample) with just the Kapton tape on which the sample was prepared. The empty allows for subtraction of the scattering due to the Kapton and not the sample under investigation. Finally, the open intensities were obtained by allowing the X-ray beam to pass through an empty sample holder, and they are used for calculating sample transmittances.

Transmission electron microscopy (TEM). The same bulk samples used for SAXS were used for microscopy after scattering experiments were completed. Samples were cryo-microtomed to a thickness between 60 and 65 nm using a Leica EM UC6 cryoultramicrotome. The microtome was operated at -110 °C for all samples except those containing 20 wt% glycerol in which case -80 °C was used. A dry pickup technique was used to collect the slices on copper grids with a square mesh size of 400 lines per inch. With such a small mesh size, a support coating was not necessary on the TEM sample grids. Samples were then stained with ruthenium tetroxide vapors from a 0.5% aqueous solution for 20 minutes. Due to the greater number of alcohol, amine, and aromatic functional groups on the protein compared with the polymer, the protein domains were selectively stained and appear dark in images.

Transmission electron microscopy was performed on a JEOL 2000FX or a JEOL 2011 microscope. Both were operated in bright field mode with LaB_6 filament and an accelerating voltage of 120 kV. Images were captured using a digital camera in a fixed bottom mount configuration. Images were processed into their final forms using ImageJ (version 1.44p) to add scale bars and Adobe Photoshop CS4 Extended (version 11.0.2) to adjust the brightness and contrast levels.

Experiments were attempted at a higher acceleration voltage of 200 kV, but this destroys the thin slices of material. Also, a few experiments were attempted using a JEOL 200CX TEM which is equipped with a tungsten filament. Because a tungsten filament is not as bright as LaB_6, the contrast was significantly reduced making the acquisition of clear images extremely difficult. As a result, it is highly recommended to use a TEM with a LaB_6 filament operating at 120 kV for imaging these protein-polymer block copolymers.

UV-vis spectrophotometry. Samples for solid state UV-vis were prepared very similarly to those for SAXS. The solvent evaporation rate was extremely important for obtaining reproducible spectroscopy results. Initial studies exposing the samples directly to full vacuum or manually controlling the vacuum level resulted in data sets with large variability. For more reproducible films, a ramp rate of 300 Torr/hr with a final setpoint of 50 Torr was used. These samples were exposed to vacuum for four hours in total. For each sample, 50 μL of conjugate solution at an mCherry concentration of 10 mg/mL was deposited on a quartz substrate and then exposed to vacuum. The UV-vis spectra were acquired immediately after removal from the vacuum chamber. A subset of samples was solvent annealed directly after removal from vacuum using the same setup as described for bulk samples. After annealing was complete, the samples were removed and allowed to dry briefly under ambient conditions until the surface was no longer shiny due to the presence of water. The absorption spectra for these samples were taken immediately after the films no longer appeared wet.

Initial UV-vis measurements for determining protein functionality in the solid state suffered from poor day-to-day reproducibility. During the first round of experiments, the vacuum level during casting was controlled manually and samples were exposed to full vacuum nearly immediately. Figure 2-15 shows the results for three distinct vacuum casting experiments. All samples came from the same stock solution at a concentration of 10 mg/mL mCherry. While there is good agreement among samples cast at the same time, there is not agreement among samples cast separately. This motivated the use of a prescribed and controlled vacuum ramp rate in order to obtain reproducible UV-vis measurements that are presented in Chapters 4 and 5.

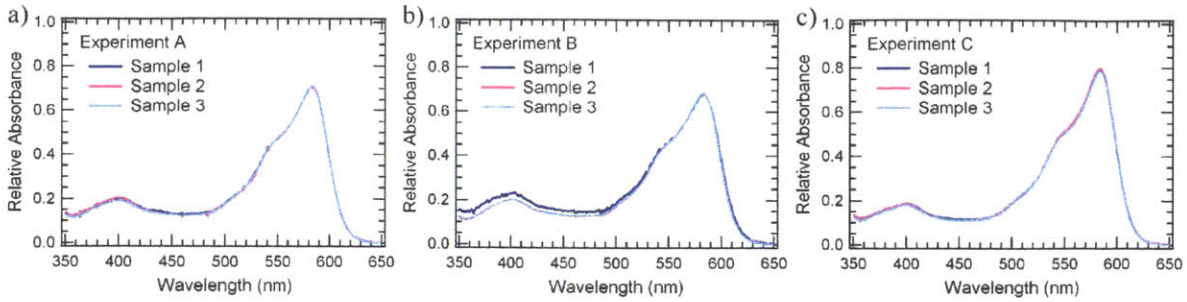

Figure 2-15. Studies investigating the reproducibility of UV-vis measurements for assessing protein functionality retention in the solid state. Three samples were identically prepared from the same solution for each of the three separate experiments performed on different days. Solid films were prepared by solvent evaporation under manually controlled vacuum levels. The averages among the three replicates were: 0.70, 0.67, and 0.78 for experiments A, B, and C, respectively.

Rehydrated UV-vis spectra were obtained directly following acquisition of solid state data. To prepare the rehydrated samples, the quartz containing the solid state sample was placed in a small beaker and 500 μL water was added to cover the sample. The solution was mixed to obtain a homogeneous solution which was then loaded in to a quartz cuvette with a 1 cm path length for data acquisition.

Both solid state and rehydrated UV-vis spectra were collected using a Cary 50 UV-vis spectrophotometer. A TLC 40 (Quantum Northwest) sample holder equipped with a Peltier temperature controller was used, and data were taken every nanometer between 190 and 800 nm. A spectrophotometric measure of protein function was calculated as A_{586} of the sample relative to A_{586} of the as-synthesized conjugate in solution, where both values were normalized by A_{280} to control for variations in protein concentration. IGOR Pro was used to perform this data analysis as well as plot the results. At least three replicates were averaged for each sample, and the best,

most reproducible results were obtained when using the same fresh solution for each replicate sample.

Thermostability. Samples for thermostability measurements were prepared the same way as samples for UV-vis spectrophotometry, except that the casting solution was at a concentration of 7 mg/mL mCherry. The quartz substrate for these samples was a rectangle which fit into the UV-vis sample holder. A cardboard spacer was used to ensure that the quartz plate remained upright in the sample holder and had good contact for heat transfer (Figure 2-16). A constant stream of nitrogen was supplied to the sample chamber at a flowrate of 50 standard cubic feet per hour to reduce the oxidative stress of the environment. A silicone rubber coating was briefly considered to further isolate the sample from its environment; however, it obscured the absorbance measurements reducing the signal to noise ratio, and did not show improvements over samples without this coating.

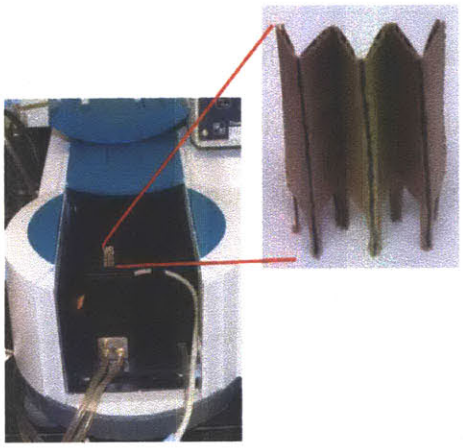

Figure 2-16. Sample holder for thermostability measurements showing how cardboard spacer is inserted into UV-vis spectrophotometer.

Thermal stability measurements were conducted by measuring A_{586} as a function of temperature between 25 and 100 °C using the Peltier temperature controlled sample holder with

a temperature ramp rate of 1 °C/min. A ramp rate of 3 °C/min was also tested for a smaller subset of samples; both ramp rates gave identical results, confirming the absence of kinetic effects. Additional experiments were conducted to confirm the absence of photobleaching of the mCherry chromophore in the timescale of a single experiment. The temperature at which the sample lost half of its initial absorption at 586 nm was taken as the apparent melting temperature. Three replicates were averaged to produce the final results. All data analysis and figure preparation was performed using IGOR Pro.

Cloud point measurements. Cloud point measurements were used to determine the transition temperature of the bioconjugate in dilute solution. Solutions of each conjugate material were prepared at a concentration of 1 mg/mL PNIPAM. Data was collected at 700 nm every 10 seconds during a temperature ramp from 20 to 50 °C at a ramp rate of 0.1 °C/min. The transition temperature was taken as the temperature at which half of the highest absorbance was observed. All data analysis and figure preparation was performed using IGOR Pro.

Circular dichroism (CD). Circular dichroism was used to assess the protein secondary structure content after the process of dehydration and self-assembly. CD experiments were attempted on solid film samples, similar to those prepared for solid-state UV-vis. However, these samples resulted in a very low signal to noise ratio which was not improved by altering the film thickness. For these experiments, mCherry at concentrations of 1 and 10 mg/mL was drop cast on quartz surfaces and dried under manually controlled vacuum. At both concentrations very little ellipticity was observed. Due to the high sensitivity of this technique on protein concentration, it was suspected that the films were not smooth or uniform enough to make these measurements accurately. As a result, CD was performed on the rehydrated samples after UV-vis measurements were acquired. The concentration of each solution was adjusted such that the

absorbance at 280 nm was approximately 0.5. The concentration based on the A_{280} was used because some of the protein may have lost its chromophore function prior to CD experiments.

CD spectra were measured on an Aviv model 202 CD spectrometer operating at 25 °C. All spectra were background corrected. Data was acquired at wavelengths between 200 and 250 nm at 1 nm intervals. Spectra were analyzed for secondary structure content with CDPro software using CONTINLL, SELCON3, and CDSSTR methods. The results from all three methods were averaged to produce the final results. For data analysis with CDPro, data were converted from raw ellipticity to molar circular dichroism using the following equation:

$$\theta_{MCD} = \frac{\theta_{meas}}{3298 \cdot L \cdot C \cdot n} \qquad \text{(Eqn. 2-3)}$$

where θ_{meas} is the measured ellipticity, L is the path length in centimeters, C is the molar concentration of protein, and n is the number of amino acids in the protein. A reference basis set of 43 proteins was used (SP43) and the data was fit over a wavelength range from 200 or 205 nm up to 240 nm.

Fourier transform infrared spectroscopy (FTIR). Samples for FTIR were cast in a similar manner as samples for solid state UV-vis spectrophotometry. The only differences were that for FTIR, silicon wafers (test grade, P type with boron dopant, (100) orientation, 500 μm thick, 1-50 ohm-cm resistivity) were used as the substrate and bioconjugate was used at an mCherry concentration of 6 mg/mL.

FTIR data was acquired using a Thermo Nexus 870 with 64 scans at a 2 cm^{-1} resolution resulting in data points every 1 cm^{-1}. Analysis was performed using OMNIC software. First, data were background corrected using the spectrum from a bare silicon wafer. Then the spectra were baseline corrected to ensure a flat baseline between 1800 and 2500 cm^{-1}. The spectra were then adjusted using the smoothing function in the OMNIC software package. This algorithm

removes the high frequency noise in the data by adjusting the current data point based on several surrounding points. This was necessary to obtain Fourier Self-Deconvolution (FSD) curves with wider bandwidths. FSD spectra were also calculated using OMNIC software in the amide I region between 1600 and 1700 cm^{-1}. An enhancement factor of 2.5 and a bandwidth around 30 cm^{-1} was chosen for general secondary structure identification. Each peak in the FSD was assigned to a secondary structure according to literature[15-22] and the relative areas under each peak were used to determine secondary structure content in the solid state samples.

Optical microscopy. Samples for optical microscopy were also cast in a similar manner as samples for solid state UV-vis spectrophotometry, except that glass coverslips were used as substrates. Samples were imaged with a Zeiss AxioSkop 2 MAT microscope operating in bright field mode immediately after removal from the vacuum chamber. Images were processed into their final form using ImageJ to add scale bars and Photoshop to adjust the brightness and contrast.

Small-angle neutron scattering (SANS). SANS experiments were performed on the Low-Q Diffractometer end station at the Lujan Neutron Science Center at Los Alamos National Laboratory. Hydrogenated conjugate samples were dialyzed into 98% deuterated water or a 20 mM formate buffer at pH = 5.7 made with deuterated water. Samples were then loaded into quartz banjo cells with a 1 mm sample path length, and scattering patterns were collected until at least 250,000 events above background. Data was collected at temperatures of 25 and 40 °C to alter the solvent quality for the polymer block. Absolute intensities were obtained by correcting for background scattering and open beam neutron flux. SANS experiments were repeated at both 1 wt% and 3 wt%, producing identical results. The resulting spectra were fit with either the

Beaucage[23] model or the Percus-Yevick[24-26] model depending on the solvent quality for the polymer block.

In good solvents for the polymer block, the Beaucage model was used according to the following equation:

$$I(q) = Bkgd + G\exp\left(-\frac{q^2R_g^2}{3}\right) + \frac{B\left[erf\left(\frac{qR_g}{\sqrt{6}}\right)\right]^{3P}}{q^P} \qquad \text{(Eqn. 2-4)}$$

where the five parameters to be fit are Bkgd, G, R_g, B, and P. The data fitting was performed in IGOR Pro using the NIST Center for Neutron Research (NCNR) SANS package.[27]

For materials in a poor solvent for the polymer block, the Percus-Yevick model was employed:[24]

$$I(q) = K \cdot S(q) \cdot F(q) + C \qquad \text{(Eqn. 2-5)}$$

where the intensity depends on a scaling factor, K, the structure factor for close packed micelles, S, the form factor describing the micellar geometry, F, and incoherent background scattering, C. The structure factor is described by:

$$S(q) = \frac{1}{1 + 24\eta\left(G(A)/A\right)} \qquad \text{(Eqn. 2-6)}$$

where

$$A = 2qr \qquad \text{(Eqn. 2-7)}$$

$$G(A) = \frac{\alpha}{A^2}\left(\sin(A) - A\cos(A)\right) + \frac{\beta}{A^3}\left(2A\sin(A) + \left(2 - A^2\right)\cos(A) - 2\right) + \frac{\gamma}{A^5}\left(-A^4\cos(A) + 4\left[\left(3A^2 - 6\right)\cos(A) + \left(A^3 - 6A\right)\sin(A) + 6\right]\right) \qquad \text{(Eqn. 2-8)}$$

and

$$\alpha = \frac{(1+2\eta)^2}{(1-\eta)^4} \qquad \text{(Eqn. 2-9)}$$

$$\beta = \frac{-6\eta\left(1+\eta/2\right)^2}{(1-\eta)^4} \qquad \text{(Eqn. 2-10)}$$

$$\gamma = \frac{\frac{1}{2}\eta(1+2\eta)^2}{(1-\eta)^4} \qquad \text{(Eqn. 2-11)}$$

In these equations, η is the packing fraction of the micellar spheres.

The form factor for polydisperse micellar spheres is given by:

$$F(q) = \frac{\int_0^\infty P(r) f^2(q,r) dr}{\int_0^\infty P(r) dr} \qquad \text{(Eqn. 2-12)}$$

where

$$f(q,r) = \frac{4}{3}\pi r^3 \frac{3}{(qr)^3}\left[\sin(qr) - qr\cos(qr)\right]\exp\left(-\sigma^2 q^2\right) \qquad \text{(Eqn. 2-13)}$$

$$P(r) = \sqrt{2\sigma_p^2 \pi}\exp\left(\frac{\left(-\ln(r) - r_0\right)^2}{2\sigma_p^2}\right) \qquad \text{(Eqn. 2-14)}$$

where σ describes the diffuseness of the micellar boundary. $P(r)$ describes a lognormal distribution characterized by parameters r_0 and σ_p. A lognormal distribution was used instead of the typical Gaussian distribution to prevent unphysical negative micellar radii.[26] Data fitting with this model was performed in Matlab using the non-linear regression tool with code developed by Matthew Glassman.

Dynamic light scattering (DLS). DLS experiments were performed on a DynaPro Nanostar at a scattering angle of 90° with a laser wavelength of 658 nm. The same 1 wt% solutions that

were used for SANS experiments were used for DLS; however, prior to these experiments, the solutions were filtered with a 0.2 μm sterile filter to remove any particulates. Data was acquired with 10 x 10 second acquisitions with at least 10 minutes equilibration at each temperature. DYNAMICS software was used for data analysis.

2.5 References

1. N. C. Shaner, R. E. Campbell, P. A. Steinbach, B. N. G. Giepmans, A. E. Palmer and R. Y. Tsien, *Nat. Biotechnol.*, 2004, **22**, 1567-1572.
2. X. K. Shu, N. C. Shaner, C. A. Yarbrough, R. Y. Tsien and S. J. Remington, *Biochemistry*, 2006, **45**, 9639-9647.
3. *The QIAexpressionist*, 2003.
4. A. A. Pakhomov, N. V. Pletneva, T. A. Balashova and V. I. Martynov, *Biochemistry*, 2006, **45**, 7256-7264.
5. L. A. Gross, G. S. Baird, R. C. Hoffman, K. K. Baldridge and R. Y. Tsien, *Proc. Natl. Acad. Sci. U. S. A.*, 2000, **97**, 11990-11995.
6. B. C. Lee and R. N. Zuckermann, *Chem. Commun.*, 2010, **46**, 1634-1636.
7. J. A. Chung, J. W. Wollack, M. L. Hovlid, A. Okesli, Y. Chen, J. D. Mueller, M. D. Distefano and T. A. Taton, *Anal. Biochem.*, 2009, **386**, 1-8.
8. E. Bays, L. Tao, C. W. Chang and H. D. Maynard, *Biomacromolecules*, 2009, **10**, 1777-1781.
9. Y. Z. You and D. Oupický, *Biomacromolecules*, 2007, **8**, 98-105.
10. B. J. Neubert and B. B. Snider, *Org. Lett.*, 2003, **5**, 765-768.
11. K. Van Durme, G. Van Assche and B. Van Mele, *Macromolecules*, 2004, **37**, 9596-9605.
12. Y. J. Zhang, S. Furyk, D. E. Bergbreiter and P. S. Cremer, *J. Am. Chem. Soc.*, 2005, **127**, 14505-14510.
13. J. C. Han and G. Y. Han, *Anal. Biochem.*, 1994, **220**, 5-10.
14. A. D. Baldwin and K. L. Kiick, *Bioconjugate Chem.*, 2011, **22**, 1946-1953.
15. D. M. Byler and H. Susi, *Biopolymers*, 1986, **25**, 469-487.
16. M. Jackson and H. H. Mantsch, *Crit. Rev. Biochem. Mol. Biol.*, 1995, **30**, 95-120.
17. J. Kong and S. Yu, *Acta Biochim. Biophys. Sin.*, 2007, **39**, 549-559.
18. K. Fu, K. Griebenow, L. Hsieh, A. M. Klibanov and L. Robert, *J. Controlled Release*, 1999, **58**, 357-366.
19. H. Herberhold, S. Marchal, R. Lange, C. H. Scheyhing, R. F. Vogel and R. Winter, *J. Mol. Biol.*, 2003, **330**, 1153-1164.
20. A. Barth and C. Zscherp, *Q. Rev. Biophys.*, 2002, **35**, 369-430.
21. W. Huang, S. Krishnaji, X. Hu, D. Kaplan and P. Cebe, *Macromolecules*, 2011, **44**, 5299-5309.
22. S. Matheus, W. Friess and H. C. Mahler, *Pharm. Res.*, 2006, **23**, 1350-1363.
23. G. Beaucage, *J. Appl. Crystallogr.*, 1995, **28**, 717-728.
24. D. J. Kinning and E. L. Thomas, *Macromolecules*, 1984, **17**, 1712-1718.

25. M. E. Seitz, W. R. Burghardt, K. T. Faber and K. R. Shull, *Macromolecules*, 2007, **40**, 1218-1226.
26. M. J. Glassman and B. D. Olsen, *Soft Matter*, 2013, **9**, 6814-6823.
27. S. Kline, *J. Appl. Crystallogr.*, 2006, **39**, 895-900.

Chapter 3 Solid-State Nanostructured Materials from Self-Assembly of a Globular Protein-Polymer Diblock Copolymer

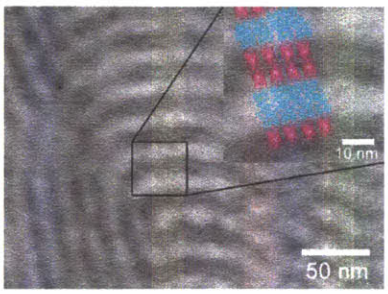

3.1 Abstract

Self-assembly of three-dimensional solid state nanostructures containing approximately 33% by weight globular protein is demonstrated using a globular protein-polymer diblock copolymer, providing a route to direct nanopatterning of proteins for use in bioelectronic and biocatalytic materials. A mutant red fluorescent protein, mCherryS131C, was prepared by incorporation of a unique cysteine residue and site-specifically conjugated to end-functionalized poly(N-isopropyl acrylamide) through thiol-maleimide coupling to form a well-defined model protein-polymer block copolymer. The block copolymer was self-assembled into bulk nanostructures by solvent evaporation from concentrated solutions. Small-angle X-ray scattering and transmission electron microscopy illustrated the formation of highly disordered lamellae or hexagonally perforated lamellae depending upon the selectivity of the solvent during evaporation. Solvent annealing of bulk samples resulted in a transition towards lamellar nanostructures with mCherry packed in a bilayer configuration and a large improvement in long range ordering. Wide-angle X-ray scattering indicated that mCherry did not crystallize within

the block copolymer nanodomains and that the β-sheet spacing was not affected by self-assembly. Circular dichroism showed no change in protein secondary structure after self-assembly, while UV-vis spectroscopy indicated approximately 35% of the chromophore remained optically active.

3.2 Introduction

Enzymes have garnered a great deal of attention for incorporation into a variety of biocatalytic and bioelectronic devices[1-3] because of their substrate specificity, high catalytic rates, and ability to operate under mild reaction conditions. Enzymes have been incorporated into highly selective and sensitive biosensors for applications such as glucose detection and medical diagnostics.[4-5] Biofuel cells have been prepared that operate on nontraditional fuels such as sugars, utilize low operating overpotentials, and do not require an electrolyte membrane.[6-8] Enzymes also continue to be widely used to catalyze the synthesis of pharmaceutical compounds,[9] and more recently, biocatalysts are being pursued for a wide variety of energy applications, including carbon sequestration,[10] carbon dioxide reduction,[11-13] and hydrogen production.[14-16] Photodiodes or photovoltaics have been prepared from reaction center proteins,[17] photosynthetic complexes,[18] and fluorescent proteins[19] in attempts to exploit the high absorption cross section and quantum efficiency of the proteins. All of these protein-based devices offer the added advantages of biodegradability and renewability, making them attractive as green chemistry techniques become increasingly prevalent.

Although proteins offer the aforementioned desirable advantages, the incorporation of these complex molecules into highly efficient and functional devices presents a large number of challenges. In order to increase the enzyme activity per unit area, a high density of enzyme

should be achieved by structuring the material in three dimensions. Diffusion of substrate/product or charge carriers into and out of the material must be rapid to minimize transport limitations, and control over the orientation of the enzyme is desired to maintain access to the substrate and cofactor binding areas. Finally, the material should be engineered to improve the stability and lifetime of the protein. These engineering design goals have motivated the development of a number of strategies for immobilizing or nanopatterning enzymes.[20] Operational stability, efficiency and lifetime of enzymes have been shown to increase through immobilization with multiple tethers on porous supports or within a crosslinked material.[21]

Nanopatterning of proteins is required to increase the density of enzymes at the surface and to ensure continuous pathways for transport of electrons, substrates, and products through the material. Nanopatterning may also be used as a method to enforce proper orientation and stabilize the fold of the protein. Layer-by-layer techniques have been used to pattern proteins and polyelectrolytes on surfaces by taking advantage of electrostatic, hydrophobic and hydrogen bond interactions between the materials.[22-23] Alternately, a variety of lithographic methods including microcontact printing, photolithography and dip-pen lithography have been used to create templates for protein immobilization by patterning an attachment site where the protein selectively binds.[24-26] Covalent binding using lysine-NHS or cysteine-maleimide chemistries,[27] or non-covalent binding using biotin-avidin[28] or His tag-NTA[29] interactions are then employed to immobilize enzymes on the pre-formed patterns. In a third approach, nanostructured templates are self-assembled from amphiphilic molecules and the proteins are inserted into the templates. This type of template has been demonstrated with the use of block copolymer thin films,[30] nanostructures formed from surfactants in solution,[31] and through the self-assembly of lipid materials.[32]

Block copolymer self-assembly provides a simple, low cost method for fabricating nanopatterns in three dimensions that may be of high value for producing enzyme-based materials. Block copolymers prepared with two or more Gaussian coil polymer blocks are well-known to self-assemble into a wide variety of nanostructures with characteristic length scales from 5-100 nm.[33-35] The multidomain structures formed by these block copolymers make them ideal candidates for building three-dimensional structures with efficient mass or charge carrier transport.[36-37] However, the thermodynamics of coil-coil block copolymers do not generalize to more complex systems. Changes in the topology of the polymer chain and liquid crystalline or other specific interactions between polymers result in large changes in the phase behavior of these systems, as has been demonstrated for rod-coil block copolymers.[38] Incorporating a globular protein as one block in a block copolymer to direct the protein's self-assembly into nanostructured materials introduces a great deal of added complexity beyond both coil-coil and rod-coil systems due to the specific chain fold in the protein domain, the strong, directional interactions between proteins that lead to macromolecular crystallization, and the complex thermodynamics of interactions between proteins and synthetic polymers. It is unclear how the traditional concepts of block copolymer self-assembly will apply to globular protein-polymer block copolymers, particularly when the constraint of maintaining protein fold and function during processing and nanostructure self-assembly is imposed.

While significant effort has been directed towards the self-assembly of bulk and thin film block copolymers with α-helical, β-sheet, coiled-coil, and cyclical peptide blocks,[39-41] studies of globular protein-polymer conjugates have been restricted primarily to self-assembly in solution. Giant amphiphiles consisting of globular proteins and synthetic polymers have been synthesized and their self-assembly has been studied in solution.[42-44] The variety of observed morphologies

including spherical, rod-like and toroid micelles is due primarily to changes in relative coil fraction as well as processing conditions which kinetically favor certain morphologies.[45] Among these amphiphilic conjugates are PEGylated proteins which have been used to improve the stability and lifetime of proteins in serum.[46-48] However, there is currently a lack of fundamental knowledge on the self-assembly of globular protein-polymer conjugates in concentrated solutions or solid state materials, and these materials have not been evaluated as a means to nanopattern protein-based devices.

Here, we demonstrate block copolymer self-assembly as an effective technique for producing nanostructured plastics from globular proteins. A model globular protein-polymer diblock copolymer is synthesized based on the site-specific conjugation of poly(N-isopropyl acrylamide) (PNIPAM) to the fluorescent protein mCherry. Self-assembly is induced by evaporation of water from concentrated solutions of the copolymers, and the kinetic effects of evaporation method and post-evaporation solvent annealing are shown to influence nanostructure formation. The fold and optical activity of mCherry within the nanostructured assembly is investigated, and the packing of mCherry within the self-assembled nanostructure is explored.

3.3 Experimental Methods

Synthesis of 2-ethylsulfanylthiocarbonylsulfanyl-2-methyl propionic acid (EMP). This procedure was adapted from the work of You and Oupický.[49] First, ethanethiol (7.21 mL, 0.1 mol), acetone (73 mL), and tricaprylylmethylammonium chloride (1.0 g, 2.5 mmol) were combined and the mixture was cooled on ice under nitrogen. Next, 9 mL of 50% (w/v) sodium hydroxide was added dropwise. After an additional 20 minutes, carbon disulfide (6.03 mL, 0.1 mol) and acetone (12.6 mL) were combined and added dropwise. Chloroform (12 mL, 0.15 mol)

was added, followed by the addition of 80 mL of 50% (w/v) sodium hydroxide over 10 minutes. The yellow-orange mixture was stirred overnight. Water (200 mL) was added, followed by concentrated hydrochloric acid (80 mL) to drop the pH below 1. The mixture was extracted three times into diethyl ether and concentrated to a dark red oil. Crude product was purified *via* silica gel chromatography (1:1 hexanes/ether) and then distilled to yield 11.0 g of a bright orange, viscous liquid (49% yield). ^{1}H NMR ($CDCl_3$, δ): 1.33 (t, 3H, $-CH_2CH_3$), 1.72 (s, 6H, $-C(CH_3)_2COOH$), 3.30 (q, 2H, $-CH_2CH_3$).

Synthesis of exo-3a,4,7,7a-tetrahydro-2-(3-hydroxypropyl)-4,7-epoxy-14-isoindole-1,3(2H)-dione (1). Following the work of Neubert and Snider,[50] 3-amino-1-propanol (4.08 g, 54.2 mmol) was added dropwise to a solution of exo-3,6-epoxy-1,2,3,6-tetrahydrophthalic anhydride (9.0 g, 54.2 mmol) in 500 mL methanol. The reaction was stirred at 56 °C for 3 days, after which the solvent was removed by rotary evaporation to give a clear yellow oil. Then 100 mL dichloromethane was added and washed three times with 100 mL brine. The organic fraction was dried over sodium sulfate and the solvent removed under reduced pressure to give 2.71 g of a white solid (22% yield). ^{1}H NMR ($CDCl_3$, δ): 1.75 (tt, 2H, $-CH_2(CH_2)CH_2-$), 2.88 (s, 2H, -NC(O)CH-), 3.52 (t, 2H, $-CH_2O-$), 3.65 (t, 2H, $-NCH_2-$), 5.27 (s, 2H, -CH(O)-), 6.52 (s, 2H, -CHCH-).

Synthesis of RAFT agent. Functional RAFT chain transfer agent (CTA) was prepared by carbodiimide coupling.[51] EMP (1.88 g, 8.40 mmol), **1** (1.50 g, 6.72 mmol), 4-dimethylaminopyridine (103.8 mg, 0.84 mmol), and N,N'-dicyclohexylcarbodiimide (3.46 g, 16.8 mmol) were combined in 58 mL dry tetrahydrofuran and stirred under nitrogen at room temperature overnight. The reaction mixture was filtered and concentrated, and the product was purified by silica gel chromatography (1:1 hexanes/ethyl acetate) to yield 1.23 g of a bright

yellow solid (34% yield). ^{1}H NMR ($CDCl_3$, δ): 1.29 (t, 3H, -S-CH_2CH_3), 1.69 (s, 6H, -$C(CH_3)_2$-), 1.85-2.00 (tt, 2H, -$CH_2(CH_2)CH_2$-), 2.83 (s, 2H, -NC(O)CH-), 3.26 (q, 2H, -CH_2CH_3), 3.55 (t, 2H, -NCH_2-), 4.05 (t, 2H, -CH_2O-), 5.24 (s, 2H, -CH(O)-), 6.49 (s, 2H, -CHCH-).

Polymerization. The CTA and azobisisobutyronitrile (AIBN) (recrystallized twice from methanol) were added to a 2.0 M solution of NIPAM (sublimated) in acetonitrile in the ratio 600:1:0.2 (monomer:CTA:initiator). The solution was degassed by three freeze-pump-thaw cycles. The polymerization was carried out in a sealed flask at 65 °C and terminated after 75 minutes by removal of heat and exposure to oxygen. The polymer was then precipitated in cold diethyl ether and dried under vacuum. The maleimide was deprotected by heating to 120 °C under vacuum for 2 hours. The molecular weight and polydispersity were determined by gel permeation chromatography using a Waters Breeze 1525 HPLC system with a series 2414 refractive index detector, calibrated with poly(methyl methacrylate) standards, and N,N-dimethylformamide with 0.01 M LiBr as the mobile phase.

Cloning and protein expression. The gene for mCherry, optimized for prokaryotic codon usage, was subcloned into the pQE9 vector (Qiagen) which encodes for an N-terminal His tag. Site directed mutagenesis was used to create the mutant mCherryS131C by replacing a serine with a cysteine at residue 131, located in a loop region on the end of the β-barrel opposite the N and C termini. The protein was expressed in the *E. coli* strain SG13009 containing the pREP4 repressor plasmid, grown in Terrific Broth at 37 °C, and induced with 1 mM Isopropyl β-D-1-thiogalactopyranoside (IPTG) at OD_{600} = 1. The cells were cultured for 4.5 hours after induction and were then harvested. The cell were resuspended in lysis buffer (50 mM NaH_2PO_4, 300 mM sodium chloride, 10 mM imidazole, 10 mM β-mercaptoethanol (BME), pH 8.0),

incubated with 1 mg/mL lysozyme at 4 °C for 30 minutes and sonicated. The lysate was clarified, and the protein was purified using Ni-NTA metal affinity chromatography. Throughout the purification, 10 mM BME was used in all buffers. Elution fractions containing purified protein were dialyzed into 20 mM Tris buffer, pH = 8. The yield in the elution fractions was determined spectrophotometrically using the absorbance peak at 586 nm (extinction coefficient of 72,000 $M^{-1}cm^{-1}$).[52-53]

The purity of the protein was confirmed by denaturing gel electrophoresis (SDS-PAGE), native state gel electrophoresis, and matrix assisted laser desorption ionization mass spectrometry (MALDI-MS). SDS-PAGE (Appendix A) shows three bands near 28, 19 and 9 kg/mol due to partial cleavage of the protein during sample boiling before loading the gel.[54] The highest molecular weight band corresponds to the expected molar mass of the whole mCherry molecule, and the sum of the molar masses of the two lower mass bands also corresponds to the mass of the whole protein, consistent with hydrolysis of the sensitive acylimine bond within the mCherry chromophore.[55] The native gel (Appendix A), run at a high protein concentration, shows only a single prominent protein band corresponding to the mCherry and a higher molecular weight band corresponding to dimerization through the formation of a disulfide bond. Consistent with previously reported expressions of mCherry,[56-57] it is noted that the lower molar mass fragments are not observed by SDS-PAGE in more dilute samples. The observation of a single dominant band in the native gel indicates that cleavage occurs only during SDS-PAGE sample preparation. The purity of the protein was further confirmed by MALDI-TOF mass spectrometry; the measured molar mass of the protein was 28,201 g/mol compared to the expected mass of 28,134.48 g/mol. No peak was observed for the higher molar mass hydrolysis product (18,896 g/mol calculated molar mass), although a small peak was observed for the low

molecular weight fragment (9,256 g/mol calculated molar mass), consistent with the preferential observation of low molecular weight species by MALDI.

Bioconjugation. The coupling reaction between mCherryS131C and maleimide end-functionalized PNIPAM was performed in 20 mM Tris buffer, pH 8.0. Tris(2-carboxyethyl)phosphine (TCEP) (0.0185g, 0.0646 mmol) was added to the mCherryS131C solution (0.173g, 0.00646 mmol, 1.8 mg/mL) one hour prior to PNIPAM addition to reduce all thiol groups. Maleimide functionalized PNIPAM (2.61201g, 0.0451 mmol) was added to the solution and allowed to react overnight. The conjugate was purified by precipitation in 1.0 M ammonium sulfate solution followed by centrifugation at room temperature. The pellet containing conjugate and unreacted PNIPAM homopolymer was then resuspended in 20 mM Tris buffer (pH 8) and precipitated a second time. The excess PNIPAM was removed from the second pellet using Ni-NTA affinity chromatography to yield purified conjugate. After collecting the flow-through, the column was washed with approximately 7 column volumes of wash buffer before elution to completely remove unconjugated PNIPAM. The purified conjugate was dialyzed into pure water. Purity was analyzed using SDS-PAGE and the yield was determined spectrophotometrically.

Sample preparation and characterization. Conjugate solution was concentrated to approximately 44 mg/mL conjugate using Millipore Ultra-15 centrifugal filters with a molecular weight cutoff of 3 kDa. Bulk samples were prepared by evaporation of water either at 40 °C under ambient pressure or at room temperature under vacuum. Solvent annealing was performed at 4 °C or room temperature in sealed jars using nanopure water as the solvent. UV-vis spectra were collected at ambient temperature on a Cary 50 UV-vis spectrophotometer using a quartz cuvette and normalized to the absorbance at 280 nm. CD spectra were obtained using an Aviv

Model 202 circular dichroism spectrometer operating at 25 °C and converted into molar ellipticity by correcting for the water background and using the concentration determined by the A_{280}. CDPro was used to analyze spectra to determine the secondary structure content using CONTINLL, SELCON3 and CDSSTR methods. Disk-shaped samples for x-ray scattering were cast on kapton tape using 7 mm diameter washers as a mould. SAXS and WAXS data were collected using a Molecular Metrology ASSY 610-004378 system, and corrected for empty cell and dark field scattering. Bulk samples were cryo-microtomed using a Leica EM UC6 at -100 °C to a thickness of 50-60 nm for TEM analysis. Samples were stained with ruthenium tetroxide vapors from a 0.5% aqueous solution for 20-40 minutes. Due to the greater number of alcohol, amine and aromatic functional groups on the protein compared with the polymer, the protein domains were selectively stained and appear dark in images. A JEOL 2000FX transmission electron microscope was used to obtain bright field images using an accelerating voltage of 120 kV and a LaB_6 filament. Images were captured using an ORCA camera in a fixed bottom mount configuration.

3.4 Results and Discussion

Globular protein-polymer diblock copolymer synthesis. A model globular protein-polymer conjugate with a single well-defined bioconjugation site was synthesized using the red fluorescent protein mCherry and the thermoresponsive synthetic polymer PNIPAM. The protein mCherry was selected because the native sequence lacked cysteine residues, the high yield expression and purification of folded protein are well-established, and the fluorescent nature provided a simple and robust spectrophotometric method for conjugate characterization. The protein mCherry[52, 55] was mutated to introduce a unique thiol conjugation site into its sequence

by replacing serine with cysteine at residue 131, yielding the mutant mCherryS131C. The mutation is located in a loop region on the end of the β-barrel structure opposite both the N and C termini, as illustrated in Scheme 3-1. A 6xHis-tagged variant of this protein was expressed in *Escherichia coli* (*E. coli*) and then purified using metal affinity chromatography under native reducing conditions to preserve the delicate chromophore bond and reduce thiol inactivation. The yield of purified protein, determined spectrophotometrically at 586 nm based on the known extinction coefficient of mCherry,[52] was 121 mg/L culture.

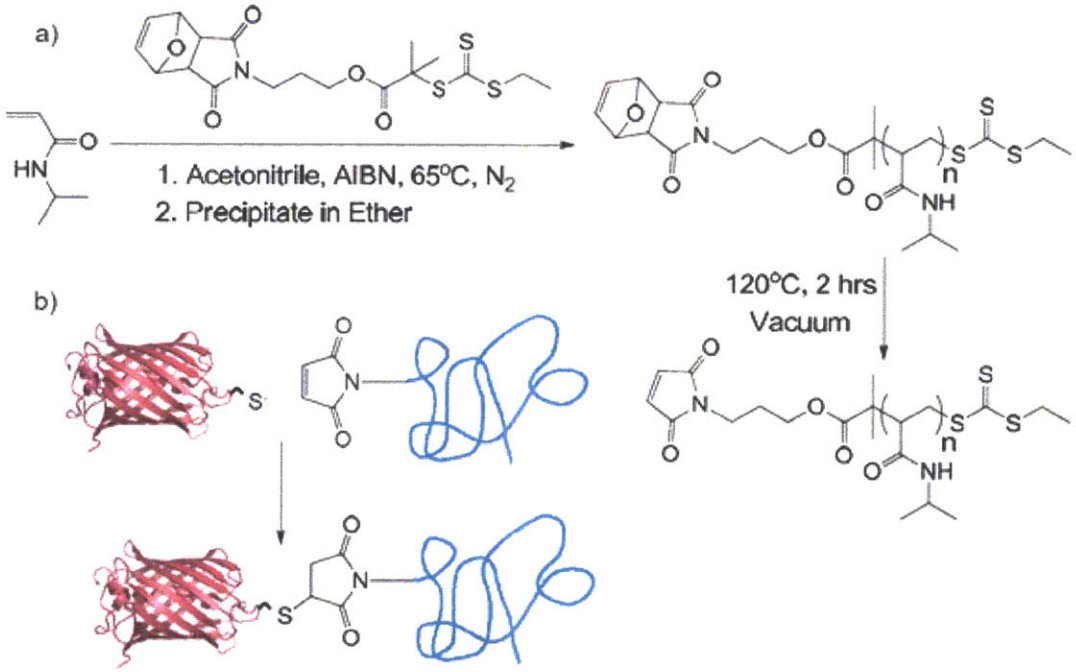

Scheme 3-1. Synthesis of maleimide-functionalized poly(N-isopropyl acrylamide) and its bioconjugation to mCherryS131C to create a protein-polymer diblock copolymer.

The diblock copolymer was synthesized by conjugating mCherryS131C to maleimide-functionalized PNIPAM. A reversible addition-fragmentation chain transfer (RAFT) agent

containing a protected maleimide group was used to synthesize low polydispersity PNIPAM (Scheme 3-1). After polymerization, the maleimide group was thermally deprotected to yield maleimide end-functionalized PNIPAM with a molar mass of 51.3 kg/mol and a polydispersity of 1.24. Gel permeation chromatography (GPC) analysis is shown in Figure 3-1. The polydispersity in these samples originates in part from a small shoulder at twice the peak molecular weight in the GPC trace that represents 8% of the total polymer mass. This minor high molecular weight fraction is believed to originate from a slight reactivity of the double bond in the protected maleimide group on the RAFT agent during polymerization to conversions greater than 50%. When an identical RAFT agent is used without the protected maleimide functionality, no coupling is observed.

Bioconjugation was then performed at room temperature in 20 mM Tris buffer (pH 8) using an 8-fold excess of PNIPAM. SDS-PAGE of the crude conjugation product and purified fractions is shown in Figure 3-2. The band at approximately 70,000 g/mol corresponds to the mCherry-PNIPAM conjugate with a PNIPAM volume fraction of 0.66 and a weight fraction of 0.66. The band at 28,000 g/mol corresponds to unconjugated mCherry, while the bands at 19,000 g/mol and 9,000 g/mol correspond to the partial hydrolysis of the mCherry chromophore acylimine bond during SDS-PAGE analysis.[54-56, 58] Lane analysis of the crude reaction mixture revealed a conversion of approximately 78%, comparable to previously reported conversions for thiol-maleimide couplings to globular proteins.[51, 59-60] Although the 8-fold excess of PNIPAM used gave maximum conversion of the mCherryS131C, decreasing to a five-fold excess still yielded approximately 70% conversion. After conjugation, unreacted mCherry was removed using ammonium sulfate precipitation; SDS-PAGE showed that after the first precipitation no additional unreacted mCherry is removed. Unconjugated PNIPAM was subsequently removed

by metal affinity chromatography; washing with 7 column volumes of buffer was used to ensure complete removal of the free PNIPAM. Analysis of the second elution lane (lane 8) suggests that the conjugate is > 90% pure, while the third elution lane (lane 9) demonstrates that at lower protein concentrations only the conjugate band is visible. The purified conjugate was obtained in a final yield of 30%. Circular dichroism and UV-vis spectroscopy (Appendix A) confirm that the protein structure and optical properties in the purified mCherry-PNIPAM diblock remain unchanged from that of the mCherryS131C in solution. Cloud point measurements (Appendix A) show that the thermal transition of the conjugate increases by ~ 5 °C relative to that of the homopolymer due to addition of the large hydrophilic protein.

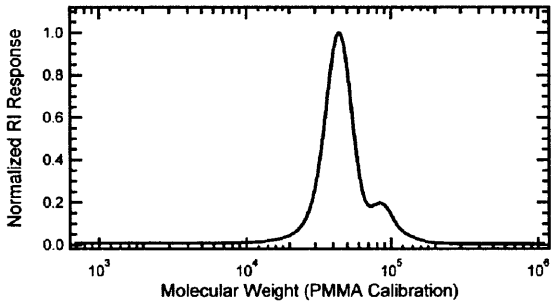

Figure 3-1. Normalized gel permeation chromatography trace of deprotected poly(N-isopropyl acrylamide) product with a poly(methyl methacrylate)-equivalent molecular weight of 51.3 kg/mol and a polydispersity of 1.24.

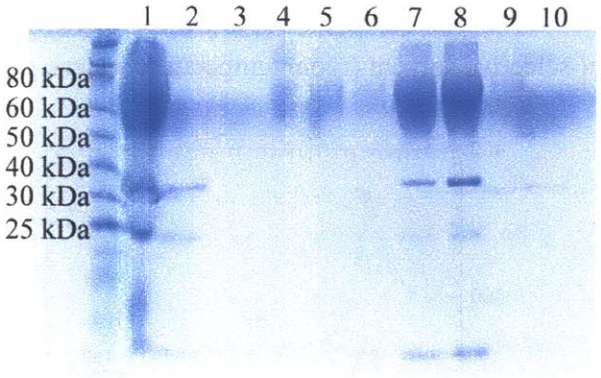

Figure 3-2. Denaturing SDS-PAGE gel showing purification of mCherryS131C-PNIPAM conjugate. The crude reaction mixture (lane 1) was purified by repeated precipitation of the conjugate using ammonium sulfate to remove unconjugated mCherryS131C. The discarded supernatants (lanes 2 and 3) contained most of the unconjugated mCherry. Metal affinity chromatography was used to remove excess PNIPAM. Minimal conjugate is lost from the column flow-through (lane 4) and the two wash steps (lanes 5 and 6). The conjugate is then eluted in four fractions (lanes 7-10).

Nanostructure formation. Self-assembly of mCherry-PNIPAM diblock copolymers was accomplished through evaporation of water from diblock copolymer solutions to form nanostructured bulk plastics. The formation of nanostructures strongly depends on the processing conditions used to prepare the material, as demonstrated by small-angle X-ray scattering (SAXS), shown in Figure 3-3, and transmission electron microscopy (TEM) images, shown in Figure 3-4. In the TEM images, the mCherry areas appear dark due to staining with ruthenium tetroxide which reacts with alcohols, amines and aromatics present on the protein surface.[61] Two processing pathways were explored for water evaporation: a protein-selective

solvent (40 °C water, above the lower critical solution temperature (LCST) of the PNIPAM homopolymer) and a non-selective solvent (room temperature water), as illustrated in Figure 3-5.

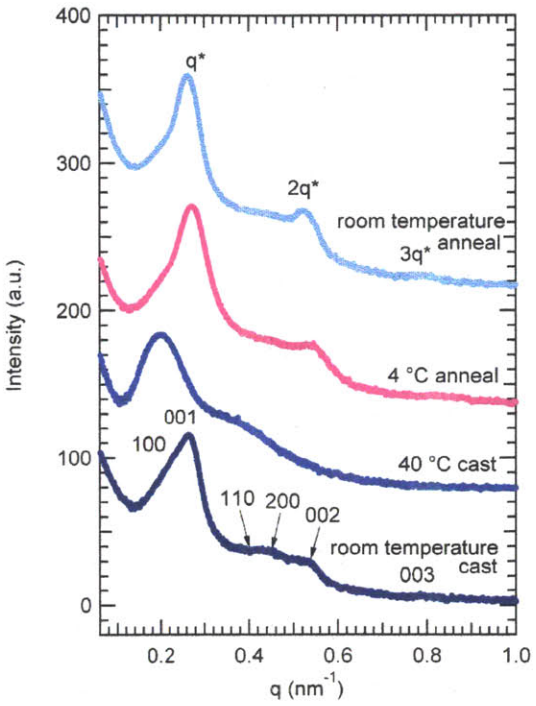

Figure 3-3. Small-angle X-ray scattering (SAXS) data of as-cast and solvent annealed mCherry-PNIPAM block copolymers. Samples were cast from both protein-selective (40 °C water) and non-selective (room temperature water) solvents. The materials form long-range ordered nanostructures with weak order. After solvent annealing in water, the samples transition to lamellar nanostructures with improved long-range order. Traces have been offset for clarity.

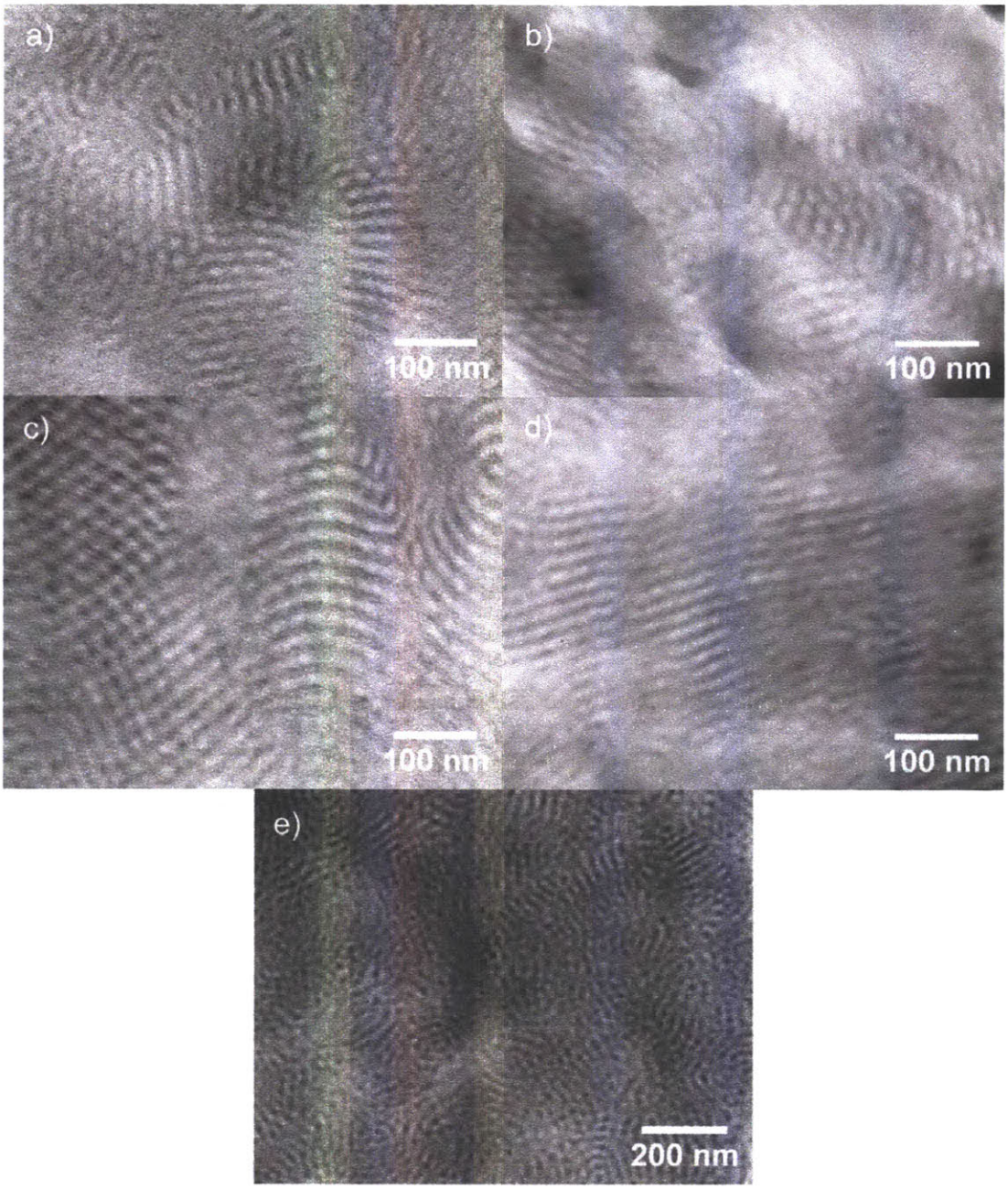

Figure 3-4. TEM images of mCherry-PNIPAM block copolymers demonstrate the formation of lamellae and hexagonally perforated lamellae in bulk samples cast at (a) 40 °C or (b) room temperature, and samples cast at room temperature followed by solvent annealing in water at (c) 4 °C or (d) room temperature. Panel e shows the 40 °C cast sample at a lower magnification.

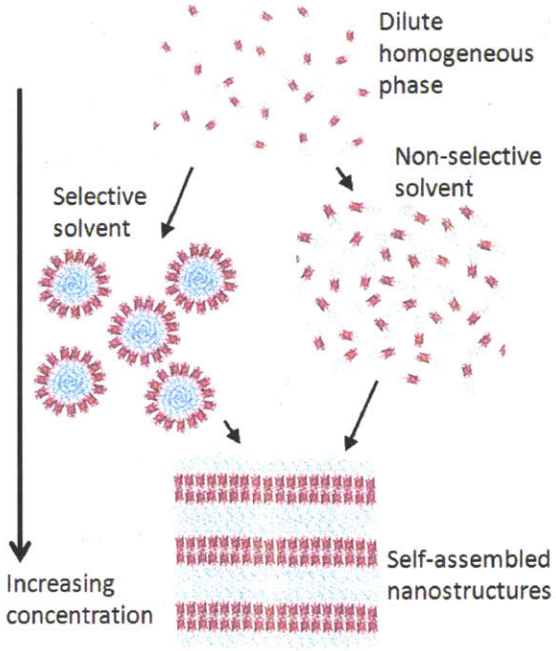

Figure 3-5. This schematic depicts two possible pathways towards self-assembly of mCherry-PNIPAM block copolymers. Room temperature water provides a non-selective solvent, whereas 40 °C water is a protein-selective solvent. Self-assembly is induced by increasing the block copolymer concentration through solvent evaporation.

Both as-cast samples contain multiple peaks in their SAXS patterns, indicating the formation of long-range ordered nanostructures. The nanostructures formed from a non-selective solvent exhibit two sets of peaks, a relatively intense set that can be indexed to a lamellar structure and a weaker set that may be indexed to a hexagonal lattice. The primary peak is asymmetric, composed of a 001 peak and a low q 100 shoulder. The first higher order reflections may be indexed to 110, 200, 002, and 003, corresponding to peaks from both a hexagonal and a lamellar lattice. These peak observations are consistent with a hexagonally

packed lamellar (HPL) morphology with a lamellar domain spacing of 23.4 nm and a hexagonal domain spacing of 26.5 nm. The 002 and 003 scattering peaks, corresponding to the lamellar spacing, are much more intense than the 110 and 200 scattering peaks corresponding to the hexagonal perforations, as is typical for HPL structures.[62] TEM images of the sample provide evidence for HPL formation and are consistent with previously reported images of HPL from coil-coil diblock copolymers.[63-64] The micrograph in Figure 3-4b shows areas of lamellar structure with perforations parallel to the lamellar normal as well as regions of the sample that have a hexagonally packed structure. These two structures are consistent with different orientations of the HPL unit cell in the sample. The formation of an HPL morphology at a PNIPAM volume fraction of 0.66 is similar to that found in coil-coil block copolymer systems where HPL morphologies are typically seen as non-equilibrium structures in a narrow window between lamellae and cylinders.[63] Even though the protein is the minority block in these copolymers, the protein domains perforate the coil regions. This suggests that the protein remains more highly hydrated than the PNIPAM during sample casting, increasing its effective volume fraction.

The assembled nanostructures from a protein-selective solvent show poorer ordering than those obtained from a non-selective solvent. The protein-selective solvent results in a relatively broad primary peak with a broad second order shoulder centered around a q value twice that of the primary peak. While the observed peak positions are consistent with the formation of lamellar nanostructures, the broad peaks indicate that the order in this sample is poorer than that in the sample cast from non-selective solvent. The TEM images in Figure 3-4a,e show the structurally heterogeneous nature of this sample containing small lamellar regions with hexagonally packed areas interspersed. These images show that the sample is composed of

undulating lamellae accompanied by regions of hexagonal structures with PNIPAM centers similar to the structure of the sample cast from a non-selective solvent. These structures may be the result of micelles that merged to form sheets. A lower magnification image (Figure 3-4e) reveals that these lamellar regions are interspersed with spherical protein aggregates, and that these domains are inverted from the observed HPL morphologies. Because this sample was prepared from a state where the protein and polymer are segregated due to immiscibility of the solvent and polymer, it is likely that kinetic barriers to nanoscale structural rearrangement during solvent evaporation result in the structural heterogeneity and a relatively low degree of order.

In comparison to the sample cast in the non-selective solvent, the sample cast from protein-selective solvent has a larger domain spacing of 32.1 nm, as measured by SAXS. However, TEM images suggest that the domain sizes for the more highly ordered (Figure 3-4a) and more disordered (Figure 3-4e) regions of the protein-selective solvent cast sample differ significantly. Fourier transforms of the images of well-ordered lamellar regions and the disordered regions indicate that the disordered regions are 40% larger than the lamellar regions. This increased domain spacing observed at larger length scales is consistent with the 37% larger domain spacing observed by SAXS of the protein-selective solvent compared to the lamellar sample from a non-selective solvent. The observed difference in domain spacing for disordered and lamellar regions of the protein-selective solvent condition suggests that the equilibrium lamellar spacing would be quite similar for both casting conditions; however, the processing-dependent effects that lead to the high degree of structural heterogeneity and kinetic trapping of non-equilibrium structures for the protein-selective solvent result in a large increase in the average domain spacing.

Solvent annealing of samples cast from the non-selective solvent condition was used to probe whether the HPL structure was at equilibrium. Annealed samples show enhanced ordering of the nanodomains with a clear lamellar symmetry and a domain spacing corresponding to the lamellar spacing observed in the as-cast sample, suggesting that the lamellar phase is closer to thermodynamic equilibrium for this sample. After annealing in water at either 4 °C or room temperature for 8 hours, the primary peak shifted to slightly lower q* than in the as-cast sample, all reflections in the SAXS pattern became sharper, and the two higher order reflections now occur at 2q* and 3q*, consistent with the formation of lamellae. TEM confirms the formation of lamellar nanostructures in the room temperature annealed sample, while some hexagonally perforated lamellae are still present in the sample annealed at 4 °C. Both annealed samples show clear layered structures and larger grain sizes than the as-cast sample. In addition, dislocations typical of lamellar block copolymers may be observed in the annealed samples. The improvements in translational and orientational order are consistent with the sharpening of scattering peaks and the observation of the third order reflection. In addition, the lamellae are relatively straight as compared to the typical fingerprint patterns observed in coil-coil diblocks. The nanodomain persistence length appears to be longer than that of coil-coil block copolymer domains, but shorter than that of typical rod-coil block copolymer domains.[65] This observation is likely due to the small, yet well-defined rigid shape of the mCherry protein, which may introduce an enhanced bending rigidity within the nanodomains relative to that of a coil-coil diblock copolymer.

Although both solvent annealed samples show an evolution towards lamellar structures, the disappearance of the low q shoulder on the primary peak and the appearance of the third order peak are both more pronounced in the sample annealed at room temperature. In addition,

the domain spacing of the sample annealed at room temperature (24.0 nm) is larger than the domain spacing of the sample annealed at 4 °C (23.1 nm). While both annealing conditions were chosen to occur in the non-selective solvent regime, both the chemical potential of water and the water-PNIPAM interactions are strongly temperature dependent. The PNIPAM block is anticipated to have a more favorable interaction with water at lower temperature, but the chemical potential of water vapor during solvent annealing decreases as a function of temperature. Both the slightly larger domain spacing and the increased degree of ordering observed in the room temperature annealed sample suggest that the increased chemical potential of water at higher temperature dominates the annealing behavior, resulting in increased swelling of the lamellar nanostructures and accounting for the increase in domain spacing. In addition, both higher temperature and higher water content will increase the mobility of the polymer, consistent with the observation of more intense higher order peaks and a stronger depletion of the hexagonally perforated lamellar phase in the sample annealed at room temperature.

Using scaling relationships for domain spacing as a function of molecular weight, the proteins may be inferred to pack in a bilayer structure within the lamellae. On the basis of the crystallographic structure of mCherry,[55] the protein has a length of approximately 4.2 nm in the folded state. Because the folded proteins are rigid, the same scaling analysis for domain spacing in rod-coil diblock copolymers[65] is expected to apply. For the mCherry-PNIPAM diblocks, this would yield an expected domain spacing of ~12.4 nm in the monolayer configuration. Because this value is approximately half that of the experimentally observed domain spacing, it is most likely that the mCherry is packed in a bilayer configuration within the lamellar nanodomains.

Protein assembly within the nanodomain structure. To enable the fabrication of nanostructured protein-based materials, the protein in these self-assembled block copolymers

must remain properly folded and functional. The functionality of mCherry in solid state mCherry-PNIPAM materials was quantified using both UV-vis spectroscopy and circular dichroism, demonstrating that the self-assembly process preserves a large fraction of the protein structure and optical activity. UV-vis spectra were measured for solid state samples (Figure 3-6a) and for rehydrated diblock copolymers (Figure 3-6b). In the solid state, the peak absorption of the mCherry chromophore at 586 nm remains unchanged, but the shoulder near 550 nm increases in intensity relative to the peak, suggesting a change in absorbance in the solid state. This change is reversed when the materials are rehydrated. The diminishing of the absorbance peak at 586 nm and the enhancement of the shoulder at 510 nm and the peak at 390 nm in both solid state and rehydrated samples indicates that the chromophore has been disrupted for some fraction of the material. A peak at 386 nm has been observed previously in similar red fluorescent proteins and has been attributed to the addition of water across the acylimine chromophore bond.[58]

Because quantum overlap in the solid state may influence the spectrum, a quantitative measure of the functionality of the materials was performed by measuring their absorbance spectrum upon rehydration in milli-Q water. Compared to the UV-vis data for as-synthesized protein-polymer conjugates in solution (Appendix A), the rehydrated samples show a decrease in the ratio of A_{586}:A_{280} from approximately 1.3 to 0.5. This indicates that for all four samples 30-40% of the protein remains active when compared to the conjugate in solution. Consistent with preservation of approximately 35% of the protein's optical activity, the bulk material appears to have a deep red color (Appendix A). Rehydration also results in a decrease in the peak absorbance at 390 nm to some level intermediate between the as-synthesized and the solid state materials. This suggests the presence of three types of mCherry chromophore in the solid state:

active, irreversibly inactive, and spectrally shifted. The active fraction is responsible for the major absorbance peak at 586 nm. The peak at 390 nm increases in the solid state material then decreases upon rehydration, suggesting that a significant contribution to this peak comes from the spectrally shifted material. The shoulder at 510 nm also increases upon rehydration, suggesting that there is a fraction of irreversibly inactivated chromophore that absorbs at this wavelength only after rehydration. Some of the irreversibly inactivated chromophore may also have no absorption within the visible region.

In the dehydrated samples, it is observed that the extent of processing correlates with a loss of optical function in the protein. The relatively rapid casting process at 40 °C tends to promote a higher fraction of active chromophore compared to other samples by about 10%. Because the sample cast at 40 °C was never exposed to high vacuum, it is likely that it contains residual water that enhances the stability of the protein through hydrogen bonding. The room temperature cast sample has the next highest fraction of active chromophore, followed by the two solvent annealed samples which show a further decrease in absorbance at 586 nm and an increase in absorbance at 390 nm. By comparison, a control sample of lyophilized mCherry retains less than 15% of its optical activity at 586 nm, worse than any of the self-assembled materials. Upon rehydration, the relative order of peak intensities in the solid state and rehydrated spectra changes. While all samples show an increase in the absorbance at 586 nm after rehydration, the sample solvent annealed at 4 °C shows the largest increase, indicating that it contains the largest fraction of reversibly inactive material.

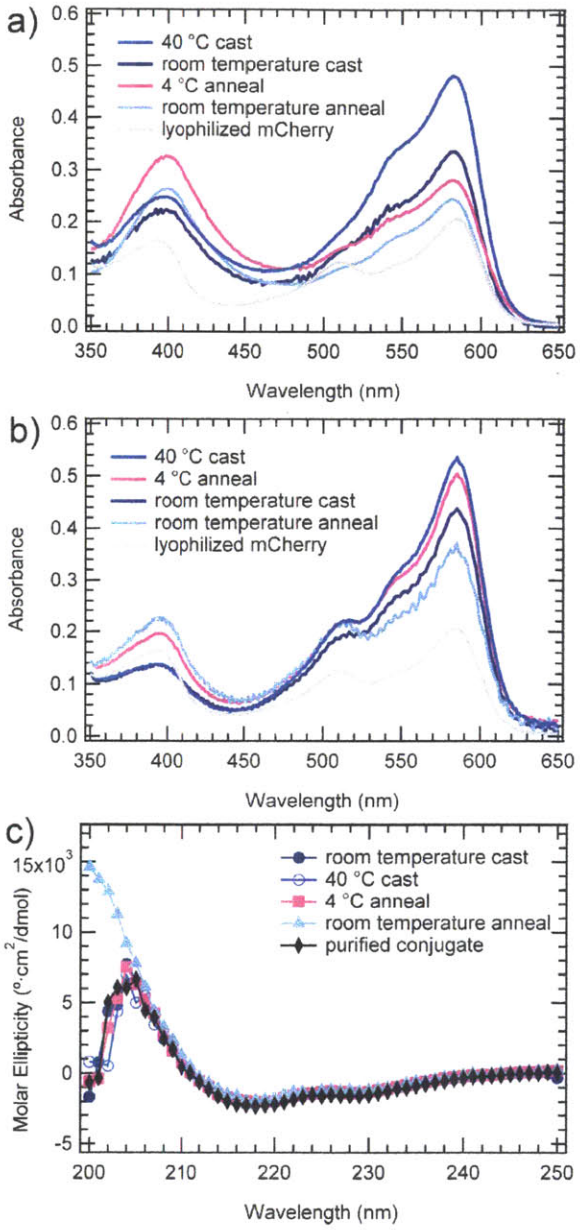

Figure 3-6. (a) Solid state UV-vis spectra of mCherry-PNIPAM conjugate normalized by A_{280}. (b) Rehydrated solid state UV-vis spectra of mCherry-PNIPAM conjugate normalized by A_{280} showing retention of the characteristic absorbance peak shape of mCherry at 586 nm. (c) Rehydrated solid state circular dichroism spectra of conjugate showing protein fold is not disturbed by self-assembly.

Circular dichroism spectra of the rehydrated conjugates show very little change from the conjugate before self-assembly. This indicates that the majority of the protein retains identical secondary structure to the native protein, even after having been dehydrated and rehydrated. Quantitative analysis of the spectra showed that the mCherry alone was composed of 50% β-sheet, as compared to a theoretically predicted 57% β-sheet content from the crystal structure. The discrepancy between the measurement and prediction is accounted for by the presence of the 6xHis tag region in the experimental protein but not in the crystal structure. The mCherry-PNIPAM block copolymer in solution after purification was 43% β-sheet, and the rehydrated samples contained 41-48% β-sheet, indicating no loss of secondary structure upon PNIPAM conjugation within the resolution of the measurement. Taken together, the circular dichroism and UV-vis data illustrate that it is possible to maintain a substantial degree of globular protein fold and function in a solid state self-assembled block copolymer. Because the fold is maintained to a much higher degree than the chromophore activity, it is likely that the activity of the sensitive chromophore is lost during self-assembly without large changes in the protein structure.

The packing and crystallinity of the mCherry within the block copolymer nanodomains was investigated using wide-angle X-ray scattering (WAXS), shown in Figure 3-7. The scattering patterns of self-assembled conjugates contain the same two peaks as a bulk sample composed of solid mCherry prepared by evaporation from solution. This demonstrates that the WAXS peaks seen for the block copolymer samples are a result of the mCherry structure and not affected by the PNIPAM. No peaks are present corresponding to the mCherry crystal structure, indicating that the mCherry is in an amorphous state. This is consistent with both kinetic limitations to crystallization during the self-assembly process, which occur on a timescale of

~2 hours, and with UV-vis results that suggest a portion of the protein may be structurally perturbed in the solid state and therefore unable to crystallize within the mCherry unit cell.

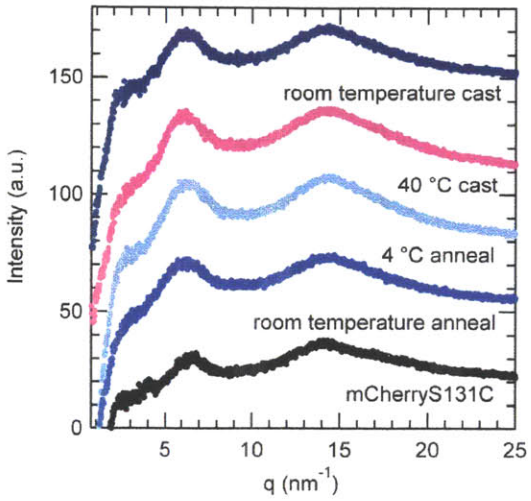

Figure 3-7. Wide-angle X-ray scattering data of as-cast and solvent annealed mCherry-PNIPAM block copolymers shows scattering due to the inter-sheet and inter-strand spacing of β-strands. The spacing of the β-strands of mCherry is not altered in conjugate materials.

WAXS data for the mCherry protein indicate that the material retains a predominantly β-barrel structure in the solid state. All of the block copolymers contain two peaks, one at approximately 6.23 nm^{-1} and the other at 14.32 nm^{-1} corresponding to 1.0 and 0.45 nm, respectively, in real space. The larger domain spacing peak is attributed to either inter-sheet spacing or inter-helix spacing for proteins containing β-sheets or α-helices, respectively.[66] The smaller domain spacing peak arises from inter-strand hydrogen bonding in β-sheet proteins or backbone hydrogen bonding in α-helices.[66] Given that circular dichroism and the known crystal structure of mCherry suggest a predominantly β-sheet secondary structure, these peaks are inferred to result from inter-sheet spacing and inter-strand hydrogen bonding between β-strands.

Because the q values of these peaks do not change between samples, it is concluded that the inter-sheet and inter-strand spacing is not changed significantly by the processing method used to induce self-assembly. The block copolymer samples all show similar intensities for both peaks with the ratio of the 6.23 nm^{-1} to the 14.32 nm^{-1} peak equal to approximately 0.98. In contrast, mCherry shows a higher intensity for the second peak with a ratio of 0.84. An increase in this ratio has previously been correlated with a decrease in β-sheet content,[66] suggesting that the β-sheet content is slightly lower in the self-assembled block copolymers than in the bulk mCherry. This result is consistent with the minor decrease in β-sheet content upon bioconjugation observed by CD.

3.5 Conclusions

Protein-polymer diblock copolymers composed of mCherryS131C and PNIPAM were synthesized and self-assembled into nanostructured materials, demonstrating an attractive route towards high density three-dimensional protein nanopatterning with precise control over protein orientation and placement. Self-assembly was induced by solvent evaporation, and the selectivity of the solvent during the evaporation process was shown to have a large effect on the nanostructure formed, resulting in a heterogeneous nanodomain structure for a protein-selective solvent and a hexagonally perforated lamellar phase for a non-selective solvent. Subsequent solvent annealing resulted in an evolution toward well-ordered lamellar structures, suggesting that this lamellar structure may be closer to thermodynamic equilibrium. After annealing at room temperature, SAXS indicated a domain spacing for the material of 24.0 nm, suggesting that the mCherry packs in bilayers within the lamellae. The mCherry structure within the lamellar domains was largely amorphous, with the only observed WAXS peaks assigned to inter-sheet

and inter-strand spacing of β-strands. While circular dichroism indicated no irreversible change in protein secondary structure after self-assembly, UV-vis spectroscopy showed that one third of the protein chromophores remained active in the solid state material.

3.6 Acknowledgements

This work was supported by the MIT Energy Initiative (award number 015728-066). GPC, SAXS, WAXS, microtome, and TEM experiments were performed at the Institute for Soldier Nanotechnologies. NMR experiments were performed at the MIT Department of Chemistry Instrumentation Facility, and CD experiments were performed at the Biophysical Instrumentation Facility for the Study of Complex Macromolecular Systems (NSF-0070319 and NIH GM68762).

3.7 References

1. I. Willner and E. Katz, *Angew. Chem., Int. Ed.*, 2000, **39**, 1180-1218.
2. D. A. LaVan and J. N. Cha, *Proc. Natl. Acad. Sci. U.S.A.*, 2006, **103**, 5251-5255.
3. S. J. Benkovic and S. Hammes-Schiffer, *Science*, 2003, **301**, 1196-1202.
4. M. M. Rahman, A. J. S. Ahammad, J. H. Jin, S. J. Ahn and J. J. Lee, *Sensors*, 2010, **10**, 4855-4886.
5. B. E. Rapp, F. J. Gruhl and K. Länge, *Anal. Bioanal. Chem.*, 2010, **398**, 2403-2412.
6. J. A. Cracknell, K. A. Vincent and F. A. Armstrong, *Chem. Rev.*, 2008, **108**, 2439-2461.
7. E. H. Yu and K. Scott, *Energies*, 2010, **3**, 23-42.
8. S. D. Minteer, B. Y. Liaw and M. J. Cooney, *Curr. Opin. Biotechnol.*, 2007, **18**, 228-234.
9. R. N. Patel, *Coord. Chem. Rev.*, 2008, **252**, 659-701.
10. N. Favre, M. L. Christ and A. C. Pierre, *J. Mol. Catal. B: Enzym.*, 2009, **60**, 163-170.
11. T. Reda, C. M. Plugge, N. J. Abram and J. Hirst, *Proc. Natl. Acad. Sci. U. S. A.*, 2008, **105**, 10654-10658.
12. B. A. Parkinson and P. F. Weaver, *Nature*, 1984, **309**, 148-149.
13. S. Kuwabata, R. Tsuda and H. Yoneyama, *J. Am. Chem. Soc.*, 1994, **116**, 5437-5443.
14. A. A. Karyakin, S. V. Morozov, E. E. Karyakina, S. D. Varfolomeyev, N. A. Zorin and S. Cosnier, *Electrochem. Commun.*, 2002, **4**, 417-420.
15. M. Hambourger, M. Gervaldo, D. Svedruzic, P. W. King, D. Gust, M. Ghirardi, A. L. Moore and T. A. Moore, *J. Am. Chem. Soc.*, 2008, **130**, 2015-2022.

16. H. Krassen, A. Schwarze, B. Friedrich, K. Ataka, O. Lenz and J. Heberle, *ACS Nano*, 2009, **3**, 4055-4061.
17. R. J. Cogdell, A. Gall and J. Köhler, *Q. Rev. Biophys.*, 2006, **39**, 227-324.
18. R. Das, P. J. Kiley, M. Segal, J. Norville, A. A. Yu, L. Y. Wang, S. A. Trammell, L. E. Reddick, R. Kumar, F. Stellacci, N. Lebedev, J. Schnur, B. D. Bruce, S. G. Zhang and M. Baldo, *Nano Lett.*, 2004, **4**, 1079-1083.
19. J. W. Choi and M. Fujihira, *Appl. Phys. Lett.*, 2004, **84**, 2187-2189.
20. S. D. Minteer, *Enzyme Stabilization and Immobilization*, Springer, New York, 2010.
21. C. Mateo, J. M. Palomo, G. Fernandez-Lorente, J. M. Guisan and R. Fernandez-Lafuente, *Enzyme Microb. Technol.*, 2007, **40**, 1451-1463.
22. F. Caruso and C. Schüler, *Langmuir*, 2000, **16**, 9595-9603.
23. Y. Wang, A. S. Angelatos and F. Caruso, *Chem. Mater.*, 2007, **20**, 848-858.
24. K. L. Christman, V. D. Enriquez-Rios and H. D. Maynard, *Soft Matter*, 2006, **2**, 928-939.
25. S. K. Kwak, G. S. Lee, D. J. Ahn and J. W. Choi, *Mater. Sci. Eng. C Biomimetic Supramol. Syst.*, 2004, **24**, 151-155.
26. S. A. Alang Ahmad, L. S. Wong, E. ul-Haq, J. K. Hobbs, G. J. Leggett and J. Micklefield, *J. Am. Chem. Soc.*, 2011, **133**, 2749-2759.
27. J. Kalia and R. T. Raines, *Curr. Org. Chem.*, 2010, **14**, 138-147.
28. D. C. Kim, J. I. Sohn, D. J. Zhou, T. A. J. Duke and D. J. Kang, *ACS Nano*, 2010, **4**, 1580-1586.
29. K. H. Kim, J. D. Kim, Y. J. Kim, S. H. Kang, S. Y. Jung and H. Jung, *Small*, 2008, **4**, 1089-1094.
30. A. D. Presley, J. J. Chang and T. Xu, *Soft Matter*, 2011, **7**, 172-179.
31. M. B. Cardoso, D. Smolensky, W. T. Heller, K. Hong and H. O'Neill, *Energy Environ. Sci.*, 2011, **4**, 181-188.
32. P. D. Laible, R. F. Kelley, M. R. Wasielewski and M. A. Firestone, *J. Phys. Chem. B*, 2005, **109**, 23679-23686.
33. F. S. Bates and G. H. Fredrickson, *Phys. Today*, 1999, **52**, 32-38.
34. I. W. Hamley, *The Physics of Block Copolymers*, Oxford University Press, New York, 1998.
35. C. Park, J. Yoon and E. L. Thomas, *Polymer*, 2003, **44**, 6725-6760.
36. E. D. Gomez, A. Panday, E. H. Feng, V. Chen, G. M. Stone, A. M. Minor, C. Kisielowski, K. H. Downing, O. Borodin, G. D. Smith and N. P. Balsara, *Nano Lett.*, 2009, **9**, 1212-1216.
37. X. Yang and J. Loos, *Macromolecules*, 2007, **40**, 1353-1362.
38. B. D. Olsen and R. A. Segalman, *Mater. Sci. Eng. R*, 2008, **62**, 37-66.
39. L. A. Canalle, D. W. P. M. Lowik and J. C. M. van Hest, *Chem. Soc. Rev.*, 2010, **39**, 329-353.
40. O. D. Krishna and K. L. Kiick, *Pept. Sci.*, 2010, **94**, 32-48.
41. O. S. Rabotyagova, P. Cebe and D. L. Kaplan, *Biomacromolecules*, 2011, **12**, 269-289.
42. C. Lavigueur, J. G. García, L. Hendriks, R. Hoogenboom, J. J. L. M. Cornelissen and R. J. M. Nolte, *Polym. Chem.*, 2011, **2**, 333-340.
43. R. Duncan, *Nat. Rev. Cancer*, 2006, **6**, 688-701.
44. E. S. Gil and S. M. Hudson, *Prog. Polym. Sci.*, 2004, **29**, 1173-1222.
45. I. C. Reynhout, J. L. M. Cornelissen and R. J. M. Nolte, *J. Am. Chem. Soc.*, 2007, **129**, 2327-2332.

46. J. M. Harris and R. B. Chess, *Nat. Rev. Drug Discovery*, 2003, **2**, 214-221.
47. M. Y. Kim, J. S. Kwon, H. J. Kim and E. K. Lee, *J. Biotechnol.*, 2007, **131**, 177-179.
48. F. M. Veronese, *Biomaterials*, 2001, **22**, 405-417.
49. Y.-Z. You and D. Oupický, *Biomacromolecules*, 2006, **8**, 98-105.
50. B. J. Neubert and B. B. Snider, *Org. Lett.*, 2003, **5**, 765-768.
51. E. Bays, L. Tao, C. W. Chang and H. D. Maynard, *Biomacromolecules*, 2009, **10**, 1777-1781.
52. N. C. Shaner, R. E. Campbell, P. A. Steinbach, B. N. G. Giepmans, A. E. Palmer and R. Y. Tsien, *Nat. Biotechnol.*, 2004, **22**, 1567-1572.
53. A. M. Dennis and G. Bao, *Nano Lett.*, 2008, **8**, 1439-1445.
54. L. A. Gross, G. S. Baird, R. C. Hoffman, K. K. Baldridge and R. Y. Tsien, *Proc. Natl. Acad. Sci. U. S. A.*, 2000, **97**, 11990-11995.
55. X. K. Shu, N. C. Shaner, C. A. Yarbrough, R. Y. Tsien and S. J. Remington, *Biochemistry*, 2006, **45**, 9639-9647.
56. J. A. Chung, J. W. Wollack, M. L. Hovlid, A. Okesli, Y. Chen, J. D. Mueller, M. D. Distefano and T. A. Taton, *Anal. Biochem.*, 2009, **386**, 1-8.
57. B. C. Lee and R. N. Zuckermann, *Chem. Commun.*, 2010, **46**, 1634-1636.
58. A. A. Pakhomov, N. V. Pletneva, T. A. Balashova and V. I. Martynov, *Biochemistry*, 2006, **45**, 7256-7264.
59. V. Lapiene, F. Kukolka, K. Kiko, A. Arndt and C. M. Niemeyer, *Bioconjugate Chem.*, 2010, **21**, 921-927.
60. F. Kukolka and C. M. Niemeyer, *Org. Biomol. Chem.*, 2004, **2**, 2203-2206.
61. Linda C. Sawyer, David T. Grubb and G. F. Meyers, *Polymer Microscopy*, Springer, New York, 2008.
62. C. Lai, Y. L. Loo, R. A. Register and D. H. Adamson, *Macromolecules*, 2005, **38**, 7098-7104.
63. A. K. Khandpur, S. Forster, F. S. Bates, I. W. Hamley, A. J. Ryan, W. Bras, K. Almdal and K. Mortensen, *Macromolecules*, 1995, **28**, 8796-8806.
64. Y. L. Loo, R. A. Register, D. H. Adamson and A. J. Ryan, *Macromolecules*, 2005, **38**, 4947-4949.
65. B. D. Olsen and R. A. Segalman, *Macromolecules*, 2007, **40**, 6922-6929.
66. W. M. Elshemey, A. A. Elfiky and W. A. Gawad, *Protein J.*, 2010, **29**, 545-550.

Chapter 4 Kinetically Controlled Nanostructure Formation in Self-Assembled Globular Protein-Polymer Diblock Copolymers

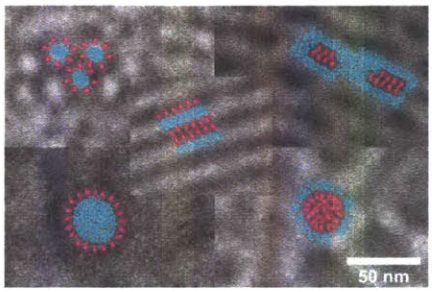

4.1 Abstract

Aqueous processing of globular protein-polymer diblock copolymers into solid state materials and subsequent solvent annealing enables kinetic and thermodynamic control of nanostructure formation to produce block copolymer morphologies that maintain a high degree of protein fold and function. With model diblock copolymers composed of mCherry-b-poly(N-isopropyl acrylamide), orthogonal control over solubility of the protein block through changes in pH and the polymer block through changes in temperature is demonstrated during casting and solvent annealing. Hexagonal cylinders, perforated lamellae, lamellae, or hexagonal and disordered micellar phases are observed depending upon the coil fraction of the block copolymer and the kinetic pathway used for self-assembly. Good solvents for the polymer block produce ordered structures reminiscent of coil-coil diblock copolymers, while an unfavorable solvent results in kinetically trapped micellar structures. Decreasing solvent quality for the protein improves long-range ordering, suggesting that the strength of protein interactions influences

nanostructure formation. Subsequent solvent annealing results in evolution of the nanostructures, with the best ordering and the highest protein function observed when annealing in a good solvent for both blocks. While protein secondary structure was found to be almost entirely preserved for all processing pathways, UV-vis spectroscopy of solid state films indicates that using a good solvent for the protein block enables up to 70% of the protein to be retained in its functional form.

4.2 Introduction

Proteins are poised to enable large advances in future materials through their incorporation into a variety of bioelectronic and biocatalytic devices,[1] pharmaceuticals[2], fuel cells[3] and photovoltaics.[4] Enzymes contribute many favorable qualities to such materials, including large activity, high selectivity, and the ability to operate on unusual substrates. The construction of functional materials often requires large enzyme loading densities, necessitating the use of three-dimensional patterning or immobilization techniques.[5] To date, protein patterning has been accomplished through a wide variety of methods including layer-by-layer assemblies,[6] monolayer films,[7] and the use of lithographic,[8] polymer,[9] and inorganic[10-11] templates. Continued challenges with protein denaturation during incorporation, protein stability within a material, and control over protein nanostructure make the development of new materials central to the improvement of biocatalytic devices.[12]

Self-assembly provides a single-step approach to protein patterning where the native and specific interactions present in proteins can be harnessed to build complex structures over large areas.[13-14] Protein-based materials capable of self-assembly may be created through site-specific bioconjugation to form a protein-polymer diblock copolymer. A variety of bioconjugation

techniques have been successfully implemented including grafting-from,[15-16] grafting-to,[16-17] cofactor reconstitution[18-19] and affinity binding[20-21] approaches. To induce self-assembly, a polymer responsive to temperature, pH or light is often used to produce an amphiphilic block copolymer upon stimulus exposure.[20, 22] These amphiphilic molecules self-assemble into a variety of solution-state morphologies depending on relative block lengths,[23] polymer hydrophobicity,[24] and solution conditions, including pH and ionic strength.[25] Many of these structures are thought to be kinetically determined due to the variety of observed morphologies.[23] While bioconjugates with polystyrene form micelles as well as vesicles with a bilayer configuration,[21] conjugates with poly(N-isopropyl acrylamide) (PNIPAM) have been observed to form micelles and other large aggregates in solution when the temperature is raised above the lower critical solution temperature (LCST) of the PNIPAM homopolymer, causing the polymer to collapse.[18, 26-28] Additionally, protein-lipid conjugates have been shown to self-assemble into lipid membranes,[19] and blends of proteins and surfactants have been shown to form lipid bilayer-like structures.[29]

Fewer studies have explored the self-assembly of globular protein-polymer block copolymer gels or solid state materials. Synthetic block copolymers can be used to template the self-assembly of the bioconjugate material, which selectively partitions to one domain of the synthetic block copolymer.[30-32] Alternatively, protein-polymer diblock copolymers may be directly nanopatterned in the solid state by employing the amphiphilic nature of the bioconjugate to induce self-assembly into block copolymer-like nanostructures when solid materials are cast from aqueous solution.[33] This method for patterning protein-based catalysts potentially enables extremely high densities of functional proteins, control over protein orientation, and engineering multiphase transport through different block copolymer nanodomains.

Block copolymer self-assembly directly from solution often results in structures with little long-range ordering,[34] necessitating an annealing step to obtain high quality patterns.[34-37] Due to the thermal sensitivity of most proteins, solvent annealing is the only general option for improving order in protein-polymer block copolymers. As the solvent swells the sample, the block copolymer mobility increases and the solvent compatibilizes the two blocks, resulting in a decrease in unfavorable interactions.[34-35] In fully synthetic block copolymers, studies show that the greatest enhancement in ordering occurs during very short annealing times, with the effect of annealing diminishing with increased time.[34] Different evaporation conditions using the same solvent can also result in different morphologies,[38] and the use of different solvents can result in a variety of morphologies due to differences in relative block solubilities.[39] Solvent annealing also provides a potential route toward improving protein activity and stability in biofunctional systems by utilizing optimal pH, ionic strength, and buffer type.[22, 40]

Both solution casting and solvent annealing processes used to fabricate solid state globular protein-polymer diblock copolymer nanostructures inherently involve both thermodynamic and kinetic effects, making the specific processing pathway used to prepare materials critical for both nanostructure formation and maintaining protein function. This study investigates processing pathways used to control nanostructure formation as a function of coil fraction, demonstrating that kinetic effects largely determine the type of nanostructure formed. Model material composed of a red fluorescent protein, mCherryS131C, and a thermoresponsive polymer, PNIPAM forms self-assembled nanostructures through water evaporation from aqueous conjugate solutions, and these structures are subsequently solvent annealed to alter ordering. Two orthogonal variables, temperature and pH, are simultaneously used to control the solvent quality for each block during the casting and annealing processes. Nanostructures from

conjugates with three different polymer coil fractions are studied to understand the effect of processing on nanodomain morphology, long-range ordering, protein fold, and protein function.

3.3 Experimental Methods

Synthesis of protein-polymer conjugates. Low polydispersity PNIPAM was synthesized using radical addition-fragmentation chain transfer (RAFT) polymerization with a protected maleimide chain transfer agent (CTA) as described previously.[33] The monomer concentration was held constant at 2.0M and the CTA/azobisisobutyronitrile (AIBN) ratio was held constant at 1:0.5. The ratio between the NIPAM monomer and the CTA was varied between 300 and 1000, and the polymerization was performed at 55 °C for 90 to 180 minutes, depending on the desired polymer molecular weight. After isolation of the polymer by precipitation, the polymer was dried under vacuum and the end-group of the CTA was deprotected at 120 °C under vacuum for 2 hours. The polymer molecular weights and polydispersities were determined by gel permeation chromatography (GPC) using an Agilent 1260 Infinity HPLC with N,N-dimethylformamide (DMF) as the mobile phase. Both a refractive index detector and a Wyatt Mini-Dawn three-angle static light scattering detector were employed to enable absolute molecular weight determination.

Protein expression of the mutant red fluorescent protein, mCherryS131C, was carried out in Luria Broth and purified following the previously described procedure.[33] Site-specific thiol-maleimide bioconjugation and purification were performed as previously reported with a 6-fold molar excess of polymer. Three coil fractions (f_{PNIPAM} = 0.42, 0.53, 0.69; Table 4-1) were chosen to span a range of molecular designs that would produce different nanostructured morphologies in a traditional coil-coil block copolymer system. Conjugate purity was assessed

by denaturing (SDS-PAGE) and native protein gels and matrix-assisted laser desorption ionization mass spectroscopy (MALDI-MS). The two lower coil fraction conjugates resulted in higher purities around 98% by mass, while the conjugate with the largest PNIPAM coil fraction was approximately 93% pure, as estimated from SDS-PAGE. Conjugate yield was determined spectrophotometrically using the protein absorption at 280 nm (extinction coefficient of 32,550 $M^{-1}cm^{-1}$). The yield of the purified product depended strongly on the molecular weight of the PNIPAM block, with M_n = 57.3 kg/mol resulting in the lowest yield (16%), while materials with M_n = 18.8 and 29.0 kg/mol were obtained in yields of 31% and 36%, respectively. The decreased yield at higher polymer molecular weight is primarily due to the lower yield of the bioconjugation reaction.

Table 4-1. mCherry-b-PNIPAM block copolymers

block copolymer	PNIPAM M_n (kg/mol)	PDI_{PNIPAM}	Conjugate M_n (kg/mol)	f_{PNIPAM}
mCherry-PNIPAM19	18.8	1.08	46.9	0.42
mCherry-PNIPAM29	29.0	1.10	57.1	0.53
mCherry-PNIPAM57	57.3	1.12	85.4	0.69

Sample preparation. Conjugate solutions, dialyzed into pure water, were concentrated to ~70 mg/mL using Millipore Ultra-15 centrifugal filters with a molecular weight cutoff of 3 kDa. Conjugate behavior was studied in four different solutions. A protein-selective solvent is achieved using an aqueous solution above the thermal transition of the conjugate materials (40 °C, pH = 7.5). In contrast, a polymer-selective solvent is realized using a solution near the isoelectric point (pI) of the protein (25 °C, pH = 5.7). Additionally, a non-selective solvent is obtained using a room temperature pH = 7.5 solution, and a non-solvent is created with a

solution at pH = 5.7 and a temperature of 40 °C. Bulk samples of nanostructured conjugate were created by evaporating the solvent at room temperature or 40 °C. The solvent evaporation rate at room temperature was controlled using a vacuum controller with a ramp rate of 300 Torr/hour and a final setpoint of 75 Torr, while evaporation at 40 °C was performed at ambient pressure. Samples were subsequently solvent vapor annealed at room temperature in either water or a 1 vol% formic acid solution for 8, 24, or 72 hours. The solvent annealing setup consisted of approximately 1 cm of solvent in the bottom of a sealed glass jar with an inverted beaker on which the sample was placed, giving a sample to liquid distance of 4 cm. No appreciable loss of solvent during annealing occurred. After annealing, samples were allowed to dry under ambient conditions (below the glass transition temperature of the material), kinetically arresting the process of structure evolution.

Sample characterization. Dynamic light scattering (DLS) experiments were performed on a DynaPro Nanostar at a scattering angle of 90° with a laser wavelength of 658 nm. UV-vis spectra were collected using a Cary 50 UV-vis spectrophotometer. A spectrophotometric measure of protein function is calculated as A_{586} of the sample relative to A_{586} of the as-synthesized conjugate, where both values are normalized by A_{280} to control for variation in protein concentration. At least three replicates were averaged for each sample to produce the final data. Circular dichroism (CD) spectra were measured on an Aviv model 202 CD spectrometer operating at 25 °C and background corrected. Spectra were analyzed for secondary structure content with CDPro software using the CONTINLL, SELCON3, and CDSSTR methods. Fourier transform infrared (FTIR) spectroscopy was performed using a Thermo Nexus 870 and analyzed using OMNIC software. Fourier self-deconvolutions (FSD) of the amide I

peak were performed using a bandwidth of 30 cm^{-1} and an enhancement factor of 2.5 for general secondary structural identification.[41-42]

Small-angle neutron scattering (SANS) experiments were performed on the Low-Q Diffractometer (LQD) end station at Los Alamos Neutron Science Center (LANSCE). Hydrogenated conjugate samples were dialyzed into 98% deuterated water and loaded into a quartz cell. Absolute intensities were obtained by correcting for background scattering and open beam neutron flux. The resulting spectra were fit with either the Beaucage[43] model or the Percus-Yevick[44-45] model, depending on the solvent quality for the polymer block. For the Percus-Yevick model, effects of polydispersity and Gaussian smearing were taken into consideration. SANS experiments were repeated at both 1 wt% and 3 wt%, producing quantitatively identical results. Small-angle X-ray scattering (SAXS) and transmission electron microscopy (TEM) samples approximately 1 mm in thickness were cast on Kapton tape using 1 mm thick anodized aluminum washers as a mould. SAXS experiments were performed on beamline X9 of the National Synchrotron Light Source (NSLS) at Brookhaven National Lab, and the data was corrected for empty cell and dark field scattering. The scattering from several replicates of similar materials was measured to ensure reproducibility of nanostructure formation, and acquisition times were chosen such that the effect of beam damage on sample nanostructure was undetectable. Bulk samples were cryo-microtomed using a Leica EM UC6 at -110 °C to a thickness of 60 nm and stained with ruthenium tetroxide vapors from a 0.5% aqueous solution for 20 minutes. This treatment preferentially stains the protein domains, making them appear darker in images. A JEOL 2000FX TEM was used to obtain bright field images using an accelerating voltage of 120 kV and a LaB_6 filament. Images were captured using an ORCA camera in a fixed bottom mount configuration.

4.4 Results and Discussion

Characterization of solution nanostructure. The solution-state processing pathway used to self-assemble solid state nanomaterials has a large impact on the final material structure due to the potential for nanostructures formed in solution to be kinetically trapped in the final solid state material. DLS and SANS are used to assess the aggregation state of the globular protein-polymer block copolymers in solution, providing insight into the initial structure during processing for different solvent conditions. While DLS provides information about the size of conjugate aggregates in solution, SANS allows the nanostructure within the aggregates to be studied. Table 4-2 shows both average particle sizes and measured polydispersities obtained by DLS as a function of solvent quality and coil fraction. The average hydrodynamic radii measured in non-selective and polymer-selective solvents increase with increasing PNIPAM coil fraction and the values are consistent with individual molecules of protein-polymer conjugate. Based on the protein length of 4.2 nm from the crystal structure[46] (PDB 2H5Q) and the root-mean-square end-to-end distance of PNIPAM with a Kuhn segment length of 0.7 nm,[47] calculated values of 6.6, 7.7, and 10.0 nm are obtained for the three PNIPAM coil fractions of 0.42, 0.53, and 0.69, respectively. These calculations assume a dumbbell configuration for the conjugate that is consistent with previous experimental observations on protein-PEG conjugates.[48] As expected, the calculations using an ideal polymer chain model slightly underestimate the experimental measurement, which is performed in a good solvent for the polymer.

Table 4-2. Dynamic light scattering from 1 wt% mCherry-PNIPAM solutions

Sample	Temperature (°C)	pH	Average radius (nm) $f_{PNIPAM} = 0.42$ (PDI)	Average radius (nm) $f_{PNIPAM} = 0.53$ (PDI)	Average radius (nm) $f_{PNIPAM} = 0.69$ (PDI)
non-selective	25	7.5	7.3 (17%)	8.0 (24%)	11.0 (25%)
protein-selective	40	7.5	> 800 (21%)	> 800 (9%)	> 800 (27%)
polymer-selective	25	5.75	7.9 (32%)	8.2 (28%)	9.6 (22%)
non-solvent	40	5.75	> 800 (9%)	> 800 (64%)	> 800 (51%)

SANS experiments, as illustrated in Figure 4-1, show similar results for the non-selective and polymer-selective solvents, with no signs of aggregation. Curves for samples in a good solvent for the polymer were fit with a Beaucage[43] model that was selected for its ability to fit the form factor of the protein-polymer conjugate without prior knowledge of the polymer configuration around the protein. At $f_{PNIPAM} = 0.53$, fits give an effective radius of gyration (R_g) for the conjugate of 7.5 ± 1.4 and 6.9 ± 1.2 nm for non-selective and polymer-selective solvents, respectively. For the conjugate with $f_{PNIPAM} = 0.69$, the R_g increased to 15.0 ± 3.8 and 18.0 ± 5.5 nm in the non-selective and polymer-selective solvents, respectively, in agreement with the hydrodynamic radii obtained by DLS. For the smaller conjugate with a coil fraction of 0.42, the R_g was measured to be 11.8 ± 2.9 and 10.2 ± 2.8 nm in the non-selective and polymer-selective solvents, respectively. These molecular sizes are similar within measurement error to the conjugate with 53% PNIPAM and to the size measured by DLS. The terminal behavior at high q is characterized by power law exponentials of 1.36 ± 0.01, 1.62 ± 0.02, and 1.41 ± 0.01 for the three PNIPAM coil fractions in order of increasing coil fraction. As expected, the power law exponents are only weakly dependent on the solvent quality for the protein block, and they are intermediate between a Gaussian coil and an ideal rod and close to that expected for a coil in a good solvent.

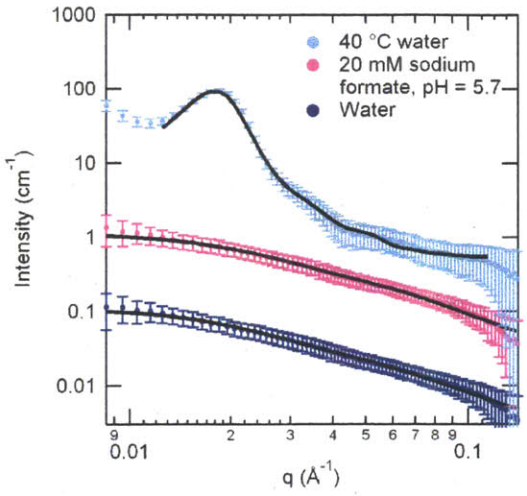

Figure 4-1. Small-angle neutron scattering patterns of a 3 wt% solution of mCherry-PNIPAM29 (f_{PNIPAM} = 0.53). Solid lines show fits to the data. Non-selective (room temperature, neutral pH) and polymer-selective (room temperature, pH 5.7) solvents contain conjugates in the monomeric state, while samples in a protein-selective solvent (40 °C, neutral pH) result in aggregation. The 20 mM sodium formate pH = 5.7 and 40 °C water traces have been vertically offset by 10 and 100 cm^{-1}, respectively, for clarity.

In poor solvents for the polymer block, large-scale aggregation occurs, as indicated by an apparent particle radius in excess of 800 nm by DLS. After several hours, a macrophase separated precipitate is clearly observable by eye, and SANS patterns show a peak characteristic of ordering in the aggregated phase. Fitting with a Percus-Yevick model[44-45] for disordered hard spheres gives hard sphere radii of 14.5 ± 0.2, 17.9 ± 0.2, and 21.2 ± 0.3 nm for increasing PNIPAM coil fractions. These results are consistent with the formation of collapsed PNIPAM domains above the thermal transition temperature, followed by phase separation of the aggregated conjugates to form nanostructured phases. SANS observes the short length scale

ordering within macrophase separated regions, while DLS predominantly detects the large scale size of the macrosphase separated aggregates.

Unlike traditional block copolymers where micelles or vesicles are observed in a selective solvent for either block,[49] these globular protein-polymer block copolymers show phase behavior that is dominated by the behavior of the polymer block. Near the pI of the protein and below the LCST of the PNIPAM homopolymer where the solvent is selective for the polymer, the block copolymers remain soluble in their monomeric form. It is important to note that monomer formation under these conditions may only be observed for proteins with relatively high solubilities such as mCherry, and that it may not be generalizable to all proteins. At elevated temperatures, where the solvent is selective for the protein, the block copolymers macrophase separate from solution regardless of the solvent quality for the protein. This behavior suggests that the protein block in the corona has insufficient electrostatic and entropic repulsive interactions to form stable aggregated structures.

Kinetically-determined structure formation. As diblock copolymers are concentrated from dilute solution to induce self-assembly, the solvent quality has a large effect on the type of nanostructure formed due to kinetic effects on block copolymer self-assembly, as illustrated by SAXS in Figure 4-2 and TEM in Figure 4-3. When cast from good solvents for the PNIPAM block, mCherry-PNIPAM19 (f_{PNIPAM} = 0.42) tends to form a hexagonal cylinder phase. The SAXS pattern of a sample cast from a non-selective solvent shows broad, overlapping higher order peaks at $\sqrt{3}q^*$ and $2q^*$, indicating a poorly-ordered hexagonal morphology. A TEM image of this sample (Figure 4-3c) shows PNIPAM cylinders in an mCherry matrix in both end-on and edge-on orientations with very small grain sizes. When the material is cast from a polymer-selective solvent, sharper SAXS peaks are observed at both $\sqrt{3}q^*$ and $2q^*$, indicating an

improvement in hexagonal order. Microscopy images (Figure 4-3a) further verify the presence of larger grains of well-formed PNIPAM cylinders in an mCherry matrix. In contrast, samples prepared from a non-solvent for the polymer block result in a disordered micellar structure. The primary SAXS peak is broader and only a broad shoulder is observable at higher q, indicating a greater degree of disorder than for samples cast from a good solvent for the polymer. A disordered micellar structure is confirmed by TEM, as shown in Figure 4-3f. In many areas of the disordered micellar sample, the PNIPAM nanodomains encircle or nearly encircle mCherry nanodomains, which is surprising because PNIPAM is the minority component.

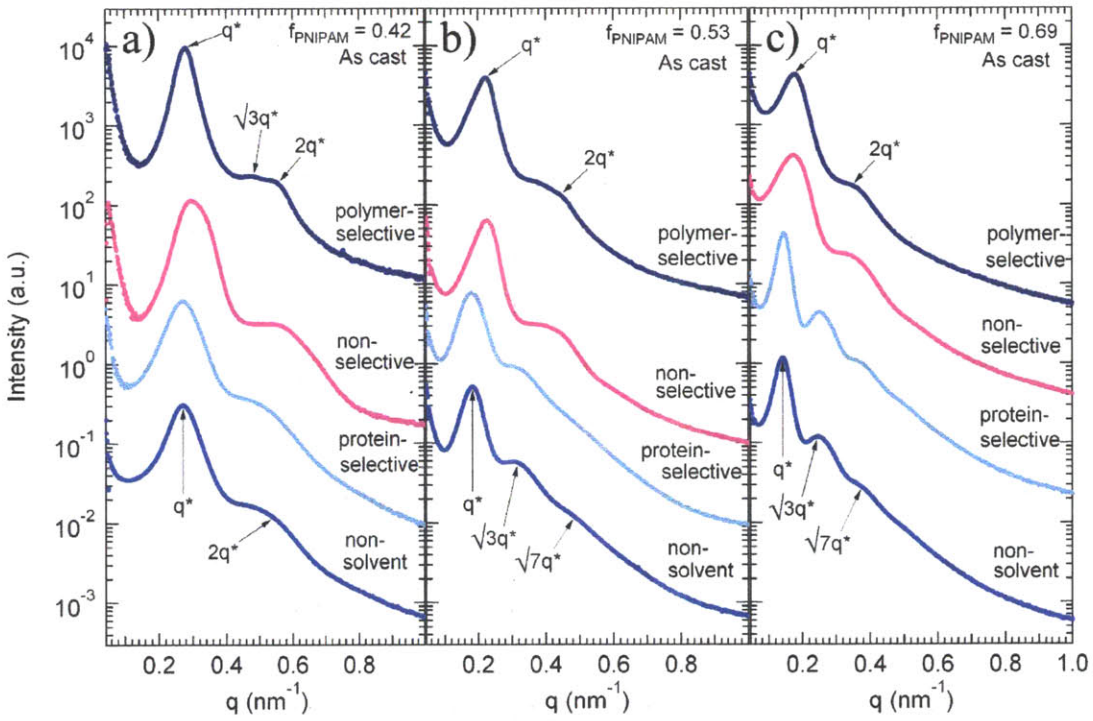

Figure 4-2. Small-angle X-ray scattering data for mCherry-PNIPAM block copolymers cast from each of the four solvent types for three different PNIPAM coil fractions: (a) f_{PNIPAM} = 0.42 (b) f_{PNIPAM} = 0.53 (c) f_{PNIPAM} = 0.69. Both the coil fraction and casting condition have a significant impact on the type of nanostructure formed. The traces have been offset for clarity.

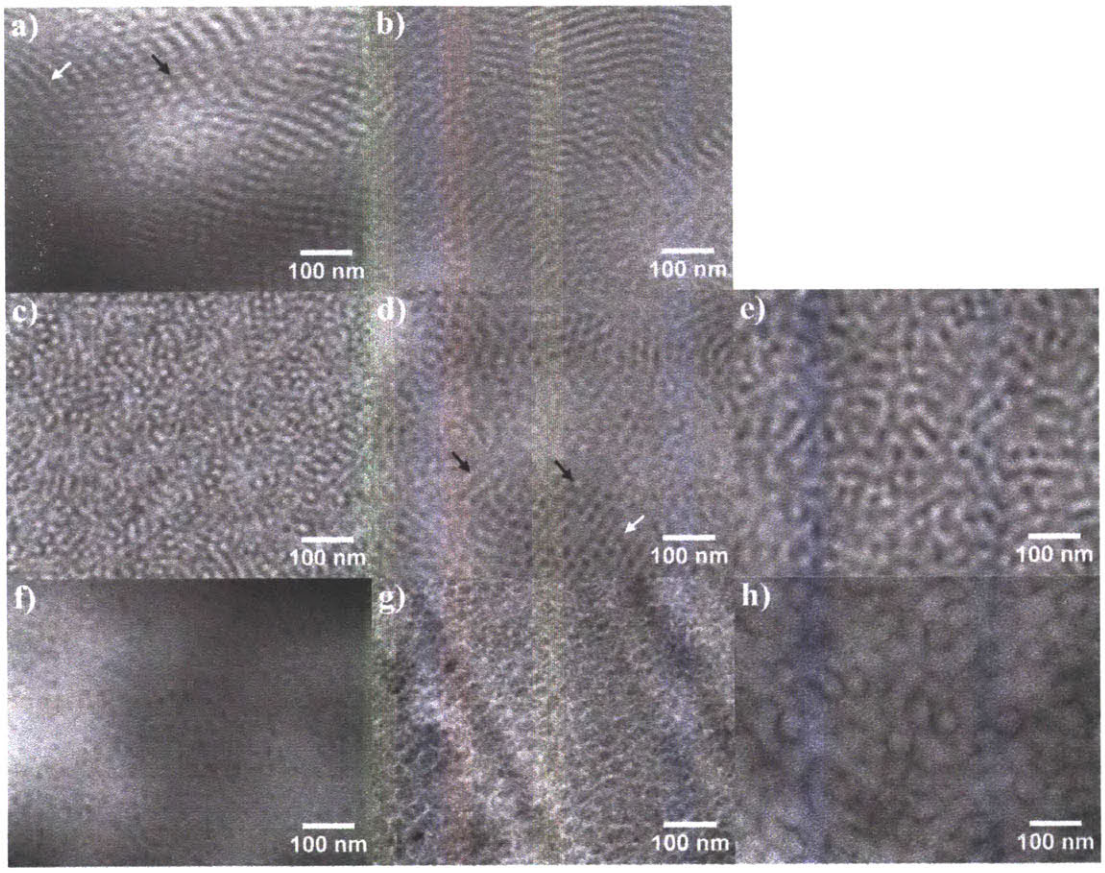

Figure 4-3. TEM images for as-cast mCherry-PNIPAM block copolymers. (a) Cylinders cast from a polymer-selective solvent, f_{PNIPAM} = 0.42. The white arrow shows an example of cylinders parallel to the field of view, and the black arrow points out perpendicular cylinders. (b) Lamellae cast from a polymer-selective solvent, f_{PNIPAM} = 0.53. (c) Cylinders cast from a non-selective solvent, f_{PNIPAM} = 0.42. (d) Nanostructure cast from a non-selective solvent, f_{PNIPAM} = 0.53. The white arrow designates a region of perforated lamellae, and the black arrows show side-on and edge-on cylindrical nanostructures. (e) Disordered lamellae cast from a non-selective solvent, f_{PNIPAM} = 0.69. (f) Disordered micelles cast from a protein-selective solvent, f_{PNIPAM} = 0.42. (g) Hexagonally packed micelles cast from a protein-selective solvent, f_{PNIPAM} = 0.53. (h) Hexagonally packed micelles cast from a protein-selective solvent, f_{PNIPAM} = 0.69.

At a coil fraction of 0.53, mCherry-PNIPAM29 also shows a strong morphology dependence on the polymer selectivity of the solvent. In samples cast from a non-selective solvent, SAXS patterns (Figure 4-2b) show an asymmetric primary peak with a low q shoulder and multiple overlapping higher order reflections that do not allow clear identification of the nanodomain structure. The patterns look similar to previously observed scattering patterns from hexagonally perforated lamellae in these materials;[33] however, the low q shoulder and higher order peaks are less pronounced. TEM images of the sample cast from a non-selective solvent (Figure 4-3d) show mCherry structures in a PNIPAM matrix with regions exhibiting both hexagonal and perforated lamellar structures. In contrast, TEM images of samples cast from a polymer-selective solvent show a predominately lamellar morphology (Figure 4-3b) with better ordering than samples cast from a non-selective solvent. However, the X-ray scattering pattern shows little change as compared with the sample cast from a non-selective solvent. When a non-solvent for the polymer block is used to prepare materials, mCherry-PNIPAM29 forms micellar structures composed of discrete mCherry nanodomains surrounded by a continuous PNIPAM nanodomain similar to mCherry-PNIPAM19. Peaks at $\sqrt{3}q^*$ and $\sqrt{7}q^*$ in the SAXS patterns suggest hexagonal ordering of the nanostructures, and TEM images (Figure 4-3g) clearly illustrate the micellar structure with hexagonal packing.

At the highest studied PNIPAM fraction (f_{PNIPAM} = 0.69), mCherry-PNIPAM57 self-assembles into highly disordered lamellar morphologies when cast from a good solvent for the polymer, while hexagonal micellar morphologies are formed during casting from a non-solvent for the polymer. SAXS curves of samples cast from a good solvent for the polymer show broad primary peaks with relatively low intensities, typical of disordered structures; however, a weak peak at $2q^*$ is observed indicating some ordering is present. TEM images of a sample cast from

a non-selective solvent, illustrated in Figure 4-3e, show a relatively disordered morphology with very short curved lamellar-like domains similar to morphologies observed in coil-coil block copolymers near the order-disorder transition.[50] The hexagonal phase formed from poor solvents for the polymer block is characterized by large polymer domains separated by thin protein-rich regions (Figure 4-3h). These structures are reminiscent of a kinetically-trapped morphology formed by the aggregation of solution nanostructures, and SAXS patterns indicate hexagonal packing of these structures with peaks at $\sqrt{3}q^*$ and $\sqrt{7}q^*$.

The combined measurements of structure in solution and in the solid state suggest that kinetics govern the effect of polymer solvent quality on nanostructure formation according to the pathways for self-assembly illustrated in Figure 4-4. In a good solvent for the polymer block, conjugates remain as individual molecules in solution until a comparatively high concentration, at which point self-assembly occurs from homogenous solution. This self-assembly pathway results in morphologies that resemble those of traditional block copolymers.[51-52] Cylinders, perforated lamellae, and lamellae are observed in order of increasing coil fraction, although the specific coil fractions at which these three morphologies are observed are higher than in coil-coil diblock copolymers. In contrast, a non-solvent for the polymer block causes aggregation even at low concentrations as the PNIPAM domains collapse, minimizing their interactions with the solvent. PNIPAM aggregation drives macrophase separation from solution, and further concentration of conjugate leads to the enrichment of these macrophase separated domains. This yields nanostructures with hexagonal symmetry due to packing of micellar nanodomains. Unexpectedly, mCherry cores are observed at low PNIPAM fractions and PNIPAM cores are observed at high PNIPAM fractions. It is hypothesized that, at low coil fractions, the unstable mCherry coronas collapse to produce inverted micellar domains, while at higher coil fractions,

the PNIPAM is kinetically trapped in the micelle core due to the higher penalty for chain diffusion at high molecular weight.

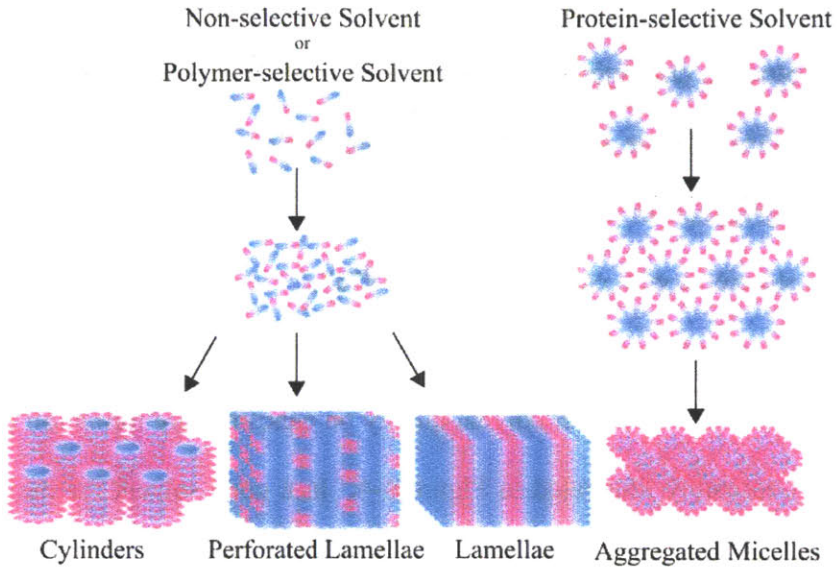

Figure 4-4. Schematic depicting two observed pathways towards the self-assembly of protein-polymer block copolymers. The first occurs in a good solvent for the polymer block and results in a variety of morphologies depending on the polymer coil fraction. The second is obtained by using a poor solvent for the polymer block in which micelles are formed and subsequently aggregate into nanostructures.

Unlike the large effect of polymer solvent quality, protein solvent quality does not significantly change the kinetic pathway for self-assembly in mCherry-PNIPAM materials. However, minimizing the electrostatic repulsion between mCherry blocks by tuning the pH to be near the pI does improve the quality of order observed, and in the case of mCherry-PNIPAM29, produces a change in the type of nanodomain formed. Although this processing strategy may result in significantly different results depending on protein solubility and protein-protein

interactions near the pI, these results suggest that tuning protein interactions is an important strategy for promoting ordered nanostructure formation. It is hypothesized that polymer solvent quality has a much larger effect than protein solvent quality in this system because of the very large change in PNIPAM solubility over the temperature range explored.

In addition to changes in the nanostructure symmetry, the samples cast from poor solvents for the polymer always produced morphologies with larger domain spacing, and the magnitude of this effect increases as the coil fraction increases. For a coil fraction of 0.42, the domain spacing increases from approximately 21.3 nm for materials cast from a good solvent for the polymer block to 23 nm for materials cast from a non-solvent for the polymer block. At a coil fraction of 0.53, the domain spacing increases from approximately 28 nm to 34 nm, while for a coil fraction of 0.69, the increase is from 36 nm to 44 nm for the same solvent conditions. These observations are consistent with the more strongly-segregated nature of the protein-selective solvent and non-solvent casting conditions, where unfavorable mixing between PNIPAM and water induces net repulsive interactions between the PNIPAM and the highly soluble mCherry. Due to the unfavorable polymer-solvent interactions, the polymer stretches to minimize interfacial contact and remains kinetically trapped in the strongly-segregated structure in the final solid state morphology.

Effect of solvent annealing on structure evolution. Solvent annealing was explored to improve the order of protein-polymer block copolymer nanostructures and to provide insight into kinetic effects in as-cast samples. Non-selective (room temperature water) and polymer-selective (1% formic acid) solvents were used for solvent annealing because poor solvents for the polymer block do not provide the necessary increase in polymer block mobility. Samples cast from a non-selective solvent were solvent annealed in either a non-selective or a polymer-

selective solvent, and samples cast from a polymer-selective solvent were annealed in only a non-selective solvent. These conditions provide at least one processing stage using a non-selective solvent and are expected to produce structures with the best ordering closest to that of the equilibrium morphology while simultaneously preserving a large fraction of protein in its functional form.

Depending on the coil fraction of the mCherry-PNIPAM block copolymer, solvent annealing in a non-selective solvent may result in improved ordering, a change in nanodomain structure, or a decrease in ordering due to the interplay between kinetic effects on structure formation and the thermodynamics of self-assembly. For mCherry-PNIPAM19 ($f_{PNIPAM} = 0.42$), all solvent annealing conditions lead to improved ordering of hexagonal cylindrical nanostructures after 8 hours, as evidenced by the decreasing width of the primary peak and more clearly resolved peaks at $\sqrt{3}q^*$ and $2q^*$ (Figure 4-5a,b,c). Samples cast from a polymer-selective solvent and annealed in a non-selective solvent for 24 to 72 hours show continuous improvements in order of increasing annealing time, as evidenced by a continuous sharpening of the primary peak in SAXS and two clearly separate higher order reflections at 72 hours. In contrast, samples cast from a non-selective solvent and annealed in a non-selective solvent for 24 to 72 hours result in a slight increase in the width of the primary SAXS peak and blurring together of the two higher order peaks, as compared to the 8 hour anneal. TEM of the sample annealed for 24 hours (Figure 4-6a) shows well-formed PNIPAM cylinders embedded in a continuous mCherry matrix with both end-on and side-on grain orientations observed. The common approach to a hexagonal cylinder phase for all materials annealed in a non-selective solvent suggests that this phase is thermodynamically favorable for mCherry-PNIPAM19. While annealing in an acidic solution results in improved ordering up to 8 hours, the 24 and 72 hour

annealed samples show a rapidly broadening primary peak and the disappearance of higher order peaks, indicative of an order-disorder transition in the materials. It is hypothesized that an increasing concentration of acid accumulates in the film during annealing, and the accumulated positive charge on the protein promotes disordering of the block copolymer.

Annealing mCherry-PNIPAM29 ($f_{PNIPAM} = 0.53$) in a non-selective solvent results in an improvement in nanodomain ordering followed by a change in nanodomain structure from hexagonal or perforated lamellar to lamellar (Figure 4-5d,e,f). Similar structural changes are observed from samples originally cast from a non-selective or a protein-selective solvent. After 8 hours of annealing in a non-selective solvent, higher order peaks become more distinct, indicating a higher degree of ordering. The domain spacing does not change appreciably after this short annealing time. After 24 hours of annealing a sample cast from a polymer-selective solvent, large perforated lamellar grains with polymer domains clearly perforating protein domains are observable by TEM (Figure 4-6b). Despite the observation of larger perforated lamellar grains in TEM at 24 hours, SAXS patterns show growth of the 001 and 002 peaks and diminishing intensity of the 100 shoulder and 200 reflection, suggesting that a transition to a lamellar phase has started. Annealing for 72 hours provides sufficient chain mobility for the nanostructures to rearrange to lamellae (Figure 4-6c), suggesting that the perforated lamellar morphology is kinetically trapped. When the sample is cast from a non-selective solvent and annealed for 24 hours in a non-selective solvent, this transition to a more lamellar structure has already begun, and few indications of perforated lamellar or hexagonal ordering remain (Figure 4-6d). When a sample cast from a non-selective solvent is instead annealed for 24 hours in a polymer-selective solvent, protein perforations of polymer domains are still observed (Figure 4-6e). As with mCherry-PNIPAM19, annealing in a polymer-selective solvent shows a rapid

increase in disorder with increasing annealing time, resulting in loss of order for annealing times longer than 24 hours. Solvent annealing results in an increase in domain spacing of 10-20% due to solvent swelling after 72 hours for all three conditions.

In contrast to smaller coil fractions where solvent annealing improves ordering, for mCherry-PNIPAM57 (f_{PNIPAM} = 0.69) the degree of ordering decreases slightly with increasing solvent annealing time, as evidenced by the decreasing intensity of the primary scattering peak. The relatively high coil fraction is anticipated to decrease the water concentration required to reach the order-disorder transition, promoting a slight loss of order with increasing swelling. SAXS (Figure 4-5g,h,i) shows that the primary peak intensity decreases, particularly from 24 to 72 hours of annealing for all samples. In addition, the second order peak intensity decreases, with the most prominent decrease occurring after acidic solvent anneals. For all three annealing conditions, the domain spacing increases with increasing annealing time from 36 nm to 40-45 nm as the polymer swells with water. A TEM image of this sample cast from a non-selective solvent and then annealed in the same solvent for 24 hours (Figure 4-6f) shows a highly disordered lamellae-like nanostructure, similar to that seen in the non-annealed sample. These results suggest that mCherry-PNIPAM57 is relatively close to the order-disorder transition, and that added solvent during annealing results in an increase in disorder due to compatibilization of the two blocks.

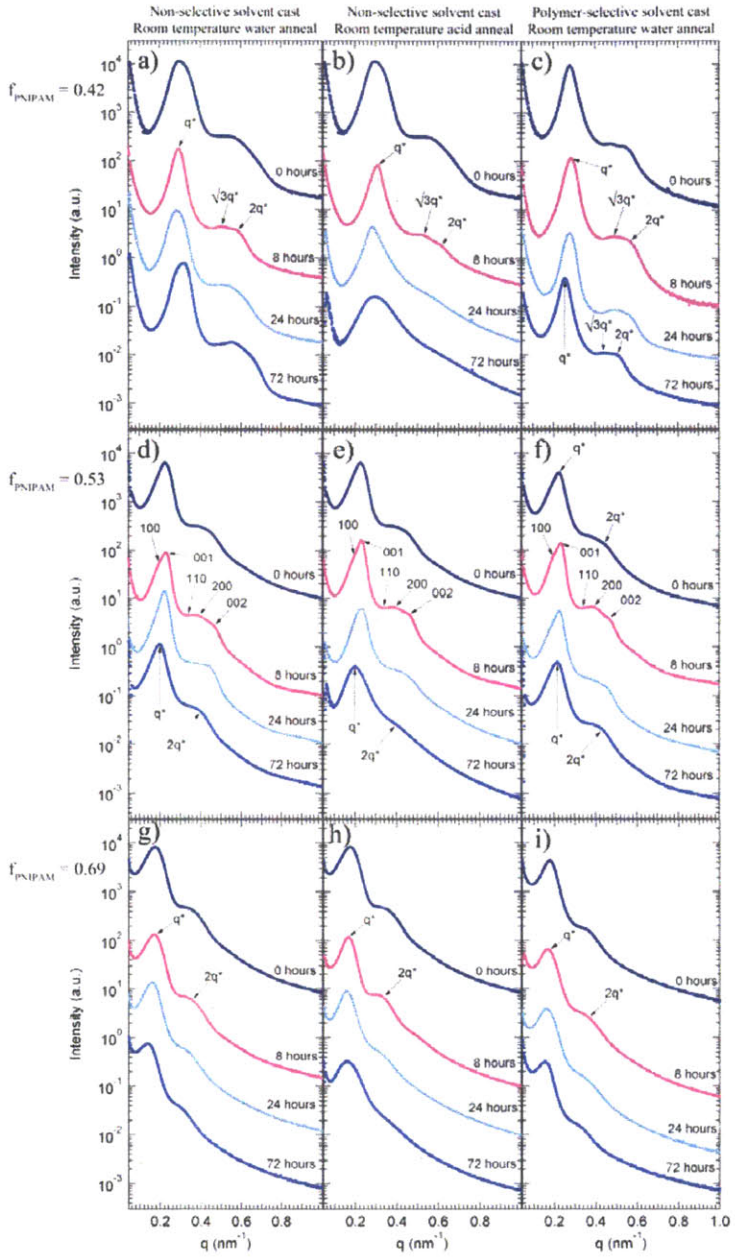

Figure 4-5. Small-angle X-ray scattering data for mCherry-PNIPAM block copolymers showing the effect of solvent annealing. (a-c) f_{PNIPAM} = 0.42 shows improved hexagonal ordering with annealing. (d-f) f_{PNIPAM} = 0.53 shows enhancement of higher order peaks when annealing for 8 and 24 hours, indicating improved long-range ordering. Longer annealing times diminish the prominence of the higher order peaks as a result of decreased ordering. A transition in morphology from perforated lamellae to lamellae is observed with increased annealing time. (g-i) f_{PNIPAM} = 0.69 shows a slight loss of ordering with increasing annealing time.

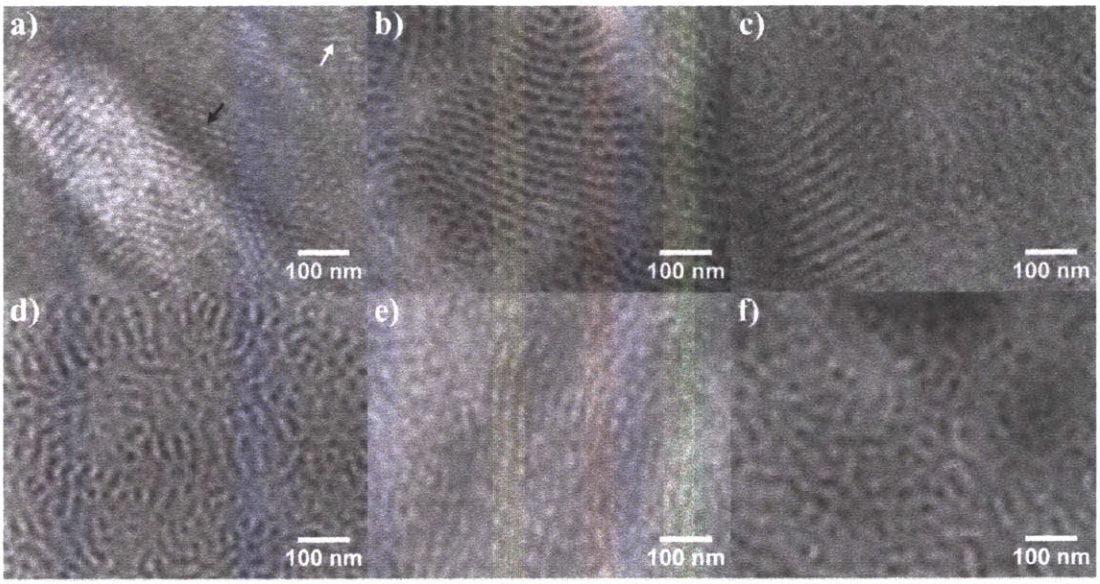

Figure 4-6. TEM images for mCherry-PNIPAM block copolymers that have been solvent annealed. (a) Hexagonally packed cylinders from a non-selective solvent cast/water anneal for 24 hours, $f_{PNIPAM} = 0.42$. The white arrow indicates a region of edge-on cylinders, and the black arrow shows end-on cylinders. (b) Perforated lamellae from a polymer-selective solvent cast/water anneal for 24 hours, $f_{PNIPAM} = 0.53$. (c) Lamellae from a non-selective cast/water anneal for 72 hours, $f_{PNIPAM} = 0.53$. (d) Disordered lamellae from a non-selective solvent cast/water anneal for 24 hours, $f_{PNIPAM} = 0.53$. (e) Perforated lamellae from a non-selective cast/1 vol% formic acid anneal for 24 hours, $f_{PNIPAM} = 0.53$. (f) Disordered lamellae from a non-selective solvent cast/water anneal for 24 hours, $f_{PNIPAM} = 0.69$.

The complex effect of solvent annealing on structure formation reflects the interplay of kinetic and thermodynamic driving forces governing structure formation during solvent annealing. While the addition of a non-selective solvent increases chain mobility and promotes relaxation towards an equilibrium morphology, it also changes the thermodynamic equilibrium

by introducing an additional component into the block copolymer system that swells the nanodomain structure. In the case of mCherry-PNIPAM19, chain mobility effects dominate, as evidenced by a very minor change in domain spacing with increasing annealing time, and enhanced ordering is observed. In the case of mCherry-PNIPAM57, a 30% increase in domain spacing leads to a decrease in ordering without a change in nanostructure, indicating that swelling effects dominate. For mCherry-PNIPAM29, both structural rearrangement and changes in domain spacing are observed. The interplay between structure evolution and increased swelling with increased annealing time yields a range of optimal annealing times from 8 to 24 hours where enhanced long-range ordering is observed without a large degree of nanodomain swelling.

In contrast to behavior during annealing with non-selective solvents, annealing with a dilute acid (polymer-selective solvent) leads to a more rapid loss of order. Unlike pH-controlled casting solutions where the formic acid molarity is constant, the film is an open system in contact with a chemical potential bath during solvent annealing. Therefore, significant formic acid is absorbed into the nanostructures during annealing, as evidenced by a change in the color of the materials from dark red to gold due to protonation of the mCherry acylimine group.[53-54] Protonation of mCherry induces a net positive charge that increases electrostatic repulsions between molecules and promotes disordering within the nanostructures. This is consistent with the observation that casting from solutions with a pH near the pI (minimizing electrostatic interactions) enhances ordering.

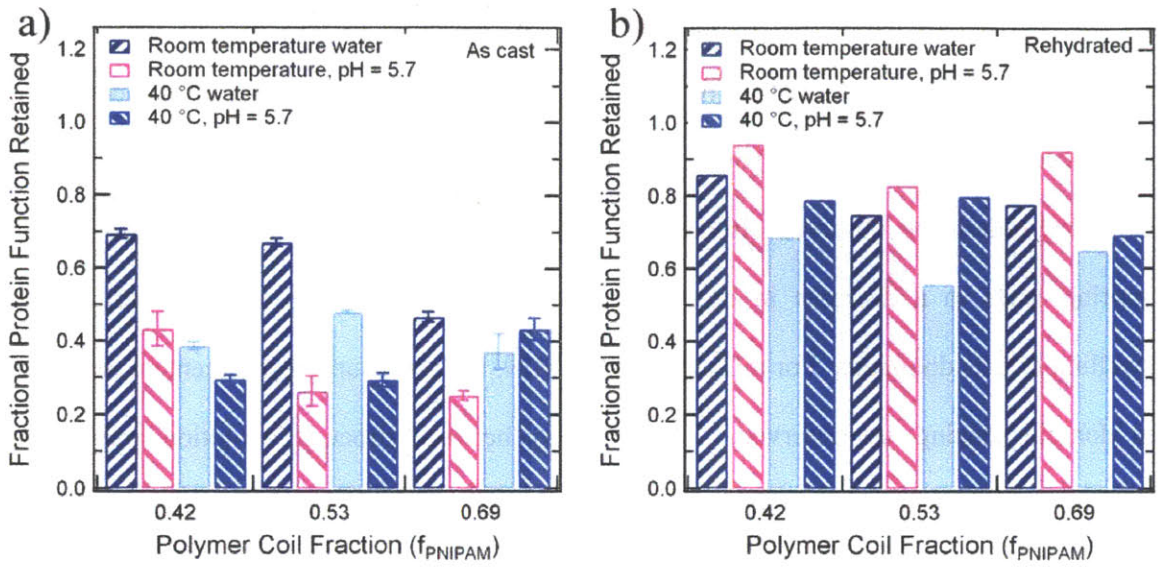

Figure 4-7. Protein optical activity as a function of PNIPAM coil fraction and casting solvent. Protein function is shown in terms of the absorbance of the fluorescent protein chromophore at 586 nm, relative to the initial solution-state absorbance of the protein-polymer conjugate. Solid state samples (a) provide a direct measure of function in solid nanostructures, while rehydrated samples (b) provide a measure of the fraction of protein that remained folded. Room temperature water is a non-selective solvent, room temperature pH = 5.7 is a polymer-selective solvent, 40 °C water is a protein-selective solvent, and 40 °C pH = 5.7 is a non-solvent for this system.

Protein structure and function. Molecular design and the processing conditions used to induce self-assembly have a large effect on the function of the protein in the solid state. Solid state UV-vis provides a measure of the protein function in the bulk self-assembled material, allowing its dependence on casting and annealing conditions to be quantified. In mCherry, the chromophore is sensitive to the surrounding environment, making UV-vis absorption an excellent indicator for the maintenance of protein fold and function. Figure 4-7a shows that for all PNIPAM coil

fractions, casting from a non-selective solvent preserved the highest levels of protein function, with up to 70% of the original solution-state absorbance preserved. Samples cast from acidic solutions show a relative decrease in absorbance at 586 nm, which corresponds to the appearance of a new peak at 440 nm, indicative of a spectral shift due to protonation of the acylimine chromopohore.[53-56] Therefore, UV-vis measurements for acid-cast samples underestimate the fraction of functional protein in the solid state. The amount of functionality preserved also depends on coil fraction. For samples cast at room temperature, protein function decreases weakly with increasing coil fraction, while for samples cast from a non-solvent, the chromophore absorbance peak increases weakly with increasing coil fraction. The variation in protein function with changing coil fraction may be due to a combination of compositional and morphological effects which cannot be clearly differentiated due to the relationship between block copolymer composition and morphology.

Comparison between solid state and rehydrated solution absorption measurements provides a method to separate functionality losses due to irreversible denaturation from losses due to spectral shifts caused by association in the solid state or protonation of the mCherry chromophore by residual acid. For all conditions, the rehydrated absorbance is lower than the as-synthesized conjugate, indicating an irreversible loss of functionality ranging from 5 to 45%, as shown in Figure 4-7b. However, the level of retained functionality is higher than in the solid state, clearly indicating that part of the decrease in absorbance in the solid state is reversible and not due to protein unfolding or chromophore degradation. Casting from a good solvent for the polymer block results in higher reconstituted protein function than casting from a poor solvent for the polymer for all coil fractions. Surprisingly, casting from an acidic solution also led to much higher activity levels after rehydration than casting from a neutral pH solution. This

suggests that the decreased functionality observed for acid-cast samples is primarily due to protonation of the chromophore and that the addition of the small molecule actually has a functionality-preserving effect. The preserving effect is speculated to be due to hydrogen bonding with residual formate ions in the film that may stabilize the protein in a manner similar to that of pharmaceutical additives.[57]

Solvent annealing may also have an impact on the function of the protein within nanostructured materials. Annealing water-cast samples in pure water does not significantly alter protein function, but for samples which become significantly swollen, like mCherry-PNIPAM57, the protein chromophore absorbance increases with annealing time by approximately 20% of the original solution value (Figure B-7). This is consistent with the effect of protein rehydration to increase absorbance. However, when annealing at an acidic pH, the fast drop in A_{586} indicates that chromophore protonation occurs rapidly and is nearly complete within 8 hours. In contrast, annealing with water after casting samples at acidic pH leads to a more gradual increase in A_{586} with longer annealing times as residual acid is slowly released from the film. It is also observed that there is a wide degree of variability between the samples cast from an acidic solution and annealed in a non-selective solvent. Regardless of the rate of increase in A_{586}, the A_{440} inversely tracks with A_{586}, consistent with variability due to inhomogeneous acid diffusion out of the film. Measurements on rehydrated protein after solvent annealing indicate that the annealing time does not greatly affect the fraction of folded protein when annealing in a non-selective solvent. For those samples annealed in an acidic solution, it is observed that a short anneal results in a small initial decrease in overall functionality (4-12% of original absorbance) due to chromophore protonation, after which there is negligible loss of functionality

with increased annealing time. Regardless of annealing condition, the lowest coil fraction always retains the highest level of protein function in samples rehydrated after annealing.

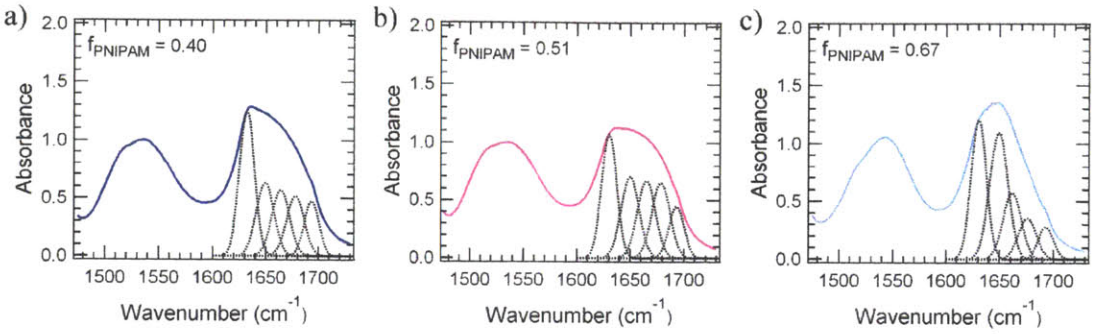

Figure 4-8. Representative solid state FTIR spectra for (a) f_{PNIPAM} = 0.42 (b) f_{PNIPAM} = 0.53 and (c) f_{PNIPAM} = 0.69, showing the amide I region with Fourier self-deconvolution (FSD) overlaid. The amide I peak has greater intensity near 1631 cm^{-1} for lower PNIPAM coil fractions, which indicates a predominately β-sheet structure, while for the highest PNIPAM coil fraction, the peak intensity shifts to 1649 cm^{-1}, indicating an increase in the amount of random coil content.

The secondary structure of the protein was assessed in both self-assembled nanostructures and rehydrated conjugates, showing that, despite changes in protein function with processing, the secondary structure is largely preserved. The FTIR spectra are used to determine the secondary structure from the amide I region between 1600 and 1700 cm^{-1} using a Fourier self-deconvolution algorithm.[41-42, 58-60] As shown in Figures B-8,9,10, the amide I peak shows no resolvable change with different processing conditions for a given PNIPAM coil fraction. Figure 4-8 provides representative spectra for each conjugate along with the corresponding deconvolutions which show that the primary difference among the conjugates is the enhancement of the deconvoluted peak centered around 1650 cm^{-1} with increasing coil fraction. The five peaks obtained upon deconvolution were attributed to secondary structures in accordance with

the literature (Table 4-3).[41-42, 58-63] The peak at 1631 cm^{-1} is the most intense for coil fractions of 0.42 and 0.53, which is consistent with a predominately β-sheet protein. At f_{PNIPAM} = 0.42 approximately 43% of the conjugate was β-sheet structures, while at f_{PNIPAM} = 0.53 this value was 40%. For the conjugate with a coil fraction of 0.69, the amide I peak maximum is shifted to 1649 cm^{-1}, indicative of a larger random coil fraction, and the β-sheet fraction was reduced to 38%. As expected, a decrease in the relative β-sheet content was observed at the larger PNIPAM coil fractions due to the increasing polymer coil fraction of the material. However, the observed decrease is smaller than predicted based on the increasing coil fraction alone (see Appendix B), which suggests that conjugates with a higher polymer coil fraction have a slightly higher β-sheet content in the protein. Circular dichroism (CD) measurements on rehydrated conjugate confirm the preservation of secondary structure after self-assembly. The spectra for each rehydrated conjugate are indistinguishable from the as-synthesized conjugate, showing predominantly β-sheet structure with the same β-sheet content as the corresponding as-synthesized conjugate (Tables B-5,6,7).

Table 4-3. FTIR peak identification according to literature

wavenumber range (cm^{-1})	peak assignment
1612-1640	beta-sheet (strong)
1640-1657	random coils
1650-1660	alpha helix
1661-1680	beta turns, loops
1681-1695	beta-sheet (weak)

While protein secondary structure retention is required to maintain high levels of protein functionality, changes in tertiary structure also contribute to overall protein function. Even

though secondary structure remained largely unaltered, displaying a high fraction of β-sheet content as expected from the mCherry crystal structure,[46] the chromophore absorbance of mCherry was found to be dependent on charge state and slightly dependent on processing time and bioconjugate coil fraction. This suggests that the tertiary structure of some fraction of the protein is disrupted during self-assembly, resulting in an irreversible loss of function ranging from 5 to 45% of the total protein. However, several processing conditions are identified that appear to maintain 80-95% of the protein in its folded form.

4.5 Conclusions

Model globular protein-polymer block copolymers composed of an mCherry protein block and a PNIPAM polymer block are shown to self-assemble into cylinders, perforated lamellae, lamellae, or hexagonal and disordered micellar phases, depending on both the polymer coil fraction and the solvent quality for each block. Temperature modulation during self-assembly alters the solvent quality and consequently the morphology; a good solvent for the polymer produces nanostructures reminiscent of coil-coil block copolymers. When a poor solvent for the polymer block is used, aggregates that form in solution are kinetically trapped in the solid state to form disordered micellar structures. Tuning protein interactions also affects nanostructure formation, as samples cast from solutions near the isoelectric point of the protein where repulsive interactions between proteins are minimized produce nanostructures with improved ordering. At the smallest polymer coil fraction studied (f_{PNIPAM} = 0.42), a hexagonal morphology is strongly preferred. However, at the largest coil fraction (f_{PNIPAM} = 0.69), disordered lamellae are observed which may indicate that these samples are near an order-disorder transition. Bioconjugates with an intermediate coil fraction (f_{PNIPAM} = 0.53) result in

several morphologies including perforated lamellae and lamellae depending on the processing history, demonstrating the importance of kinetic effects on structure control. Solvent annealing materials with f_{PNIPAM} = 0.53 results in a trend toward lamellar nanostructure under many conditions. As the coil fraction in the block copolymer is increased, solvent annealing for 8-24 hours in a non-selective solvent is shown to enhance the quality of nanostructures (f_{PNIPAM} = 0.42), change the morphology (f_{PNIPAM} = 0.53), or simply swell existing nanodomains (f_{PNIPAM} = 0.69).

Depending upon the block copolymer coil fraction and processing technique used to induce self-assembly, a large fraction of the protein function could be preserved in the solid state. Using a neutral pH solution, up to 70% of the initial protein function is maintained when in a solid film with the highest retention observed at the lowest coil fraction. In contrast, using an acidic solution results in a spectral shift due to chromophore protonation that is reversed upon rehydration to recover up to 95% of the original protein function. Despite variations in protein function, the secondary structure remains intact regardless of the processing conditions used in this study. Overall, these results indicate that a large majority of the protein tertiary structure can be preserved in self-assembled materials.

4.6 Acknowledgements

This research was supported by the Department of Energy Office of Basic Energy Sciences (award number DE-SC0007106). SANS experiments were performed on the LQD at the Los Alamos Neutron Science Center. SAXS experiments were performed at Beamline X9 at the National Synchrotron Light Source at Brookhaven National Laboratory, and TEM experiments were performed at the MIT Institute for Soldier Nanotechnologies. CD and DLS experiments

were performed at the Biophysical Instrumentation Facility for the Study of Complex Macromolecular Systems (NSF-0070319 and NIH GM68762). We also thank Rex Hielm for experimental assistance with SANS, Lin Yang for experimental assistance with SAXS, and Karen Gleason for use of the FTIR.

4.7 References

1. I. Willner and E. Katz, *Angew. Chem., Int. Ed.*, 2000, **39**, 1180-1218.
2. R. N. Patel, *Coord. Chem. Rev.*, 2008, **252**, 659-701.
3. T. Reda, C. M. Plugge, N. J. Abram and J. Hirst, *Proc. Natl. Acad. Sci. U. S. A.*, 2008, **105**, 10654-10658.
4. R. Das, P. J. Kiley, M. Segal, J. Norville, A. A. Yu, L. Y. Wang, S. A. Trammell, L. E. Reddick, R. Kumar, F. Stellacci, N. Lebedev, J. Schnur, B. D. Bruce, S. G. Zhang and M. Baldo, *Nano Lett.*, 2004, **4**, 1079-1083.
5. J. Ge, D. N. Lu, Z. X. Liu and Z. Liu, *Biochem. Eng. J.*, 2009, **44**, 53-59.
6. Y. Wang, A. S. Angelatos and F. Caruso, *Chem. Mater.*, 2008, **20**, 848-858.
7. Y. Kulmashiro, Y. Ikezoe, K. Tamada and M. Hara, *J. Phys. Chem. B*, 2008, **112**, 8291-8297.
8. D. C. Kim, J. I. Sohn, D. J. Zhou, T. A. J. Duke and D. J. Kang, *ACS Nano*, 2010, **4**, 1580-1586.
9. P. D. Laible, R. F. Kelley, M. R. Wasielewski and M. A. Firestone, *J. Phys. Chem. B*, 2005, **109**, 23679-23686.
10. G. Luo, Q. Zhang, A. R. D. Castillo, V. Urban and H. O'Neill, *ACS Appl. Mater. Interfaces*, 2009, **1**, 2262-2268.
11. M. Vinoba, K. S. Lim, S. H. Lee, S. K. Jeong and M. Alagar, *Langmuir*, 2011, **27**, 6227-6234.
12. R. C. Rodrigues, A. Berenguer-Murcia and R. Fernandez-Lafuente, *Adv. Synth. Catal.*, 2011, **353**, 2216-2238.
13. N. K. Dutta and N. R. Choudhury, *Self-Assembly and Supramolecular Assembly in Nanophase Separated Polymers and Thin Films*, Springer, New York, 2008.
14. R. P. Sear, *Curr. Opin. Colloid Interface Sci.*, 2006, **11**, 35-39.
15. K. L. Heredia, D. Bontempo, T. Ly, J. T. Byers, S. Halstenberg and H. D. Maynard, *J. Am. Chem. Soc.*, 2005, **127**, 16955-16960.
16. J. C. M. van Hest, *Polym. Rev.*, 2007, **47**, 63-92.
17. J. Kalia and R. T. Raines, *Curr. Org. Chem.*, 2010, **14**, 138-147.
18. X. J. Wan and S. Y. Liu, *Macromol. Rapid Commun.*, 2010, **31**, 2070-2076.
19. I. Hamachi, K. Nakamura, A. Fujita and T. Kunitake, *J. Am. Chem. Soc.*, 1993, **115**, 4966-4970.
20. C. Boyer, X. Huang, M. R. Whittaker, V. Bulmus and T. P. Davis, *Soft Matter*, 2011.
21. H. Y. Cho, M. A. Kadir, B. S. Kim, H. S. Han, S. Nagasundarapandian, Y. R. Kim, S. B. Ko, S. G. Lee and H. J. Paik, *Macromolecules*, 2011, **44**, 4672-4680.

22. A. K. Shakya, H. Sami, A. Srivastava and A. Kumar, *Prog. Polym. Sci.*, 2010, **35**, 459-486.
23. I. C. Reynhout, J. L. M. Cornelissen and R. J. M. Nolte, *J. Am. Chem. Soc.*, 2007, **129**, 2327-2332.
24. I. C. Reynhout, J. L. M. Cornelissen and R. J. M. Nolte, *Acc. Chem. Res.*, 2009, **42**, 681-692.
25. P. van Rijn and A. Böker, *J. Mater. Chem.*, 2011, **21**, 16735-16747.
26. N. C. Mougin, P. van Rijn, H. Park, A. H. E. Müller and A. Böker, *Adv. Funct. Mater.*, 2011, **21**, 2470-2476.
27. M. Li, P. De, H. Li and B. S. Sumerlin, *Polym. Chem.*, 2010, **1**, 854-859.
28. S. Kulkarni, C. Schilli, A. H. E. Müller, A. S. Hoffman and P. S. Stayton, *Bioconjugate Chem.*, 2004, **15**, 747-753.
29. A. E. F. Nassar, Z. Zhang, V. Chynwat, H. A. Frank, J. F. Rusling and K. Suga, *J. Phys. Chem.*, 1995, **99**, 11013-11017.
30. A. D. Presley, J. J. Chang and T. Xu, *Soft Matter*, 2011, **7**, 172-179.
31. Y. X. Hu, D. Samanta, S. S. Parelkar, S. W. Hong, Q. A. Wang, T. P. Russell and T. Emrick, *Adv. Funct. Mater.*, 2010, **20**, 3603-3612.
32. B. Kim, C. N. Lam and B. D. Olsen, *Macromolecules*, 2012.
33. C. S. Thomas, M. J. Glassman and B. D. Olsen, *ACS Nano*, 2011, **5**, 5697-5707.
34. S. H. Kim, M. J. Misner, T. Xu, M. Kimura and T. P. Russell, *Adv. Mater.*, 2004, **16**, 226-231.
35. K. A. Cavicchi, K. J. Berthiaume and T. P. Russell, *Polymer*, 2005, **46**, 11635-11639.
36. R. A. Segalman, *Mater. Sci. Eng., R*, 2005, **48**, 191-226.
37. J. N. L. Albert and T. H. Epps, *Mater. Today*, 2010, **13**, 24-33.
38. G. Kim and M. Libera, *Macromolecules*, 1998, **31**, 2569-2577.
39. T. P. Lodge, B. Pudil and K. J. Hanley, *Macromolecules*, 2002, **35**, 4707-4717.
40. A. Saluja and D. S. Kalonia, *Int. J. Pharm.*, 2008, **358**, 1-15.
41. D. M. Byler and H. Susi, *Biopolymers*, 1986, **25**, 469-487.
42. M. Jackson and H. H. Mantsch, *Crit. Rev. Biochem. Mol. Biol.*, 1995, **30**, 95-120.
43. G. Beaucage, *J. Appl. Crystallogr.*, 1995, **28**, 717-728.
44. D. J. Kinning and E. L. Thomas, *Macromolecules*, 1984, **17**, 1712-1718.
45. M. E. Seitz, W. R. Burghardt, K. T. Faber and K. R. Shull, *Macromolecules*, 2007, **40**, 1218-1226.
46. X. K. Shu, N. C. Shaner, C. A. Yarbrough, R. Y. Tsien and S. J. Remington, *Biochemistry*, 2006, **45**, 9639-9647.
47. W. Zhang, S. Zou, C. Wang and X. Zhang, *J. Phys. Chem. B*, 2000, **104**, 10258-10264.
48. S. S. Pai, B. Hammouda, K. Hong, D. C. Pozzo, T. M. Przybycien and R. D. Tilton, *Bioconjugate Chem.*, 2011, **22**, 2317-2323.
49. K. J. Hanley, T. P. Lodge and C. I. Huang, *Macromolecules*, 2000, **33**, 5918-5931.
50. N. Sakamoto and T. Hashimoto, *Macromolecules*, 1998, **31**, 3815-3823.
51. F. S. Bates and G. H. Fredrickson, *Phys. Today*, 1999, **52**, 32-38.
52. C. Park, J. Yoon and E. L. Thomas, *Polymer*, 2003, **44**, 6725-6760.
53. A. A. Pakhomov, N. V. Pletneva, T. A. Balashova and V. I. Martynov, *Biochemistry*, 2006, **45**, 7256-7264.
54. L. A. Gross, G. S. Baird, R. C. Hoffman, K. K. Baldridge and R. Y. Tsien, *Proc. Natl. Acad. Sci. U. S. A.*, 2000, **97**, 11990-11995.

55. F. V. Subach, V. N. Malashkevich, W. D. Zencheck, H. Xiao, G. S. Filonov, S. C. Almo and V. V. Verkhusha, *Proc. Natl. Acad. Sci. U. S. A.*, 2009, **106**, 21097-21102.
56. K. B. Bravaya, O. M. Subach, N. Korovina, V. V. Verkhusha and A. I. Krylov, *J. Am. Chem. Soc.*, 2012, **134**, 2807-2814.
57. T. J. Kamerzell, R. Esfandiary, S. B. Joshi, C. R. Middaugh and D. B. Volkin, *Adv. Drug Deliv. Rev.*, 2011, **63**, 1118-1159.
58. J. Kong and S. Yu, *Acta Biochim. Biophys. Sin.*, 2007, **39**, 549-559.
59. K. Fu, K. Griebenow, L. Hsieh, A. M. Klibanov and L. Robert, *J. Controlled Release*, 1999, **58**, 357-366.
60. H. Herberhold, S. Marchal, R. Lange, C. H. Scheyhing, R. F. Vogel and R. Winter, *J. Mol. Biol.*, 2003, **330**, 1153-1164.
61. A. Barth and C. Zscherp, *Q. Rev. Biophys.*, 2002, **35**, 369-430.
62. W. Huang, S. Krishnaji, X. Hu, D. Kaplan and P. Cebe, *Macromolecules*, 2011, **44**, 5299-5309.
63. S. Matheus, W. Friess and H. C. Mahler, *Pharm. Res.*, 2006, **23**, 1350-1363.

Chapter 5 The Effect of Small Molecule Osmolytes on the Self-Assembly and Functionality of Globular Protein-Polymer Diblock Copolymers

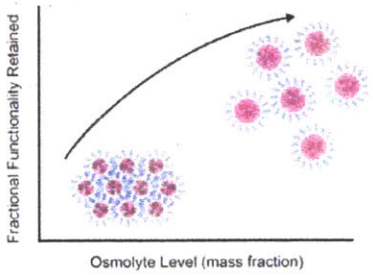

5.1 Abstract

Blending the small molecule osmolytes glycerol and trehalose with the model globular protein-polymer block copolymer mCherry-b-poly(N-isopropyl acrylamide) (mCherry-b-PNIPAM) is demonstrated to improve protein functionality in self-assembled nanostructures. The incorporation of either additive into block copolymers results in functionality retention in the solid state of 80% and 100% for PNIPAM volume fractions of 40 and 55%, respectively. This represents a large improvement over the 50-60% functionality observed in the absence of any additive. Furthermore, glycerol decreases the thermal stability of block copolymer films by 15-20 °C, while trehalose results in an improvement in the thermal stability by 15-20 °C. These results suggest that hydrogen bond replacement is responsible for the retention of protein function, but suppression or enhancement of thermal motion based on the glass transition of the osmolyte primarily determines thermal stability. While both osmolytes are observed to have a

disordering effect on the nanostructure morphology with increasing concentration, this effect is less pronounced in materials with a larger polymer volume fraction. Glycerol preferentially localizes in the protein domains and swells the nanostructures, inducing disordering or a change in morphology depending on the PNIPAM coil fraction. In contrast, trehalose is observed to macrophase separate from the block copolymer, which results in nanodomains becoming more disordered without changing significantly in size.

5.2 Introduction

The wide range of functions exhibited by enzymes and other globular proteins makes them attractive for incorporation into a variety of bioelectronic and biocatalytic devices.[1-3] In order to optimize the performance of these materials, it is often desirable to control protein orientation and provide nanostructured transport pathways for substrates and products in a material that contains a very high density of active protein sites.[4] To date, many approaches for nanopatterning proteins have been developed: covalent immobilization,[1, 5] physical adsorption on surfaces,[6-7] and the use of nanostructured templates[8-11] to control protein packing. Self-assembly provides an alternate, bottom-up approach toward directly nanopatterning proteins. Through a single site-specific bioconjugation, a protein-polymer diblock copolymer is created which has been shown to self-assemble in a manner analogous to coil-coil block copolymers into solid state nanostructures,[12-14] structured gels,[15] or micellar aggregates.[16-18] A variety of synthetic approaches have been demonstrated in the literature to create these types of macromolecules including grafting to, grafting from and grafting through approaches all utilizing a wide range of controlled polymerization techniques to ensure materials remain monodisperse.[19-25] Additionally, it has been demonstrated that bioconjugates can be constructed

through non-covalent interactions including avidin-biotin and carbohydrate-protein specific interactions.[21-22] Many studies have investigated the self-assembly behavior of these bioconjugate materials in solution where the formation of a variety of aggregate structures including spherical and elongated micelles, toroids and vesicles have been demonstrated.[16-18, 26] Studies of the behavior of protein-polymer ionic complexes with multiple polymers associated with each protein molecule have also found that proteins are able to retain significant functionality in a solvent-free environment.[27] However, maintaining high levels of enzyme activity after protein immobilization remains an ongoing challenge.[28] Obstruction of the active site and protein unfolding, especially at interfaces, are major contributors to the dramatic decrease in enzyme activity often observed when comparing immobilized activity levels to those measured in solution.[29] In addition, increased thermal stability and extended protein lifetimes are often required for the fabrication of industrially relevant materials.

A number of different methods for protein stabilization have been developed based upon modifications to the protein or the surrounding environment.[30-31] Site-directed mutagenesis is used to improve the intrinsic stability of the protein to thermal or chemical stressors.[32-33] Chemical modification of the protein with poly(ethylene glycol) (PEG) molecules or other polymers[28, 33] can also increase the stability of proteins, in part by encapsulating the protein to form a protective shell in solution.[34] Encapsulation in silk fibroin,[35] sol-gels[36-37] or polyurethanes[38] has been demonstrated as an effective technique to improve the chemical and thermal stability as well as extend the lifetime of enzymes in non-ideal environments. The creation of a rigid, crosslinked network surrounding proteins has also been shown to improve stability and reduce unwanted leakage of proteins from the material; however, this is often accompanied by a loss in total protein activity.[28]

Another technique employed to increase the fraction of active protein is the use of additives or preservatives. These types of materials have most notably been shown to dramatically improve enzyme activity after lyophilization,[39] and are broadly grouped into the following categories:[30, 33, 40-41] osmolytes (including sugars), polymers,[37] chelating agents,[42] salts,[43] and surfactants. Trehalose is one of the most popular osmolytes in part due to its thermophysical properties, including a relatively high glass transition temperature and low reactivity.[39, 44-45] The early work of Crowe and coworkers demonstrated the exceptional ability of trehalose to act as a lyoprotectant to stabilize lipid membranes against aggregation and the loss of their contents upon rehydration.[46] Studies examining the ability of sugars to improve the thermal stability of proteins such as bovine serum albumin,[47] trypsin,[48] RNase A,[45] and firefly luciferase[49] have demonstrated the superior performance of trehalose as compared with other osmolytes. Glycerol, another osmolyte commonly employed to improve protein stability, has been shown to maintain and promote protein hydration in solution[50] and can act as an antiplasticizer in conjunction with trehalose.[51] The mechanism by which these additives enhance stability in a dehydrated environment is still uncertain; however, several theories have been proposed.[39, 45, 48] The two primary theories are that the additive molecule replaces hydrogen bonds which would normally be fulfilled by water, or that the additive creates a glassy matrix which restricts protein movement. More recent work suggests protein stability may be related to β-relaxation of the sugar matrix encapsulating the protein.[52]

In addition to improving the activity and stability of proteins, small molecule additives are expected to alter the self-assembly behavior of protein-polymer block copolymers. For example, the addition of homopolymers to block copolymer nanostructures can be used to swell the characteristic domain spacing of coil-coil block copolymers as well as facilitate the

fabrication of complex geometries using chemoepitaxial templates.[53-54] A number of studies have investigated the addition of small molecules which interact selectively with one of the blocks, oftentimes through hydrogen bonds, and their effects on the supramolecular assembly of block copolymers.[55-56] Depending on the relative loading and segregation of the small molecule within the block copolymer, several previously unobserved morphologies have been identified, such as lamellae-within-lamellae nanostructures.[55, 57] The addition of solvent molecules also results in a rich and varied phase behavior that depends on solvent selectivity for each block, temperature, and polymer concentration.[58-62] For example, preferential solvation has been observed to increase the effective volume fraction of one block which can induce a change in morphology from cylinders to lamellae to reverse cylinders with increasing solvent content.[60-62]

In this study, the addition of osmolytic additives to protein-polymer block copolymer nanostructures is demonstrated as a promising route to increase the stability and activity of proteins in nanomaterials. Trehalose and glycerol are used to improve protein performance in bulk self-assembled protein-polymer block copolymers in a model material composed of a red fluorescent protein, mCherry, and poly(N-isopropyl acrylamide) (PNIPAM). Although temperature dependent self-assembly is not considered in this study, the thermoresponsive behavior of PNIPAM in water allows for easy, cost-effective purification of bioconjugate material. Nanostructures are self-assembled with each additive through solvent evaporation, and the retention of functionality and thermal stability of the proteins in the dehydrated state is assessed as a function of additive loading. The effect of these additives on self-assembly behavior and morphology is then investigated, demonstrating a region of additive loadings where both nanostructured morphologies and quantitative retention of protein function can be achieved.

5.3 Experimental Methods

Low polydispersity PNIPAM was synthesized using radical addition-fragmentation chain transfer (RAFT) polymerization with a protected maleimide chain transfer agent (CTA) as described previously.[13] Polymer molecular weights and polydispersities were determined by gel permeation chromatography (GPC) using an Agilent 1260 Infinity HPLC with N,N-dimethylformamide (DMF) as the mobile phase. Both a refractive index detector and a Wyatt Mini-Dawn 3-angle static light scattering detector were employed to enable absolute molecular weight determination. Protein expression, purification, and bioconjugation were also performed as previously described.[13] The materials used in this study are shown in Table 5-1.

Table 5-1. mCherry-b-PNIPAM block copolymers

Block copolymer	PNIPAM M_n (kg/mol)	PDI_{PNIPAM}	Conjugate M_n (kg/mol)	f_{PNIPAM}	Final purity* (%)
mCherry-PNIPAM14	14.4	1.18	42.5	0.40	100
mCherry-PNIPAM26	26.4	1.07	54.5	0.55	97

*As determined by native protein gel electrophoresis

Sample preparation. Conjugate solutions, dialyzed into pure water, were concentrated to ~100 mg/mL using Millipore Ultra-15 centrifugal filters with a molar mass cutoff of 10 kDa. Glycerol or trehalose was then added to these solutions such that it would make up 5 to 50% of the total dry mass. Water evaporation was performed at room temperature, and the solvent evaporation rate was controlled using a vacuum controller. To prepare samples for absorption spectroscopy and optical microscopy, a ramp rate of 300 Torr/hr with a final setpoint of 50 Torr was used to obtain reproducible films. For the preparation of small-angle X-ray scattering (SAXS) samples,

a ramp rate of 50 Torr/hr with a setpoint of 300 Torr was used initially to remove water slowly to minimize kinetic effects. This was directly followed by exposure to full vacuum overnight to complete the drying process.

Sample characterization. UV-vis spectra were collected using a Cary 50 UV-vis spectrophotometer. A spectrophotometric measure of protein function is calculated as A_{586} of the sample relative to A_{586} of the as-synthesized conjugate, where both values are normalized by A_{280} to control for variations in protein concentration. At least 3 replicates were averaged for each sample. At the highest trehalose loading levels in this study, there is greater variation among sample replicates due to challenges in producing smooth films for spectroscopic analysis. Thermal stability measurements were conducted by measuring A_{586} as a function of temperature between 25 and 100 °C using a Peltier heater under a blanket of dry nitrogen with a temperature ramp rate of 1 °C/minute. A ramp rate of 3 °C/minute was also tested for a smaller subset of samples; both ramp rates gave identical results, confirming the absence of kinetic effects. The temperature at which the sample lost half of its initial absorption at 586 nm was taken as the apparent melting temperature.[63-64] Three replicates were averaged to produce the final results. Optical microscopy was performed on a Zeiss AxioSkop 2 MAT microscope.

SAXS and transmission electron microscopy (TEM) samples approximately 1 mm in thickness were cast on Kapton tape using 1 mm thick anodized aluminum washers as a mould. SAXS experiments were performed on beamlines X27C and X9 of the National Synchrotron Light Source (NSLS) at Brookhaven National Lab and beamline 12-ID-B of the Advanced Photon Source (APS) at Argonne National Lab. The data were corrected for empty cell and dark field scattering. Acquisition times were chosen such that the effect of beam damage on sample nanostructure was undetectable. Bulk samples containing no additives were cryo-microtomed to

a thickness of 60 nm using a Leica EM UC6 cryoultramicrotome operating at -110 °C and stained with ruthenium tetroxide vapors from a 0.5% aqueous solution for 20 minutes. Samples containing 20% trehalose were also microtomed at -110 °C, while samples containing 20% glycerol were microtomed at -80 °C. The same staining treatment was applied to all samples and acts on alcohol, amine and aromatic functional groups,[65] so regions containing protein and/or additive will appear darker in images. A JEOL 2011 transmission electron microscope was used to obtain bright field images using an accelerating voltage of 120 kV and a LaB_6 filament. Images were captured using a digital camera in a fixed bottom mount configuration.

5.4 Results and Discussion

Protein function. The presence of osmolytic additives within globular protein-polymer block copolymer nanostructures significantly increases the fraction of functional protein within the materials. Absorption is used to measure chromophore functionality of the fluorescent protein mCherry because it acts as an excellent indicator of proper protein fold and structure due to the high sensitivity of the chromophore to its local environment. When no additives are present, the films retain 49% and 63% of the original solution chromophore absorption for $f_{PNIPAM} = 0.40$ and 0.55, respectively. This is already a significant improvement over simple lyophilization of mCherry, which results in the loss of more than 80% of the chromophore.[12] By combining this data with the results from a previous study[13] (Figure C-3), it is evident that there exists a range of PNIPAM coil fractions between $f_{PNIPAM} = 0.40$ and 0.55 for which optimal protein functionality retention is observed due to the effect of the polymer alone.

The incorporation of glycerol or trehalose into the films significantly increases the fraction of protein retained in its functional form. Neither osmolyte alters the absorption

spectrum of the mCherry (Figure 5-1), which is nearly identical in shape to that of both films without additives and the as-synthesized conjugate. However, both osmolytes significantly increase the chromophore absorption peak at 586 nm. The darkest shaded bars in Figure 5-2 show the fraction of protein functionality retained after casting into the solid state. At $f_{PNIPAM} = 0.40$, an increase in functionality is seen with glycerol levels between 0 and 10 wt% (Figures 5-2a and C-4a). After reaching approximately 80% functionality retention with 10 wt% glycerol in the films, additional glycerol up to 50 wt% does not have a significant effect on protein function, which reaches a plateau between 80 and 85%. While the majority of the improvement due to glycerol is observed at relatively low concentration, trehalose shows more gradual improvement with increasing mass fraction to the same final plateau level as glycerol. For $f_{PNIPAM} = 0.40$, an increase in functionality retention is observed with increasing trehalose content up to approximately 30 wt% (Figures 5-2b and C-4a), where a plateau around 80% functionality retained is reached. For both glycerol and trehalose, the block copolymer with the higher polymer coil fraction retains the most functionality in the solid state as osmolyte is introduced. At $f_{PNIPAM} = 0.55$ with glycerol additive, a plateau is reached at nearly 100% retention of function after the addition of 10 wt% glycerol (Figures 5-2c and C-4c). With trehalose additive, an increase in functionality with increasing trehalose concentration is observed (Figures 5-2d and C-4c) until 100% of the protein functionality is preserved at a loading of 20 wt%.

A fraction of the protein's lost function is recovered upon rehydration, indicating that loss of protein chromophore absorbance for low additive loadings can be attributed partially to irreversible loss due to changes in protein secondary and tertiary structure and partially to reversible loss due to spectrally shifted chromophores or reversible changes in protein

structure.[12, 66] Measurements of A_{586} for the rehydrated conjugates (Figure 5-2 and C-4b,d) show that in the absence of osmolyte a significant fraction of the absorbance is recovered upon rehydration. Samples without osmolytes were able to recover an additional 20% and 24% of the as-synthesized protein functionality at f_{PNIPAM} = 0.40 and 0.55, respectively. The remaining 31 and 13% of the as-synthesized protein functionality is lost irreversibly upon dehydration. Although the material with a higher polymer coil fraction shows a greater improvement upon rehydration relative to the as-synthesized material, in both cases the improvement observed upon rehydration was equal to 50% of the protein functionality retained in the solid state.

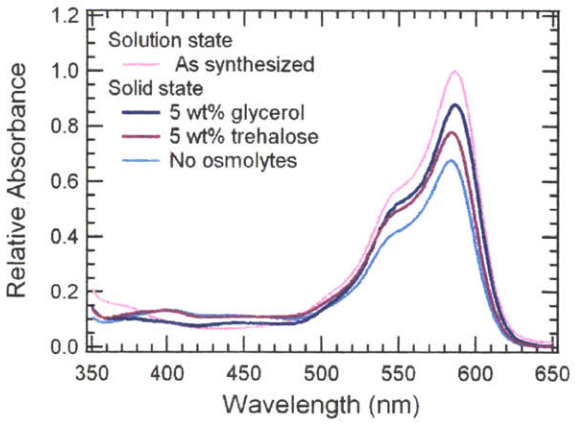

Figure 5-1. Absorption spectra of mCherry-PNIPAM26 both in solution and in the solid state demonstrate that glycerol and trehalose do not affect the characteristic shape of the mCherry absorption peak and that they improve the fraction of protein function retained in the solid state. All spectra have been normalized by total protein content using A_{280}.

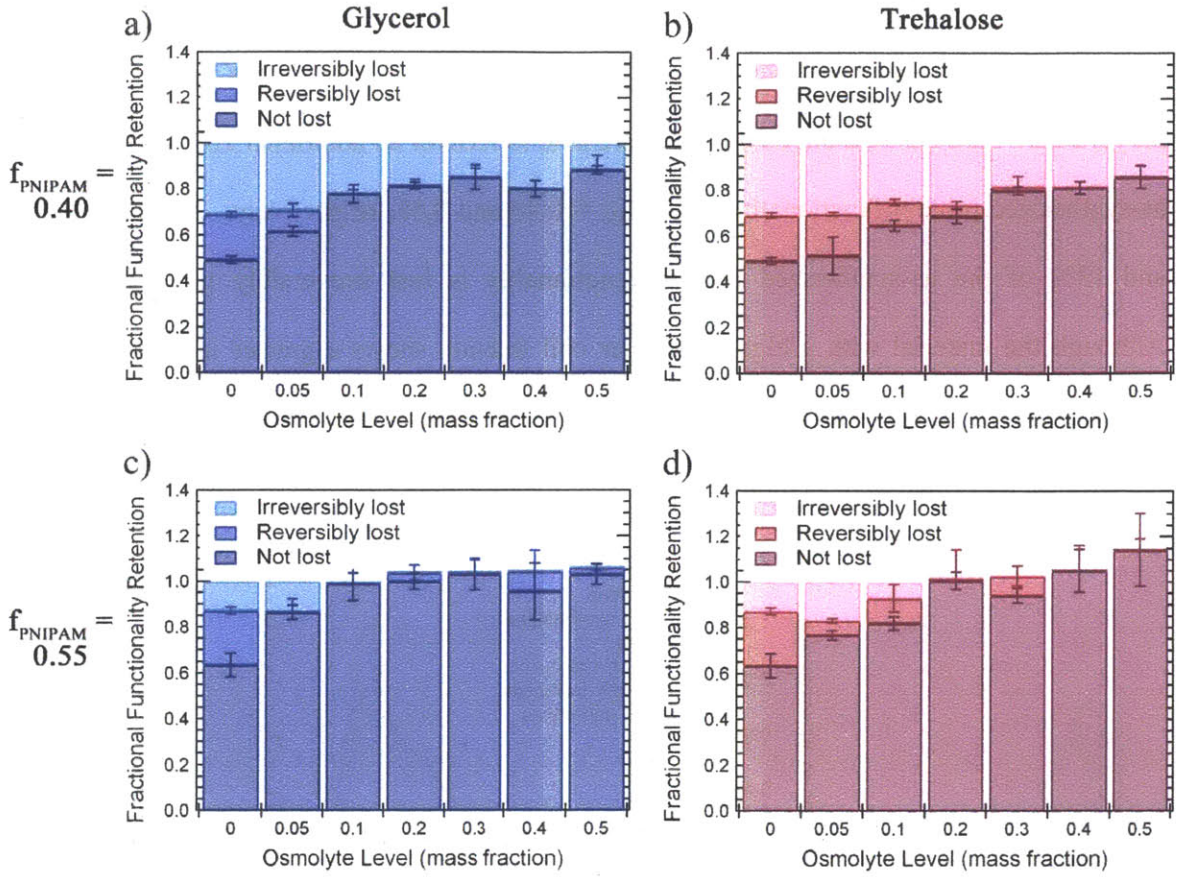

Figure 5-2. Retained protein functionality as a function of additive loading for f_{PNIPAM} = 0.40 with (a) glycerol or (b) trehalose and f_{PNIPAM} = 0.55 with (c) glycerol or (d) trehalose. Measurements of normalized UV-vis absorption peaks at 586 nm in the solid state (darkest shade) provide a direct measure of protein function in solid nanostructures. The difference in the peak absorbance at 586 nm between the rehydrated samples (medium shade) and solid state samples represents the portion of functional material which is reversibly lost upon dehydration. The remaining difference between the peak absorbance in the as-synthesized block copolymer (lightest shade) and the rehydrated samples corresponds to chromophore function which has been irreversibly lost during the self-assembly process. Error bars represent 95% confidence intervals.

After rehydration, there is no resolvable difference in functionality among samples containing either trehalose or glycerol. At $f_{PNIPAM} = 0.55$, there is only a minor increase in the rehydrated protein functionality with the incorporation of osmolytes at any level. However, at $f_{PNIPAM} = 0.40$, there is an increase of approximately 8-18% for osmolyte levels of 5 wt%, after which only a small increase is observed with increasing additive levels. For both $f_{PNIPAM} = 0.40$ and $f_{PNIPAM} = 0.55$, the plateau level reached in the rehydrated state is the same as that reached in the solid state, indicating that higher osmolyte levels completely eliminate the reversible loss of chromophore function in the solid state. In the case of $f_{PNIPAM} = 0.40$, the irreversible functionality loss is reduced but not eliminated by the osmolytes, while for $f_{PNIPAM} = 0.55$, the irreversible loss is completely removed.

Both trehalose and glycerol performed similarly with respect to protein functionality over the range of concentrations examined in this study, which suggests that they function through similar mechanisms. The low glass transition temperature of glycerol implies that the formation of a glassy matrix is not responsible for the preservation of functionality. Additionally, the additive levels in this study are not sufficient to form a complete encapsulating matrix around the proteins; experiments examining the stability of lyophilized proteins typically find that upwards of 70 wt% of an additive such as trehalose is needed to preserve more than half of the initial protein activity.[48] Combined with the fact that both additives have an effect similar to simple hydration with water in terms of eliminating the reversible loss of function when added at high concentration, this data suggests that hydrogen bond replacement by the osmolytes is most likely responsible for the observed improvement in functionality retention.

Protein thermostability. The ideal osmolyte would not only improve protein functionality, but also improve protein stability in the solid state. While many proteins operate best in natural

systems within a narrow physiological temperature range, practical devices often benefit from a wider window of operating conditions. To explore the effects of glycerol and trehalose on thermostability, temperature ramp assays for solid state materials with various levels of osmolytes are shown in Figure 5-3. When no osmolytes are present in the films, the apparent melting temperature of mCherry is 56 °C regardless of PNIPAM coil fraction. For the two different coil fractions studied, this indicates that although the polymer volume fraction has a large impact on protein functionality, it does not impact thermostability. The addition of 20 wt% glycerol drops the apparent melting temperature to around 40 °C, and a further increase in glycerol loading to 40 wt% results in only a small additional effect. In contrast to glycerol, trehalose incorporation results in an increase in the transition temperature to 70-75 °C. Similar increases in thermostability at both 20 wt% and 40 wt% trehalose indicate that above some moderate level of trehalose, additional amounts have a small impact on further improving the thermostability of protein in films.

The effect of the additives on improving thermostability is correlated to the glass transition of the additive molecules. Because glycerol is a fluid at the temperatures used in this study, it has a plasticizing effect on the protein and polymer, increasing molecular mobility that facilitates thermal denaturation. The enhanced thermostability of materials containing trehalose may be attributed to the relatively high glass transition temperature of trehalose (115 °C).[44] This reduces the molecular mobility of the protein, delaying protein unfolding to higher temperatures.

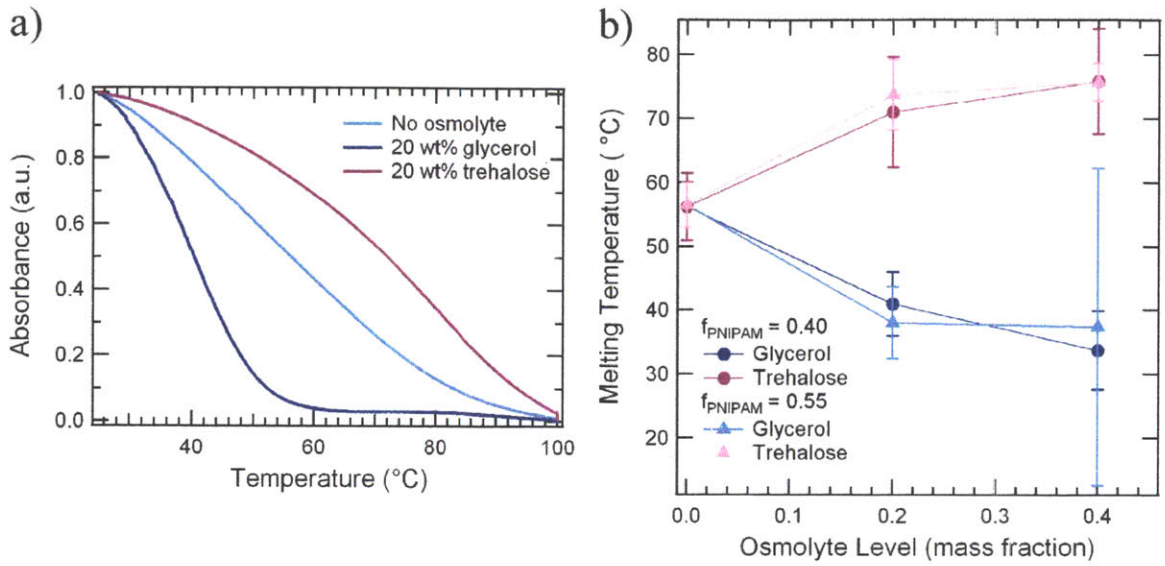

Figure 5-3. (a) Representative peak absorbance (A_{586}) curves during temperature ramping showing the different characteristic shapes obtained with glycerol and trehalose as additives. (b) The temperature at which half of the absorbance at 586 nm is lost is shown as a function of osmolyte level for f_{PNIPAM} = 0.40 and f_{PNIPAM} = 0.55. Trehalose is shown to increase thermostability, while glycerol decreases thermostability.

Effect of osmolytes on self-assembly. In addition to the effects on protein functionality and stability, increasing glycerol or trehalose content within self-assembled mCherry-PNIPAM block copolymers leads to changes in the nanostructured morphology and nanodomain size as observed by both SAXS and TEM. In the absence of any additives, mCherry-PNIPAM14 self-assembles into a cylindrical nanostructure morphology (Figure 5-4) with a domain spacing of 17.7 nm. Weak higher order peaks at $\sqrt{3}q^*$ and $2q^*$ suggest the formation of cylinders with poor long-range ordering. TEM confirms the cylindrical morphology, showing regions of both end-on and edge-on cylinders of polymer in a protein matrix (Figure 5-5a). mCherry-PNIPAM26 forms

hexagonally packed cylindrical nanodomains as well with a characteristic domain spacing of 23.1 nm. Although the higher order peaks expected at $\sqrt{3}q^*$ and $2q^*$ are broad and overlapping, TEM imaging clearly shows a cylindrical morphology for this block copolymer (Figure 5-5d).

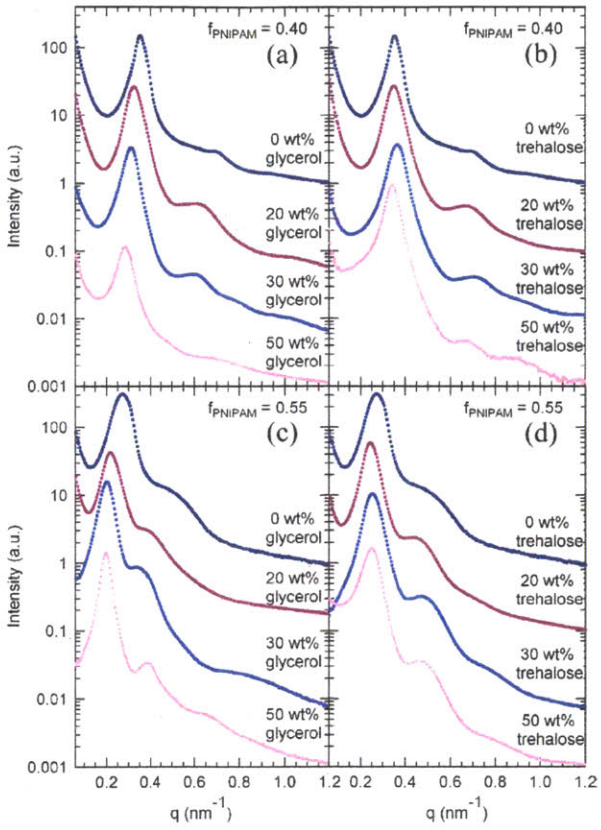

Figure 5-4. Small-angle X-ray scattering data for mCherry-PNIPAM block copolymers showing the effects of increasing levels of osmolyte on nanostructure for f_{PNIPAM} = 0.40 with (a) glycerol or (b) trehalose and f_{PNIPAM} = 0.55 with (c) glycerol or (d) trehalose. Traces have been offset for clarity.

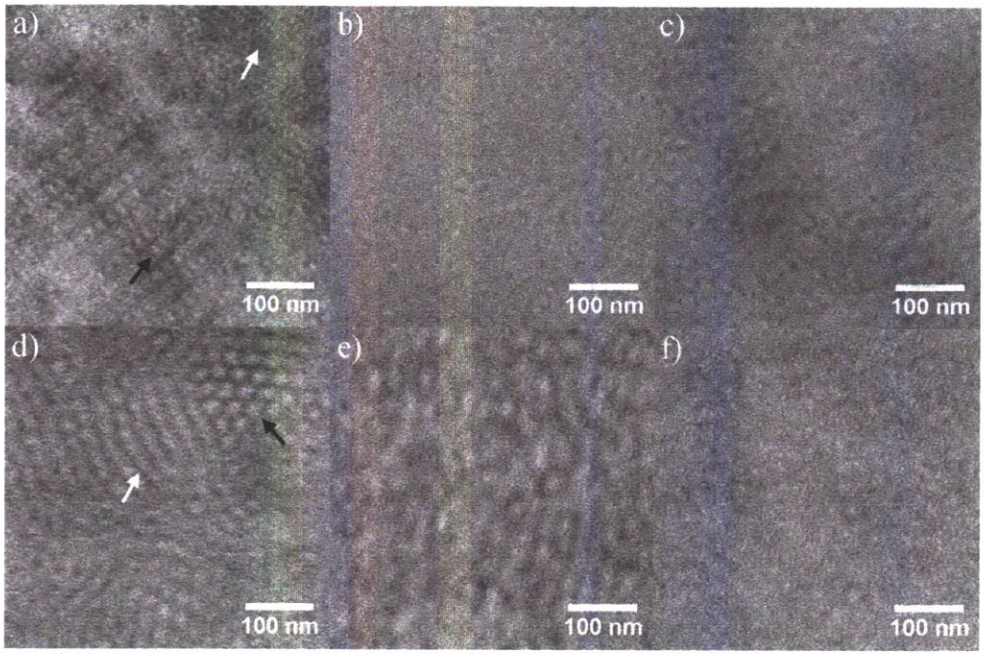

Figure 5-5. TEM images for as-cast mCherry-PNIPAM block copolymers. (a) Cylinders from neat block copolymer at f_{PNIPAM} = 0.40 oriented both perpendicular (black arrow) and parallel (white arrow) to the field of view. (b) f_{PNIPAM} = 0.40 with 20 wt% glycerol. (c) f_{PNIPAM} = 0.40 with 20 wt% trehalose. (d) Cylinders from neat block copolymer at f_{PNIPAM} = 0.55 oriented both perpendicular (black arrow) and parallel (white arrow) to the field of view. (e) f_{PNIPAM} = 0.55 with 20 wt% glycerol. (f) f_{PNIPAM} = 0.55 with 20 wt% trehalose.

With the addition of small amounts of glycerol, changes in the nanostructure morphology begin to appear. At f_{PNIPAM} = 0.40, the addition of 5 wt% glycerol produces a scattering pattern in which the higher q region still does not allow distinction between different morphologies. With 20 wt% glycerol, the primary peak broadens and the higher order peak also broadens but increases in intensity. The structure observed by TEM no longer shows signs of hexagonal packing and appears much more disordered than the neat block copolymer (Figure 5-5b). At

30 wt% glycerol, the second peak becomes less intense and small oscillations appear at higher q. Further increases in concentration result in a loss of higher order peak intensity, suggesting disordering of the block copolymer nanostructure with increasing glycerol concentration. Optical microscopy experiments reveal that glycerol does not macrophase separate from the mCherry-PNIPAM block copolymer, even at loadings up to 50 wt% (Figure C-6). Blending experiments on each individual block show that up to 40 wt% glycerol does not macrophase separate from mCherry, but that glycerol does macrophase separate from PNIPAM by 20 wt% loading (Figure C-7). This suggests that glycerol can be treated as a solvent that is somewhat selective for mCherry domains in this system. Therefore, at higher loadings the glycerol will preferentially segregate into the mCherry domains, resulting in swelling of these domains and the observed structural disordering at 30 wt% glycerol and above.

At f_{PNIPAM} = 0.55, better ordering is maintained with the addition of glycerol. The addition of up to 20 wt% glycerol results in swelling of the nanodomains without significant changes in the broad and overlapping higher order peaks. TEM of these structures at 20 wt% glycerol shows that the cylinder phase is more disordered and that the grain size is smaller (Figure 5-5e); however, the structure does not appear as disordered as in similar samples at f_{PNIPAM} = 0.40. At 30 and 40 wt% the scattering peaks narrow, creating a slight splitting between the $\sqrt{3}q^*$ and $2q^*$ peaks in the higher order region. Finally, by 50 wt% glycerol, higher order peaks are observed at $2q^*$ and $3q^*$, suggesting a transition to a lamellar phase.

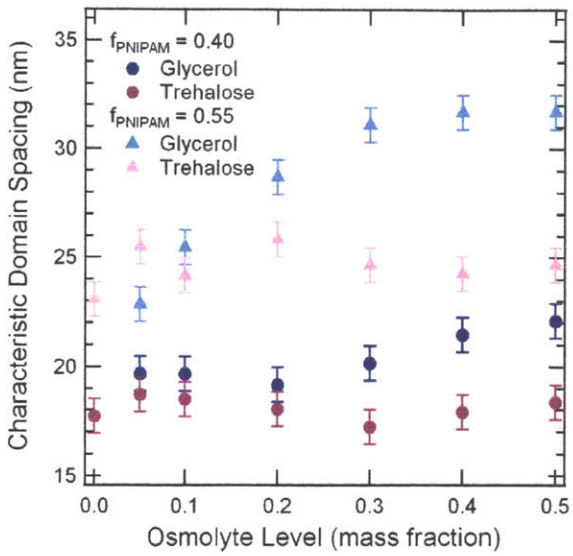

Figure 5-6. Characteristic domain spacing of nanostructures as determined by SAXS at $f_{PNIPAM} = 0.40$ and $f_{PNIPAM} = 0.55$ as a function of osmolyte loading level.

The addition of glycerol to mCherry-PNIPAM generally increases the characteristic domain spacing of the block copolymer. At $f_{PNIPAM} = 0.40$, the addition of 5 wt% glycerol results in a small increase in domain spacing to 19.7 nm (Figure 5-6). Between 5 and 30 wt% glycerol, the changes in the nanostructure symmetry are accompanied by a small decrease in domain spacing, and above 30 wt% glycerol, the domain spacing begins to increase as the block copolymer becomes more disordered. At $f_{PNIPAM} = 0.55$, between 5 and 30 wt% glycerol a large steady increase in domain spacing from 23.1 nm up to 31.7 nm is observed. However, between 30 and 50 wt% glycerol where the change in nanodomain structure is observed by SAXS, the domain spacing remains relatively constant. Several studies have found that the domain spacing increases with increasing solvent content when using a sufficiently selective solvent.[58, 60-61] This increase has been attributed to a decrease in the interfacial width between the domains in order to

minimize unfavorable interactions of one block with the solvent which leads to increased chain stretching normal to the interface for lamellar systems. While the general trend of increasing domain spacing with increasing glycerol content is consistent with these previous studies of traditional block copolymers, the rate at which the domain spacing increases does not follow expected scaling laws, suggesting that additional effects associated with the protein domain are important for phase behavior in this system.

The addition of trehalose to the conjugate with $f_{PNIPAM} = 0.40$ results in similar structural evolution as observed with increasing glycerol content. Between 5 and 30 wt% trehalose, SAXS patterns show a change in higher order peak shape and intensity, indicative of a gradual shift in morphology. At a 20 wt% trehalose loading, TEM images show a disordered structure similar to that observed in samples containing glycerol (Figure 5-5c). Optical microscopy experiments show that trehalose does not macrophase separate from the block copolymer at 20 wt% loading; however macrophase separation is observed by 40 wt% loading. Blend experiments show that trehalose macrophase separates from mCherry at 6 wt% and from PNIPAM at 4wt% loading. Importantly, wide-angle X-ray scattering experiments indicate that trehalose does not crystallize within the nanodomains or macrophase separated regions (Figure C-8). As the trehalose begins to macrophase separate from the block copolymer between 20 and 30 wt% trehalose, the higher order SAXS peaks experience a more dramatic decrease in intensity while the primary peak shows little change in intensity or width, suggesting poorer long-range ordering with the increasing trehalose content. The trend towards the disappearance of the higher order peaks continues up to 50 wt% trehalose.

Block copolymers with a polymer volume fraction of $f_{PNIPAM} = 0.55$ produce better ordered structures than those at $f_{PNIPAM} = 0.40$ upon the addition of trehalose. Samples

containing up to 10 wt% trehalose produce very similar SAXS patterns as samples without any additives. At a 20 wt% loading, an increase in intensity along with a change in peak symmetry of the higher order peak is observed, suggesting a transition in the nanostructure morphology. TEM shows a lack of hexagonal ordering and a more disordered structure than the neat block copolymer; however, the imaging contrast is much lower as well (Figure 5-5f).

The addition of trehalose to mCherry-PNIPAM block copolymers does not significantly increase the domain spacing of the block copolymer, likely because trehalose does not strongly prefer to localize within one domain of the block copolymer. At f_{PNIPAM} = 0.40 and low trehalose concentrations, a small decrease in domain spacing is observed, but as the trehalose loading increases and the block copolymer disorders the domain spacing increases slightly. In the case of f_{PNIPAM} = 0.55, added trehalose increases the domain spacing to approximately 25 nm for all loading levels examined. The smaller domains observed when using trehalose as compared with glycerol suggest more compact packing of chains within the nanodomains which is likely the result of macrophase separation of trehalose from the block copolymer.

5.5 Conclusions

mCherry-PNIPAM block copolymers with two different coil fractions were self-assembled in blends with glycerol or trehalose to enhance protein functionality in the solid state. The osmolytes improved functionality to a maximum of 100% and 80% of protein levels in solution for PNIPAM coil fractions f_{PNIPAM} = 0.55 and 0.40, respectively. Glycerol reached this maximum level at lower osmolyte fractions than trehalose, and the similar performance of both additives suggests that the mechanism by which they improve protein functionality is the replacement of hydrogen bonds lost during water evaporation. Although both osmolytes

produced similar results with respect to functionality retention, glycerol resulted in a 15-20 °C decrease in thermal stability while trehalose was able to increase the thermal stability of the protein by roughly the same amount. The high glass transition temperature of trehalose is able to suppress thermal motions in the protein, while the plasticizing effect of glycerol promotes thermal motions leading to functionality loss.

In the absence of any osmolyte, both block copolymers formed cylindrical nanostructures, and the presence of osmolytes resulted in a gradual disordering of the nanostructures. Added glycerol was observed to be somewhat selective for the mCherry domains and led to swelling of the nanodomains. At $f_{PNIPAM} = 0.40$, this resulted in disordering, while at $f_{PNIPAM} = 0.55$, a transition in nanostructure morphology from cylinders to lamellae was observed. Trehalose, on the other hand, was not very soluble in either the protein or the polymer domains, and as a result did not significantly alter the domain spacing. With increasing trehalose levels, rapid disordering was again seen at $f_{PNIPAM} = 0.40$, and at $f_{PNIPAM} = 0.55$ some disordering was observed to accompany a change in nanostructure symmetry.

5.6 Acknowledgements

This research was supported by the Department of Energy Office of Basic Energy Sciences (award number DE-SC0007106) and by the Air Force Office of Scientific Research (award number FA9550-12-0259). X-ray scattering experiments were performed at Beamline X27C and X9 at the National Synchrotron Light Source at Brookhaven National Laboratory and at Beamline 12-ID-B at the Advanced Photon Source at Argonne National Laboratory. Cryoultramicrotome and optical microscopy experiments were performed at the MIT Institute for Soldier Nanotechnologies and TEM experiments were performed at the MIT Center for

Materials Science and Engineering. We also thank Lixia Rong, Lin Yang, and Xiaobing Zuo for experimental assistance with SAXS and Karen Gleason for use of the FTIR.

5.7 References

1. I. Willner and E. Katz, *Angew. Chem., Int. Ed.*, 2000, **39**, 1180-1218.
2. T. Reda, C. M. Plugge, N. J. Abram and J. Hirst, *Proc. Natl. Acad. Sci. U. S. A.*, 2008, **105**, 10654-10658.
3. R. Das, P. J. Kiley, M. Segal, J. Norville, A. A. Yu, L. Y. Wang, S. A. Trammell, L. E. Reddick, R. Kumar, F. Stellacci, N. Lebedev, J. Schnur, B. D. Bruce, S. G. Zhang and M. Baldo, *Nano Lett.*, 2004, **4**, 1079-1083.
4. J. Ge, D. N. Lu, Z. X. Liu and Z. Liu, *Biochem. Eng. J.*, 2009, **44**, 53-59.
5. J. Kalia and R. T. Raines, *Curr. Org. Chem.*, 2010, **14**, 138-147.
6. Y. Wang, A. S. Angelatos and F. Caruso, *Chem. Mater.*, 2008, **20**, 848-858.
7. Y. Kumashiro, Y. Ikezoe, K. Tamada and M. Hara, *J. Phys. Chem. B*, 2008, **112**, 8291-8297.
8. D. C. Kim, J. I. Sohn, D. J. Zhou, T. A. J. Duke and D. J. Kang, *ACS Nano*, 2010, **4**, 1580-1586.
9. A. J. Patil and S. Mann, *J. Mater. Chem.*, 2008, **18**, 4605-4615.
10. M. Vinoba, K. S. Lim, S. H. Lee, S. K. Jeong and M. Alagar, *Langmuir*, 2011, **27**, 6227-6234.
11. B. Kim, C. N. Lam and B. D. Olsen, *Macromolecules*, 2012, **45**, 4572-4580.
12. C. S. Thomas, M. J. Glassman and B. D. Olsen, *ACS Nano*, 2011, **5**, 5697-5707.
13. C. S. Thomas, L. Xu and B. D. Olsen, *Biomacromolecules*, 2012, **13**, 2781-2792.
14. C. N. Lam and B. D. Olsen, *Soft Matter*, 2013, **9**, 2393-2402.
15. O. D. Krishna and K. L. Kiick, *Pept. Sci.*, 2010, **94**, 32-48.
16. I. C. Reynhout, J. L. M. Cornelissen and R. J. M. Nolte, *Acc. Chem. Res.*, 2009, **42**, 681-692.
17. N. C. Mougin, P. van Rijn, H. Park, A. H. E. Müller and A. Böker, *Adv. Funct. Mater.*, 2011, **21**, 2470-2476.
18. M. Li, P. De, H. Li and B. S. Sumerlin, *Polym. Chem.*, 2010, **1**, 854-859.
19. K. L. Heredia and H. D. Maynard, *Org. Biomol. Chem.*, 2007, **5**, 45-53.
20. J. C. M. van Hest, *Polym. Rev.*, 2007, **47**, 63-92.
21. J. Nicolas, G. Mantovani and D. M. Haddleton, *Macromol. Rapid Commun.*, 2007, **28**, 1083-1111.
22. B. Le Droumaguet and J. Nicolas, *Polym. Chem.*, 2010, **1**, 563-598.
23. H. A. Klok, *J. Polym. Sci., Part A: Polym. Chem.*, 2005, **43**, 1-17.
24. R. J. Mancini, J. Lee and H. D. Maynard, *J. Am. Chem. Soc.*, 2012, **134**, 8474-8479.
25. T. H. Nguyen, S. H. Kim, C. G. Decker, D. Y. Wong, J. A. Loo and H. D. Maynard, *Nat. Chem.*, 2013, **5**, 221-227.
26. P. van Rijn and A. Böker, *J. Mater. Chem.*, 2011, **21**, 16735-16747.
27. A. W. Perriman, A. P. S. Brogan, H. Cölfen, N. Tsoureas, G. R. Owen and S. Mann, *Nat. Chem.*, 2010, **2**, 622-626.

28. R. C. Rodrigues, A. Berenguer-Murcia and R. Fernandez-Lafuente, *Adv. Synth. Catal.*, 2011, **353**, 2216-2238.
29. A. E. Nel, L. Mädler, D. Velegol, T. Xia, E. M. V. Hoek, P. Somasundaran, F. Klaessig, V. Castranova and M. Thompson, *Nat. Mater.*, 2009, **8**, 543-557.
30. C. Ó'Fágáin, *Enzyme Microb. Technol.*, 2003, **33**, 137-149.
31. K. M. Polizzi, A. S. Bommarius, J. M. Broering and J. F. Chaparro-Riggers, *Curr. Opin. Chem. Biol.*, 2007, **11**, 220-225.
32. F. H. Arnold, P. L. Wintrode, K. Miyazaki and A. Gershenson, *Trends Biochem.Sci.*, 2001, **26**, 100-106.
33. M. C. Manning, K. Patel and R. T. Borchardt, *Pharm. Res.*, 1989, **6**, 903-918.
34. A. K. Shakya, H. Sami, A. Srivastava and A. Kumar, *Prog. Polym. Sci.*, 2010, **35**, 459-486.
35. P. B. Dennis, A. Y. Walker, M. B. Dickerson, D. L. Kaplan and R. R. Naik, *Biomacromolecules*, 2012, **13**, 2037-2045.
36. G. Luo, Q. Zhang, A. R. D. Castillo, V. Urban and H. O'Neill, *ACS Appl. Mater. Interfaces*, 2009, **1**, 2262-2268.
37. N. A. Mohidem and H. Bin Mat, *J. Sol-Gel Sci. Technol.*, 2012, **61**, 96-103.
38. G. F. Drevon, K. Danielmeier, W. Federspiel, D. B. Stolz, D. A. Wicks, P. C. Yu and A. J. Russell, *Biotechnol. Bioeng.*, 2002, **79**, 785-794.
39. N. K. Jain and I. Roy, *Curr. Protoc. Protein Sci.*, 2010, **59**, 4.9.1-4.9.12.
40. T. J. Kamerzell, R. Esfandiary, S. B. Joshi, C. R. Middaugh and D. B. Volkin, *Adv. Drug Deliv. Rev.*, 2011, **63**, 1118-1159.
41. H. Hamada, T. Arakawa and K. Shiraki, *Curr. Pharm. Biotechnol.*, 2009, **10**, 400-407.
42. M. M. Andersson, J. D. Breccia and R. Hatti-Kaul, *Biotechnol. Appl. Biochem.*, 2000, **32**, 145-153.
43. A. O. Triantafyllou, E. Wehtje, P. Adlercreutz and B. Mattiasson, *Biotechnol. Bioeng.*, 1997, **54**, 67-76.
44. D. P. Miller, J. J. de Pablo and H. Corti, *Pharm. Res.*, 1997, **14**, 578-590.
45. J. K. Kaushik and R. Bhat, *J. Biol. Chem.*, 2003, **278**, 26458-26465.
46. J. H. Crowe, L. M. Crowe, J. F. Carpenter and C. A. Wistrom, *Biochem. J.*, 1987, **242**, 1-10.
47. S. Damodaran, *Langmuir*, 2012, **28**, 9475-9486.
48. E. C. López-Díez and S. Bone, *Biochim. Biophys. Acta*, 2004, **1673**, 139-148.
49. S. Rasouli, S. Hosseinkhani, P. Yaghmaei and A. Ebrahim-Habibi, *Appl. Biochem. Biotechnol.*, 2011, **165**, 572-582.
50. K. Gekko and S. N. Timasheff, *Biochemistry-Us*, 1981, **20**, 4667-4676.
51. D. Averett, M. T. Cicerone, J. F. Douglas and J. J. de Pablo, *Soft Matter*, 2012, **8**, 4936-4945.
52. M. T. Cicerone and J. F. Douglas, *Soft Matter*, 2012, **8**, 2983-2991.
53. M. P. Stoykovich, M. Müller, S. O. Kim, H. H. Solak, E. W. Edwards, J. J. de Pablo and P. F. Nealey, *Science*, 2005, **308**, 1442-1446.
54. T. Hashimoto, H. Tanaka and H. Hasegawa, *Macromolecules*, 1990, **23**, 4378-4386.
55. W. H. Binder and R. Zirbs, *Adv. Polym. Sci.*, 2007, **207**, 1-78.
56. H. A. Klok and S. Lecommandoux, *Adv. Mater.*, 2001, **13**, 1217-1229.
57. J. Ruokolainen, M. Saariaho, O. Ikkala, G. ten Brinke, E. L. Thomas, M. Torkkeli and R. Serimaa, *Macromolecules*, 1999, **32**, 1152-1158.

58. P. Alexandridis, D. Zhou and A. Khan, *Langmuir*, 1996, **12**, 2690-2700.
59. T. Hashimoto, M. Shibayama and H. Kawai, *Macromolecules*, 1983, **16**, 1093-1101.
60. T. P. Lodge, B. Pudil and K. J. Hanley, *Macromolecules*, 2002, **35**, 4707-4717.
61. K. J. Hanley, T. P. Lodge and C. I. Huang, *Macromolecules*, 2000, **33**, 5918-5931.
62. C. Lai, Y. L. Loo, R. A. Register and D. H. Adamson, *Macromolecules*, 2005, **38**, 7098-7104.
63. N. Poklar, G. Vesnaver and S. Lapanje, *Biophys. Chem.*, 1993, **47**, 143-151.
64. S. H. Bokman and W. W. Ward, *Biochem. Biophys. Res. Commun.*, 1981, **101**, 1372-1380.
65. L. C. Sawyer, D. T. Grubb and G. F. Meyers, *Polymer Microscopy*, Springer, New York, 2008.
66. S. Enoki, K. Saeki, K. Maki and K. Kuwajima, *Biochemistry*, 2004, **43**, 14238-14248.

Chapter 6 Coil Fraction-Dependent Phase Behavior of a Model Globular Protein-Polymer Diblock Copolymer

Soft Matter, to be submitted for publication - Reproduced by permission of The Royal Society of Chemistry.

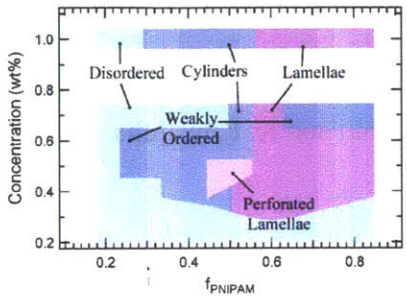

6.1 Abstract

The self-assembly of the model globular protein-polymer block copolymer mCherry-*b*-poly(N-isopropyl acrylamide) is explored across a range of polymer coil fractions from 0.21 to 0.82 to produce a phase diagram for these materials as a function of molecular composition. Overall, four types of morphologies were observed: hexagonally packed cylinders, perforated lamellae, lamellae, and disordered nanostructures. Across all coil fractions and morphologies, a lyotropic re-entrant order-disorder transition in water was observed, with disordered structures below 30 wt% and above 70 wt% and well-ordered morphologies at intermediate concentrations. Solid state samples prepared by solvent evaporation show moderately ordered structures similar to those observed in 60 wt% solutions, suggesting that bulk structures result from kinetic trapping of morphologies which appear at lower concentrations. While highly ordered cylindrical nanostructures are observed around a bioconjugate polymer volume fraction of 0.3 and well-ordered lamellae are seen near a volume fraction of 0.6, materials at lower or higher coil fractions become increasingly disordered. Notable differences between the phase behavior of globular protein-polymer block copolymers and coil-coil diblock copolymers include the lack

of spherical nanostructures at either high or low polymer coil fractions as well as shifted phase boundaries between morphologies which result in an asymmetric phase diagram.

6.2 Introduction

The self-assembly of protein-polymer block copolymers is an attractive, bottom-up approach that enables the nanopatterning of proteins which may further increase the efficiency of a variety of biocatalytic and bioelectronic materials.[1-3] The use of enzymes in the fabrication of such devices is alluring due to their large catalytic efficiencies, high turnover rates, and the wide variety of possible reactions that can be catalyzed. Improved enzyme performance in devices can be attained through nanopatterning, resulting in higher loading densities, proper enzyme orientation for easy access to the active site, and efficient transport of substrates and products.[4-6] Block copolymer self-assembly has been used extensively as a template for nanopatterning a variety of materials, including proteins.[7-10] Direct self-assembly of block copolymers containing a protein of interest could simplify the fabrication of functional materials by eliminating the need for pattern transfer processing steps after self-assembly and increasing the loading levels of the material of interest.

A number of studies have investigated the self-assembly of globular protein-polymer block copolymers, often as amphiphilic molecules in solution. Several researchers have developed novel synthetic approaches to create monodisperse conjugates with well-defined molecular architecture in high yields.[11-14] In dilute solution, these materials self-assemble into a variety of nanostructures including micelles, vesicles and toroids.[15-18] Protein-polymer hybrid materials made from ionic complexes between proteins and polymers[19] or by encapsulation of a protein in a block copolymer[20] have also been processed into bulk nanomaterials in which the

protein secondary structure is preserved and significant levels of protein function remain even in a solvent-free environment.

While the self-assembly of traditional coil-coil block copolymers both in the bulk and in solution is well-understood, it is not clear how the globular shape and specific interactions between amino acids on the protein surface will alter the physics of self-assembly. In ideal coil-coil block copolymer systems, only the relative volume fraction of one block (f_A) and the Flory-Huggins interaction parameter between the two blocks (χN) are needed to fully define the system.[21-23] Molecular asymmetry, such as is observed in rod-coil,[24] disk-coil,[25] and dendrimer-coil[26-27] block copolymers, results in significant changes to the phase diagram, including shifted phase boundaries as well as morphologies unique to the new molecular geometries. In addition to introducing more complex chain topologies, the incorporation of proteins introduces specific ionic and hydrophobic interactions which are not necessarily arranged in a regular repeating pattern. These effects are also expected to contribute to deviations from classic block copolymer behavior.

Another dimension of complexity arises upon the addition of solvent to a block copolymer system. Solvent-based processing is a necessary condition for the self-assembly of globular protein-polymer conjugates which generally do not have an accessible melt state due to thermal denaturation of protein secondary and tertiary structure at high temperatures. Incompatibility with traditional melt processing techniques highlights the need for a clear understanding of the solution behavior of protein-based materials. In coil-coil block copolymers, depending upon the relative selectivity of the solvent for each block, a variety of order-order transitions (OOTs) can be observed with changing concentrations in solution due to preferential segregation of the solvent.[28-36] Because temperature often changes the interaction strength

between the solvent and the block copolymer, OOTs are also observed with changes in temperature.[29-30, 33] In some systems at select concentrations near lyotropic order-disorder transitions (ODTs), a re-entrant thermotropic ODT can be observed with well-ordered nanostructures flanked by disordered structures at higher and lower temperatures.[29] In Pluronic/water systems, several re-entrant ODTs are also observed with increasing polymer concentrations.[33, 37]

Our previous work with a model globular protein-polymer block copolymer, mCherry-b-poly(N-isopropyl acrylamide) (mCherry-PNIPAM), clearly demonstrated the dependence of bulk morphology on solution processing steps utilized to create solid state samples, and showed that up to 70% of the protein remained in its active form even after processing into solid samples.[38-39] A subsequent study investigated the nanostructured morphology of a small set of representative block copolymers as a function of temperature and concentration in water.[40] This study discovered the presence of a concentration-dependent ODT for mCherry-PNIPAM block copolymers that is typically located between 30 and 40 wt%. OOTs were also observed with increasing temperature, primarily due to the dramatic change in solvent quality for PNIPAM at temperatures above its thermoresponsive transition. At 40 and 50 wt%, nanostructures with good long-range ordering were observed; however, bulk samples with a similar coil fraction unexpectedly showed reduced ordering such that it became difficult to distinguish between different morphologies based solely on scattering data.

Here, the coil fraction and concentration dependence of the mCherry-PNIPAM phase diagram is examined in detail, exposing the origins of the loss of order in solid state materials and highlighting key differences between coil-coil and protein-polymer self-assembly. The phase behavior of mCherry-PNIPAM is studied at concentrations up to 70 wt%, illustrating a re-

entrant order-disorder transition that leads to kinetic trapping of poorly ordered structures in the solid state. The dependence of domain spacing on polymer composition is explored, revealing little dependence on concentration as well as different scaling regimes with respect to polymer molecular weight at high and low polymer volume fractions.

6.3 Experimental Methods

Synthesis. Radical addition-fragmentation chain transfer (RAFT) polymerization was used to synthesize maleimide-end functionalized PNIPAM with low polydispersity as described previously.[39] Gel permeation chromatography (GPC) using an Agilent 1260 Infinity HPLC with N,N-dimethylformamide (DMF) as the mobile phase was used to obtain polymer molecular weights and polydispersities. Both a refractive index detector and a Wyatt Mini-Dawn 3-angle static light scattering detector were employed to enable absolute molecular weight determination. Protein expression, purification, and bioconjugation were performed as previously described.[39] The materials used in this study are summarized in Table 6-1.

Table 6-1. mCherry-PNIPAM block copolymers

Block Copolymer	PNIPAM M_n (kg/mol)	PDI_{PNIPAM}	Conjugate M_n (kg/mol)	f_{PNIPAM}	Final Purity* (%)
mCherry-PNIPAM6	5.7	1.16	33.9	0.21	92
mCherry-PNIPAM8	7.5	1.05	35.6	0.26	98
mCherry-PNIPAM10	9.8	1.09	37.9	0.31	98
mCherry-PNIPAM13	12.5	1.10	40.7	0.36	98
mCherry-PNIPAM17	16.6	1.13	44.7	0.43	95
mCherry-PNIPAM19	18.9	1.10	47.0	0.46	97
mCherry-PNIPAM24	24.4	1.07	52.6	0.53	91
mCherry-PNIPAM32	32.0	1.08	60.2	0.59	92
mCherry-PNIPAM44	44.5	1.09	72.6	0.67	93
mCherry-PNIPAM67	66.6	1.07	94.7	0.75	92
mCherry-PNIPAM97	97.3	1.13	125.5	0.82	93

*As determined by native protein gel electrophoresis

Sample preparation. Conjugate solutions, dialyzed into nanopure water, were concentrated to ~100 mg/mL using Millipore Ultra-15 centrifugal filters with a molecular weight cutoff of 10 kDa. Solution small-angle X-ray scattering (SAXS) samples were prepared by rehydrating small pellets (1-2 mg) of dried bioconjugate with nanopure water to the desired concentration, followed by equilibration for several days at 4 °C. Water evaporation for bulk samples was performed at room temperature, and the solvent evaporation rate was controlled using a vacuum controller. All SAXS and TEM samples were prepared using the following protocol, unless noted otherwise. The ~100 mg/mL conjugate solutions were subjected to a vacuum ramp rate of 50 Torr/hr with a setpoint of 300 Torr to initially remove water slowly. This was directly followed by exposure to full vacuum overnight to complete the drying process. A handful of experiments were conducted in which the effect of the evaporation conditions was tested. In one instance, the slow evaporation protocol detailed above was performed with the vacuum chamber

thermostated at 4 °C. In another set of experiments, a faster ramp rate was achieved at room temperature by immediately pulling full vacuum to encourage more rapid water evaporation. A final set of experiments began with hydrated solution samples at 40 or 50 wt% which were subjected to full vacuum to prepare bulk samples.

Sample characterization. Bulk SAXS and transmission electron microscopy (TEM) samples approximately 1 mm in thickness were cast on Kapton tape using 1 mm thick anodized aluminum washers as a mould. Solution SAXS samples were loaded into 1 mm thick washers and sealed with Kapton tape. SAXS experiments were performed on beamline X27C of the National Synchrotron Light Source (NSLS) at Brookhaven National Laboratory and on beamline 12-ID-B of the Advanced Photon Source at Argonne National Laboratory. The data were corrected for empty cell and dark field scattering. Acquisition times were chosen such that the effect of beam damage on sample nanostructure was undetectable. Hydrated samples were equilibrated at each temperature for 10 minutes prior to data acquisition. Bulk samples were cryo-microtomed using a Leica EM UC6 at -110 °C to a thickness of 60 nm, and stained with ruthenium tetroxide vapors from a 0.5 % aqueous solution for 20 minutes. A JEOL 2011 transmission electron microscope was used to obtain bright field images using an accelerating voltage of 120 kV and a LaB_6 filament.

6.4 Results and Discussion

Re-entrant order-disorder transition behavior. mCherry-PNIPAM conjugates investigated at concentrations between 40 and 70 wt% reveal the presence of a re-entrant lyotropic order-disorder transition as evidenced by SAXS (Figure 6-1, Figure D-3). With increasing concentration, the structures first become ordered, typically at concentrations between 30 and

40 wt% as previously established.[40] Increasing the concentration further up to 70 wt% leads to disordering of the nanostructured morphology, as evidenced by the disappearance of higher order peaks and a broadening of the primary peak. In most mCherry-PNIPAM block copolymer samples, highly ordered nanostructures are observed only at 40 and 50 wt%. SAXS patterns of these samples are characterized by narrow primary peaks with clearly defined higher order peaks. Cylinder-forming block copolymers show distinct peaks at $\sqrt{3}q^*$ and $2q^*$ (Figure 6-1b), while lamellae-forming block copolymers present a clear peak at $2q^*$ (Figure 6-1c) which is sometimes accompanied by the next expected higher order peak at $3q^*$. Regardless of nanostructure, samples at 60 wt% begin to show signs of disordering as the primary peak and higher order peaks start to broaden. In the case of cylindrical nanostructures, the peaks at $\sqrt{3}q^*$ and $2q^*$ overlap and are no longer clearly distinguishable. The scattering pattern in the q-range where higher order peaks are found is broader and flatter for a cylinder-forming block copolymer than for one which forms lamellae. By a concentration of 70 wt%, almost all ordering is lost and a scattering pattern similar to that of disordered polymer melts is observed.[41] In addition to the lack of higher order peaks at this concentration, the primary peak becomes very broad and shifts towards lower q-values. At moderate to high polymer volume fractions (f_{PNIPAM} = 0.53-0.82, Figure D-3), significant but incomplete disordering is observed at 70 wt%. In these cases, there are still signs of weak higher order peaks, and it is hypothesized that complete disordering would be observed at slightly higher concentrations. However, studies at even higher concentrations are impeded by very long equilibration times for homogeneous dispersion of water within these solid-like samples.

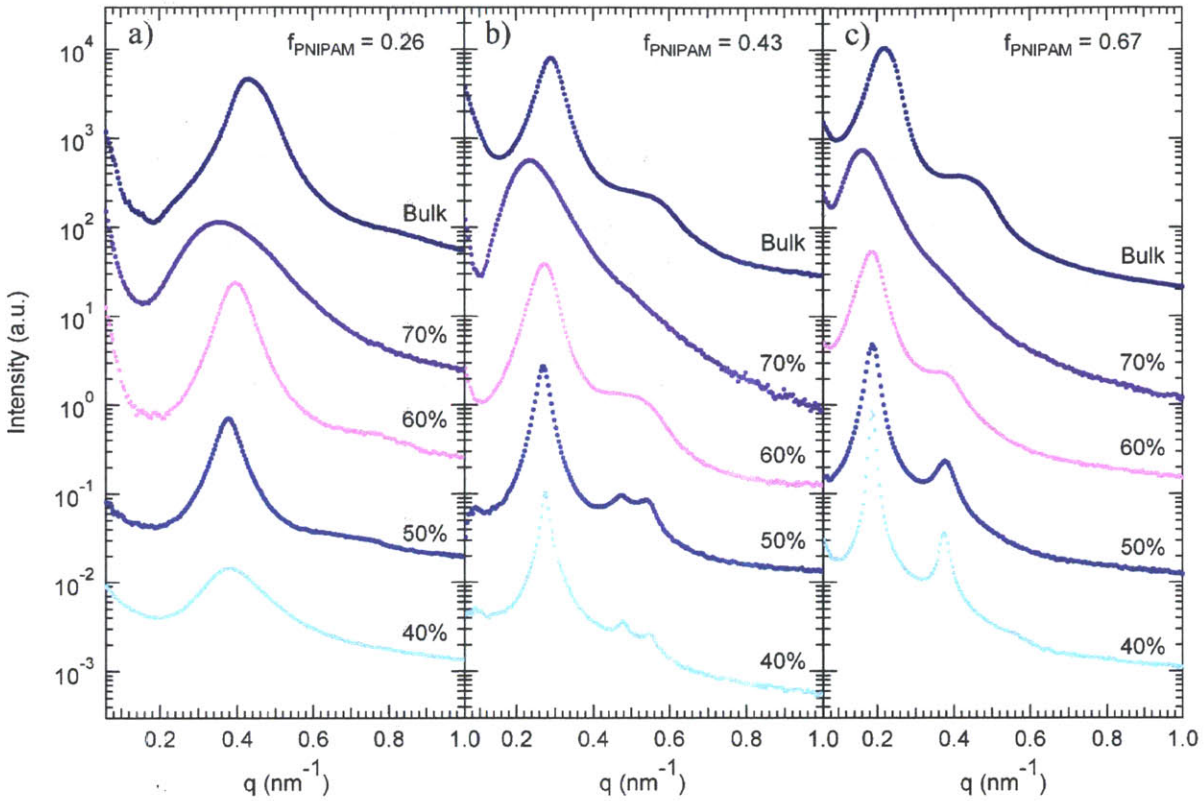

Figure 6-1. Representative small-angle X-ray scattering patterns for mCherry-PNIPAM block copolymers at 25 °C which span the range of observed morphologies. (a) Disordered and weakly ordered nanostructures are formed at f_{PNIPAM} = 0.26. (b) Cylindrical nanostructures are observed at f_{PNIPAM} = 0.43. (c) Lamellar domains formed at f_{PNIPAM} = 0.67. Well-ordered nanostructures are generally observed in aqueous block copolymer solutions prepared at 40 and 50 wt%. Moderately well-ordered structures are seen at 60 wt% and in bulk samples, and highly disordered samples are produced in 70 wt% solutions. Traces have been vertically offset for clarity.

Surprisingly, given the observed disordering at high block copolymer concentrations, these materials are observed to form relatively well-ordered nanostructures in the bulk. The

scattering patterns of bulk samples resemble those observed at 60 wt%, with broadened primary peaks and higher order peaks which often overlap. This suggests that the structures observed in solid state samples became kinetically trapped near 60 wt% concentration during solvent evaporation, similar to the 56% protein concentration in the mCherry protein crystal structure[42] (although there is no sign of protein crystallization in any of the materials[38]). As the water content drops below this level, the protein should lose mobility which would prevent further block copolymer rearrangement in self-assembled nanostructures.

Although block copolymers with small PNIPAM volume fractions do not form highly ordered nanostructures at any concentration investigated, they still experience a window of increased repulsive interactions reflective of the lyotropic re-entrant ODT observed in materials at higher polymer fractions. At the lowest investigated coil fraction ($f_{PNIPAM} = 0.21$), no signs of ordering were observed at any of the tested concentrations. As the polymer content is increased up to $f_{PNIPAM} = 0.26$ (Figure 6-1a), SAXS patterns consistent with very weakly ordered nanostructures are observed at 50 and 60 wt% with a faint and broad higher order peak. This block copolymer composition is very close to the ODT as a function of PNIPAM volume fraction. Even in these two low molecular weight samples which show little or no ordering, the primary peak still becomes significantly more broad at 70 wt% than at 50 wt%. According to the random phase approximation for coil-coil block copolymer self-assembly, the correlation peak for nearest neighbors intensifies and narrows as the repulsive interaction strength between blocks (χ parameter) increases.[43] The same trend has also been shown in different block copolymer geometries such as rod-coil block copolymers.[44] This indicates that the effective solvent-mediated interaction parameter must increase between 40 and 50 wt% and then decrease between 60 and 70 wt% as the primary scattering peak narrows and then increases.

The re-entrant lyotropic ODT observed in this system is unlike typical behavior of coil-coil block copolymers in a solvent. Usually, below some concentration, the block copolymer is disordered in solution. As the concentration is increased, the order monotonically increases.[45-46] In the case of a poly(ethylene oxide)-b-poly(propylene oxide)-b-poly(ethylene oxide) (PEO-b-PPO-b-PEO) triblock copolymer in water, several lyotropic re-entrant ODTs are observed.[33, 37] In one instance, the morphology evolved from isotropic to hexagonal to isotropic to lamellar and finally back to isotropic with increasing concentration.[33] In these low molecular weight systems (~2900-3700 g/mol), ordered phases can be observed up until 80 or 90 wt%, and an isotropic phase is observed at all higher concentrations due to a decrease in the repulsive interaction in the absence of sufficient solvent.[33, 37] A thermotropic re-entrant ODT is observed in a 20 vol% solution of polystyrene-b-polyisoprene (PS-b-PI) in a selective solvent with disordered micellar nanostructures followed by a spherical morphology and then disordered material with increasing temperature.[29-30] In this coil-coil system, the thermotropic transition to an ordered phase is believed to be driven by micelle core swelling as the solvent becomes less selective with increasing temperature. Whereas in the mCherry-PNIPAM/water system, the re-entrant ODT is observed at all block copolymer compositions (Figure 6-2), in the PS-b-PI system, a re-entrant thermotropic ODT has only been observed within a narrow compositional window near the lyotropic ODT between micelles and spherical nanostructures.

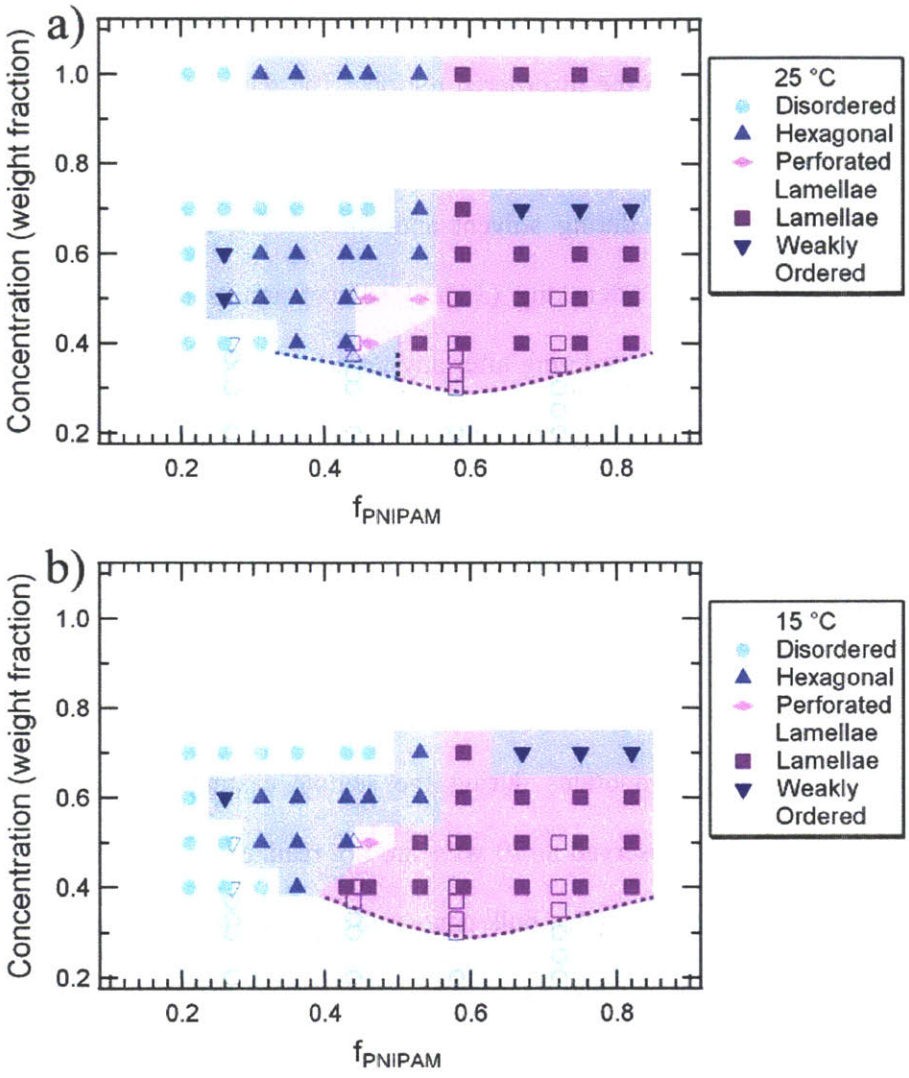

Figure 6-2. Phase diagrams for the self-assembly of mCherry-PNIPAM block copolymers as a function of polymer coil fraction and concentration at (a) 25 °C and (b) 15 °C. Open symbols represent previously published data obtained from similar mCherry-PNIPAM block copolymers[40] and show good agreement with the data collected in this study.

The observation of re-entrant ODTs across a wide range of block copolymer compositions explains why solvent annealing is of limited effectiveness for improving order in

mCherry-PNIPAM. The amount of solvent required to increase mobility of the polymer chains swells the nanostructure into the disordered region. The data from 70 wt% solutions suggests that prolonged solvent annealing should result in disordered equilibrium structures if water uptake is less than 30-40% during solvent annealing. This is consistent with our previous observations of disordering after long (3 day) solvent annealing processes, and the limited improvement in nanostructure ordering after any tested solvent annealing conditions.[39] Typical solvent contents in annealed block copolymer films range between 20 and 45 vol%,[47-48] which includes much of the range over which mCherry-PNIPAM block copolymers exhibit disordered nanostructures.

Because the scattering patterns obtained from 60 wt% and bulk samples appear very similar, it is hypothesized that the nanostructures become kinetically trapped around this concentration as solvent evaporates during the sample casting process. Therefore, highly disordered nanostructures observed at 70 wt% are not realized in the solid state. Our previous work with this system has shown that bulk nanostructure formation is kinetically determined,[38-39] so changes in the rate of nanostructure formation which enable kinetic trapping at lower concentrations may enable improved structures in the solid state. Bulk samples were prepared by removing solvent more rapidly either from a solution at approximately 100 mg/mL block copolymer or from a hydrated sample prepared at 40 or 50 wt% (Figure 6-3). These experiments were performed on four block copolymers which demonstrated changes in nanostructure or quality of ordering with increasing concentration. Similar results were obtained at all investigated coil fractions, so only one representative sample of each morphology is presented. For the cylinder-forming block copolymer at $f_{PNIPAM} = 0.43$, more rapid solvent removal was not able to improve the quality of ordering in bulk samples. Similarly, a lamellae-forming block

copolymer at f_{PNIPAM} = 0.67 formed poorly ordered structures in the bulk when the solvent was removed from the relatively dilute solution at the faster rate. The SAXS pattern for this sample shows a broader primary peak than the bulk sample cast at a slower rate with no signs of any higher order peaks, and somewhat resembles the pattern observed at 70 wt%. In the case of removing water from a 40 wt% sample, only poorly ordered structures were observed in the bulk. In contrast, after dehydrating a 50 wt% sample of a lamellae-forming block copolymer, improved ordering in comparison with the slowly cast bulk sample is observed with a narrower primary peak and a very well-defined peak at 2q*.

Because solution SAXS experiments performed at 15 °C and below (Figure D-4) demonstrated that some block copolymers exhibit slightly better ordering or occasionally a different morphology than observed at 25 °C, solvent evaporation to form bulk samples was attempted at a lower temperature of 4 °C. Bulk samples prepared at 4 °C showed worse ordering, similar to that observed in 70 wt% samples. Therefore, at these lower temperatures solvent casting is unable to trap any ordered structure in these materials.

Combined, these results demonstrate that the kinetic trapping of well-ordered nanostructures in bulk samples is difficult and sensitive to initial block copolymer concentration. Because the evaporation of water from these materials (approximately 1 hour to completely dehydrate a sample) is relatively slow in comparison to the time necessary for structural rearrangement of the block copolymer (a few minutes for thermal equilibration[40]), it is to be expected that changes in solvent evaporation rate have only a minor ability to trap highly ordered nanostructures formed in 40 and 50 wt% solutions.

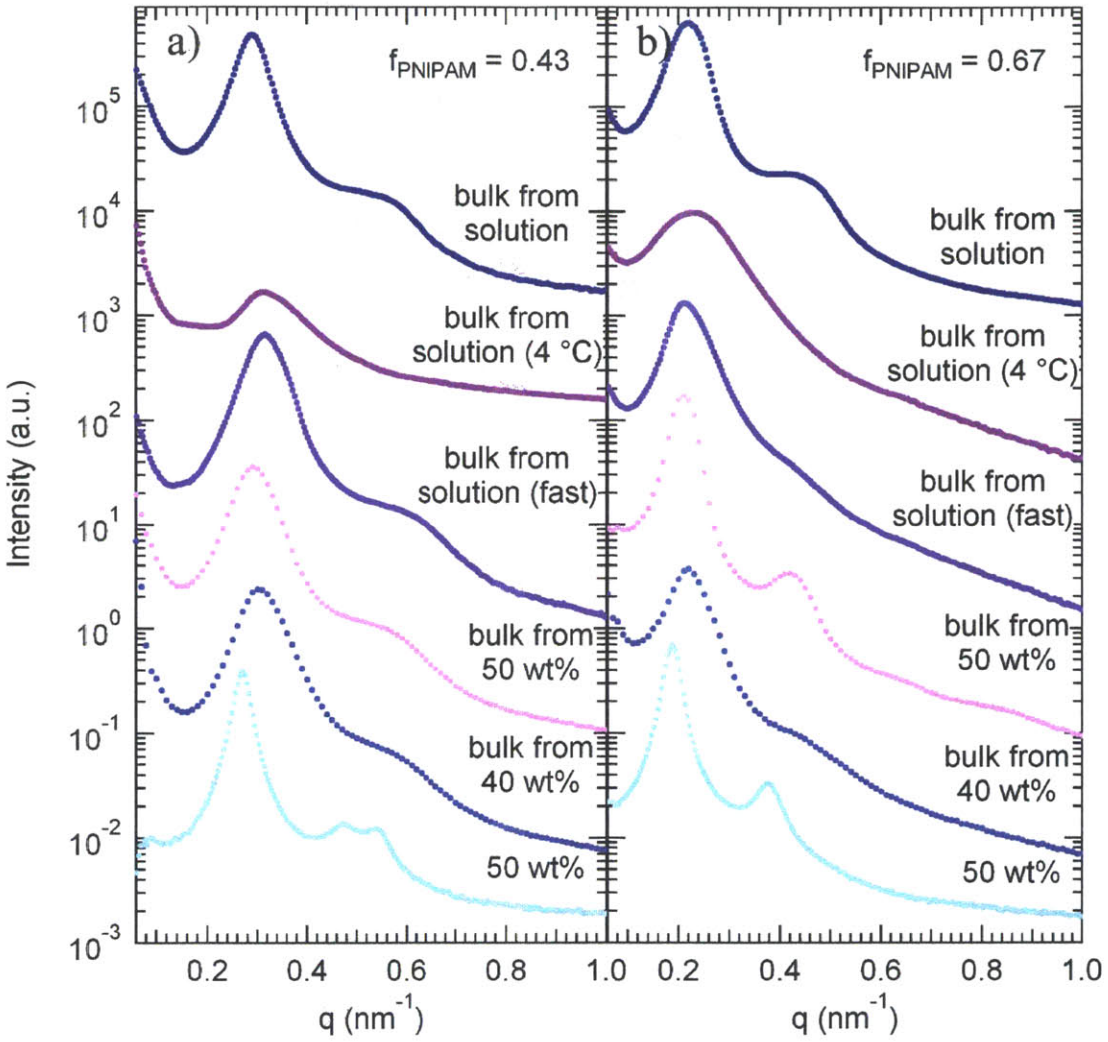

Figure 6-3. Small-angle X-ray scattering patterns of mCherry-PNIPAM block copolymers with (a) f_{PNIPAM} = 0.43 and (b) f_{PNIPAM} = 0.67 demonstrating the effects of initial sample concentration and solvent evaporation rate on the kinetic trapping of nanostructures. The nanostructures from bulk samples prepared by slow solvent evaporation from relatively dilute solution (~100 mg/mL) are compared with samples prepared by fast solvent evaporation from solution and from hydrated samples at 40 and 50 wt%. The scattering patterns obtained for hydrated samples at 40 and 50 wt% are shown for comparison. Traces have been vertically offset for clarity.

Phase diagram as a function of polymer fraction. The phase behavior of mCherry-PNIPAM as a function of coil fraction shows significant differences from that of coil-coil block copolymers due to the structure of the conjugate molecule. A phase diagram for the self-assembly of mCherry-PNIPAM at 25 °C is presented in Figure 6-2a as function of polymer volume fraction and block copolymer concentration in water. This work significantly expands upon the small number of coil fractions previously studied,[38-40] demonstrating good agreement with previously published results. From a set of eleven block copolymers spanning a range of coil fractions from 0.21 to 0.82, four types of nanostructures are observed: cylinders, lamellae, perforated lamellae, and a disordered phase.

At the lowest PNIPAM coil fraction studied ($f_{PNIPAM} = 0.21$) ordered structures are never observed at any concentration or temperature investigated. From $f_{PNIPAM} = 0.26$ to $f_{PNIPAM} = 0.36$, the ODT at which the materials go from disordered to ordered nanostructures with increasing concentration decreases from 50 wt% to 40 wt%. Above this concentration, weakly ordered or cylindrical nanostructures are observed. Based on previously published data,[40] the ODT with concentration continues to extend to lower concentrations with increasing polymer volume fraction until approximately $f_{PNIPAM} = 0.6$, at which point the ODT is at about 30 wt%. As the polymer volume fraction is increased further, the ODT begins to increase slowly again to at least 35 wt%.[40] At these higher coil fractions from $f_{PNIPAM} = 0.53$ to 0.82, lamellar nanostructures are observed.

The region containing ordered nanostructures is generally bounded at higher concentrations near 70 wt% where the lyotropic ODT is located. Interestingly, at two coil fractions between the cylindrical and lamellar regions ($f_{PNIPAM} = 0.53$ and 0.59) some weak ordering is still present at 70 wt% (Figure D-3). Therefore, intermediate polymer volume

fractions between f_{PNIPAM} = 0.5 and 0.6 have the widest concentration window for well-ordered nanostructure self-assembly. This is expected for instances where protein-polymer repulsive interactions drive self-assembly because these repulsive interactions are at a maximum for symmetric block copolymers.[49]

Within the ordered region, cylindrical nanostructures extend from f_{PNIPAM} = 0.31 to f_{PNIPAM} = 0.43 between the lyotropic ODT at lower concentration and the onset of the other lyotropic ODT near 60 wt%. A small region of cylinders extends out to higher polymer volume fractions (f_{PNIPAM} = 0.53) at 60 wt% concentration, and then also up to 70 wt% at f_{PNIPAM} = 0.53. At lower concentrations between f_{PNIPAM} = 0.46 and 0.53 below the cylindrical nanostructures, there exists a small region of perforated lamellar structures. An OOT between perforated lamellar and lamellar nanostructures extends from roughly f_{PNIPAM} = 0.5 at 40 wt% up to f_{PNIPAM} = 0.55 at 50 wt%. From f_{PNIPAM} = 0.59 to 0.82, a large region of lamellar nanostructures is observed at concentrations between 40 and 60 wt%.

Comparison between previous studies of mCherry-PNIPAM conjugates and materials in this study show good agreement for phase identifications with the exception of a single point. In a previous study, a lamellar morphology was observed with f_{PNIPAM} = 0.44 at 40 wt% and 25 °C, whereas the materials in this study at f_{PNIPAM} = 0.43 and 0.46 at 40 wt% form cylindrical and perforated lamellar nanostructures, respectively. The more complete phase behavior of the material with f_{PNIPAM} = 0.44 clearly shows that this material is near several phase boundaries in concentration, temperature and composition[40] such that small differences in any of these parameters can result in either a cylindrical, perforated lamellar, or lamellar nanostructure. This indicates that batch-to-batch variability including variations of a few percent in purity, polymer

molecular weight, or concentration account for the observed differences and make precise localization of phase boundaries challenging.

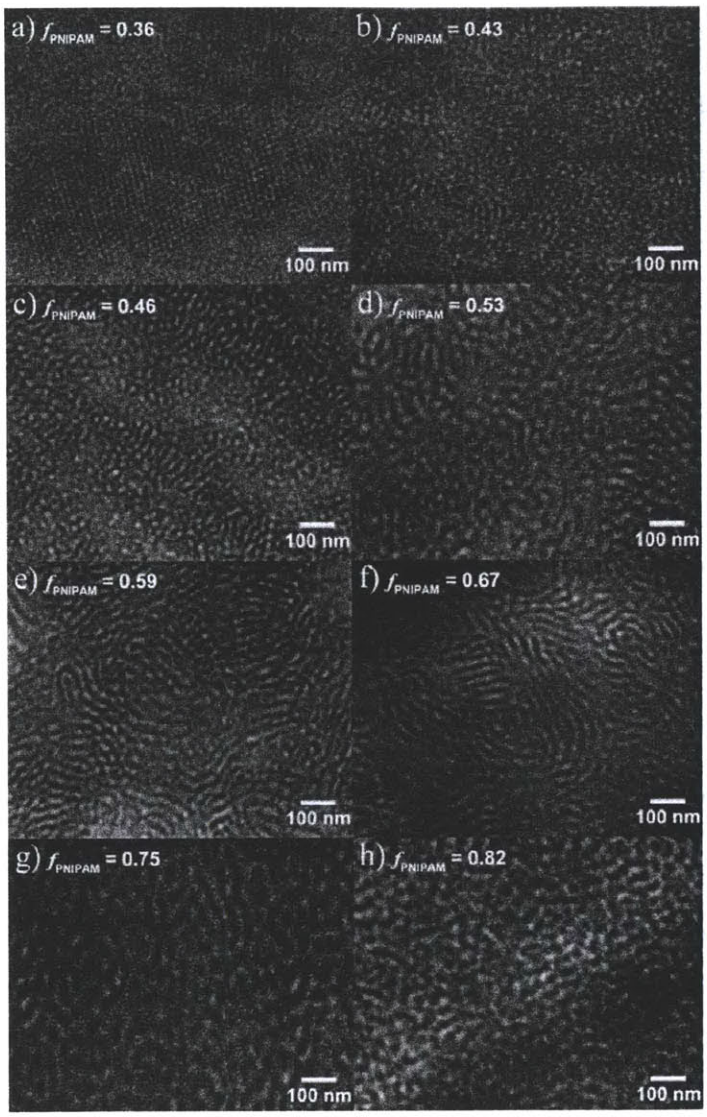

Figure 6-4. TEM images for mCherry-PNIPAM block copolymers. (a) Cylinders from f_{PNIPAM} = 0.36 (b) Poorly ordered cylinders from f_{PNIPAM} = 0.43 (c) Poorly ordered cylinders from f_{PNIPAM} = 0.46 (d) Poorly ordered cylinders from f_{PNIPAM} = 0.53 (e) Lamellae form f_{PNIPAM} = 0.59 (f) Lamellae from f_{PNIPAM} = 0.67 (g) Poorly ordered lamellae from f_{PNIPAM} = 0.75 (h) Poorly ordered lamellae from f_{PNIPAM} = 0.82. Samples were stained such that protein-rich regions appear dark.

TEM images of ordered bulk samples (Figure 6-4) show the morphology progression in the solid state as polymer coil fraction is increased. The structures observed by microscopy in the bulk are believed to be very similar to those found in 60 wt% solutions due to the similar scattering patterns. Below $f_{PNIPAM} = 0.36$, largely disordered structures are observed in SAXS patterns. At a polymer volume fraction of 0.36, hexagonally packed cylindrical nanostructures with a PNIPAM core in an mCherry matrix are observed. Below a polymer coil fraction of 0.53, a hexagonal morphology continues to be observed in the bulk. However, as the coil fraction increases over this range, microscopy shows the hexagonal order deteriorates as the material transitions towards a lamellar nanostructure. At $f_{PNIPAM} = 0.53$, a microphase separated yet disordered structure is observed between hexagonal and lamellar regions in the phase diagram. The increase in disorder of nanostructures between regions of well-defined cylinders and lamellae could potentially indicate a lamellae-cylinder coexistence region, implying that during complete dehydration, a mixed phase is kinetically trapped.

With a further increase in polymer content to $f_{PNIPAM} = 0.59$, the self-assembled morphology transitions to a lamellar nanostructure, and well-ordered lamellae are observed at $f_{PNIPAM} = 0.67$. For materials with polymer volume fractions of 0.75 and 0.82, the nanostructures become more disordered. TEM images of these samples (Figure 6-4g,h) show polymer nanodomains with shorter persistence lengths which tend to bend around protein-rich regions. These more tortuous nanostructures suggest that at high coil fractions there is some tendency for protein-polymer block copolymers to form curved interfaces; however, there is not a sufficient driving force to form well-ordered cylinders or spheres with mCherry cores. The increase in observed disorder over these polymer coil fractions may result from increased packing frustration as the polymer volume fraction increases well above 50% without inducing enough

curvature to form a cylindrical nanostructure.

The phase diagram presented in Figure 6-2a for mCherry-PNIPAM is significantly different from that of coil-coil block copolymers. One of the most notable differences is that the phase diagram of coil-coil block copolymers is approximately symmetric about $f_A = 0.5$, while the phase diagram of mCherry-PNIPAM is not symmetric, likely as a result of the molecular asymmetry caused by the presence of the globular protein. Additionally, even though cylinders and lamellae were observed in the protein-polymer system, a spherical morphology was not observed over the range of coil fractions examined. In coil-coil block copolymers, a transition from disordered to spherical nanostructures occurs around $f_A = 0.05$ in the strong segregation limit, and the block fraction at which the transition occurs increases as the segregation strength is decreased.[23] The spherical morphology extends up to approximately $f_A = 0.15$, at which point a transition to hexagonally packed cylinders is observed which extends to $f_A = 0.3$.[23] However, in the case of mCherry-PNIPAM, a direct transition from disordered to cylindrical nanostructures is observed near $f_{PNIPAM} = 0.26$, and the cylindrical phase extends until approximately $f_{PNIPAM} =$ 0.43 or 0.53, depending on the concentration.

For the protein-polymer conjugate system, a perforated lamellar nanostructure is observed, which is not an equilibrium phase in coil-coil block copolymers and cannot be definitively established as an equilibrium phase in this system either. In coil-coil block copolymer systems, an equilibrium gyroid phase is located in a narrow window between coil fractions of 0.3 and 0.32. This gyroid phase was not observed in the mCherry-PNIPAM system; however, due to the narrow range over which this morphology is formed in coil-coil block copolymers, it is possible that a stable gyroid phase could exist in mCherry-PNIPAM block copolymers at a coil fraction not investigated in this study.

In coil-coil block copolymers, the OOT between gyroid and lamellar structures is dependent primarily on polymer volume fraction and occurs around $f_A = 0.33$. In the case of mCherry-PNIPAM, the OOT between lamellae and cylinders or perforated lamellae is also largely dependent on PNIPAM volume fraction and occurs around $f_{PNIPAM} = 0.55$; however, there is some dependence on concentration as the OOT dividing line in Figure 6-2a has a positive slope at lower concentrations. The lamellar nanostructures which begin around $f_{PNIPAM} = 0.59$ extend through $f_{PNIPAM} = 0.82$. This implies that no inverse cylinder or spherical morphologies are observed in this protein-polymer system, similar to the rod-coil system[50-51] in which these phases are also not observed. However, in the rod-coil system, the lamellar region extends to the higher rod fraction side of the phase diagram, where in mCherry-PNIPAM the lamellar region extends to the lower protein fraction side of the phase diagram. In a particle-polymer bock copolymer system composed of hydroxylated polyhedral oligomeric silsesquioxane (POSS) and polystyrene, the lamellar nanostructure is also observed to extend to high polymer volume fractions of 0.76.[52] However, in this system, transitions to inverse double gyroid, cylindrical, and spherical morphologies are observed with increasing polymer content at volume fractions of 0.78, 0.81, and 0.93, respectively.[52]

The extension of lamellar nanostructures up to such high polymer volume fractions in mCherry-PNIPAM may be the result of folded protein structure which is relatively rigid and may limit the introduction of high curvature regions into block copolymer nanostructures. The observation of cylindrical nanodomains where mCherry is the majority component demonstrates the ability of the protein to form positive curvature with a larger radius at the end of the protein where the polymer is not attached. However, inverse cylinders were not observed, indicating that the formation of curvature in the opposite direction is not favored. This could be the result

of geometrical constraints wherein the proteins cannot pack compactly enough such that the interfacial area per polymer chain is too large for the single polymer chain to accommodate. This is in contrast to rod-coil block copolymers which do not form curvature, and have only been observed to form a hexagonal phase with the rod polymer as the minority block.[50]

Changes in the interaction strength between the solvent and the protein-polymer block copolymer result in somewhat different structures at a temperature of 15 °C compared with 25 °C. While this temperature range still falls below the thermoresponsive transition of PNIPAM and therefore does not cause drastic changes in the solvent selectivity, it does modulate the solvent mediated interactions sufficiently to cause the appearance of a handful of thermotropic OOTs.[40] To better understand how these OOTs affect phase behavior across a broad range of polymer coil fractions, a second phase diagram is constructed at 15 °C (Figure 6-2b). All of the changes between the two temperatures occur at concentrations of 50 wt% or lower where there is sufficient water present to alter the block copolymer solubility causing measurable shifts in OOT and ODT concentrations. First, the slope of the ODT line at low PNIPAM volume fractions and concentrations becomes more negative at lower temperatures. Second, the region of perforated lamellar nanostructures becomes significantly smaller as the OOT between perforated lamellae and lamellae shifts towards lower PNIPAM coil fractions, and at 15 °C, lamellae extend down to $f_{PNIPAM} = 0.43$ in 40 wt% solutions. The origin of the OOTs with temperature may be attributed to a small change in solvent quality as water becomes a slightly polymer-selective solvent at lower temperatures.[40] This extends the lamellar phase to lower PNIPAM coil fractions by preferentially swelling the polymer domains.

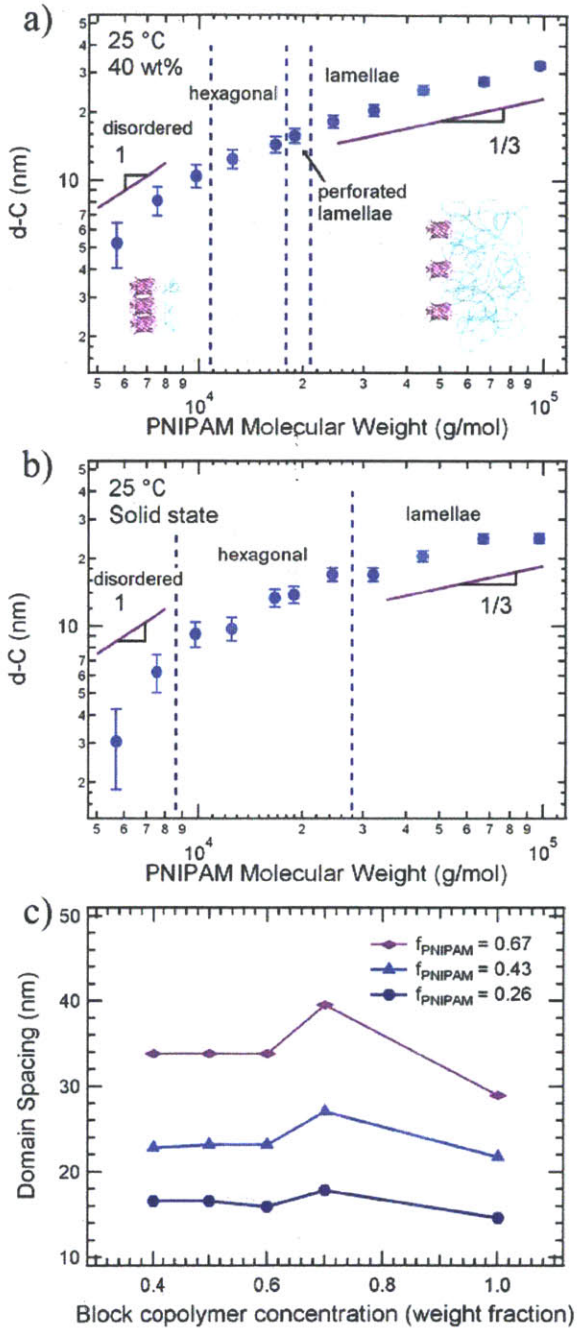

Figure 6-5. Domain spacing of self-assembled mCherry-PNIPAM block copolymers as a function of PNIPAM molecular weight in (a) 40 wt% solution and (b) the solid state. (c) Domain spacing is also shown as a function of concentration at 25 °C for three representative block copolymers.

The characteristic domain spacing of mCherry-PNIPAM as a function of molecular weight was found to differ from conventional power law scaling typically observed in coil-coil block copolymers (Figure 6-5, Figures D-6,7,8). First, in coil-coil block copolymers, the domain spacing is typically discontinuous across phase boundaries, especially in solution;[49, 53-54] however, in mCherry-PNIPAM, the domain spacing continuously increases and does not show a clear discontinuity as the morphology evolves between different ordered nanostructures with increasing coil fraction. Second, the domain spacing of coil-coil block copolymers in the melt state scales with the total degree of polymerization, N, to the two thirds power in the strong segregation limit and to the one half power in the weak segregation limit.[37, 49] In mCherry-PNIPAM, a power law cannot describe the domain spacing dependence on total molecular weight (Figure D-8).

The compact folded structure of mCherry may be approximated as a solid object which occupies a constant domain width, suggesting that the block copolymer domain spacing may be approximated as

$$d = N^{\alpha} + C \qquad \text{(Eqn. 6-1)}$$

where d is the nanostructure domain spacing, N is the number of PNIPAM monomers, and C is a constant representing the contribution of mCherry to domain spacing. Because previous experiments suggested that the protein packs in a bilayer configuration,[38] the constant C is expected to be approximately 8.4 nm, twice the length of the mCherry protein, although the presence of water during solution self-assembly may increase this domain width. The predicted scaling behavior in Equation 6-1 suggests that a plot of log(d-C) *vs* log(N) will provide insight into the behavior of domain spacing. The slope of this plot decreases with increasing PNIPAM molecular weight and is bounded by α=1 in the limit of low polymer coil fraction and α=1/3 in

the limit of high polymer coil fraction (Figure 6-5a,b), indicating that the domain spacing of this material does not follow power law scaling. At low coil fractions, the protein size determines the interfacial area occupied by the block copolymer, and the polymer chain must stretch to accommodate that constraint, so as the polymer chain grows, the domain spacing should increase approximately linearly with PNIPAM molecular weight. In contrast, in the high polymer volume fraction limit, the large polymers define the interfacial width, effectively increasing the lateral spacing of protein molecules. A dependence of $N^{1/2}$ would be expected if the chains were freely swelling; however, here a dependence tending towards $N^{1/3}$ is observed consistent with interpenetrating polymer chains. At all polymer molecular weights, water can move between PNIPAM and mCherry nanodomains to accommodate the increase in protein-protein spacing.

mCherry-PNIPAM shows no dependence of domain spacing on concentration in ordered structures between 40 and 60 wt%, with an increase observed for most coil fractions at 70 wt% as the material disorders (Figure 6-5c). This is in contrast with studies of coil-coil block copolymers in solution which demonstrated a power law dependence of domain spacing on concentration with an exponent of 1/3 for lamellar nanostructures in a neutral solvent.[29, 32, 55] However, in Pluronic solutions, the domain spacing is found to remain relatively constant as a function of concentration with a small decrease of 1-2 nm with increasing concentration between approximately 50 and 80 wt% where ordered nanostructures were observed.[33, 37] For mCherry-PNIPAM block copolymers, the domain spacing measured in solutions below 70 wt% are nearly identical to those measured in the solid state for PNIPAM coil fractions of 0.53 and lower. At higher coil fractions, the solid state samples have domain spacings that are smaller than those in solution. Both of these observations are in contrast with the expected increase in domain spacing in a solvent-free environment that has been observed in coil-coil systems.[29, 32, 55]

6.5 Conclusions

A lyotropic re-entrant ODT was observed in all ordered mCherry-PNIPAM block copolymers. Disordered structures are observed below 30 or 40 wt% and above 70 wt%, with nicely ordered nanostructures at intermediate concentrations. This type of re-entrant ODT is not typical of coil-coil block copolymers in solution where order usually improves monotonically with increasing concentration. The highest quality nanostructures were observed at 40 and 50 wt%. Solid state materials showed moderately well-ordered nanostructures with scattering patterns similar to those observed at 60 wt%. This suggested that bulk morphologies were the result of kinetically trapped nanostructures at 60 wt%. Because solvent evaporation generally occurs on a slower timescale than structural rearrangement in these block copolymers, kinetic trapping of the solid state materials in highly ordered nanostructures formed at 40-50 wt% is only successful for some materials. The limited efficacy of solvent annealing to improve ordering is also explained by the presence of a disordered phase at high polymer concentrations.

Aggregation of data for 11 separate polymer coil fractions yields the first phase diagram which systematically explores the effect of polymer volume fraction. The four morphologies observed across phase space were hexagonally packed cylinders, lamellae, perforated lamellae and a disordered phase. Scattering patterns indicate that a region exists around $f_{PNIPAM} = 0.40$ in which well-ordered cylinders are formed and that in a region around $f_{PNIPAM} = 0.60$, nicely ordered lamellae are produced. Between these regions, as well as at very low or high polymer coil fractions, the nanostructures become more disordered. Key differences between this system and traditional coil-coil block copolymers include an asymmetrical phase diagram as a function of coil fraction as well as shifted locations of phase boundaries. The shape of the folded protein is likely a major factor in these differences and the inability of the protein to accommodate

regions of high curvature is believe to contribute to the lack of a spherical morphology. By creating a detailed phase map for a single model material, mCherry-PNIPAM, this research enables future work to target a block copolymer composition to form a desired morphology in materials with different protein and/or polymer blocks.

6.6 Acknowledgements

This research was supported by the Department of Energy Office of Basic Energy Sciences (award number DE-SC0007106). X-ray scattering experiments were performed at Beamline X27C at the National Synchrotron Light Source at Brookhaven National Laboratory, and at Beamline 12-ID-B at the Advanced Photon Source at Argonne National Laboratory. Cryoultramicrotome experiments were performed at the MIT Institute for Soldier Nanotechnologies and TEM experiments were performed at the MIT Center for Materials Science and Engineering. We also thank Lixia Rong for experimental assistance with SAXS.

6.7 References

1. I. Willner and E. Katz, *Angew. Chem., Int. Ed.*, 2000, **39**, 1180-1218.
2. T. Reda, C. M. Plugge, N. J. Abram and J. Hirst, *Proc. Natl. Acad. Sci. U. S. A.*, 2008, **105**, 10654-10658.
3. R. Das, P. J. Kiley, M. Segal, J. Norville, A. A. Yu, L. Y. Wang, S. A. Trammell, L. E. Reddick, R. Kumar, F. Stellacci, N. Lebedev, J. Schnur, B. D. Bruce, S. G. Zhang and M. Baldo, *Nano Lett.*, 2004, **4**, 1079-1083.
4. J. Turková, *J. Chromatogr. B*, 1999, **722**, 11-31.
5. L. Q. Cao, *Curr. Opin. Chem. Biol.*, 2005, **9**, 217-226.
6. C. Garcia-Galan, A. Berenguer-Murcia, R. Fernandez-Lafuente and R. C. Rodrigues, *Adv. Synth. Catal.*, 2011, **353**, 2885-2904.
7. K. H. A. Lau, J. Bang, D. H. Kim and W. Knoll, *Adv. Funct. Mater.*, 2008, **18**, 3148-3157.
8. A. D. Presley, J. J. Chang and T. Xu, *Soft Matter*, 2011, **7**, 172-179.
9. D. Liu, T. Wang and J. L. Keddie, *Langmuir*, 2009, **25**, 4526-4534.
10. N. Kumar, O. Parajuli and J. Hahm, *J. Phys. Chem. B*, 2007, **111**, 4581-4587.

11. K. L. Heredia, D. Bontempo, T. Ly, J. T. Byers, S. Halstenberg and H. D. Maynard, *J. Am. Chem. Soc.*, 2005, **127**, 16955-16960.
12. J. C. M. van Hest, *Polym. Rev.*, 2007, **47**, 63-92.
13. J. Kalia and R. T. Raines, *Curr. Org. Chem.*, 2010, **14**, 138-147.
14. B. Le Droumaguet and J. Nicolas, *Polym. Chem.*, 2010, **1**, 563-598.
15. I. C. Reynhout, J. L. M. Cornelissen and R. J. M. Nolte, *Acc. Chem. Res.*, 2009, **42**, 681-692.
16. N. C. Mougin, P. van Rijn, H. Park, A. H. E. Müller and A. Böker, *Adv. Funct. Mater.*, 2011, **21**, 2470-2476.
17. P. van Rijn and A. Böker, *J. Mater. Chem.*, 2011, **21**, 16735-16747.
18. M. Li, P. De, H. Li and B. S. Sumerlin, *Polym. Chem.*, 2010, **1**, 854-859.
19. A. W. Perriman, A. P. S. Brogan, H. Colfen, N. Tsoureas, G. R. Owen and S. Mann, *Nature Chemistry*, 2010, **2**, 622-626.
20. E. A. Simone, T. D. Dziubla, F. Colon-Gonzalez, D. E. Discher and V. R. Muzykantov, *Biomacromolecules*, 2007, **8**, 3914-3921.
21. I. W. Hamley, *The Physics of Block Copolymers*, Oxford University Press, New York, 1998.
22. F. S. Bates and G. H. Fredrickson, *Phys. Today*, 1999, **52**, 32-38.
23. E. W. Cochran, C. J. Garcia-Cervera and G. H. Fredrickson, *Macromolecules*, 2006, **39**, 2449-2451.
24. B. D. Olsen and R. A. Segalman, *Mater. Sci. Eng. R*, 2008, **62**, 37-66.
25. Y. Kim, E. Ha and A. Alexander-Katz, *Macromolecules*, 2011, **44**, 7016-7025.
26. D. J. Pochan, L. Pakstis, E. Huang, C. Hawker, R. Vestberg and J. Pople, *Macromolecules*, 2002, **35**, 9239-9242.
27. M. A. Johnson, J. Iyer and P. T. Hammond, *Macromolecules*, 2004, **37**, 2490-2501.
28. T. P. Lodge, K. J. Hanley, B. Pudil and V. Alahapperuma, *Macromolecules*, 2003, **36**, 816-822.
29. K. J. Hanley, T. P. Lodge and C. I. Huang, *Macromolecules*, 2000, **33**, 5918-5931.
30. T. P. Lodge, B. Pudil and K. J. Hanley, *Macromolecules*, 2002, **35**, 4707-4717.
31. M. Shibayama, T. Hashimoto, H. Hasegawa and H. Kawai, *Macromolecules*, 1983, **16**, 1427-1433.
32. T. Hashimoto, M. Shibayama and H. Kawai, *Macromolecules*, 1983, **16**, 1093-1101.
33. P. Alexandridis, D. Zhou and A. Khan, *Langmuir*, 1996, **12**, 2690-2700.
34. C. Lai, W. B. Russel and R. A. Register, *Macromolecules*, 2001, **35**, 841-849.
35. K. Mori, A. Okawara and T. Hashimoto, *J. Chem. Phys.*, 1996, **104**, 7765-7777.
36. K. Mori, H. Hasegawa and T. Hashimoto, *Polymer*, 2001, **42**, 3009-3021.
37. M. Svensson, P. Alexandridis and P. Linse, *Macromolecules*, 1999, **32**, 637-645.
38. C. S. Thomas, M. J. Glassman and B. D. Olsen, *ACS Nano*, 2011, **5**, 5697-5707.
39. C. S. Thomas, L. Xu and B. D. Olsen, *Biomacromolecules*, 2012, **13**, 2781-2792.
40. C. N. Lam and B. D. Olsen, *Soft Matter*, 2013, **9**, 2393-2402.
41. A. K. Khandpur, S. Forster, F. S. Bates, I. W. Hamley, A. J. Ryan, W. Bras, K. Almdal and K. Mortensen, *Macromolecules*, 1995, **28**, 8796-8806.
42. X. K. Shu, N. C. Shaner, C. A. Yarbrough, R. Y. Tsien and S. J. Remington, *Biochemistry*, 2006, **45**, 9639-9647.
43. L. Leibler, *Macromolecules*, 1980, **13**, 1602-1617.
44. B. Hammouda, *J. Chem. Phys.*, 1993, **98**, 3439-3444.

45. D. A. Hajduk, M. B. Kossuth, M. A. Hillmyer and F. S. Bates, *J. Phys. Chem. B*, 1998, **102**, 4269-4276.
46. S. Jain, M. H. E. Dyrdahl, X. Gong, L. E. Scriven and F. S. Bates, *Macromolecules*, 2008, **41**, 3305-3316.
47. J. N. L. Albert, W.-S. Young, R. L. Lewis, T. D. Bogart, J. R. Smith and T. H. Epps, *ACS Nano*, 2011.
48. K. A. Cavicchi and T. P. Russell, *Macromolecules*, 2007, **40**, 1181-1186.
49. M. W. Matsen and F. S. Bates, *Macromolecules*, 1996, **29**, 1091-1098.
50. B. D. Olsen and R. A. Segalman, *Macromolecules*, 2007, **40**, 6922-6929.
51. B. D. Olsen, M. Shah, V. Ganesan and R. A. Segalman, *Macromolecules*, 2008, **41**, 6809-6817.
52. X. Yu, K. Yue, I. F. Hsieh, Y. Li, X. H. Dong, C. Liu, Y. Xin, H. F. Wang, A. C. Shi, G. R. Newkome, R. M. Ho, E. Q. Chen, W. B. Zhang and S. Z. D. Cheng, *Proc. Natl. Acad. Sci. U. S. A.*, 2013, **110**, 10078-10083.
53. C. I. Huang and H. Y. Hsueh, *Polymer*, 2006, **47**, 6843-6856.
54. M. W. Matsen and F. S. Bates, *J. Chem. Phys.*, 1997, **106**, 2436-2448.
55. K. J. Hanley and T. P. Lodge, *J. Polym. Sci., Part B: Polym. Phys.*, 1998, **36**, 3101-3113.

Chapter 7 Conclusions

7.1 Summary

This thesis began with the demonstration of the ability of a model protein-polymer block copolymer, mCherry-PNIPAM, to self-assemble into regular nanostructures in the bulk. This was the first time that a block copolymer containing a globular protein had ever been demonstrated to self-assemble into a solid material. Several important observations were made including the retention of a significant level of protein functionality in the solid state material and the dependence of nanostructure on processing history. The observation of a perforated lamellar nanostructure further hinted that kinetic effects would play a large role in the self-assembly behavior of this class of materials. While this first effort primarily served as an early demonstration of the bulk self-assembly of a single example of this type of material, it also uncovered many more questions concerning the physics behind self-assembly and it's applicability to a multitude of other systems A handful of these questions were addressed in subsequent chapters of this thesis.

In the next major study, the effects of processing history were studied in a more detailed and controlled manner. The solvent selectivity towards each block in the copolymer was found to alter the nanostructure in solution and subsequently in the solid state with the most striking changes being observed when temperature was used to dramatically change polymer solubility. Throughout this work, the necessity for reproducibility became increasingly apparent, and efforts were taken to standardize procedures to obtain consistent, meaningful results that could be compared across different experiments. This requirement was especially true when it came to measurements of solid state protein functionality. While the highest protein functionality

measurements at this time were a respectable 80%, higher retention levels nearing 100% would make this nanopatterning technique more attractive for future applications in biofunctional devices.

The next area of research was dedicated to increasing the fraction of retained protein functionality in the solid state using small molecule osmolytes. Even though polymer content in the block copolymer still influenced protein functionality levels, trehalose and glycerol were observed to contribute to the retention of up to 100% protein functionality in some materials. In addition to enhancing protein functionality, these osmolytes were also shown to alter the thermal stability and self-assembly behaviors of these materials.

Finally, the model mCherry-PNIPAM block copolymer was used to create a phase diagram as a function of polymer coil fraction and block copolymer concentration in water under conditions where water is a good solvent for PNIPAM. This work highlighted many key differences between classic coil-coil and protein-polymer block copolymer phase behavior including the lack of high curvature phases as well as large anisotropies in the phase diagram for the protein-polymer system. Additionally, the studies conducted in concentrated solutions provided further evidence for the kinetic effects governing self-assembly of these materials and uncovered a lyotropic re-entrant order-disorder transition. These results highlighted the need to identify and quantify the driving force interactions in order to develop a deeper understanding of the underlying thermodynamics governing the self-assembly of this class of materials.

7.2 Outlook

Exciting opportunities exist for future work studying protein-polymer block copolymers composed of different materials. Choosing catalytically active enzymes will undoubtedly increase the broader impact of the work, as well as add several new challenges. Maintaining

pathways for substrate and product transport will be crucially important. Striking the right balance between a supporting framework to prevent protein denaturation and allowing for the small motions necessary for normal catalytic function of enzymes will pose an added complexity for enzymatic systems. In these applications, the polymer chemistry can also be tailored such that it acts as more than just an inert block necessary to create an amphiphilic molecule. The polymer could be constructed such that it facilitates small molecule transport or acts to improve enzymatic activity retention.

While the prospect of being able to choose materials designed specifically for new applications is certainly exciting, perhaps more interesting scientifically are the effects of these changes on the self-assembly behavior of these materials. Using the work presented in this thesis as a reference, future work could examine the effects of systematic changes to block copolymer architecture and chemistry to determine the universality of the phase diagram presented for the mCherry-PNIPAM system. Different protein shapes and amino acid surface chemistries will likely affect self-assembly behavior, but at this time, it is unclear whether these differences will significantly impact final morphologies. Similarly, further geometrical constraints to the system imposed by choosing a polymer which does not behave as a conventional coil could result in new morphologies and phase diagrams. The use of highly stable proteins (for example proteins derived from extremophiles) may allow for a wider processing window and perhaps help to answer questions concerning the relationship between kinetically controlled structures and thermodynamic equilibrium. Studies with different materials would also aid in determining which forces are primarily responsible for driving self-assembly, deepening our knowledge of the system. Experiments combined with theoretical work may allow more accurate predictions of self-assembly behavior of new proposed materials of interest.

To make these materials commercially viable, significant efforts will have to be devoted towards the development of processes which are capable of retaining high levels of enzymatic activity. Additionally, advancements in large-scale protein synthesis will be required to ensure the availability of sufficient raw materials for the construction of a commercial product. Due to the expected high initial cost of fabricating such devices, early applications could be in the area of high-value commodity chemical synthesis. Looking forward, chemical syntheses which rely on redox chemistry could find benefits from the use of nanopatterned proteins due to the very high conversion efficiencies possible with enzymes. If specialty polymers capable of fast and effective proton or electron transport prove to be compatible with the enzymes, biofuel cells constructed out of protein-polymer block copolymers would certainly be a very exciting area of research because substrates and products would only need to be transported over distances of several nanometers.

The work of this thesis focused on characterizing the self-assembly behavior of a single model system and provides a starting point for future researchers. In particular, the phase diagram prepared for the mCherry-PNIPAM system can guide future endeavors in choosing relevant block copolymer compositions in a variety of new materials and devices. It is important to remember that the range of applications for new systems is limited only by the number of enzymatically catalyzed reactions.

Appendix A:

Supporting Information for

Chapter 3: Solid-State Nanostructured Materials from Self-Assembly of a Globular Protein-Polymer Diblock Copolymer

Sequence of mutant mCherryS131C protein including the 6xHis tag:

MRGSHHHHHHGSMVSKGEEDNMAIIKEFMRFKVHMEGSVNGHEFEIEGEGEGRPYEGT
QTAKLKVTKGGPLPFAWDILSPQFMYGSKAYVKHPADIPDYLKLSFPEGFKWERVMNF
EDGGVVTVTQDSSLQDGEFIYKVKLRGTNFPCDGPVMQKKTMGWEASSERMYPEDGA
LKGEIKQRLKLKDGGHYDAEVKTTYKAKKPVQLPGAYNVNIKLDITSHNEDYTIVEQYE
RAEGRHSTGGMDELYK

Sample	Thermal Transition (°C)
PNIPAM	33.5
mCherryS131C-PNIPAM	38.6

Table A-1. Cloud points of mCherryS131C-PNIPAM and the corresponding homopolymer. Solutions were prepared at 1.26 mg/mL PNIPAM and the absorbance at 700 nm was monitored as the temperature was ramped from 20 to 50 °C at 0.1 °C/min. A PNIPAM molecular weight of 35.5 kg/mol was used for both conjugate and homopolymer measurements. Increasing PNIPAM molecular weight would decrease the transition temperatures.

Figure A-1. Photograph of mCherry-PNIPAM block copolymer sample cast at room temperature and used for SAXS data acquisition showing the deep red color of mCherry. The sample is 7 mm in diameter and approximately 0.5 mm in height.

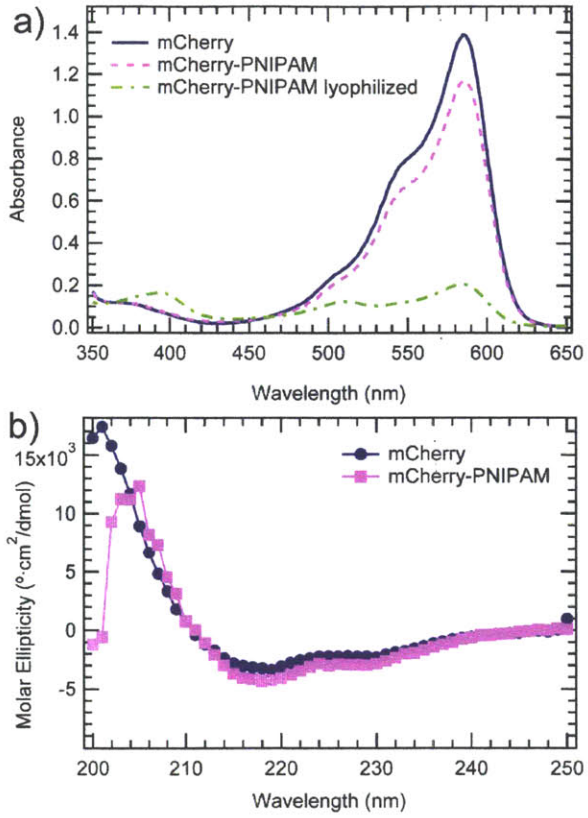

Figure A-2. (a) UV-vis spectra in solution show minimal change in mCherryS131C chromophore after conjugation to PNIPAM. The spectrum of the mutant mCherryS131C is quantitatively identical to that of the parent protein.[1-2] This is contrasted with the dramatic change observed after lyophilization. (b) Circular dichroism spectra of mCherryS131C and its conjugate with PNIPAM in solution indicate the protein fold is not disrupted by conjugation.

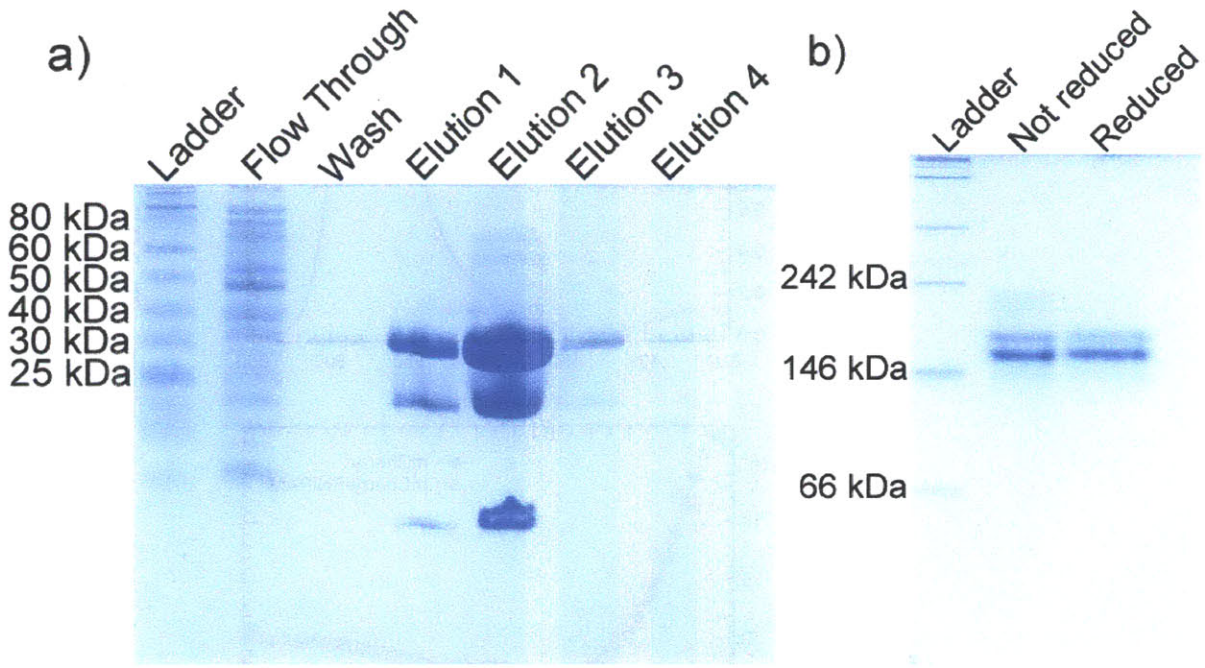

Figure A-3. (a) SDS PAGE denaturing gel showing mCherryS131C purity. The two smaller molecular weight segments are the result of the chromophore acylimine bond breaking during protein boiling. (b) Native gel showing that mCherry remains intact throughout the purification process. A higher molecular weight band shows the presence of dimers formed through disulfide linkages; the dimers are more prevalent under non-reducing conditions. Reduced mCherry was obtained by adding an equimolar amount of β-mercaptoethanol and allowing the reaction to occur at room temperature for one hour.

Table A-2. Quantitative analysis of circular dichroism spectra using CD Pro software.

Sample	Method	Fraction helix	Fraction sheet	Fraction turn	Fraction unordered	Average fraction helix	Average fraction sheet	Average fraction turn	Average fraction unordered
mCherryS131C	CONTINLL	0.057	0.503	0.183	0.257	0.041	0.497	0.192	0.270
	SELCON3	0.071	0.501	0.142	0.286				
	CSDDTR	-0.004	0.486	0.251	0.267				
mCherryS131C-PNIPAM	CONTINLL	0.027	0.393	0.202	0.378	-0.003	0.433	0.219	0.351
	SELCON3								
	CSDDTR	-0.033	0.473	0.235	0.325				
Room temperature cast	CONTINLL	0.021	0.394	0.198	0.386	-0.067	0.462	0.224	0.381
	SELCON3	0.026	0.436	0.204	0.334				
	CSDDTR	-0.248	0.557	0.271	0.421				
40 C cast	CONTINLL	0.029	0.390	0.203	0.377	0.001	0.428	0.215	0.356
	SELCON3	-0.006	0.427	0.213	0.366				
	CSDDTR	-0.019	0.467	0.228	0.324				
4 C anneal	CONTINLL	0.020	0.381	0.196	0.404	-0.016	0.413	0.206	0.396
	SELCON3	-0.036	0.403	0.179	0.454				
	CSDDTR	-0.032	0.456	0.244	0.332				
Room temperature anneal	CONTINLL	0.033	0.508	0.192	0.267	0.029	0.480	0.215	0.276
	SELCON3	0.037	0.480	0.217	0.266				
	CSDDTR	0.018	0.452	0.235	0.295				

Volume fraction calculation. The volume fraction of PNIPAM in the mCherry-PNIPAM block copolymer was calculated using mCherry crystallographic data[2] along with a PNIPAM density[3] of 1.05 g/cm^3. First, the mCherry density is calculated.

$$\rho = \frac{MW \cdot z}{V \cdot N_A} \qquad \text{(Eqn. A-1)}$$

The molar mass, MW, is 28,134.48 g/mol including the 6xHis tag. Z, the number of formula units per unit cell, is 3. N_A is Avogadro's number, and the volume, V, is calculated using the dimensions of the unit cell.

$$V = a \cdot b \cdot c \cdot \sin(\beta)$$

where a = 4.876 nm, b = 4.285 nm, c = 6.106 nm, and β = 112.31°.

The volume fraction of PNIPAM is then calculated using the following formula:

$$f_{PNIPAM} = \frac{\frac{MW_{PNIPAM}}{\rho_{PNIPAM}}}{\frac{MW_{PNIPAM}}{\rho_{PNIPAM}} + \frac{MW_{mCherry}}{\rho_{mCherry}}}$$

References

1. N. C. Shaner, R. E. Campbell, P. A. Steinbach, B. N. G. Giepmans, A. E. Palmer and R. Y. Tsien, *Nat. Biotechnol.*, 2004, **22**, 1567-1572.
2. X. K. Shu, N. C. Shaner, C. A. Yarbrough, R. Y. Tsien and S. J. Remington, *Biochemistry*, 2006, **45**, 9639-9647.
3. L. Zhang, E. S. Daniels, V. L. Dimonie and A. Klein, *J. Appl. Polym. Sci.*, 2010, **118**, 2502-2511.

Appendix B:

Supporting Information for

Chapter 4: Kinetically Controlled Nanostructure Formation in Self-Assembled Globular Protein-Polymer Diblock Copolymers

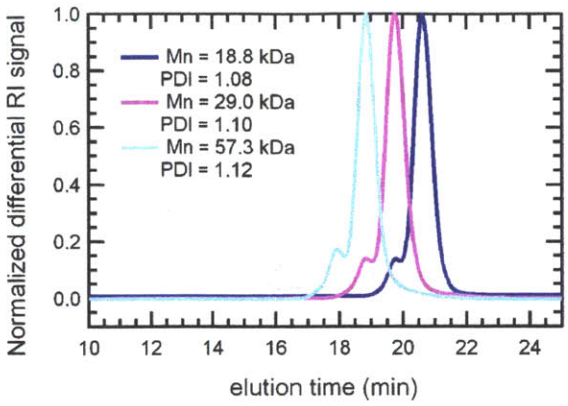

Figure B-1. Gel permeation chromatography traces of each deprotected poly(N-isopropyl acrylamide) used in this study. Three columns were used to enhance resolution, and light scattering detectors were used to determine the absolute molecular weights. The small peak at twice the average molecular weight present in all traces is caused by slight coupling of two polymers through the RAFT chain transfer agent.[1] Peak fitting of the traces reveals that coupled polymer accounts for 4-7% of the total polymer mass.

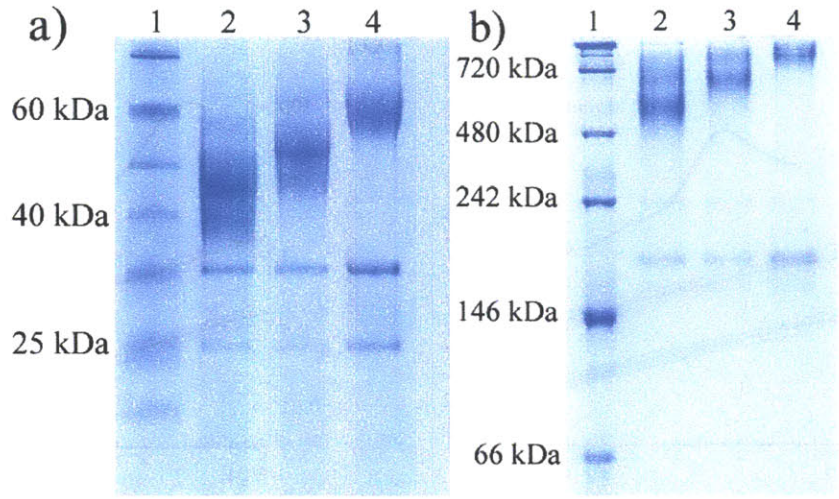

Figure B-2. (a) Denaturing SDS-PAGE shows the conjugates used in this study after purification. The lanes contain conjugates with coil fractions of 0.42 (lane 2), 0.53 (lane 3), and 0.69 (lane 4). Unconjugated mCherry is observed in three distinct bands at approximately 28, 19, and 9 kDa. The largest molecular weight species of the three is attributed to intact protein, while the two smaller fragments appear as a result of chromophore cleavage during gel preparation.[2-5] The conjugate is also seen in three bands. The middle, most prominent band corresponds to conjugate composed of an intact protein and polymer at the average molecular weight. The slightly smaller molecular weight band corresponds to conjugate material in which the mCherry chromophore bond has been cleaved. The bioconjugation site is located on the larger of the two pieces created during chromophore cleavage, so this lower molecular weight conjugate band is observed very close to the intact conjugate band. Finally, the faint higher molecular weight conjugate band is attributed to material in which coupled PNIPAM was bioconjugated to mCherry. These three conjugate bands are not resolvable for high PNIPAM molecular weights due to the relatively small difference in the total conjugate molecular weight. The purity of each conjugate material was estimated using lane analysis software. (b) Native gel of each conjugate after purification with coil fractions of 0.42 (lane 2), 0.53 (lane 3), and 0.69 (lane 4). The weak unconjugated mCherry bands at apparent molecular weights of 170 kDa (very faint) and 200 kDa correspond to protein monomers and dimers, respectively. Each conjugate is seen in two bands: one band of conjugate with the average molecular weight PNIPAM attached and a higher molecular weight band with the coupled PNIPAM attached. At high polymer molecular weights, these bands are not clearly resolvable.

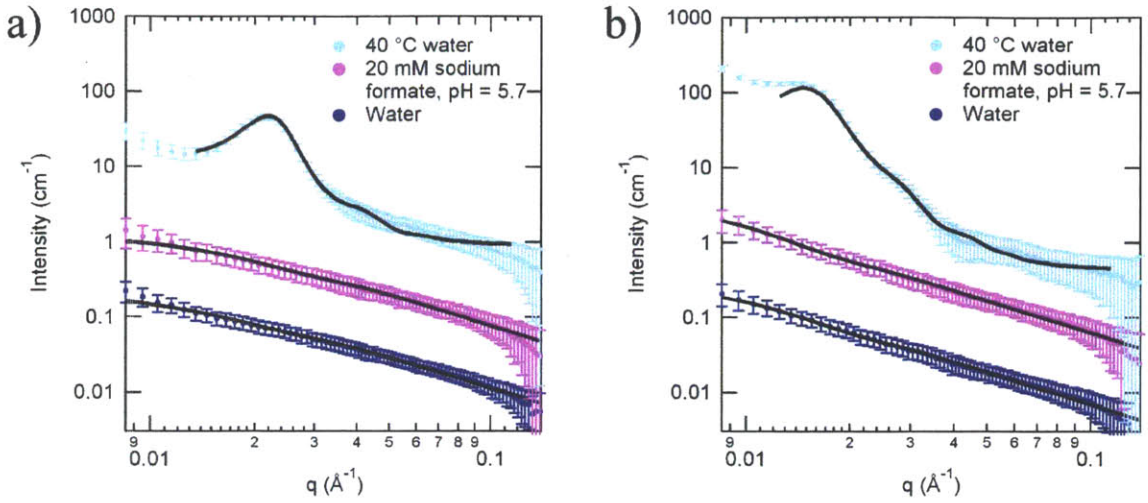

Figure B-3. SANS of hydrogenated bioconjugate in D_2O for (a) f_{PNIPAM} = 0.42 and (b) f_{PNIPAM} = 0.69. Room temperature solutions of both neutral pH (non-selective) and pH = 5.7 (polymer-selective) show no signs of aggregation, while bioconjugate in 40 °C water (protein-selective) shows large-scale aggregation. Samples in good solvents for the polymer block were fit with a Beaucage[6] model, while samples in a non-solvent for the polymer were fit with a Percus-Yevick[7-8] model for disordered hard spheres. The 20 mM sodium formate pH = 5.7, and 40 °C water traces have been vertically offset by 10 and 100 cm^{-1}, respectively, for clarity.

SANS data fitting. SANS spectra from samples in a good solvent for the polymer block were fitted using the Beaucage model.[6]

$$I(q) = Bkgd + G\exp\left(-\frac{q^2 R_g^2}{3}\right) + \frac{B\left[erf\left(qR_g/\sqrt{6}\right)\right]^{3P}}{q^P} \qquad \text{(Eqn. B-1)}$$

SANS spectra from samples in a poor solvent for the polymer block were fitted using the Percus-Yevick hard-sphere model.[7]

$$I(q) = K \cdot P(q) \cdot S(q) + C \qquad \text{(Eqn. B-2)}$$

where K is a constant dependent on the sample properties, P(q) is the form factor, S(q) is the structure factor, and C is a constant.

The form factor for polydisperse spheres is defined as

$$P(q) = \frac{\int_0^\infty p(r) f^2(q,r) dr}{\int_0^\infty p(r) dr} \qquad \text{(Eqn. B-3)}$$

where

$$p(r) = \left(2\pi\sigma_r^2\right)^{-1/2} \exp\left[\frac{-\left(r-\bar{r}\right)^2}{2\sigma_r^2}\right] \qquad \text{(Eqn. B-4)}$$

$$f(q,r) = 4/3\,\pi r^3 \Phi(q,r) \exp\left(-\sigma^2 q^2\right) \qquad \text{(Eqn. B-5)}$$

$$\Phi(q,r) = \frac{3}{(q\cdot r)^3}\left[\sin(q\cdot r) - q\cdot r\cos(q\cdot r)\right] \qquad \text{(Eqn. B-6)}$$

The structure factor is described by

$$S(q,R,\eta) = \frac{1}{1+24\eta\left(G(A)/A\right)} \qquad \text{(Eqn. B-7)}$$

where

$$A = 2q\cdot R \qquad \text{(Eqn. B-8)}$$

$$G(A) = \frac{\alpha}{A^2}\left(\sin A - A\cos A\right) + \frac{\beta}{A^3}\left(2A\sin A + (2-A^2)\cos A - 2\right) + \frac{\gamma}{A^5}\left(-A^4\cos A + 4\left[\left(3A^2-6\right)\cos A + \left(A^3-6A\right)\sin A + 6\right]\right) \qquad \text{(Eqn. B-9)}$$

In these equations, R is the hard sphere radius, η is the packing fraction, $\bar{r}$ is the core radius, σ_r is the diffuse sphere parameter which is equal to one, σ is the polydispersity parameter for the spheres, and C is a constant.

Table B-1. Fitted parameters[a] obtained from SANS spectra using (a) Beaucage model and (b) Percus-Yevick model

a)

Sample	R_g (nm)	P	B ($cm^{-1}sr^{-1}$)	G ($cm^{-1}sr^{-1}$)	Bkgd ($cm^{-1}sr^{-1}$)[b]
f_{PNIPAM} = 0.42					
non-selective	11.8 ± 2.9	1.35 ± 0.01	5.1E-04 ± 1E-05	0.2086 ± 0.004	4.6E-13
polymer-selective	10.2 ± 2.8	1.38 ± 0.01	3.2E-04 ± 1E-05	0.1253 ± 0.003	4.0E-15
f_{PNIPAM} = 0.53					
non-selective	7.5 ± 1.4	1.58 ± 0.01	2.1E-04 ± 8E-06	0.1136 ± 0.002	7.0E-21
polymer-selective	6.9 ± 1.2	1.66 ± 0.02	2.0E-04 ± 8E-06	0.1161 ± 0.002	1.0E-15
f_{PNIPAM} = 0.69					
non-selective	15.0 ± 3.8	1.42 ± 0.01	2.6E-04 ± 5E-06	0.2909 ± 0.010	1.6E-15
polymer-selective	18.0 ± 5.5	1.41 ± 0.01	2.5E-04 ± 5E-06	0.3716 ± 0.019	1.3E-19

b)

Sample	R (nm)	$\bar{r}$ (nm)	η	σ (nm)	K (cm^{-1})	C (cm^{-1})
f_{PNIPAM} = 0.42						
protein-selective	14.5 ± 0.2	7.7 ± 0.6	0.40 ± 0.01	0.03 ± 0.004	60 ± 5	0.0091±0.0003
f_{PNIPAM} = 0.53						
protein-selective	17.9 ± 0.2	11.2 ± 0.2	0.40 ± 0.01	0.02 ± 0.001	30 ± 1	0.0052±0.0001
f_{PNIPAM} = 0.69						
protein-selective	21.2 ± 0.3	11.3 ± 0.3	0.36 ± 0.02	0.02 ± 0.002	22 ± 1	0.0044±0.0001

[a] Parameter bounds are represented by the 95% confidence interval.
[b] Zero error reported by fitting algorithm due to round off

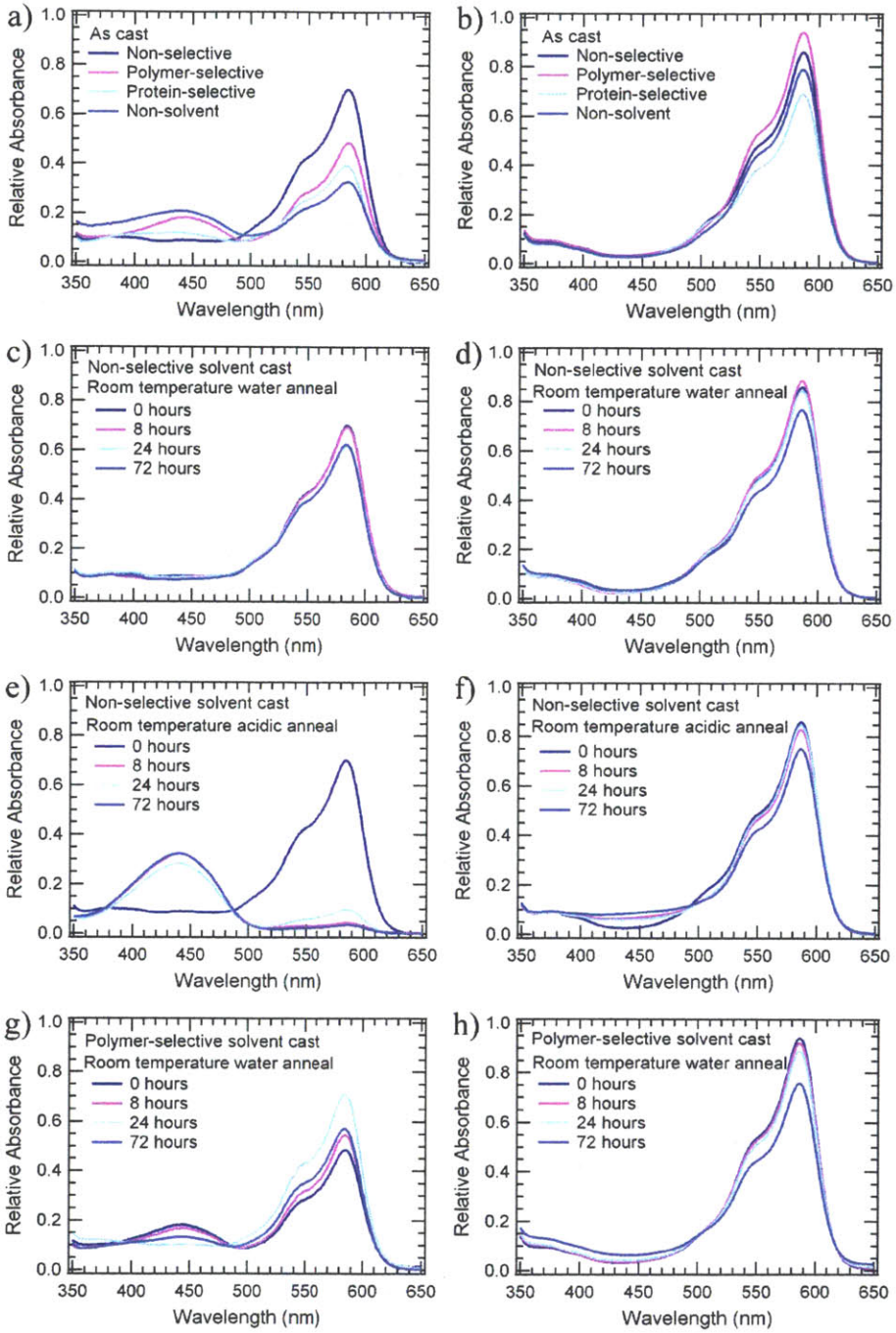

Figure B-4. Representative UV-vis absorption spectra for f_{PNIPAM} = 0.42 for both solid-state (a,c,e,g) and rehydrated (b,d,f,h) samples. The absorbances have been normalized based on the total concentration of protein present, with a relative peak absorbance of 1.0 indicating the A_{586} of the as-synthesized conjugate material. The primary peak (500-600 nm) is the characteristic absorbance peak for mCherry,[2, 9] and it intensifies upon rehydration. The smaller peak at 440 nm occurs as a result of chromophore protonation in the presence of acids[3-4, 10-11] and is no longer visible after sample rehydration.

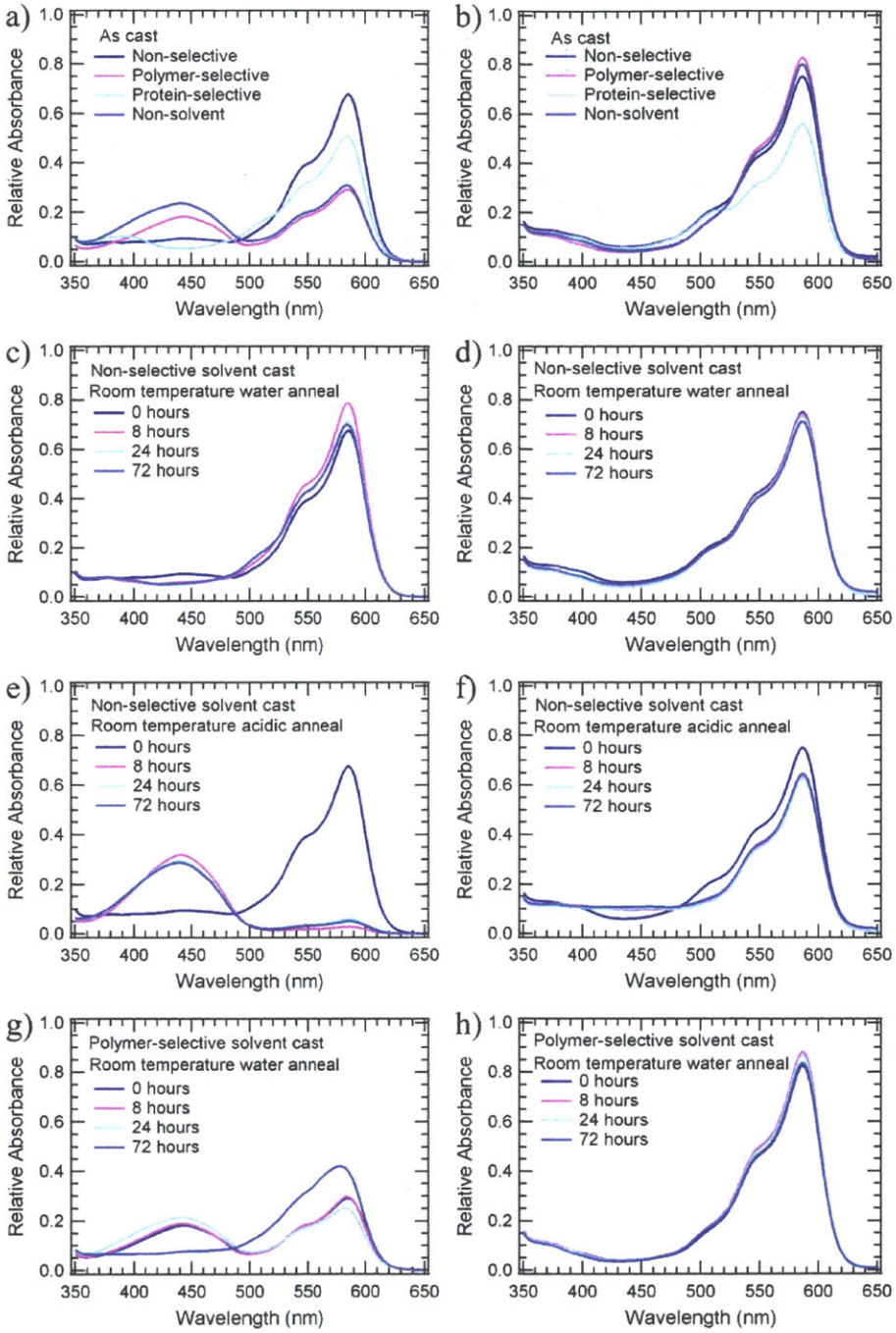

Figure B-5. Representative UV-vis absorption spectra for f_{PNIPAM} = 0.53 for both solid-state (a,c,e,g) and rehydrated (b,d,f,h) samples.

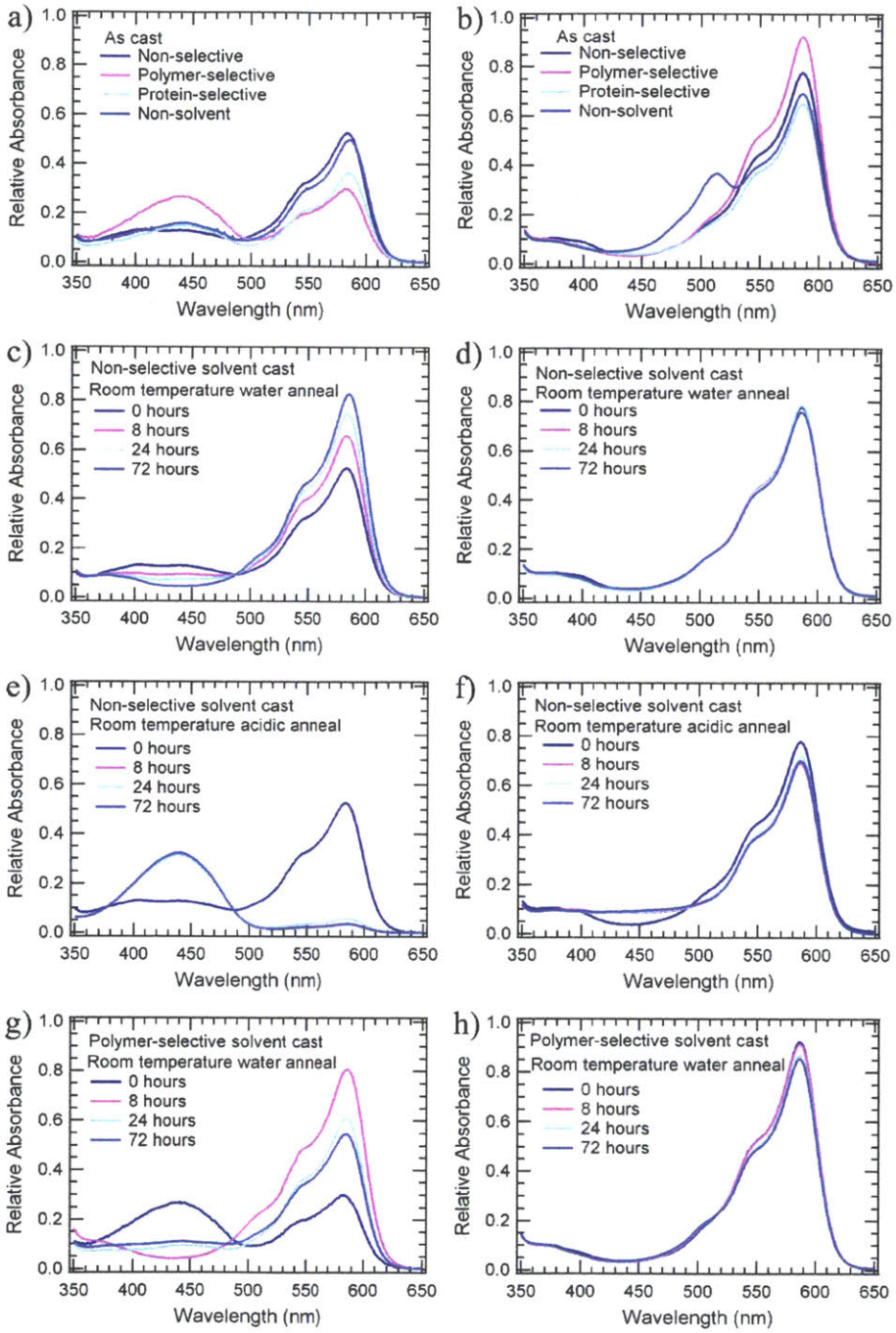

Figure B-6. Representative UV-vis absorption spectra for f_{PNIPAM} = 0.69 for both solid-state (a,c,e,g) and rehydrated (b,d,f,h) samples.

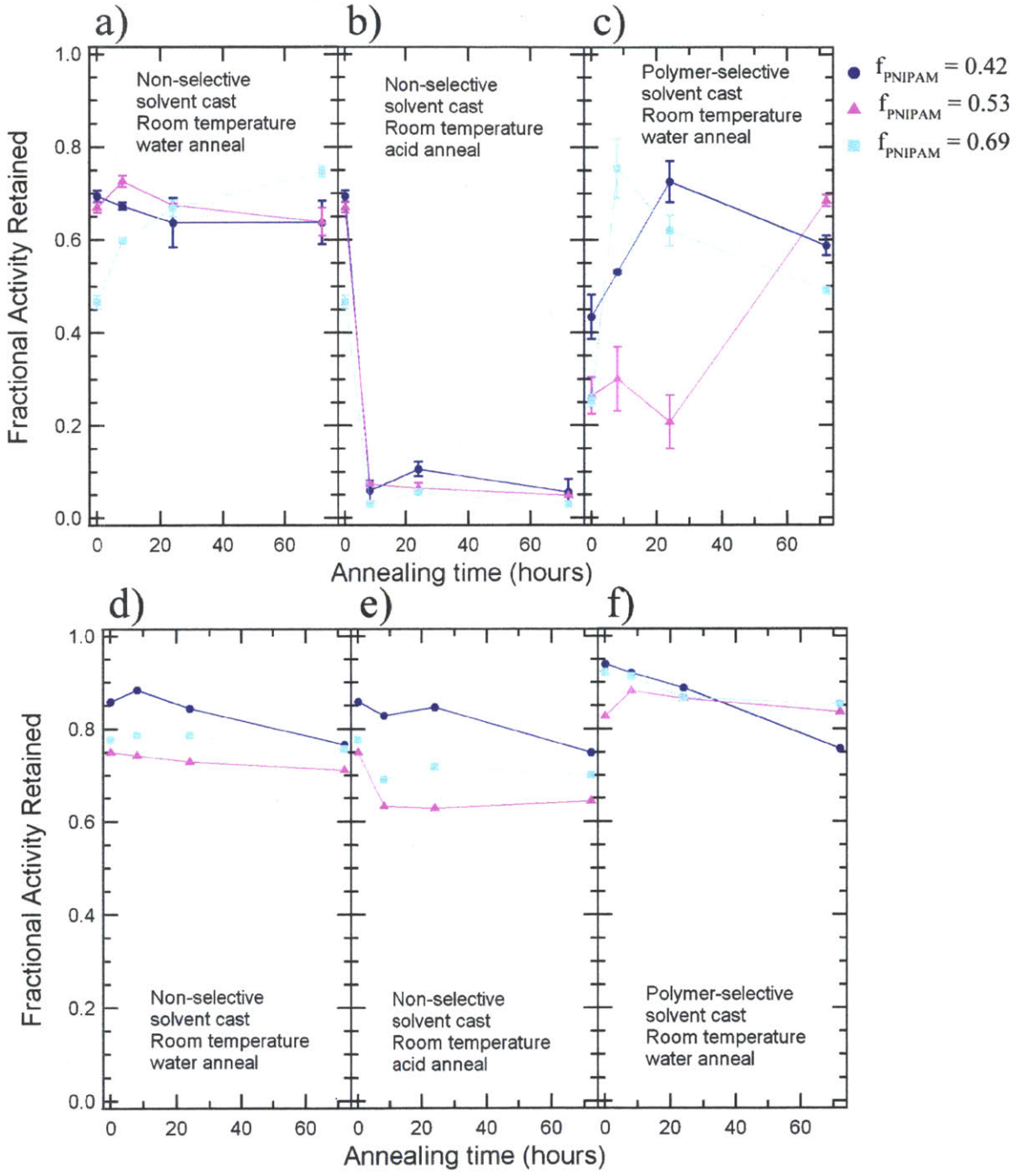

Figure B-7: Protein absorbance at 586 nm as a function of annealing time and PNIPAM coil fraction in the solid-state (a-c) and rehydrated (d-f). Error bars in (a-c) represent the standard deviation among replicates.

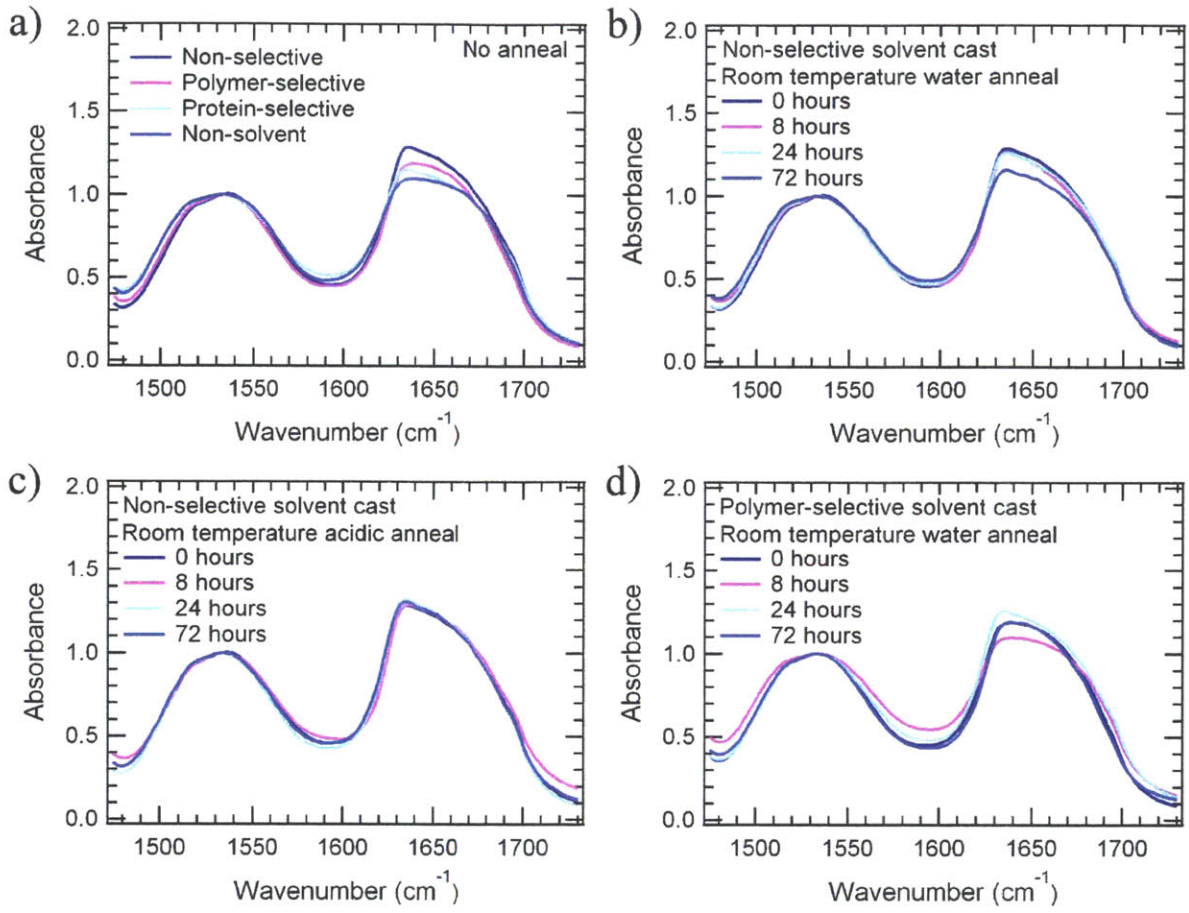

Figure B-8. Baseline corrected and normalized FTIR spectra of samples with PNIPAM weight fraction, $f_{PNIPAM} = 0.42$. Traces have been baseline corrected using the region between 1900 and 2500 cm^{-1}, and normalized to an absorbance of 1 at the peak of the amide II region (1480-1575 cm^{-1}). The amide I peak (1600-1700 cm^{-1}) provides information about the secondary structure of proteins.[12-19] Fourier self-deconvolution of the amide I peak shows that the mCherry in the conjugate material maintains its predominately β-sheet structure with no resolvable effect of processing conditions, as is evidenced by the higher absorbance around 1635 cm^{-1} compared with wavelengths at 1650 cm^{-1} and above.

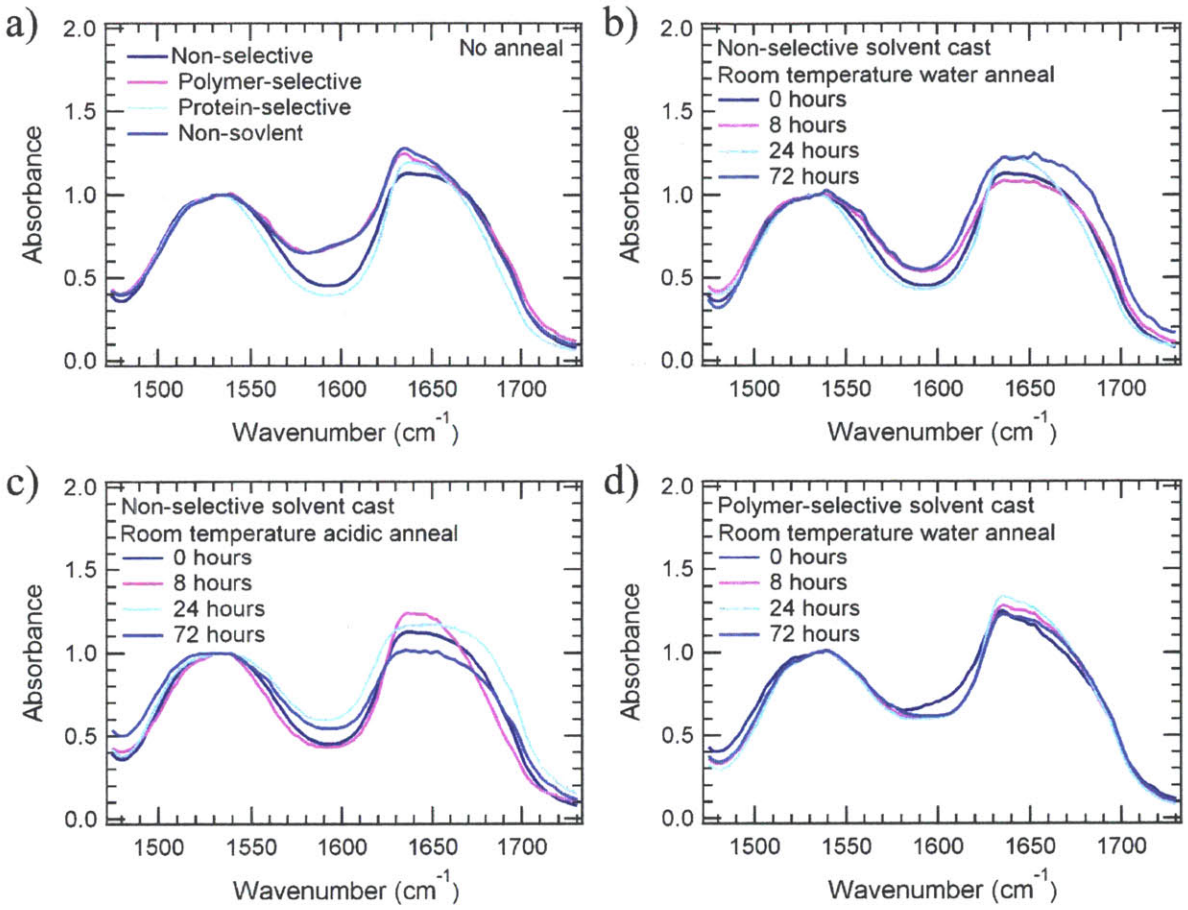

Figure B-9. Baseline corrected and normalized FTIR spectra of samples with PNIPAM weight fraction, $f_{PNIPAM} = 0.53$. As with the samples at $f_{PNIPAM} = 0.42$, the mCherry secondary structure remains predominately β-sheet regardless of processing conditions with a maximum absorbance around 1635 cm^{-1}.

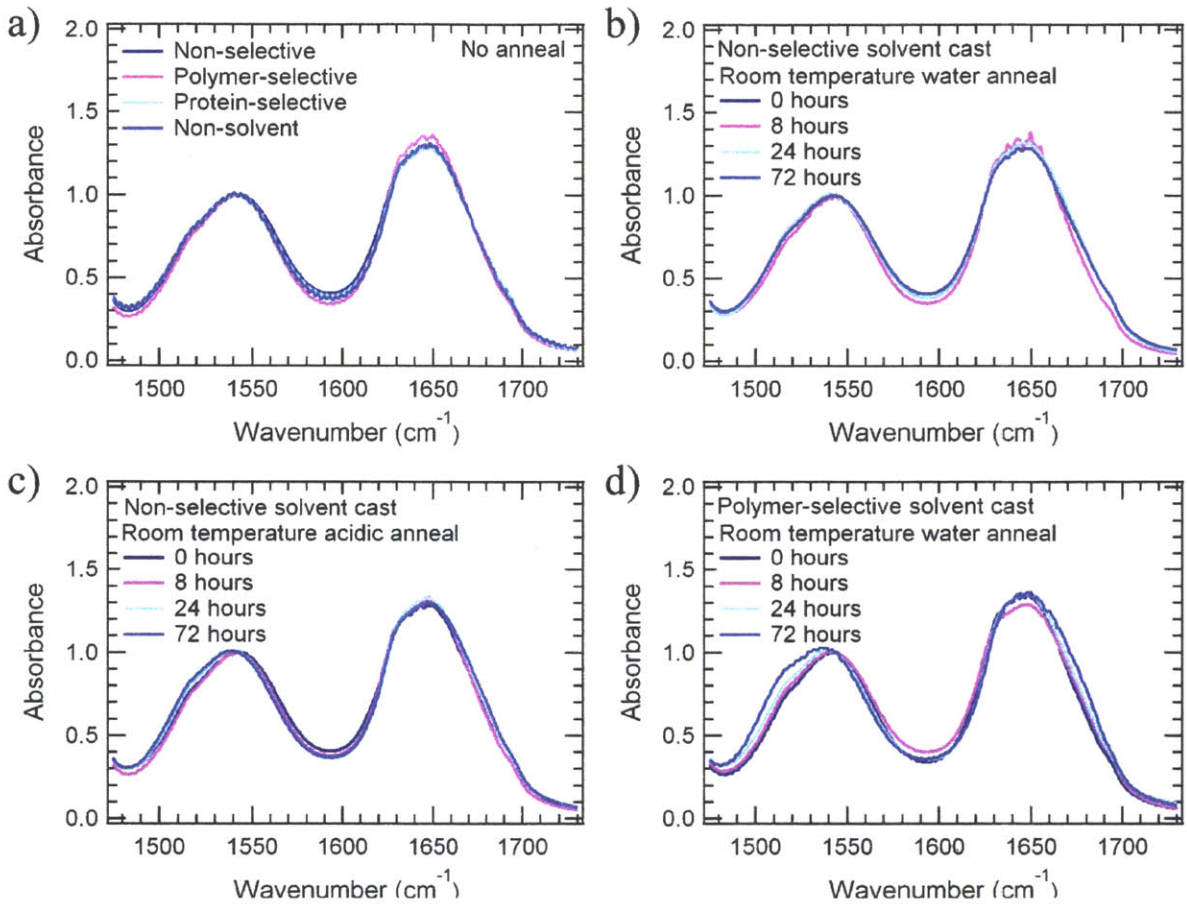

Figure B-10. Baseline corrected and normalized FTIR spectra of samples with PNIPAM weight fraction, $f_{PNIPAM} = 0.69$. In contrast to samples at $f_{PNIPAM} = 0.42$ and 0.53, the maximum of these spectra occur at 1649 cm^{-1}, which is consistent with the greater random coil content of this material due to the larger PNIPAM fraction.

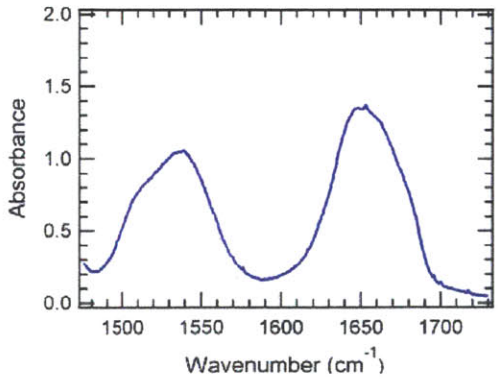

Figure B-11. Baseline corrected and normalized FTIR spectrum of PNIPAM.

Table B-2. Fourier self-deconvolution analysis of FTIR spectra for $f_{PNIPAM} = 0.42$.

Sample	Average fraction helix	Average fraction sheet	Average fraction turn	Average fraction unordered
Non-selective solvet cast No anneal	0.18	0.46	0.16	0.20
Polymer-selective solvent cast No anneal	0.20	0.41	0.17	0.22
Protein-selective solvent cast No anneal	0.19	0.44	0.18	0.20
Non-solvent cast No anneal	0.20	0.39	0.21	0.20
Non-selective solvet cast Room temperature water anneal 8 hours	0.18	0.46	0.16	0.20
Non-selective solvet cast Room temperature water anneal 24 hours	0.19	0.46	0.17	0.19
Non-selective solvet cast Room temperature water anneal 72 hours	0.18	0.44	0.17	0.21
Non-selective solvet cast Room temperature acid anneal 8 hours	0.18	0.45	0.17	0.20
Non-selective solvet cast Room temperature acid anneal 24 hours	0.18	0.45	0.17	0.19
Non-selective solvet cast Room temperature acid anneal 72 hours	0.18	0.46	0.16	0.21
Polymer-selective solvent cast Room temperature water anneal 8 hours	0.20	0.41	0.19	0.20
Polymer-selective solvent cast Room temperature water anneal 24 hours	0.18	0.45	0.17	0.20
Polymer-selective solvent cast Room temperature water anneal 72 hours	0.20	0.40	0.17	0.23

Table B-3. Fourier self-deconvolution analysis of FTIR spectra for $f_{PNIPAM} = 0.53$.

Sample	Average fraction helix	Average fraction sheet	Average fraction turn	Average fraction unordered
Non-selective solvet cast No anneal	0.20	0.39	0.20	0.21
Polymer-selective solvent cast No anneal	0.18	0.44	0.15	0.24
Protein-selective solvent cast No anneal	0.20	0.41	0.17	0.23
Non-solvent cast No anneal	0.19	0.43	0.16	0.22
Non-selective solvet cast Room temperature water anneal 8 hours	0.20	0.38	0.19	0.22
Non-selective solvet cast Room temperature water anneal 24 hours	0.21	0.38	0.16	0.24
Non-selective solvet cast Room temperature water anneal 72 hours	0.20	0.37	0.20	0.24
Non-selective solvet cast Room temperature acid anneal 8 hours	0.21	0.37	0.15	0.27
Non-selective solvet cast Room temperature acid anneal 24 hours	0.20	0.40	0.20	0.21
Non-selective solvet cast Room temperature acid anneal 72 hours	0.20	0.37	0.21	0.22
Polymer-selective solvent cast Room temperature water anneal 8 hours	0.20	0.41	0.16	0.24
Polymer-selective solvent cast Room temperature water anneal 24 hours	0.18	0.45	0.14	0.22
Polymer-selective solvent cast Room temperature water anneal 72 hours	0.18	0.44	0.16	0.21

Table B-4. Fourier self-deconvolution analysis of FTIR spectra for $f_{PNIPAM} = 0.69$.

Sample	Average fraction helix	Average fraction sheet	Average fraction turn	Average fraction unordered
Non-selective solvet cast No anneal	0.18	0.38	0.11	0.34
Polymer-selective solvent cast No anneal	0.18	0.39	0.11	0.32
Protein-selective solvent cast No anneal	0.19	0.38	0.14	0.29
Non-solvent cast No anneal	0.20	0.37	0.12	0.30
Non-selective solvet cast Room temperature water anneal 8 hours	0.15	0.39	0.10	0.36
Non-selective solvet cast Room temperature water anneal 24 hours	0.20	0.37	0.13	0.29
Non-selective solvet cast Room temperature water anneal 72 hours	0.21	0.40	0.12	0.27
Non-selective solvet cast Room temperature acid anneal 8 hours	0.20	0.37	0.12	0.31
Non-selective solvet cast Room temperature acid anneal 24 hours	0.19	0.37	0.14	0.30
Non-selective solvet cast Room temperature acid anneal 72 hours	0.19	0.37	0.15	0.28
Polymer-selective solvent cast Room temperature water anneal 8 hours	0.17	0.40	0.14	0.29
Polymer-selective solvent cast Room temperature water anneal 24 hours	0.18	0.39	0.13	0.29
Polymer-selective solvent cast Room temperature water anneal 72 hours	0.24	0.33	0.16	0.27

Calculating secondary structure content contributions from FTIR. The disordered structure content of the protein in the conjugate ($d_{protein}$) was obtained through a least squares fit of the following equation:

$$d_{conjugate,measured} = \frac{d_{protein}N_{protein} + d_{polymer}N_{polymer}}{N_{protein} + N_{polymer}} \quad \text{(Eqn. B-10)}$$

where d is the average disorder content and N is the number of monomers or amino acids present in the molecule. $N_{protein}$ = 248 and $N_{polymer}$ = 166, 256 or 506 for f_{PNIPAM} = 0.42, 0.53 or 0.69, respectively. $d_{polymer}$ was measured to be 0.444 by Fourier self-deconvolution for all molecular weights and is assumed to remain unchanged after bioconjugation. A good fit was obtained with $d_{protein}$ = 0.025 (squared 2-norm of the residual = 1.98e-4).

A similar equation is constructed to evaluate the β-sheet content:

$$\beta_{conjugate,measured} = \frac{\beta_{protein}N_{protein} + \beta_{polymer}N_{polymer}}{N_{protein} + N_{polymer}} \quad \text{(Eqn. B-11)}$$

In this case, a single value of $\beta_{protein}$ (0.79) was not sufficient to describe the behavior of $\beta_{conjugate\ measured}$ (squared 2-norm of the residual = 0.012), indicating that protein β-sheet content in the conjugates was dependent on PNIPAM coil fraction, with the fraction of β-sheet increasing as coil fraction increases.

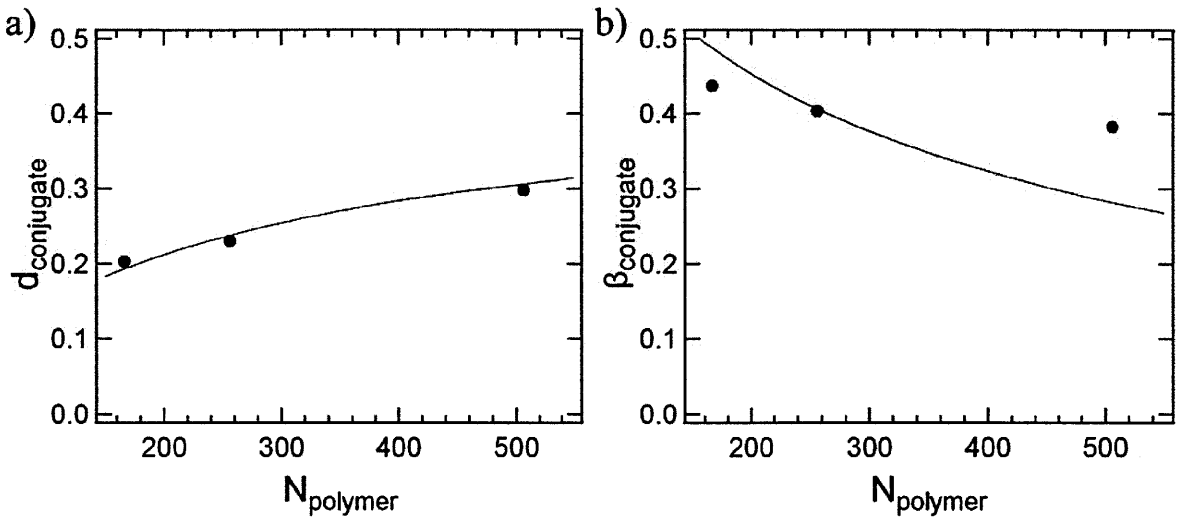

Figure B-12. Plots showing measured (a) disorder or (b) β-sheet secondary structure content in the conjugate along with the values predicted by equations B-10 and B-11 as a function of the number of monomers in a polymer.

Table B-5. Analysis of circular dichroism spectra using CDPro software for $f_{PNIPAM} = 0.42$. Variations in measured protein secondary structure with casting condition are within the uncertainty due to the choice of fitting algorithm.

Sample	Average fraction helix	Average fraction sheet	Average fraction turn	Average fraction unordered
Non-selective solvet cast No anneal	0.018	0.501	0.204	0.275
Polymer-selective solvent cast No anneal	0.019	0.495	0.203	0.283
Protein-selective solvent cast No anneal	0.024	0.460	0.206	0.307
Non-solvent cast No anneal	0.021	0.486	0.209	0.283
Non-selective solvet cast Room temperature water anneal 8 hours	0.012	0.488	0.205	0.288
Non-selective solvet cast Room temperature water anneal 24 hours	0.029	0.506	0.205	0.261
Non-selective solvet cast Room temperature water anneal 72 hours	0.017	0.496	0.204	0.279
Non-selective solvet cast Room temperature acid anneal 8 hours	0.029	0.447	0.210	0.315
Non-selective solvet cast Room temperature acid anneal 24 hours	0.016	0.490	0.204	0.282
Non-selective solvet cast Room temperature acid anneal 72 hours	0.024	0.480	0.206	0.283
Polymer-selective solvent cast Room temperature water anneal 8 hours	0.025	0.453	0.206	0.310
Polymer-selective solvent cast Room temperature water anneal 24 hours	0.021	0.490	0.211	0.272
Polymer-selective solvent cast Room temperature water anneal 72 hours	0.019	0.497	0.206	0.278

Table B-6. Analysis of circular dichroism spectra using CDPro software for $f_{PNIPAM} = 0.53$. Variations in measured protein secondary structure with casting condition are within the uncertainty due to the choice of fitting algorithm.

Sample	Average fraction helix	Average fraction sheet	Average fraction turn	Average fraction unordered
Non-selective solvet cast No anneal	0.012	0.451	0.200	0.340
Polymer-selective solvent cast No anneal	0.009	0.446	0.218	0.325
Protein-selective solvent cast No anneal	0.019	0.474	0.198	0.300
Non-solvent cast No anneal	0.005	0.456	0.206	0.314
Non-selective solvet cast Room temperature water anneal 8 hours	0.017	0.461	0.211	0.305
Non-selective solvet cast Room temperature water anneal 24 hours	0.008	0.456	0.206	0.324
Non-selective solvet cast Room temperature water anneal 72 hours	0.022	0.464	0.203	0.303
Non-selective solvet cast Room temperature acid anneal 8 hours	0.015	0.435	0.206	0.335
Non-selective solvet cast Room temperature acid anneal 24 hours	0.006	0.463	0.194	0.326
Non-selective solvet cast Room temperature acid anneal 72 hours	0.010	0.457	0.213	0.313
Polymer-selective solvent cast Room temperature water anneal 8 hours	0.023	0.462	0.206	0.306
Polymer-selective solvent cast Room temperature water anneal 24 hours	0.028	0.459	0.203	0.307
Polymer-selective solvent cast Room temperature water anneal 72 hours	0.029	0.432	0.210	0.332

Table B-7. Analysis of circular dichroism spectra using CDPro software for $f_{PNIPAM} = 0.69$. Variations in measured protein secondary structure with casting condition are within the uncertainty due to the choice of fitting algorithm.

Sample	Average fraction helix	Average fraction sheet	Average fraction turn	Average fraction unordered
Non-selective solvet cast No anneal	-0.010	0.380	0.211	0.398
Polymer-selective solvent cast No anneal	-0.004	0.365	0.225	0.406
Protein-selective solvent cast No anneal	-0.006	0.368	0.185	0.404
Non-solvent cast No anneal	-0.011	0.377	0.211	0.397
Non-selective solvet cast Room temperature water anneal 8 hours	-0.009	0.358	0.227	0.410
Non-selective solvet cast Room temperature water anneal 24 hours	-0.015	0.369	0.245	0.387
Non-selective solvet cast Room temperature water anneal 72 hours	0.002	0.372	0.216	0.395
Non-selective solvet cast Room temperature acid anneal 8 hours	-0.010	0.377	0.218	0.404
Non-selective solvet cast Room temperature acid anneal 24 hours	-0.027	0.362	0.247	0.394
Non-selective solvet cast Room temperature acid anneal 72 hours	-0.004	0.371	0.218	0.400
Polymer-selective solvent cast Room temperature water anneal 8 hours	-0.023	0.369	0.223	0.409
Polymer-selective solvent cast Room temperature water anneal 24 hours	-0.014	0.367	0.231	0.404
Polymer-selective solvent cast Room temperature water anneal 72 hours	0.020	0.367	0.206	0.407

References

1. C. S. Thomas, M. J. Glassman and B. D. Olsen, *ACS Nano*, 2011, **5**, 5697-5707.
2. X. K. Shu, N. C. Shaner, C. A. Yarbrough, R. Y. Tsien and S. J. Remington, *Biochemistry*, 2006, **45**, 9639-9647.
3. L. A. Gross, G. S. Baird, R. C. Hoffman, K. K. Baldridge and R. Y. Tsien, *Proc. Natl. Acad. Sci. U. S. A.*, 2000, **97**, 11990-11995.
4. A. A. Pakhomov, N. V. Pletneva, T. A. Balashova and V. I. Martynov, *Biochemistry*, 2006, **45**, 7256-7264.
5. J. A. Chung, J. W. Wollack, M. L. Hovlid, A. Okesli, Y. Chen, J. D. Mueller, M. D. Distefano and T. A. Taton, *Anal. Biochem.*, 2009, **386**, 1-8.
6. G. Beaucage, *J. Appl. Crystallogr.*, 1995, **28**, 717-728.
7. D. J. Kinning and E. L. Thomas, *Macromolecules*, 1984, **17**, 1712-1718.
8. M. E. Seitz, W. R. Burghardt, K. T. Faber and K. R. Shull, *Macromolecules*, 2007, **40**, 1218-1226.
9. N. C. Shaner, R. E. Campbell, P. A. Steinbach, B. N. G. Giepmans, A. E. Palmer and R. Y. Tsien, *Nat. Biotechnol.*, 2004, **22**, 1567-1572.
10. F. V. Subach, V. N. Malashkevich, W. D. Zencheck, H. Xiao, G. S. Filonov, S. C. Almo and V. V. Verkhusha, *Proc. Natl. Acad. Sci. U. S. A.*, 2009, **106**, 21097-21102.
11. K. B. Bravaya, O. M. Subach, N. Korovina, V. V. Verkhusha and A. I. Krylov, *J. Am. Chem. Soc.*, 2012, **134**, 2807-2814.
12. D. M. Byler and H. Susi, *Biopolymers*, 1986, **25**, 469-487.
13. J. Kong and S. Yu, *Acta Biochim. Biophys. Sin.*, 2007, **39**, 549-559.
14. M. Jackson and H. H. Mantsch, *Crit. Rev. Biochem. Mol. Biol.*, 1995, **30**, 95-120.
15. H. Herberhold, S. Marchal, R. Lange, C. H. Scheyhing, R. F. Vogel and R. Winter, *J. Mol. Biol.*, 2003, **330**, 1153-1164.
16. A. Barth and C. Zscherp, *Q. Rev. Biophys.*, 2002, **35**, 369-430.
17. W. Huang, S. Krishnaji, X. Hu, D. Kaplan and P. Cebe, *Macromolecules*, 2011, **44**, 5299-5309.
18. K. Fu, K. Griebenow, L. Hsieh, A. M. Klibanov and L. Robert, *J. Controlled Release*, 1999, **58**, 357-366.
19. S. Matheus, W. Friess and H. C. Mahler, *Pharm. Res.*, 2006, **23**, 1350-1363.

Appendix C:

Supporting Information for

Chapter 5: The Effect of Small Molecule Osmolytes on the Self-Assembly and Functionality of Globular Protein-Polymer Diblock Copolymers

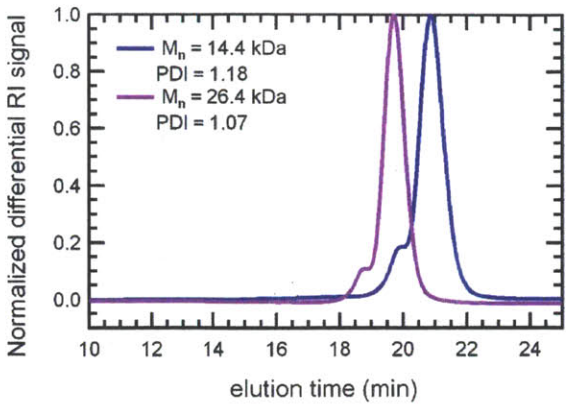

Figure C-1. Gel permeation chromatography traces of each deprotected poly(N-isopropyl acrylamide) (PNIPAM) used in this study. Three columns were used to enhance resolution, and light scattering detectors were used to determine the absolute molecular weights. The small peak at twice the average molecular weight present in all traces is caused by slight coupling of two polymers through the RAFT chain transfer agent.[1] Peak fitting of the traces reveals that coupled polymer accounts for 4-6% of the total polymer mass.

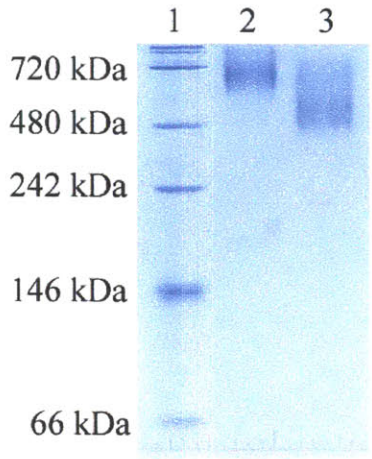

Figure C-2. Native gel of each conjugate after purification with PNIPAM coil fractions of 0.55 (lane 2) and 0.40 (lane 3). Unconjugated mCherry bands that appear at apparent molecular weights of 170 kDa (very faint) and 200 kDa correspond to protein monomers and dimers, respectively.[2] Each conjugate is seen in two bands: one band of conjugate with the average molecular weight PNIPAM attached and a higher molecular weight band with the coupled PNIPAM attached. At high polymer molecular weights, these two bands are not clearly resolvable. The purity of each conjugate was estimated using lane analysis software by dividing the integrated intensity resulting from the bioconjugate band by the total integrated intensity from all bands. This molar purity is then converted to a mass-based purity using the molar masses of mCherry and PNIPAM.

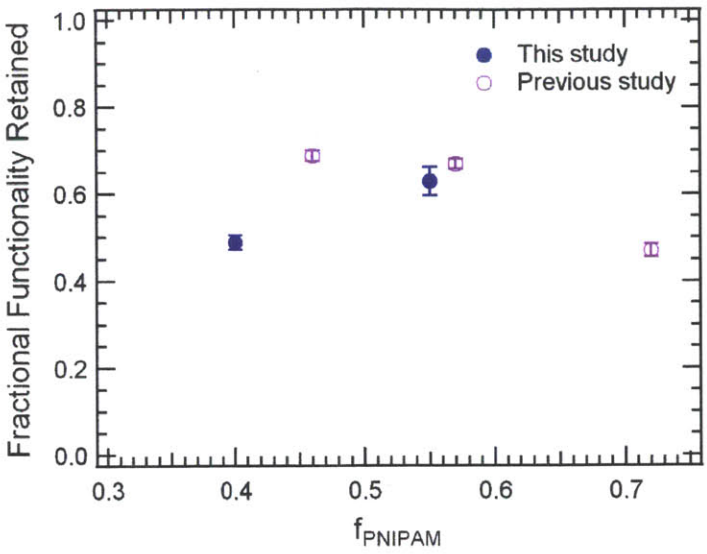

Figure C-3. UV-vis measurements at 586 nm of solid-state mCherry-PNIPAM as a function of PNIPAM volume fraction. Combining the data from this work with previous work[2] demonstrates that optimal protein functionality retention occurs over a range between f_{PNIPAM} = 0.40 and 0.55. Error bars show the standard deviation among replicates.

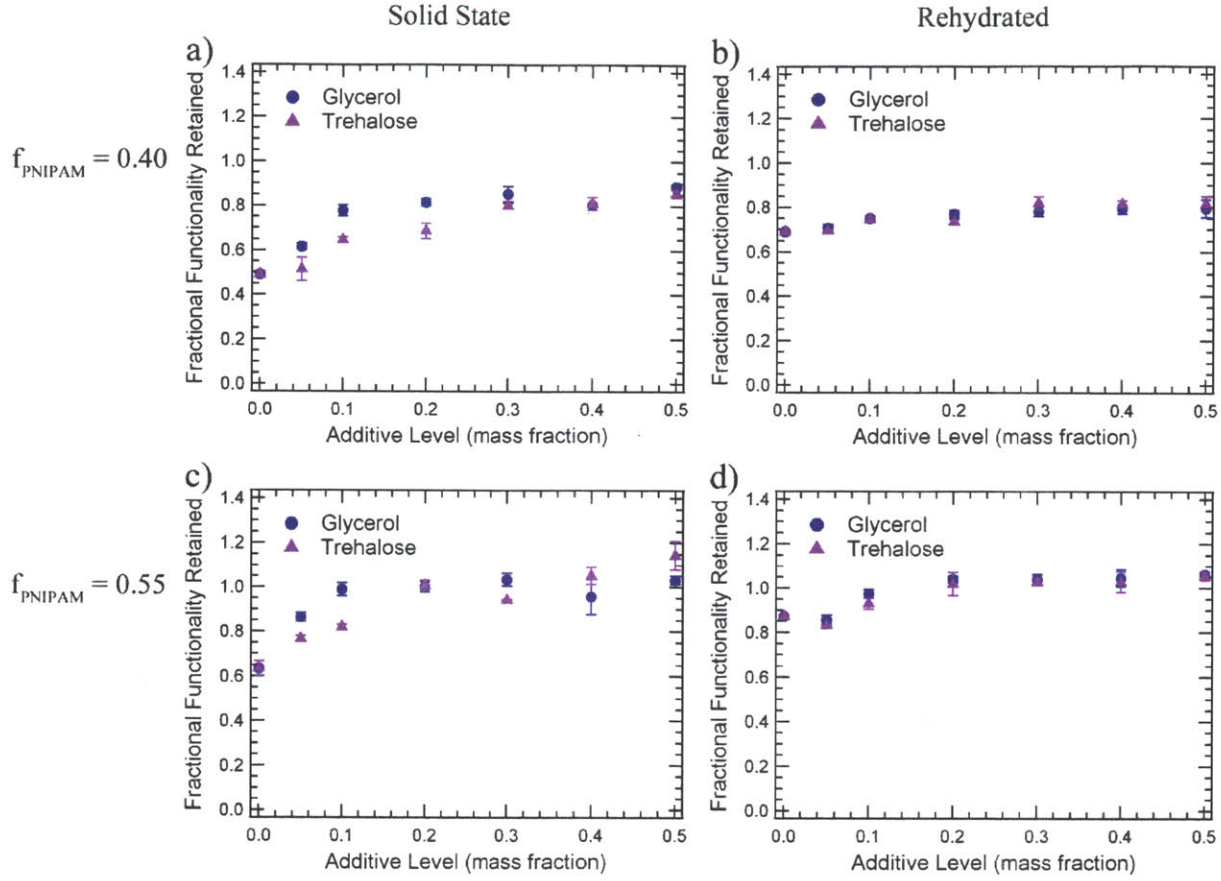

Figure C-4. Retained protein functionality as a function of osmolyte loading for f_{PNIPAM} = 0.40 (a,b) and f_{PNIPAM} = 0.55 (c,d). Measurements of normalized UV-vis absorption peaks at 586 nm in the solid state (a,c) provide a direct measure of protein function in solid nanostructures, while rehydrated samples (b,d) provide information on the fraction of material which is irreversibly denatured during solid state processing. Error bars show the standard deviation among replicates.

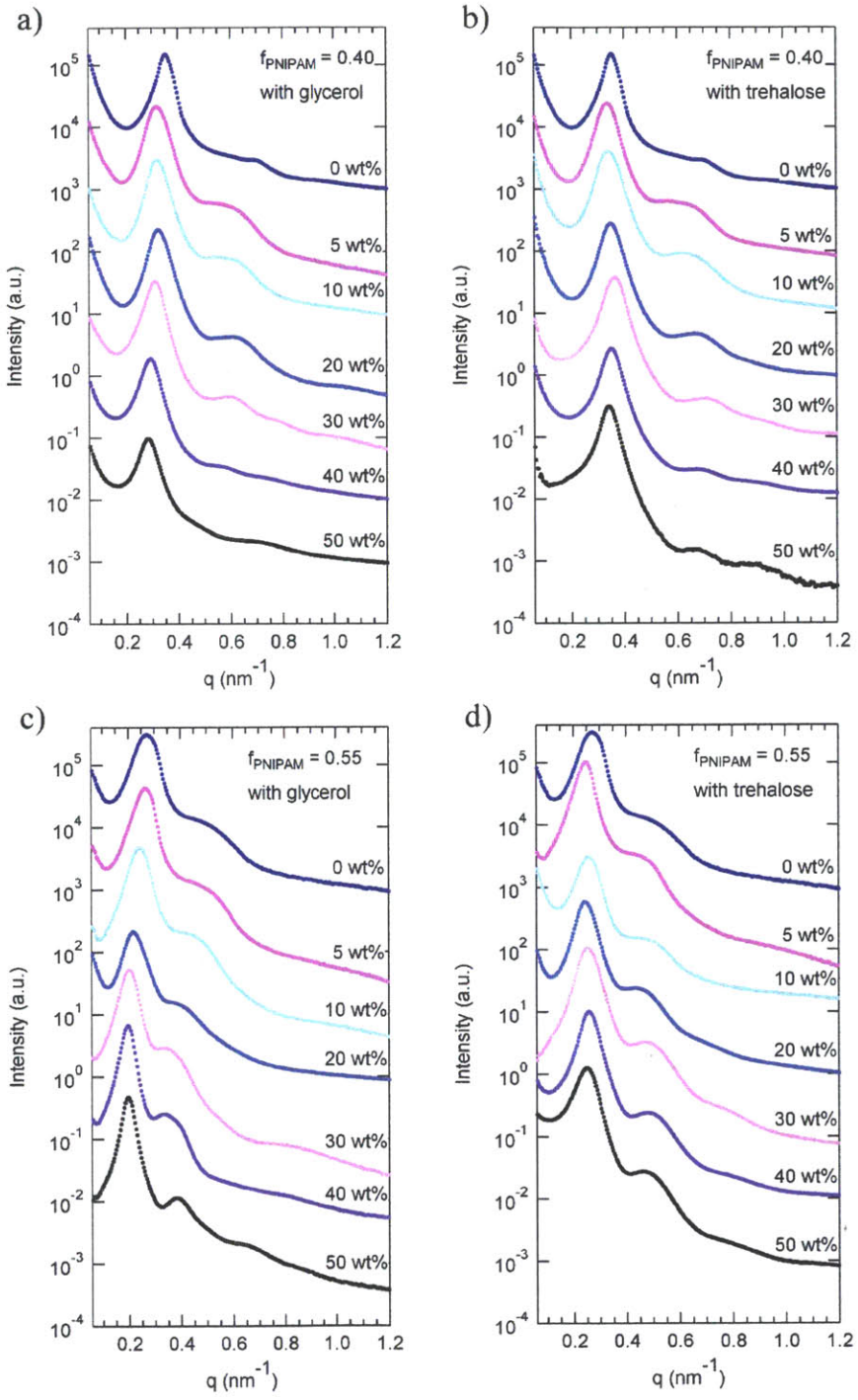

Figure C-5. SAXS of mCherry-PNIPAM block copolymers showing the effects of all loading levels of glycerol and trehalose tested in this study on the resulting nanostructure. (a,b) $f_{PNIPAM} = 0.40$ (c,d) $f_{PNIPAM} = 0.55$. Traces have been offset for clarity.

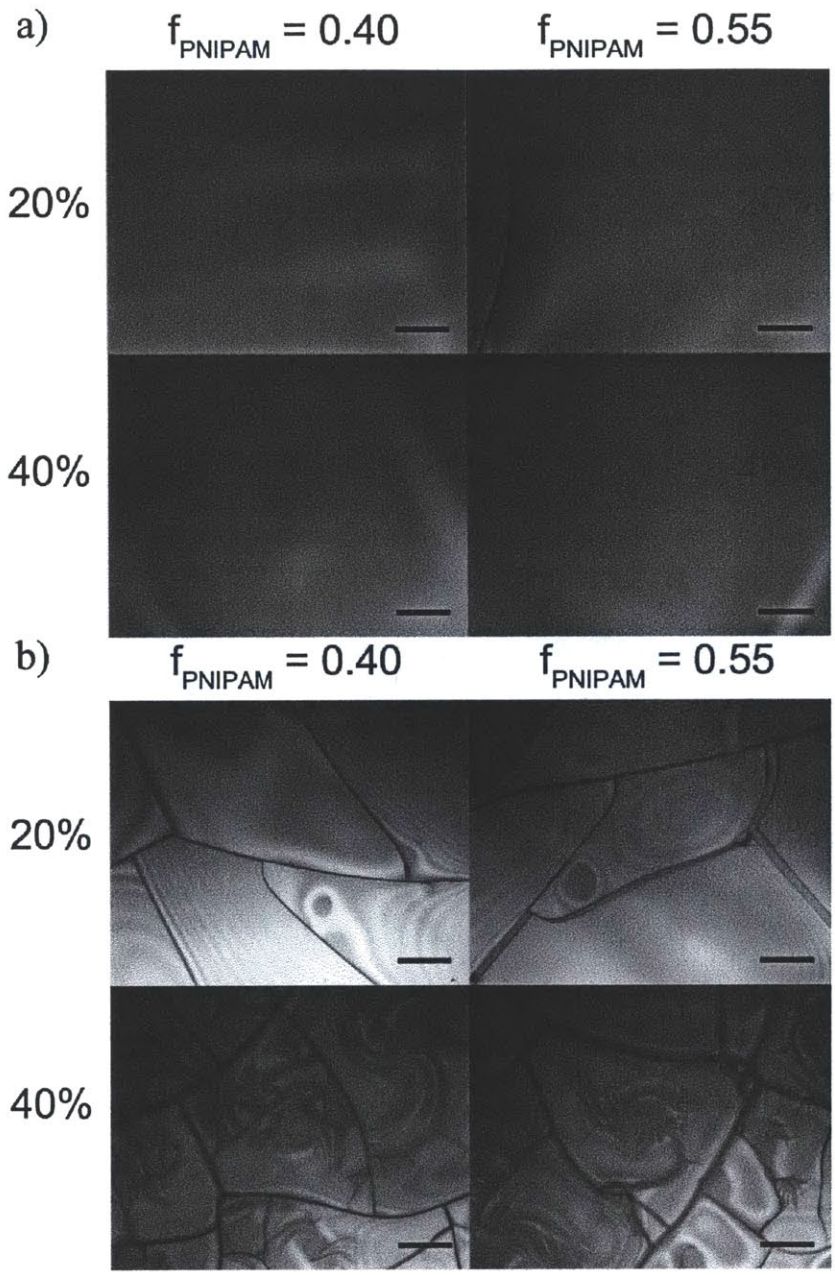

Figure C-6. Optical microscopy images of solid state mCherry-PNIPAM block copolymer blends with (a) glycerol and (b) trehalose. Films containing glycerol remain homogeneous even at loadings of 50% glycerol by weight. In contrast, films containing trehalose show the appearance of branched needle structures within the block copolymer rich regions beginning at 30 wt% and 35 wt% trehalose for $f_{PNIPAM} = 0.40$ and $f_{PNIPAM} = 0.55$, respectively, indicating the onset of macrophase separation. The needle structures are also observed to grow with increasing trehalose concentration. The spots and the surrounding concentric rings are a result of variations in film thickness after drop casting. Scale bar corresponds to 50 μm.

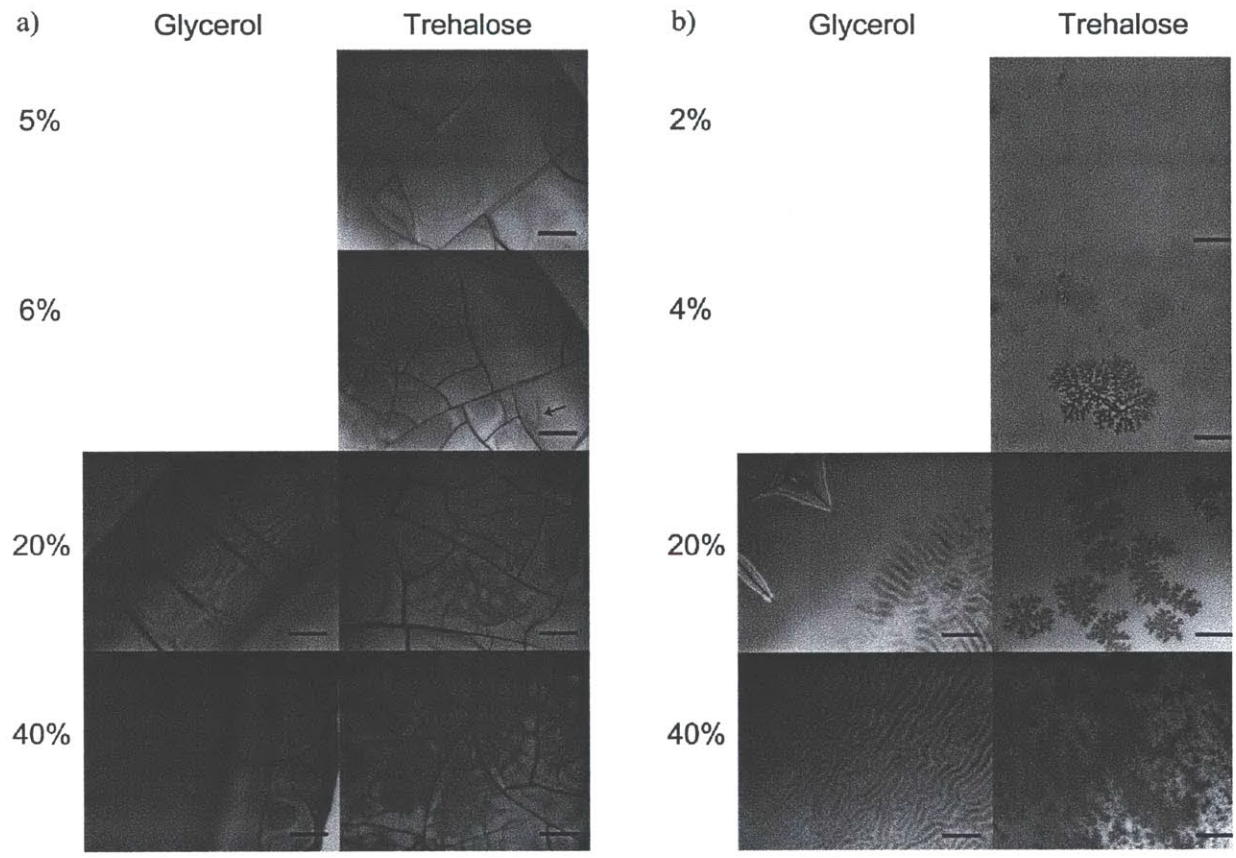

Figure C-7. Optical microscopy images of solid state (a) mCherry and (b) PNIPAM blends with glycerol and trehalose. While glycerol does not show signs of phase separation from mCherry, it does phase separate from PNIPAM. Trehalose also macrophase separates from PNIPAM and shows the same needle-like macrophase separated structures in mCherry as were observed in the block copolymer. Onset of macrophase separation of trehalose begins at 6 wt% trehalose in mCherry (black arrow) and at 4 wt% in PNIPAM. Scale bar corresponds to 50 μm.

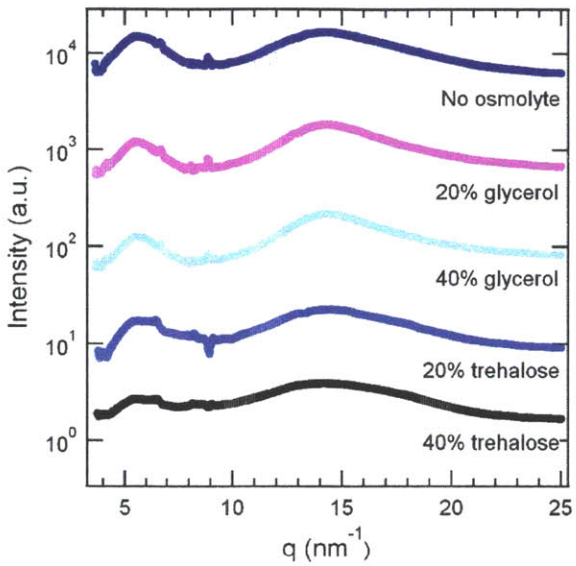

Figure C-8. Wide-angle X-ray scattering (WAXS) performed on mCherry-PNIPAM39 (f_{PNIPAM} = 0.64, PNIPAM M_n = 38.78 kg/mol, PDI = 1.10) showing little to no effect of glycerol or trehalose on the protein structure of mCherry. The broad peaks at 6 and 14 nm^{-1} are consistent with intersheet and interstrand spacing of the β-sheets in the protein, as observed previously.[1] The lack of sharp peaks corresponding to the crystal structure of trehalose indicates that trehalose is not crystallized within the self-assembled nanostructures.

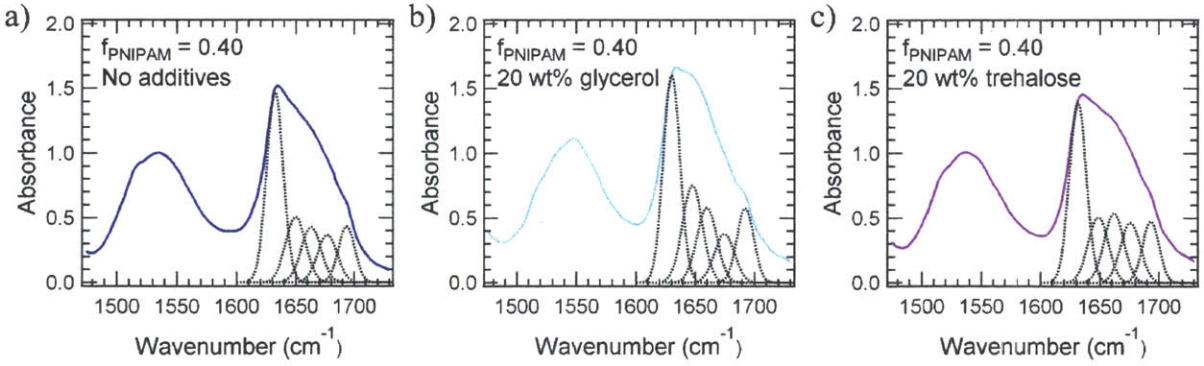

Figure C-9. Representative baseline corrected and normalized FTIR spectra for f_{PNIPAM} = 0.40 for samples containing (a) no osmolytes (b) 20 wt% glycerol (c) 20 wt% trehalose showing only small effects of glycerol and trehalose on protein secondary structure. The amide I region is shown with the Fourier self-deconvolution (FSD) overlaid.

Table C-1. Fourier self-deconvolution analysis of FTIR spectra for bioconjugates used in this study.

Sample	Average fraction helix	Average fraction sheet	Average fraction turn	Average fraction unordered
mCherry-PNIPAM14 No additives	0.190	0.513	0.109	0.188
mCherry-PNIPAM14 20% glycerol	0.177	0.515	0.091	0.218
mCherry-PNIPAM14 40% glycerol	0.149	0.503	0.086	0.262
mCherry-PNIPAM14 20% trehalose	0.215	0.483	0.122	0.179
mCherry-PNIPAM14 40% trehalose	0.218	0.471	0.123	0.187
Average for mCherry-PNIPAM14	0.190	0.497	0.106	0.207
mCherry-PNIPAM26 No additives	0.210	0.449	0.123	0.219
mCherry-PNIPAM26 20% glycerol	0.244	0.467	0.058	0.231
mCherry-PNIPAM26 40% glycerol	0.223	0.449	0.072	0.256
mCherry-PNIPAM26 20% trehalose	0.212	0.417	0.099	0.272
mCherry-PNIPAM26 40% trehalose	0.222	0.408	0.090	0.281
Average for mCherry-PNIPAM26	0.222	0.438	0.088	0.252

Volume Fraction Calculation. The PNIPAM volume fraction is calculated using the crystallographic structure of mCherry[3] (PBD ID 2H5Q) and a PNIPAM density[4] of 1.05 g/cm^3. The protein density is calculated from crystallographic data as:

$$\rho_{\text{protein}} = \left(\frac{1}{1-\phi_s}\right)\left(\frac{MW_{\text{protein, no His tag}} \cdot z}{V_{\text{unit cell}} \cdot N_A}\right)$$

The molar mass of the mCherry $MW_{\text{protein, no His tag}}$, is 26,740.4 g/mol. The number of formula units per unit cell, z, is 2. N_A is Avogadro's number and φ_s is the crystal structure water content (44.28 %). The unit cell volume, V, is calculated with the following equation:

$$V = a \cdot b \cdot c \cdot \sin(\beta)$$

where a = 4.876 nm, b = 4.285 nm, c = 6.106 nm, and β = 112.31°.

The volume fraction of PNIPAM in the block copolymers is then calculated as:

$$f_{\text{PNIPAM}} = \frac{\dfrac{MW_{\text{PNIPAM}}}{\rho_{\text{PNIPAM}}}}{\dfrac{MW_{\text{PNIPAM}}}{\rho_{\text{PNIPAM}}} + \dfrac{MW_{\text{protein, Hi tag}}}{\rho_{\text{protein}}}}$$

where the protein molecular weight now includes a 6x His tag ($MW_{\text{protein, His tag}}$ = 28,134.48 g/mol).

References

1. C. S. Thomas, M. J. Glassman and B. D. Olsen, *ACS Nano*, 2011, **5**, 5697-5707.
2. C. S. Thomas, L. Xu and B. D. Olsen, *Biomacromolecules*, 2012, **13**, 2781-2792.
3. X. K. Shu, N. C. Shaner, C. A. Yarbrough, R. Y. Tsien and S. J. Remington, *Biochemistry*, 2006, **45**, 9639-9647.
4. L. Zhang, E. S. Daniels, V. L. Dimonie and A. Klein, *J. Appl. Polym. Sci.*, 2010, **118**, 2502-2511.

Appendix D:

Supporting Information for

Chapter 6: Coil Fraction-Dependent Phase Behavior of a Model Globular Protein-Polymer Diblock Copolymer

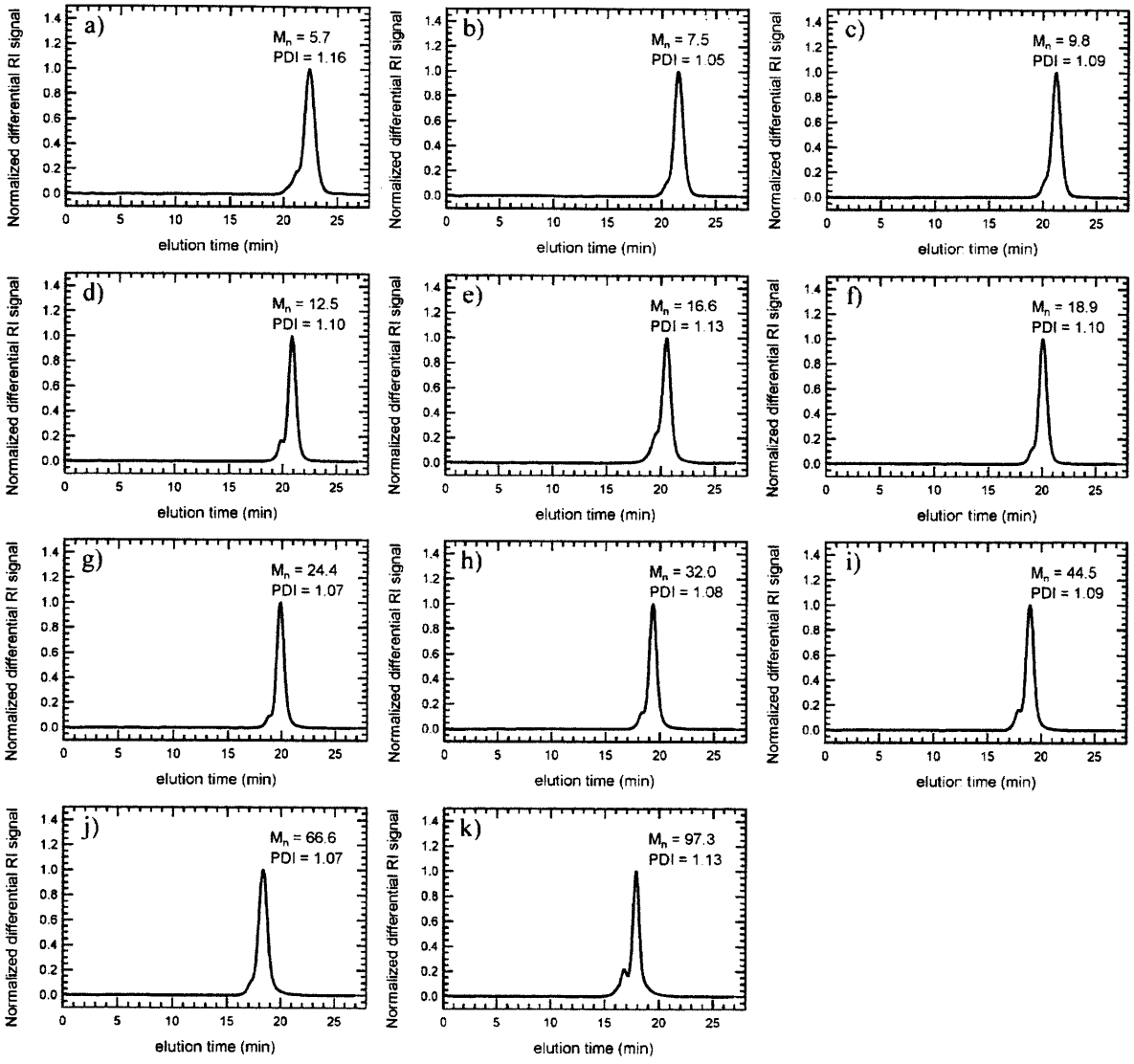

Figure D-1. Gel permeation chromatography traces of each deprotected poly(N-isopropyl acrylamide) (PNIPAM) used in this study. Three columns were used to enhance resolution, and light scattering detectors were used to determine the absolute molecular weights. The small peak (< 6% of total polymer mass) at twice the average molecular weight present in all traces is caused by slight coupling of two polymers through the RAFT chain transfer agent.[1]

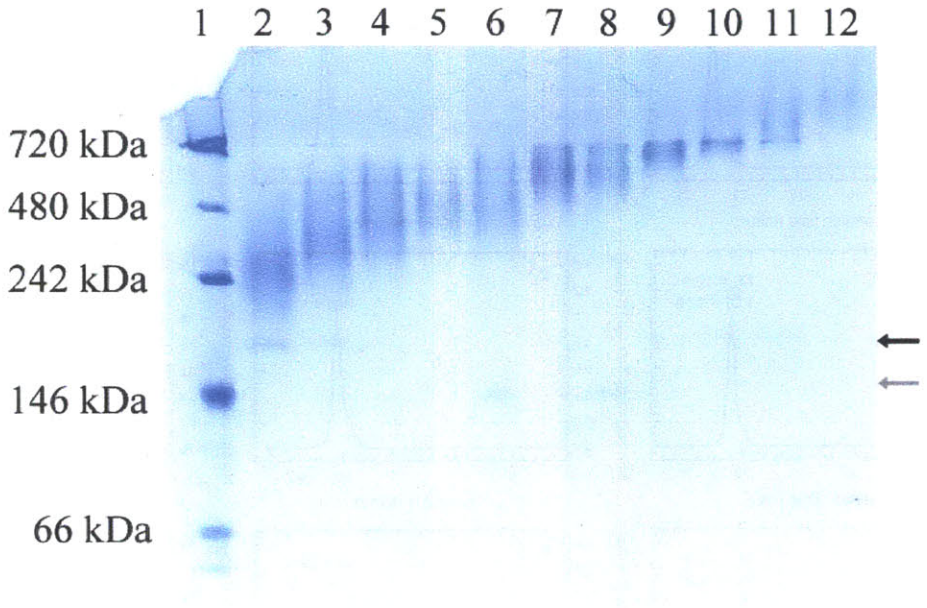

Figure D-2. Native gel of each conjugate after purification with PNIPAM coil fractions of 0.21 (lane 2), 0.26 (lane 3), 0.31 (lane 4), 0.36 (lane 5), 0.43 (lane 6), 0.46 (lane 7), 0.53 (lane 8), 0.59 (lane 9), 0.67 (lane 10), 0.75 (lane 11), and 0.82 (lane 12). Unconjugated mCherry bands correspond to protein monomers (gray arrow) and dimers (black arrow).[2] The purity of each conjugate was estimated using lane analysis software by dividing the integrated intensity resulting from the bioconjugate band by the total integrated intensity from all bands. This molar purity is then converted to a mass-based purity using the molar masses of mCherry and PNIPAM.

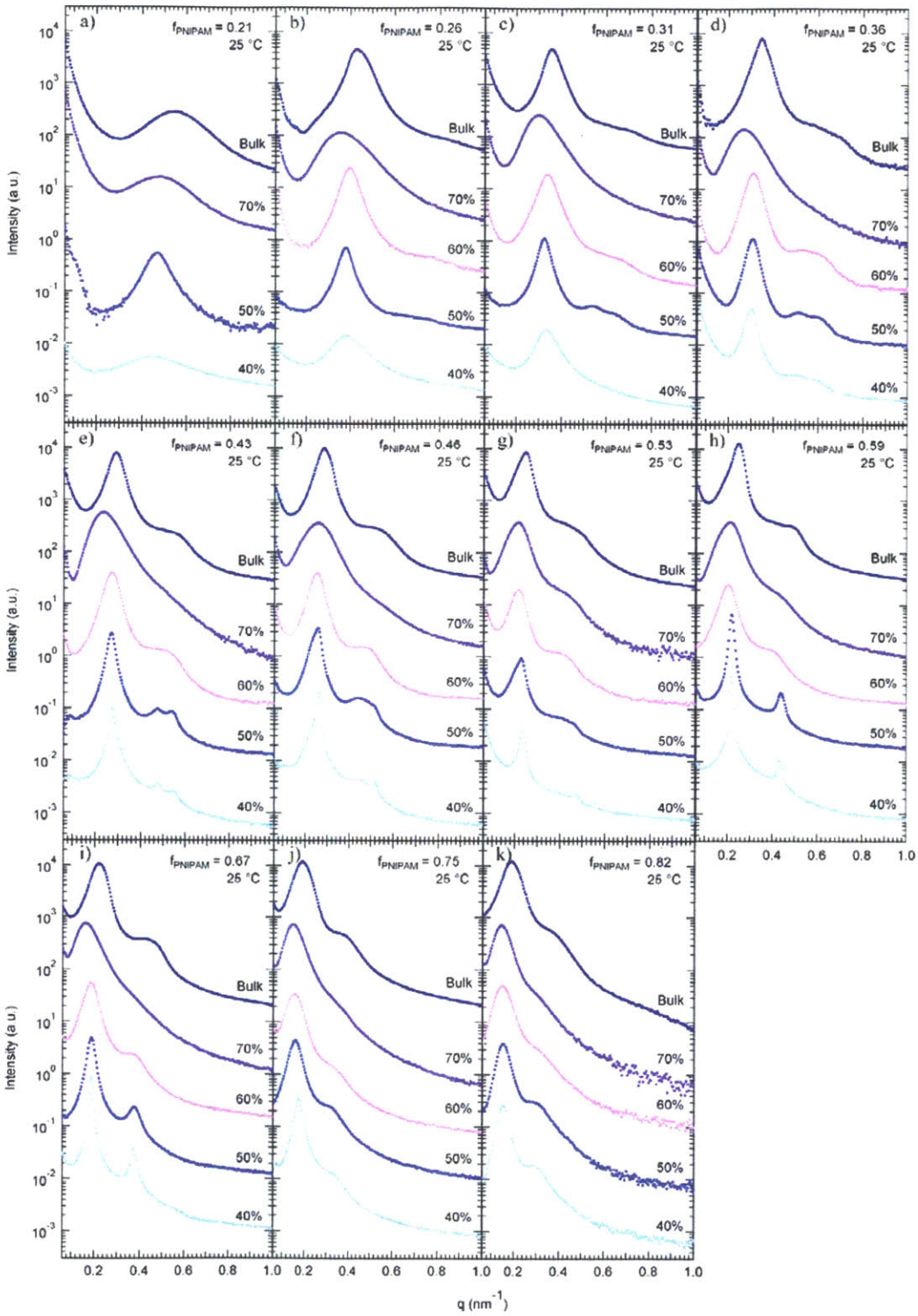

Figure D-3. SAXS of mCherry-PNIPAM block copolymers in concentrated solutions and in the bulk at 25 °C. Traces have been offset for clarity.

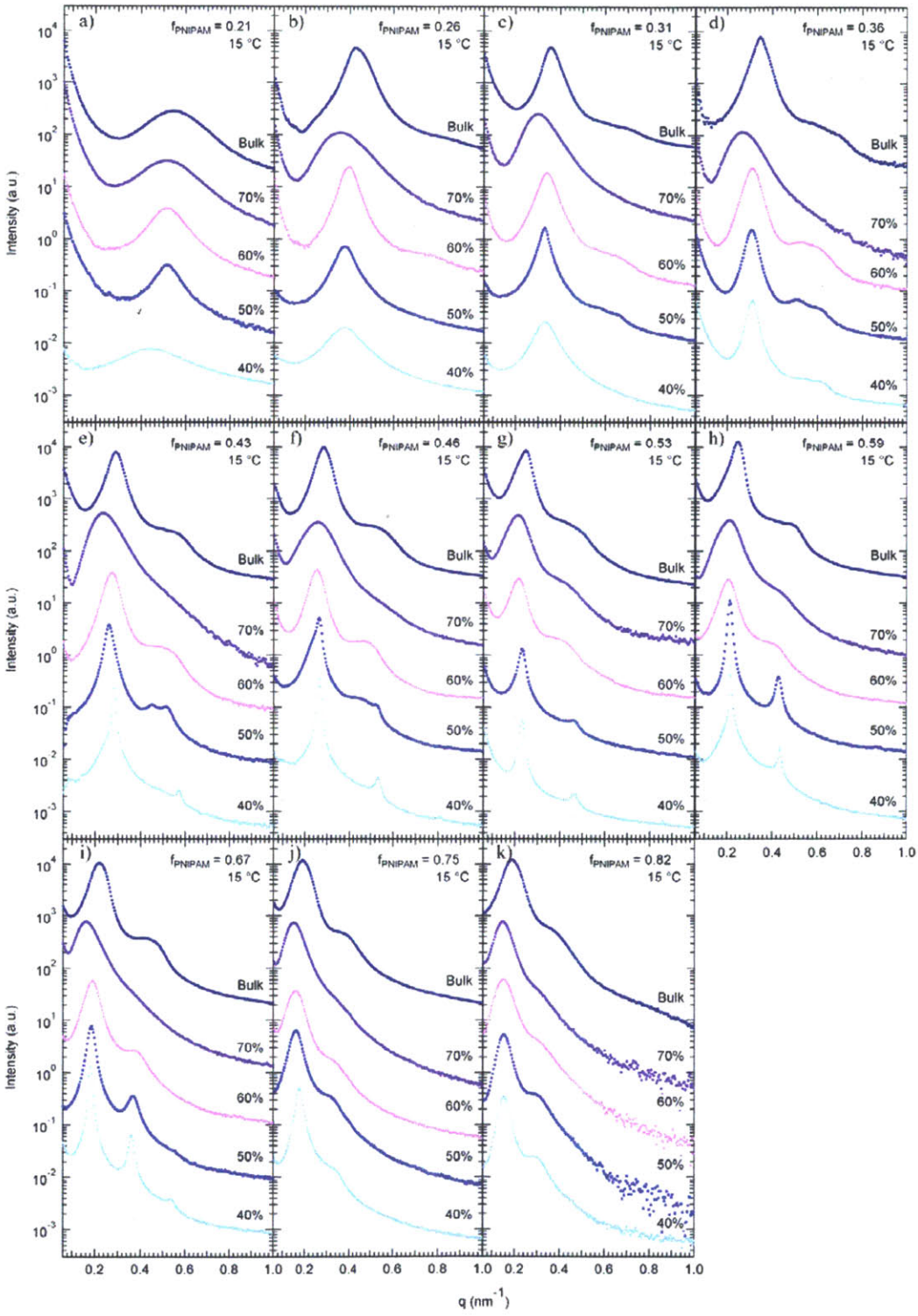

Figure D-4. SAXS of mCherry-PNIPAM block copolymers in concentrated solutions at 15 °C. Traces have been offset for clarity.

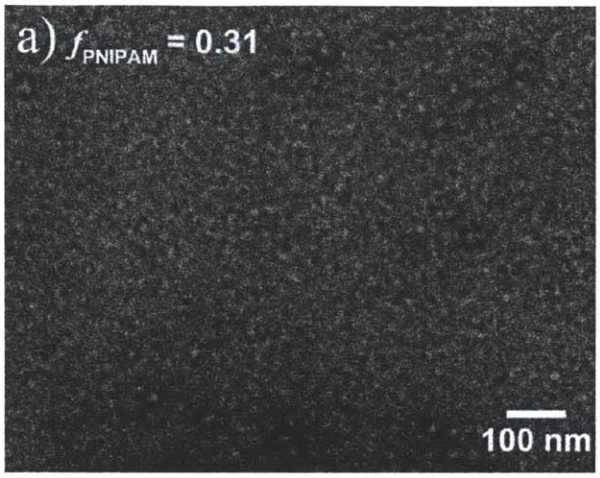

Figure D-5. TEM image of largely disordered nanostructures from mCherry-PNIPAM block copolymer with $f_{PNIPAM} = 0.31$.

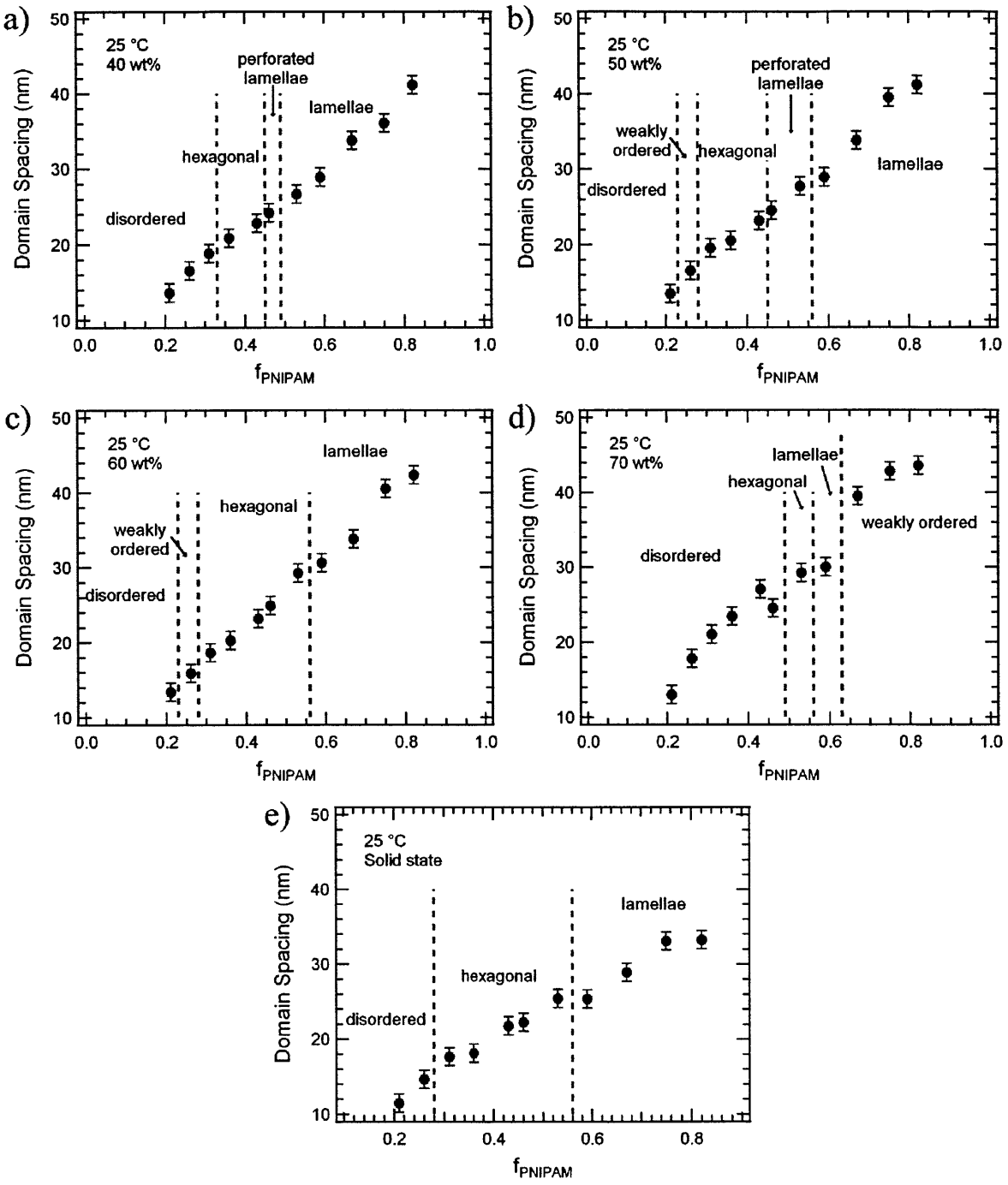

Figure D-6. Domain spacing of mCherry-PNIPAM block copolymers as a function of PNIPAM volume fraction in concentrated solutions at 25 °C and in the bulk, as measured by SAXS.

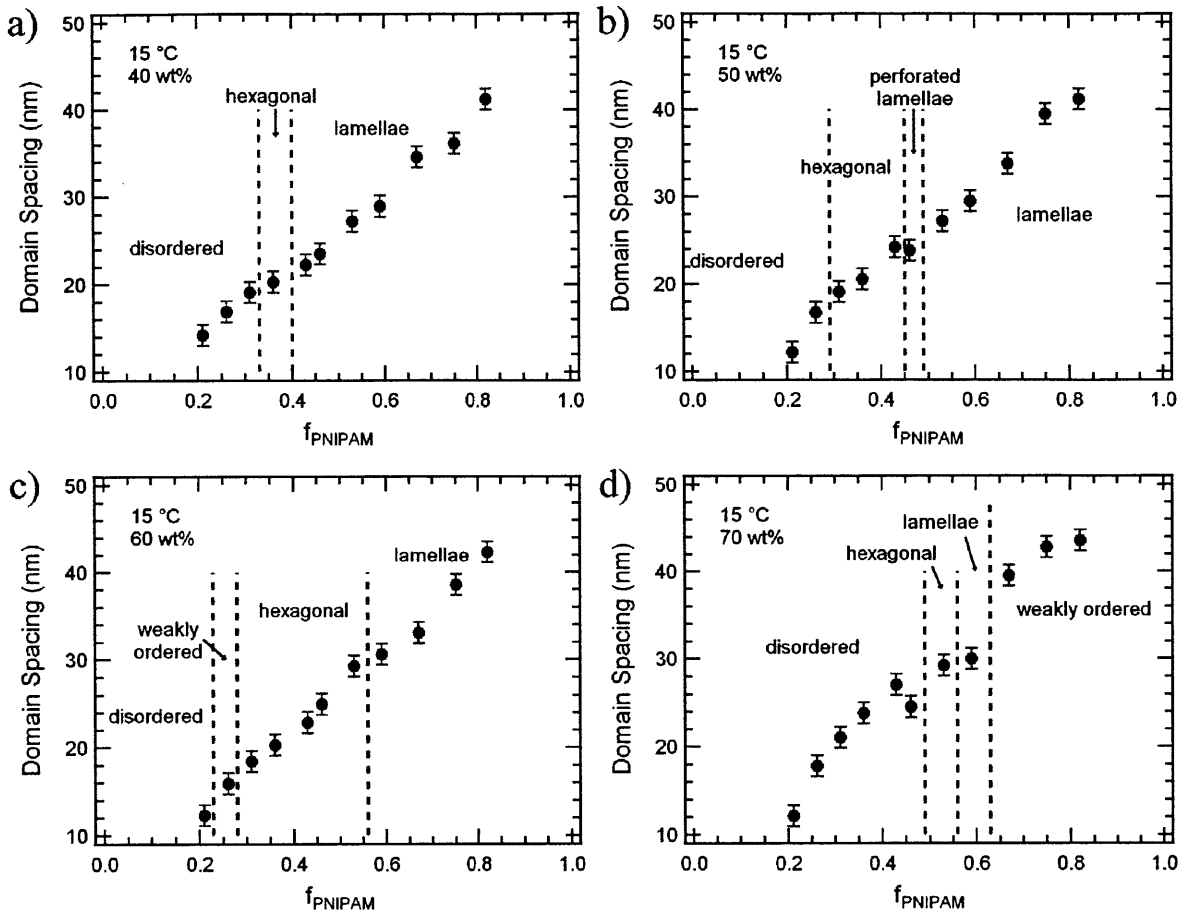

Figure D-7. Domain spacing of mCherry-PNIPAM block copolymers as a function of PNIPAM volume fraction in concentrated solutions at 15 °C, as measured by SAXS.

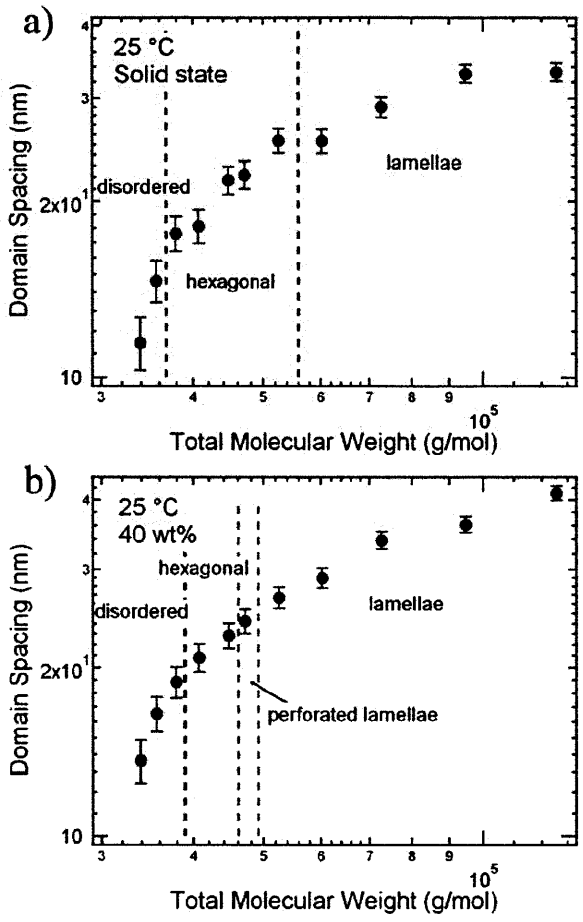

Figure D-8. Domain spacing of mCherry-PNIPAM block copolymers as a function of total molecular weight in (a) the solid state and (b) a 40 wt% solution at 25 °C, as measured by SAXS.

References

1. C. S. Thomas, M. J. Glassman and B. D. Olsen, *ACS Nano*, 2011, **5**, 5697-5707.

2. C. S. Thomas, L. Xu and B. D. Olsen, *Biomacromolecules*, 2012, **13**, 2781-2792.